APPLICATIONS OF GROUND PENETRATING RADAR TO STRUCTURAL ANALYSIS OF CARBONATE TERRACES ON THE ISLAND OF BONAIRE, CARIBBEAN NETHERLANDS

A Thesis

by

ROY DOUGLAS BOWLING

Submitted to the Office of Graduate and Professional Studies of
Texas A&M University
in partial fulfillment of the requirements for the degree of

MASTER OF SCIENCE

Chair of Committee,	Mark E. Everett
Committee Members,	Juan Carlos Laya
	Haly Neely
Head of Department,	Michael Pope

August 2017

Major Subject: Geophysics

ABSTRACT

This thesis utilized the method of ground penetrating radar to investigate the structural geology of carbonate units in relation to the evolution of the island of Bonaire, Caribbean Netherlands. Two surveys were completed on the island for this purpose: a long continuous cross-island transect, as well as a smaller set of lines that facilitated three-dimensional interpretation at an outcrop known as Seru Grandi. In the detailed processing workflow implemented for the collected datasets, steps were taken to remove unwanted signal noise, and advanced imaging techniques where then applied to generate interpretable subsurface cross-sections.

A novel numerical interpretation tool was developed for use on the cross-island transect, which adapted a traditional k-means clustering algorithm for use with structure-parallel vectors derived from structure tensors. The results of this method were utilized in defining a set of radar facies for the cross-island transect. Mapping of these radar facies identified subsurface features related to subtidal-to-foreshore depositional sequences in the southern part of the transect, a potential lagoon system in the south-central portion, eolianites within the center of the transect, and clinoforms related to platform slope deposits in the northeast portions of the survey.

Using the small-scale dataset at the Seru Grandi outcrop, subsurface geometries of a previously identified geologic unconformity were described. This unconformity was

identified here to be the remnants of a wave cut-platform occurring at the site. The specific geometry of this feature was related to external controls on wave cut-platform development. In addition, the data collected at Seru Grandi identified a set of clinoform surfaces in the subsurface below the mapped unconformity. These observations were compared to previously identified clinoforms observed on the face of the outcrop.

Observations and interpretations from both surveys in this study were used to provide additional information relating to the geologic evolution of Bonaire.

DEDICATION

To those who taught me the meaning of peace, love, and geophysics

ACKNOWLEDGMENTS

I would like to thank my advisor Dr. Mark E. Everett as well as my committee members Dr. Juan Carlos Laya and Dr. Haly Neely for their mentorship and guidance throughout my studies.

I would also like to thank those who traveled to Bonaire to aid in data collection. Specifically, I would like to Charles Stanford and Timothy de Smet, for their hard work and commitment to excellence in data acquisition.

Lastly I would like to thank my family and friends. This work would not have been possible without their encouragement and support

CONTRIBUTORS AND FUNDING SOURCES

Contributors

This work was supervised by a thesis committee consisting of Dr. Mark E. Everett [advisor] and Dr. Juan Carlos Laya of the Department of Geology and Geophysics and Dr. Haly Neely of the Department of Soil and Crop Sciences.

The data collection as outlined in Section 4.2.1 was performed in part by Dr. Mark E. Everett of the Department of Geology and Geophysics and Timothy de Smet, Ph.D. of the Department of Anthropology, Binghamton University. The data collection as outlined in Section 4.2.2 was performed in part by Charles Stanford of the Department of Geology and Geophysics. The data for the core samples listed in Section 6.1.3 as well as the digital outcrop model of Seru Grandi as analyzed in Section 6.2 were provided by Dr. Juan Carlos Laya of the Department of Geology and Geophysics.

All other work conducted for the thesis was completed by the student independently.

Funding Sources

This work was made possible in part by assistantships provided by the Department of Geology and Geophysics, and additional funding was provided by contributions from Dr. Mark E. Everett through the Howard Karren Professorship and Dr. Juan Carlos Laya of the Department of Geology and Geophysics.

TABLE OF CONTENTS

Page

LIST OF FIGURES

Page

LIST OF TABLES

Page

1. INTRODUCTION

This master's thesis aims to implement techniques and gain detailed understandings of both acquisition and processing methods for ground penetrating radar (GPR) data with express the purpose of identifying and mapping structural features of the carbonate geology on the island of Bonaire, Caribbean Netherlands. GPR operates similarly to seismic reflection in that receivers record the amplitudes of reflected energy that is propagated into the subsurface by a source. Yet in GPR, the source is an antenna radiating an electromagnetic (EM) wave, and reflections of the EM wave occur at subsurface interfaces that have a contrast in electromagnetic impedance. Typical acquisitions involve a single source and receiver pair that are moved at a fixed offset along a transect. GPR images have been shown to be useful in classifying and locating near surface targets [*Everett*, 2013]. Although, GPR is infrequently used for larger scale geologic analysis because of its shallow investigation depths, which are typically less than several meters for most earth materials [*Daniels*, 2007], and lack of scalability to surveys of large spatial extent. However, the limestone lithologies of Bonaire represent a low-attenuation material for EM energy, resulting in depths of investigation estimations to be larger than typical mediums, which facilitates geologic interpretation. In addition, Bonaire is a relatively small island, having a width of ~6km and a length of ~35km. The size of Bonaire means that it is feasible to collect GPR profiles spanning the width of island within a single transect.

To achieve the overall goal of utilizing GPR to understand the structural geology of Bonaire, two field campaigns were undertaken to acquire GPR data on the island.

The first field campaign was performed in the summer of 2015 where a 3900 m cross-island transect in the central portion was traversed. The purpose of the cross-island transect was to identify features that provide insight into the regional-scale geologic evolution of Bonaire over time. Given that the cross-island transect is a large volume of high resolution data, a specialized k-means clustering algorithm was designed to help provide confidence and consistency in identifying structural geometries across the dataset.

The second field campaign was performed in the summer of 2016 with the goal of acquiring data at the outcrop scale. During this second session of field work, four intersecting transects were collected at the Seru Grandi outcrop located in the northern region of the island. Utilizing the data collected at Seru Grandi, subsurface structural geometries for the carbonate successions comprising the outcrop were mapped. As this site is well exposed and is the subject of other recent [*Laya et al.*, 2015; *Sulacia et al.*, 2015] and current [*Laya et al.*, 2017] research efforts, opportunities exist for ground-truthing observations and interpretations.

This project represents the first set of geophysical investigations aimed at characterizing the subsurface geologies on the interior of the island of Bonaire. As such, implications exist for corroboration and modification of previous interpretations of the island geologies.

2. GEOLOGIC BACKGROUND

The island of Bonaire is located in the Southern Caribbean as part of the Leeward Antilles islands (Figure 1). Formerly part of the Netherlands Antilles, Bonaire is a now special municipality within the Netherlands.

Geographic Location of Bonaire

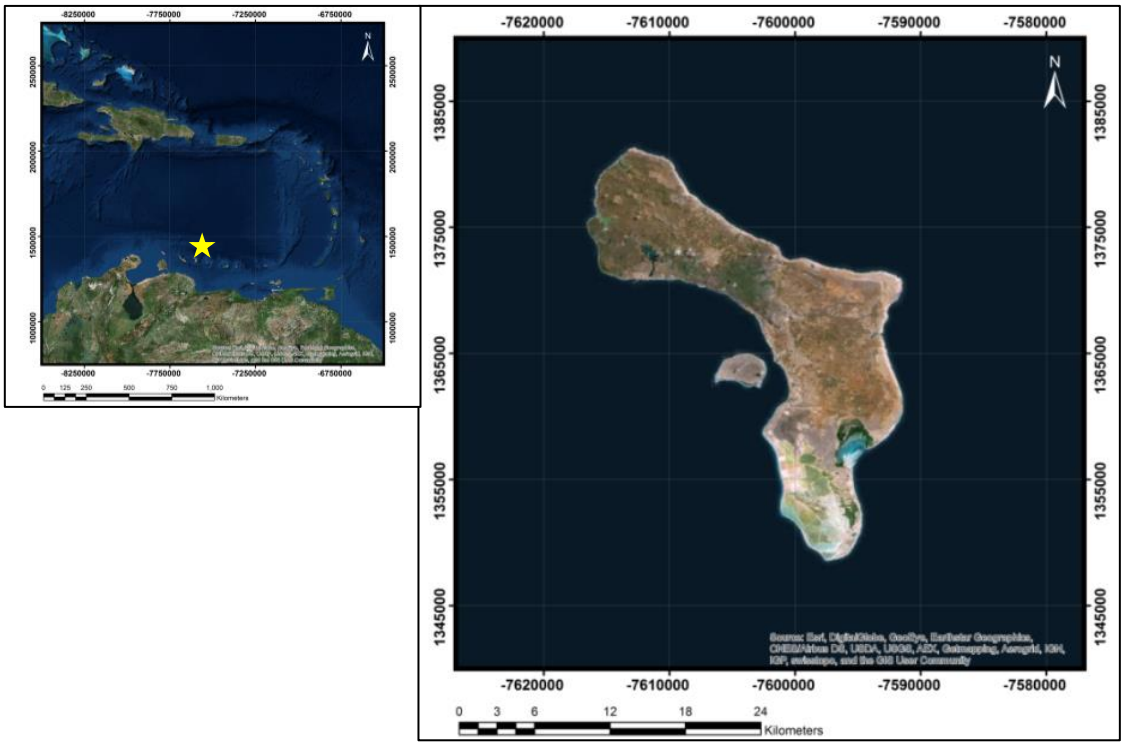

Figure 1: Geographic location of Bonaire. **(top left)** Southern Caribbean showing island of Bonaire as yellow star off of the west coast of Venezuela. **(right)** Island of Bonaire.

Geologically, the island is composed of a Cretaceous volcanic basement overlain by Paleogene to Quaternary carbonate rocks [*de Buisonjé*, 1974]. The volcanic basement has been attributed to volcanism resulting from the shallow subduction of the Caribbean

plate beneath the South American plate which created the South Caribbean deformed belt and the Leeward Antilles ridge [*Van der Hilst and Mann*, 1994; *Hippolyte and Mann*, 2011]. Uplift and erosion caused deposition of clastic sediments such a marls on the volcanic slopes, with consistent carbonate factory production beginning sometime in the middle Eocene with the deposition of the Rincon Limestone [*Hippolyte and Mann*, 2011] on the island. The Miocene saw the deposition of an extensive carbonate unit across Bonaire and neighboring islands, Aruba and Curaçao, called the Sero Domi Formation. Continued tectonic activity along the Caribbean-South American plate boundary has caused uplift of the island, resulting in progradation and exposure of Pliocene-Pleistocene carbonate successions that overly older units [*Hippolyte and Mann*, 2011; *Sulaica*, 2015]. Previous workers have mapped the geologic units present on the island today; showing a significant majority of the island being covered by Pliocene-Pleistocene carbonate terraces [*Bandoian and Murray*, 1974; *de Buisonjé*, 1974; *Hippolyte and Mann*, 2011; *Sulaica*, 2015]. Four distinct terraces have been mapped on the island (Figure 2c). These features exist due the uplift from tectonic forces causing exposure of carbonate reefs followed by erosion by wave action [*Sulaica*, 2015]. In addition to the few outcrops of volcanic units among the terraced carbonates, serval maps show outcroppings of the Miocene-aged Seroe Domi formation trending south along Boanire's western coast. Serval patches of eolian sediments have also been observed and mapped in the central part of the island. Hypothesis for origins of these sediments is trade-wind carried calcareous sand from early east-coast beaches on Bonaire [*de Buisonjé*, 1974]. Also, geologic mapping as included the small subaerially

exposed reef known as Klien Bonire, located to the west of mainland Bonaire, in interpretations of the Plio-Pleistocene deposits (Figure 2a). Recent work on the island, done by *Sulaica* [2015], includes lithofacies mapping (Figure 2b) and environment of deposition (EOD) descriptions for the observed lithologies. Even more recently, work by *Laya et al.* [2015, 2017] performed digital outcrop modeling of carbonate exposures and studies of the exposures of modern dolomites [*Deffeyes et al.*, 1964]. These two sets of recent studies consisted of mainly outcrop observations of corroborated by core drilling samples. Subsurface geologic information has been largely inferred from surface observations on the island due to the lack of geophysical exploration of the island. Figures 2 and 3 show geologic maps and cross-sections synthesizing the results of geologic investigations performed on Bonaire.

Geologic Maps of Bonaire

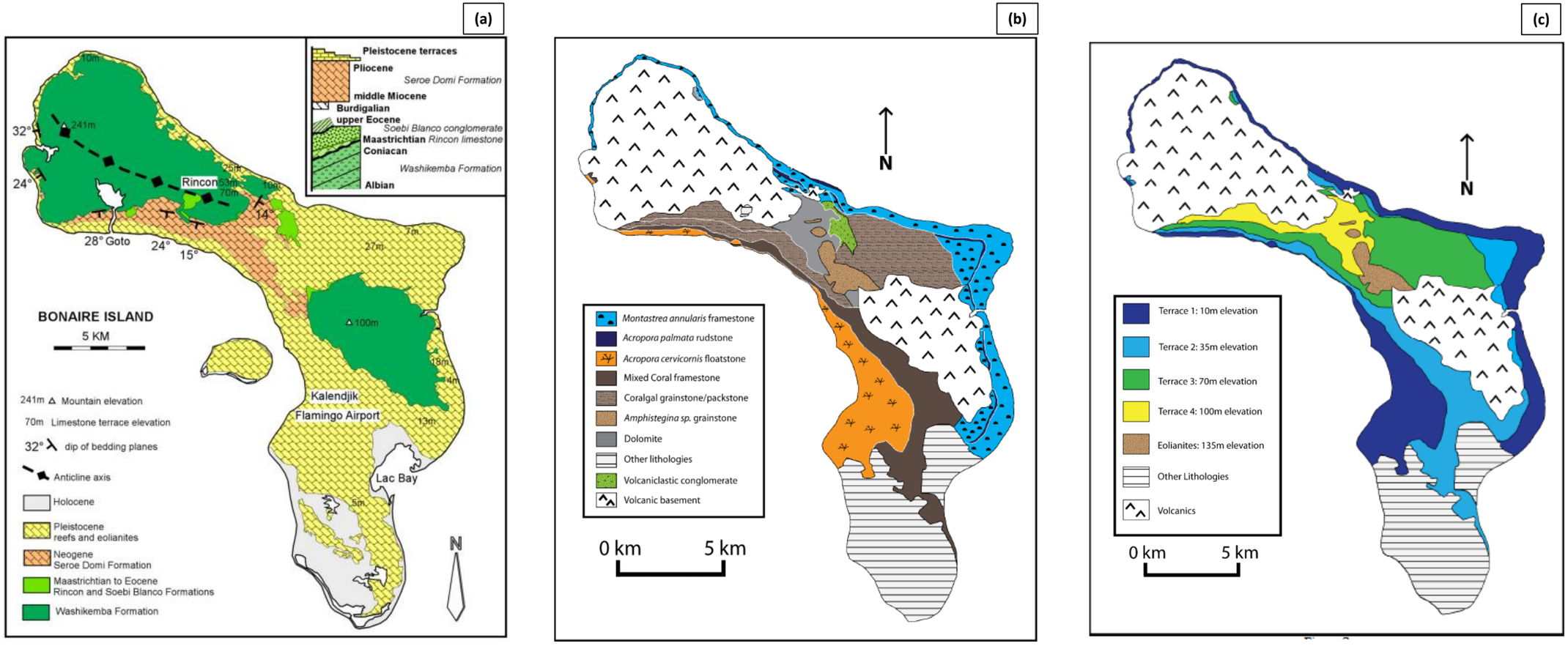

Figure 2: Geologic maps of Bonaire. **(a)** Lithologic map, (from *Hippolyte and Mann* 2011]), showing volcanics overlain by carbonate successions. **(b)** Facies distribution map of carbonate rocks. (from *Sulaica* [2015]) **(c)** Carbonate terrace map showing the four terrace morphologies as well as the eolian deposits on the island, from ([*Sulaica*, 2015]).

Geologic Cross-Section of Bonaire

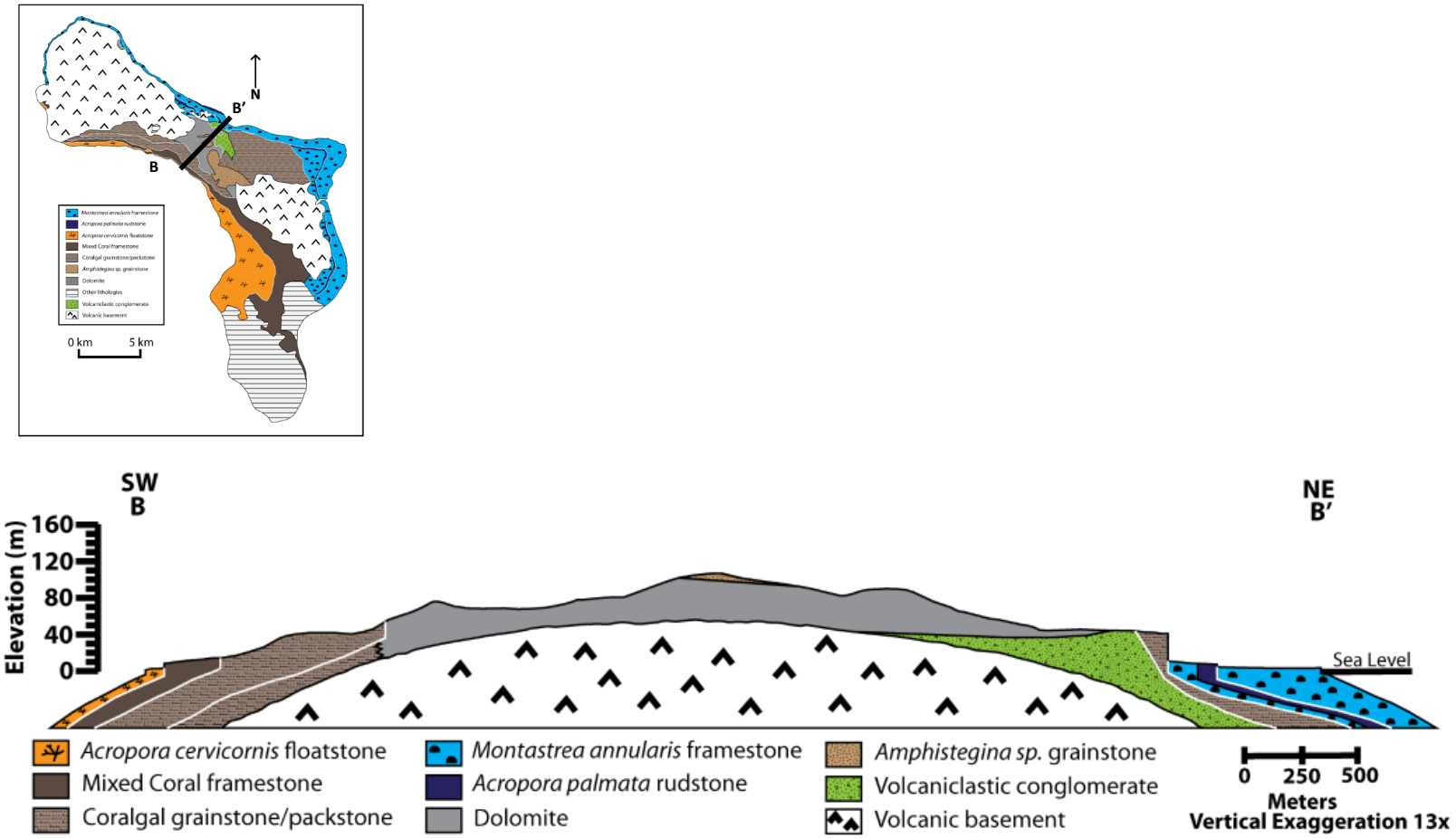

Figure 3: Geologic cross-section of Bonaire. Cross section showing distribution of mapped lithofacies occurring across the center of the island. From *Sulaica*, [2015])

3. THE GROUND PENETRATING RADAR METHOD

Ground penetrating radar (GPR) is an active source geophysical method, in which electromagnetic (EM) waves are radiated, in the form of a pulse, from a transmitting antenna (TX), and propagate through the subsurface. These waves also decay with time due to attenuation characteristics of the subsurface materials. Similarly to seismic methods, contrasts in material properties of the earth (here electromagnetic impedance) causes some of the source energy to be reflected. This reflected energy travels back to the surface where some of it is recorded with a corresponding receiving antenna (RX) (Figure 4a). This recorded energy is stored as a digital signal trace indicating voltage induced in the receiving antenna (often described as amplitude) versus time (Figure 4b).

Illustration of the Ground Penetrating Radar Method

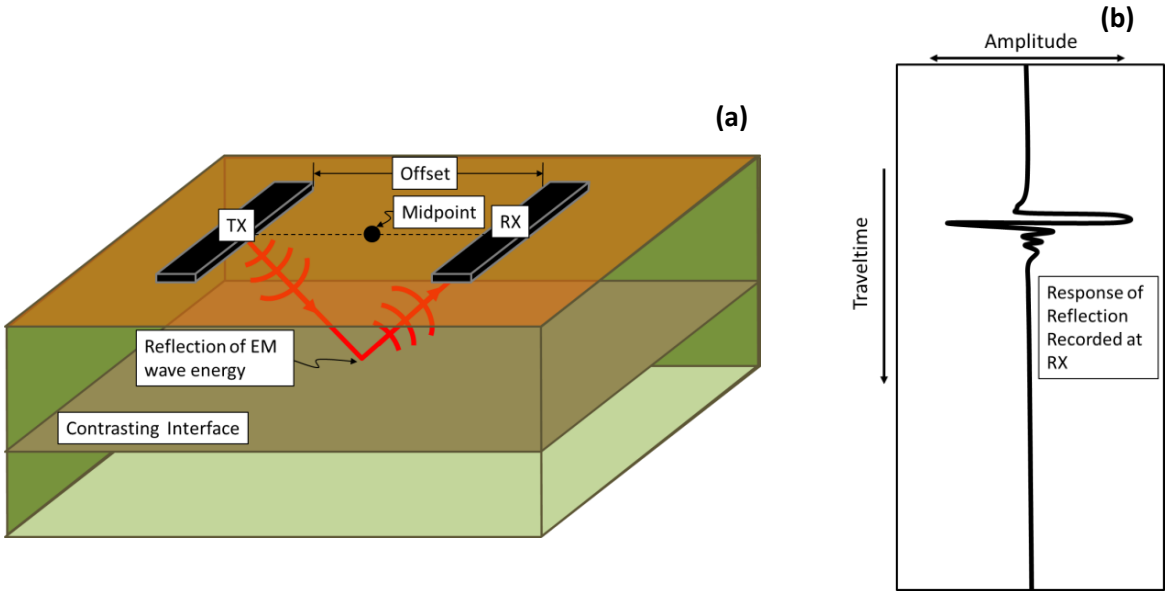

Figure 4: Schematic illustration of the GPR method. **(a)** Cartoon describing the reflection of EM energy from a dipole-style transmitting antenna at an interface of electrical impedance contrast, and subsequent recording of the reflected energy at a corresponding receiving antenna. **(b)** Illustration of recorded reflected EM wave as a function of wave traveltime and amplitude

3.1 Electromagnetic Theory

The governing relations describing electromagnetic fields are Maxwell's equations, and for fields present in matter, where charge densities and current can exist, they can be written as [*Griffiths*, 1999]:

$$\nabla \cdot \boldsymbol{D} = \rho_f \,, \tag{1}$$

$$\nabla \cdot \boldsymbol{B} = 0, \tag{2}$$

$$\nabla \times \boldsymbol{E} = -\frac{\partial \boldsymbol{B}}{\partial t}, \tag{3}$$

$$\nabla \times \boldsymbol{H} = \boldsymbol{J}_f + \frac{\partial \boldsymbol{D}}{\partial t}. \tag{4}$$

In the previous equations, $\boldsymbol{D}$ is the electric displacement field in the material, ρ_f is the free-charge density, $\boldsymbol{B}$ is the magnetic field, $\boldsymbol{E}$ is the electric field, $\boldsymbol{H}$, from the notation by [*Griffiths*, 1999], is the auxiliary magnetic field, and $\boldsymbol{J}_f$ is the free-current density. To describe how specific materials respond to the electromagnetic fields as shown in Maxwell's equations, a set of constitutive relationships, for linear media, are defined as,

$$\boldsymbol{J}_f = \sigma \boldsymbol{E}, \tag{5}$$

$$\boldsymbol{D} = \varepsilon \boldsymbol{E}, \tag{6}$$

$$\boldsymbol{B} = \mu \boldsymbol{H}. \tag{7}$$

Here σ is the bulk electrical conductivity (S/m) of a material, ε is the electrical permittivity (F/m), and μ is the magnetic permeability (H/m) [*Annan*, 2009]. The material properties σ, ε, and μ given in Equations (5)-(7) are in general complex-valued for time-harmonic excitation and can vary spatially in inhomogeneous or with direction in anisotropic media [*Cassidy*, 2009a].

From *Griffiths* [1999], the electrical permittivity can be written as $\varepsilon = \varepsilon_0 \varepsilon_r = \varepsilon_0(1 + \chi_e)$, where ε_0 is the permittivity of free space, and ε_r is the relative permittivity

which is related to χ_e, the material electric susceptibility. The magnetic permeability can also be rewritten as $\mu = \mu_0\mu_r = \mu_0(1 + \chi_m)$ with μ_0 being the permeability of free space, and χ_m being the magnetic susceptibility of the material. For most geologic media, the relative permittivity, $\varepsilon_{r,}$ is in the range of 1-30 [*Cassidy*, 2009a], and the effect of magnetic susceptibly, χ_m, is small [*Olhoeft*, 1998; *Cassidy*, 2009a] such that it is normally assumed $\mu = \mu_0$ for GPR applications.

Following a similar derivation to *Griffiths* [1999], Maxwell's equations can be decoupled by first applying the constitutive relationships to $\boldsymbol{J}$, $\boldsymbol{D}$, and $\boldsymbol{H}$ in Equations (1) and (4) respectively, to give a set of equations only in terms of $\boldsymbol{E}$ and $\boldsymbol{B}$:

$$\nabla \cdot \boldsymbol{E} = \frac{\rho_f}{\varepsilon}, \tag{8}$$

$$\nabla \times \boldsymbol{B} = \mu\sigma\boldsymbol{E} + \mu\varepsilon\frac{\partial \boldsymbol{E}}{\partial t}. \tag{9}$$

Taking the curl of (3) results in,

$$\nabla \times \nabla \times \boldsymbol{E} = -\frac{\partial}{\partial t}(\nabla \times \boldsymbol{B}). \tag{10}$$

Substituting (9) into (10) then gives,

$$\nabla \times \nabla \times \boldsymbol{E} = -\mu\sigma \frac{\partial \boldsymbol{E}}{\partial t} - \mu\varepsilon \frac{\partial^2 \boldsymbol{E}}{\partial t^2}. \tag{11}$$

A similar exercise by taking the curl of (9) and then substituting (3) results in,

$$\nabla \times \nabla \times \boldsymbol{B} = -\mu\sigma \frac{\partial \boldsymbol{B}}{\partial t} - \mu\varepsilon \frac{\partial^2 \boldsymbol{B}}{\partial t^2}. \tag{12}$$

Using the vector identity, $\nabla \times \nabla \times \boldsymbol{A} = \nabla(\nabla \cdot \boldsymbol{A}) - \nabla^2 \boldsymbol{A}$, (11) and (12) can be respectfully rewritten as,

$$\nabla(\nabla \cdot \boldsymbol{E}) - \nabla^2 \boldsymbol{E} = -\mu\sigma \frac{\partial \boldsymbol{E}}{\partial t} - \mu\varepsilon \frac{\partial^2 \boldsymbol{E}}{\partial t^2}, \tag{13}$$

$$\nabla(\nabla \cdot \boldsymbol{B}) - \nabla^2 \boldsymbol{B} = -\mu\sigma \frac{\partial \boldsymbol{B}}{\partial t} - \mu\varepsilon \frac{\partial^2 \boldsymbol{B}}{\partial t^2}. \tag{14}$$

Now assuming the fields exist in a region without any free-charge density, or this density has dissipated in a time characteristic for a given medium [*Griffiths*, 1999], Equation (8) becomes,

$$\nabla \cdot \boldsymbol{E} = 0. \tag{15}$$

By respectively substituting Equations (15) and (2) into the first terms on the left hand sides of Equations (13) and (14), this derivation arrives at the damped vector wave equations for $\boldsymbol{E}$ and $\boldsymbol{B}$,

$$\nabla^2 \boldsymbol{E} = \mu\sigma \frac{\partial \boldsymbol{E}}{\partial t} + \mu\varepsilon \frac{\partial^2 \boldsymbol{E}}{\partial t^2}, \tag{16}$$

$$\nabla^2 \boldsymbol{B} = \mu\sigma \frac{\partial \boldsymbol{B}}{\partial t} + \mu\varepsilon \frac{\partial^2 \boldsymbol{B}}{\partial t^2}. \tag{17}$$

The second term on the right-hand-side of both Equations (16) and (17) contains the dielectric permittivity, which describes the energy storage ability of a medium facilitating wave propagation [*Olhoeft*, 1998]. Whereas the first term contains the conductivity, which describes a material's ability to dissipate energy through charge motion [*Olhoeft*, 1998], damping the EM waves. GPR operates most effectively when the energy dissipation terms in the wave equations are small compared to the propagative terms, thus allowing the electromagnetic waves to travel and reflect within the earth.

3.2 Depth of Investigation

The depth of investigation for GPR is defined here in as the depth at which a reflected arrival can be distinguished from background noise in a radar time series observed at the surface. Insights into depths of investigation, and consequently the suitability for GPR at a given survey location, can be gained by examining the attenuation, and reciprocally the

skin-depth, for propagating damped EM waves. However, the depth of investigation depends on many other factors than attenuation, including: transmitter power, the presence of site-specific electromagnetic noise, RX sensitivity, etc., and can often be qualitatively assessed only after acquisition and examination of data.

Using the notation provided by *Griffiths* [1999], plane wave solutions of a constant frequency, ω, to the vector wave equation in $\boldsymbol{E}$ (Equation (12)) have the form

$$\boldsymbol{E}(\boldsymbol{r}, t) = E_0 e^{i(\boldsymbol{k}\cdot\boldsymbol{r}-\omega t)}\hat{\boldsymbol{n}}. \tag{18}$$

Here the electric field at observation location $\boldsymbol{r}$ has an exponential form where E_0 is the amplitude of the electric field, $\boldsymbol{k}$ is the wavenumber vector, which points in the direction of propagation, and $\hat{\boldsymbol{n}}$ is the direction of polarization of the electric field given the vectoral nature of electromagnetic waves. Plane wave solutions to the wave equation for $\boldsymbol{B}$ have a similar form, although the polarization direction is orthogonal to both the propagation direction and the polarization of $\boldsymbol{E}$**.** This orthogonality can be seen by the relationship between the curl of the electric field, and the magnetic field in Equation (3). For simplicity, further analysis in this section will focus only on the plane wave solution for the electric field (Equation (18)). It must be noted that plane wave solutions to the damped vector wave equation approximate wave-fields created by GPR systems only in the far-field, otherwise radiation patterns of the antennas need to be considered [*Annan*, 1973].

The magnitude, k, of the wavenumber vector, $\boldsymbol{k}$, can be decomposed into its real and imaginary components as shown in *Griffiths* [1999], and *Everett* [2013],

$$|\boldsymbol{k}| = k = \beta + i\alpha, \tag{19}$$

with real component, β, relating to the velocity of the wave via, $v = \omega/\beta$, and the imaginary component, α, describing the attenuation of the wave with the form:

$$\alpha = \omega \left[\frac{\varepsilon\mu}{2} \left(\sqrt{1 + \left(\frac{\sigma}{\varepsilon\omega} \right)^2} - 1 \right) \right]^{1/2}. \tag{20}$$

Under the so called low-loss approximation where $\sigma \ll \varepsilon\omega$ for the medium through which the EM wave is propagating, (20) is approximated by [*Griffiths*, 1999],

$$\alpha \cong \frac{\sigma}{2} \sqrt{\frac{\mu}{\varepsilon}}. \tag{21}$$

However, when the conductivity term in (20) dominates such that $\sigma \gg \varepsilon\omega$, attenuation is approximated as,

$$\alpha \cong \sqrt{\frac{\omega\mu\sigma}{2}}. \tag{22}$$

Examples of very poor conductors where the low-loss approximation of attenuation is valid include pure deionized water, whereas excellent conductors such as metals allow for the use of the high-loss approximation [*Griffiths*, 1999]. The electromagnetic properties of geologic materials can vary widely however. Limestones for example may largely be considered poor conductors, where conductivity is on the order of $5x10^{-4}$-0.002 S/m compared to $\varepsilon\omega$, which has a range of 0.002-0.4 [*Davis and Annan*, 1989]. In contrast, clay materials have relatively high conductivity 0.002-1 S/m compared to their range for $\varepsilon\omega$, which is 0.002-3 [*Davis and Annan*, 1989]. To avoid confusion and eliminate the need to classify geologic materials as either low or high-loss, further analysis of attenuation will focus on the full expression derived from the imaginary component of the wavenumber shown in Equation (20).

Permittivity can be defined as complex and frequency-dependent,

$$\varepsilon^*(\omega) = \varepsilon'(\omega) - i\varepsilon''(\omega). \tag{23}$$

with the imaginary component representing energy loss due to dielectric relaxation [*Olhoeft*, 1998]. *Annan*, [1996] redefines conductivity and permittivity as,

$$\sigma = \sigma_{DC} + \omega\varepsilon(\omega)'', \tag{24}$$

$$\varepsilon = \varepsilon(\omega)', \tag{25}$$

where σ_{DC} is the conductivity measured under a static electric field. Although both free and bound charge effects are combined, this redefinition expressly illustrates that attenuation due to dielectric loss is indistinguishable in experimental measurements from losses due to an increase in conductivity [*Annan*, 1996]. Thus, from Equations (24) and (25), measurements used to examine attenuation in this section contain both dielectric losses as well as conductive losses.

As mentioned previously, the inverse of attenuation is known as the skin-depth,

$$\delta = \frac{1}{\alpha}. \tag{26}$$

This is the depth at which the amplitude of a propagating plane EM wave has decreased by a factor of $1/e$ from its original amplitude [*Reynolds*, 1997].

To understand this property I terms of GPR, skin-depth was computed for both limestones and clay materials as shown in Figure 5.

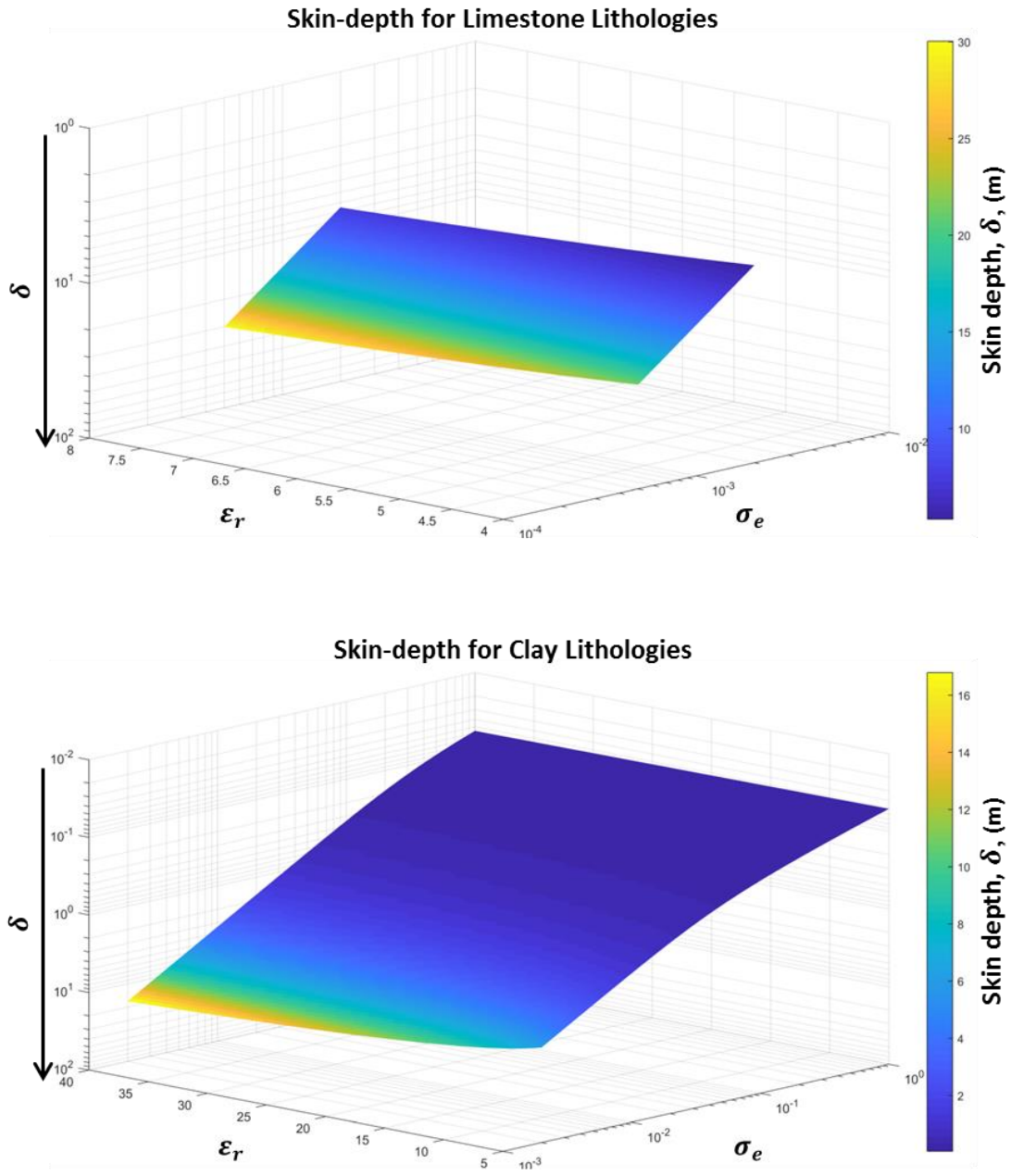

Figure 5: Skin-depth as a function of conductivity and relative dielectric permittivity. **(a)** Skin-depth for limestones. **(b)** Skin-depth for clay materials. Both plots computed using Equation (20).

The conductivities and permittivities used in Figure 5 come from observations by *Davis and Annan* [1989] using EM waves at 100 MHz. The range of reported conductivities for limestone is $5x10^{-4}$-0.002 S/m and corresponding range of relative permittivities is 4-8. The ranges of conductivities and relative permittivities reported for clay materials are 0.002-1 S/m and 4-50, respectively.

The geometric mean for skin-depths of limestone in Figure 5a is 13 m. In contrast, skin-depths for clay materials (Figure 5b) are considerably less than for limestones, having a geometric mean of only 0.6 m. In terms of attenuation characteristics, this suggests that limestone lithologies represent a material that is relatively well suited for using GPR as a subsurface imaging tool.

Until this point, the discussion has been focused on EM waves propagating as plane waves (Equation (14)). It must be noted that, in general, a dipole antenna (as shown in Figure 4a) produces a radiation pattern that in the far-field locally approximates a spherical wave [*Everett*, 2013]. For spherical EM waves, amplitude also decays as $1/r$, where r is the distance from the source [*Griffiths*, 1999]. This decay, known as spherical divergence, will affect the depth of investigation for a given GPR survey in addition to attenuation due to the subsurface material properties

4. FIELD WORK

4.1 Common-Offset Acquisition

Common-offset survey geometry was used for the GPR data acquisition in this study. Here, the TX and the RX are kept a fixed distance (offset) apart. By moving both the TX and RX in unison during acquisition, a set of traces can be recorded to create a two-dimensional (2D) image, known as a time section, of the reflected electromagnetic energy along a transect. Each trace comprising this time section is positioned at the midpoint between the TX and RX (Figure 4a). This survey geometry was chosen mainly for its speed of acquisition and ease of set-up. Carts or sleds carrying the equipment, including the TX, RX, and corresponding data-logger can be moved quickly using few people as seen in Figure 6. Using the common-offset set up, two individuals were tasked with moving the TX-RX assembly to each midpoint location along the line, while another individual was responsible for triggering the transmitter to radiate the EM signal from the source at each position.

Common Offset Acquisition

Figure 6: Common-offset acquisition. Showing two individuals (left and right) moving the equipment along a transect with another (center) operating the transmitter trigger and data logger, (foreground). Black arrow indicating transect direction.

As can be seen in Figure 6, acquisition efficiency at the survey site was optimized by having each operator perform a specific task, thus allowing relatively large survey distances to be covered in short periods of time. The GPR equipment used in this field work was the Sensors and Software PulseEKKO PRO system with specifications listed in Table 1.

GPR System Specifications

System Specification	Value
Manufacturer	Sensors and Software
Model	PulseEKKO PRO
Transmitter Voltage (V)	1000/400*
Antenna Style	Horizontal Dipole
Antenna Center Frequency (Hz)	100 MHz

*1000 V transmitter used along cross-island transect, whereas 400 V transmitter used at Seru Grandi.

Table 1: List of GPR system specifications used in this study.

4.2 Surveys

Two separate GPR surveys were performed for this project, each of which was completed on a separate trip to the island of Bonaire. The first survey, completed between July 25th and August 1st 2015, was performed along a 4 km bike trail spanning the center of the island to give a cross-island transect (Figure 7b). This survey was designed with the goal of providing subsurface imaging for a more detailed understanding of regional-scale geologic structures in support of previous surficial mapping across this portion of the island [*de Buisonjé*, 1974; *Hippolyte and Mann*, 2011; *Sulaica*, 2015]. The weather during this trip was quire mild, with no rainfall occurring. The aridity observed is quite common for Bonaire with the mean yearly rainfall being on the order of 500 mm [*Stoffers*, 1956]. The lack of rainfall during the field campaign was important in that it kept the moisture content of the thin soil along the bike trail relatively constant. Increased water content of soil can cause scattering of EM waves

[*Everett*, 2013], and dramatic water content changes during the days of field work would have been detrimental to consistent surveying.

The second survey was performed atop the Seru Grandi outcrop in the northern portion of Bonaire (Figure 7a). Here several smaller transects were completed to provide subsurface evidence and investigations of structural features previously only observed in outcrop [*Laya et al.*, 2015, 2017; *Sulacia et al.*, 2015]. The Seru Grandi survey was completed on August 20th-28th 2016. Again, no rainfall occurred during this second field campaign. Although there is little to no soil occurring on the outcrop, the lack of rainfall kept the pore-water content of the exposed bedrock constant during surveying.

Map of GPR Survey Locations

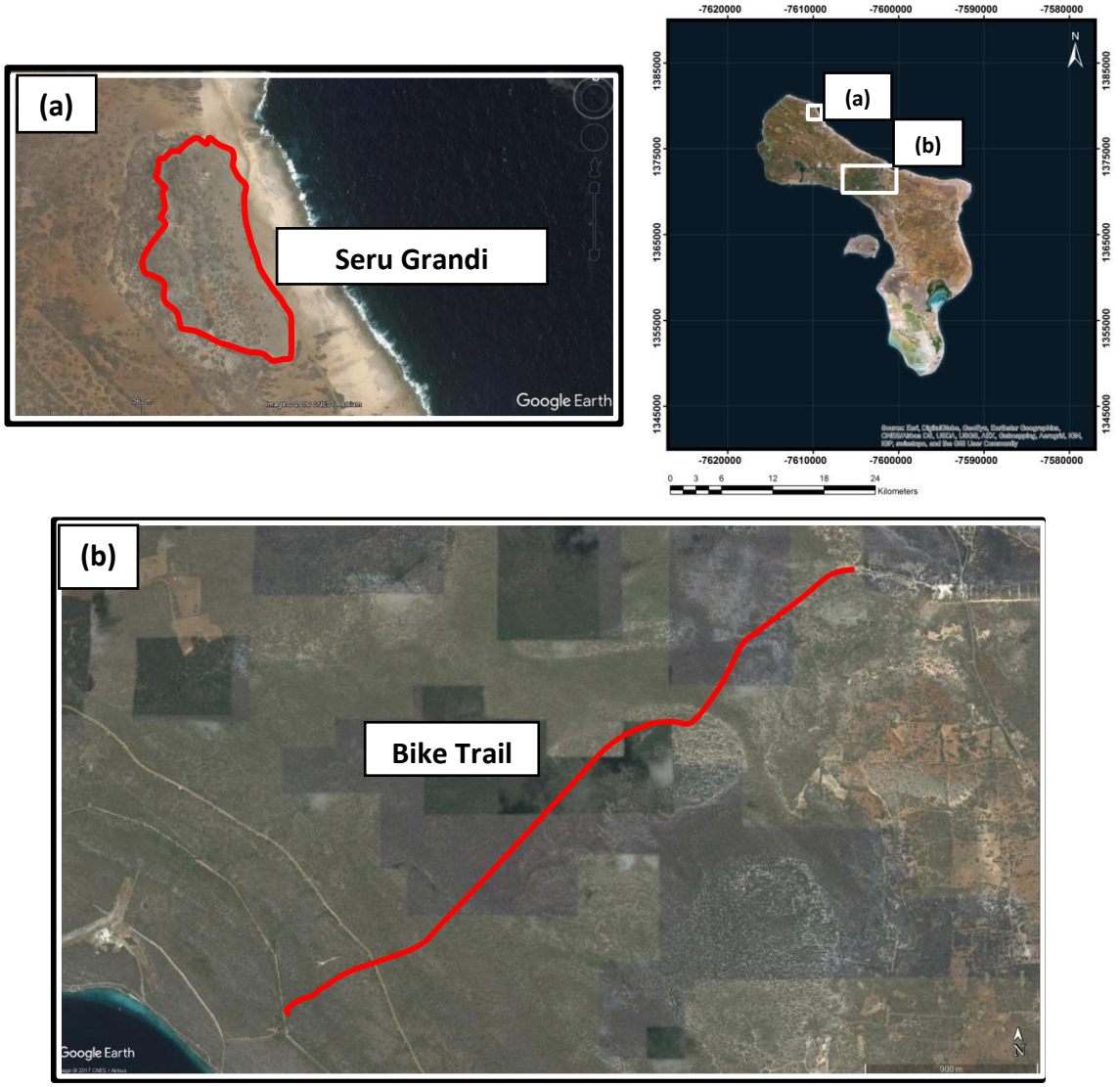

Figure 7: Satellite photography of survey locations. (a) Seru Grandi outcrop outlined in red. (b) Bike trail along center of island outlined in red showing location of cross-island transect. Inset map of entire island in top right.

4.2.1 Cross-Island Transect

As shown in Figure 7a, the cross-island transect runs along a 4 km bike trail that nearly bisects the island of Bonaire. Given the significant vegetation covering much of the

interior of the island, this bike trail provided rare access for a long continuous survey. When considering survey parameters such as trace spacing, trace time-window, sampling rate, number of trace stacks, etc. the goal was to select parameters that allowed for high resolution mapping along the line while maintaining acquisition speed so as to be able to complete the transect within the 4-5 days allotted for the 2015 field work.

The limit of vertical resolution, Δr, for a given survey is defined as the smallest vertical separation between reflectors such that arrivals in a GPR trace are still distinguishable from one another. This vertical length scale is expressed in terms of the wavelength of a propagating EM wave and can be written as (after *Annan*, [2009]):

$$\Delta r = \frac{\lambda_c}{4}, \tag{27}$$

where λ_c is the EM wavelength at an antenna center frequency of f_c. Given the basic relationship between frequency and velocity, $\lambda_c = v/f_c$, and also the relationship between the material properties of the subsurface and velocity, $v \approx 1/\sqrt{\mu\varepsilon}$ [*Annan*, 2009], Equation (27) can be rewritten as:

$$\Delta r \approx \frac{1}{4 f_c \sqrt{\mu\varepsilon}} . \tag{28}$$

It can be seen here that for a given antenna center frequency (in this survey 100 MHz; see Table 1), the limit of vertical resolution does not depend on choices for other survey parameters such as trace spacing, time window, etc. Nevertheless, it is possible to compute an estimate for the limit of vertical resolution for the surveys conducted on Bonaire. Using the assumption that $\mu = \mu_0$ from Section 3.1, and taking the range of values for ε_r for limestone lithologies to be 4-8 from Section 3.2, the limit of vertical resolution for GPR surveys on Bonaire is estimated at Δr =0.37-0.27 m =37-27 cm. Although the $\lambda_c/4$ approximation for the limit of vertical resolution is widely used, other workers have described situations where this limit varies from convention. *Widess*, [1973] shows that in ideal noise-free conditions, the limit of vertical resolution can be up to $\lambda_c/8$, which would give Δr =19-14 cm for the limestone lithologies on Bonaire. In contrast, semiempirical work by *Bradford and Deeds* [2006] shows that thin bed reflections are only *well* resolved when the thickness of the bed is greater than or equal to half of the EM wavelength, which would give Δr =74-54 cm. With these considerations, confidence is high in being able to identify beds as thin as 74 cm, and it is theoretically impossible to discern beds thinner than 14 cm the limestone lithologies of Bonaire at an EM frequency of 100 MHz.

Analogously, the limit of lateral resolution, Δl, is the minimum horizontal distance between reflectors in the subsurface for which the reflections can be unambiguously distinguished, and can be approximated as [*Cassidy*, 2009a]

$$\Delta l = \sqrt{\frac{d\lambda_c}{2}}, \tag{29}$$

where d is the vertical depth of the reflectors. This limit is also known more generally as the Fresnel zone radius [Everett, 2013], and describes the acquisition footprint of a GPR survey. Again using the antenna center frequency of 100 MHz and $\varepsilon_r = 4 - 8$, the limit of lateral resolution is plotted as function of reflection depth as shown in Figure 8.

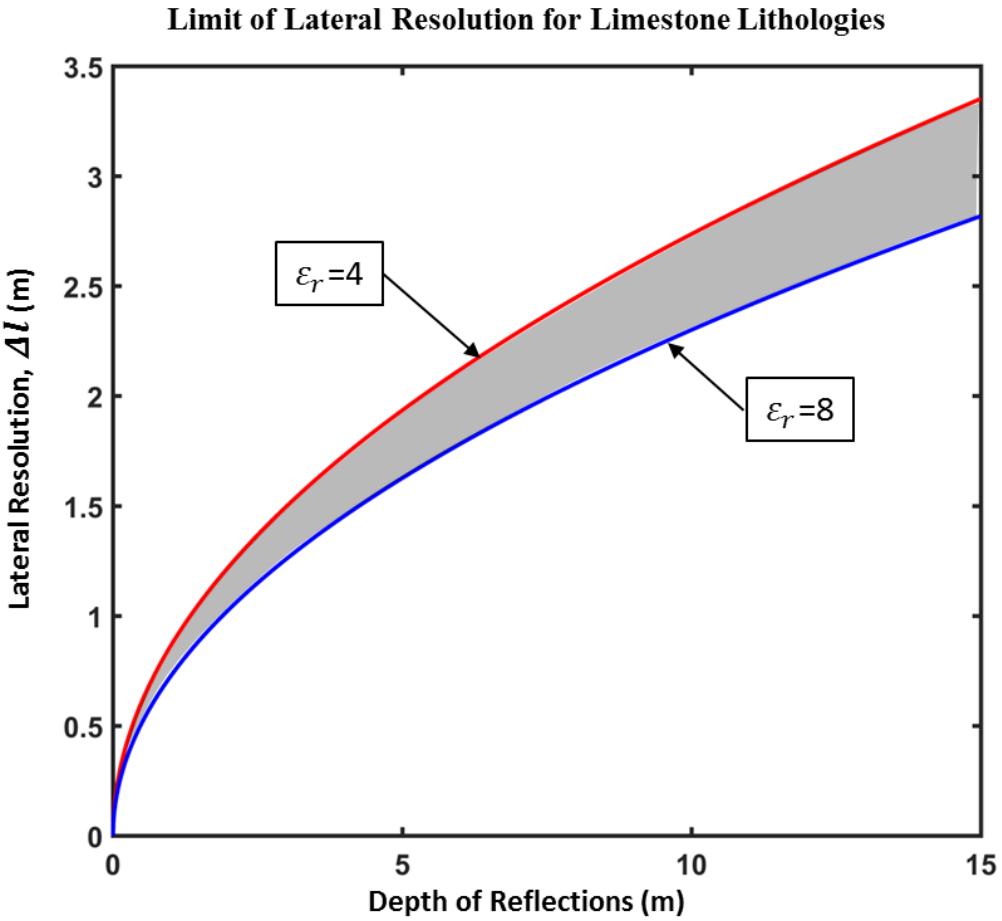

Figure 8: Limit of lateral resolution as a function of depth to reflector. Red line indicating $\boldsymbol{\Delta l}$ for $\boldsymbol{\varepsilon_r} = 4$ at100 MHz. Blue line indicating $\boldsymbol{\Delta l}$ for $\boldsymbol{\varepsilon_r} = 8$ at100 MHz.

For a range of reflector depths from 0-15 m, Figure 8 shows lateral resolutions ranging from less than several centimeters to over 3 m. This illustrates that smaller spaced features are discernable at shallower depths, with only more broadly spaced features being resolved at larger depths.

In addition to the effects of resolution with depth, GPR surveys must consider how frequently reflections are sampled to avoid ambiguities in determining reflection orientation, known as spatial aliasing [*Yilmaz*, 2001]. Taking from the Shannon-Nyquist sampling theorem [*Shannon*, 1948], the required sampling interval Δx to avoid spatial aliasing is [*Annan*, 2009]

$$\Delta x \leq \frac{\lambda}{2}, \tag{30}$$

with, λ being the wavelength of the EM wave at a given frequency. However, dipole antennas used in GPR systems do not produce single frequency wavefields but instead produce a range of frequencies described by the bandwidth. The bandwidth is here defined as the range of frequencies produced by an antenna that have powers greater than or equal to half the maximum power, i.e. have less than an approximately -3 dB roll-off. For the antennas used in this study, the bandwidth contains frequencies between 50 MHz and 150 MHz [*Annan*, 2003] with the center frequency being 100 MHz (as mentioned previously). With this consideration, the required sampling interval to avoid spatial aliasing becomes [*Annan*, 2009],

$$\Delta x \leq \frac{\lambda_c}{3}. \tag{31}$$

Note that λ has now been replaced by the center wavelength, λ_c, at the antenna center frequency. Using the 100 MHz center frequency and $\varepsilon_r = 4 - 8$ to compute the center wavelength, Δx must fall between 0.5 m and 0.4 m to avoid spatial aliasing of reflections from limestone lithologies on Bonaire. *Annan*, [2009] states that values half as large as those computed for Equation (31) are more appropriate for most surveys, therefore Δx was chosen as 0.2 m for the cross-island transect. Although this value is conservative in terms of theoretical sampling requirements, it did not affect the rate of acquisition significantly.

The TX-RX separation was chosen for this survey to be 1 m. This choice placed the TX-RX close enough together so that acquisition was not unnecessarily cumbersome and could be effectively carried out by a team of three persons (Figure 6). This also allowed for the ray-paths between the TX and RX to approximate zero-offset acquisition for reflector depths greater than 1 m, thus facilitating subsequent processing. Lastly, the 1 m TX-RX separation is not so close that the amplitude of the direct wave exceeds the dynamic range of the RX such that shallow reflections would become distorted [*Annan*, 2003].

The time window of acquisition represents the length of time that the GPR RX is "listening" and recording reflected energy arriving from the subsurface. It is necessary to choose a time window that is at least as long as the estimated time it takes for energy to travel from the transmitter to the deepest reflector of interest and back up to the receiver.

As mentioned, the TX-RX separation is small enough in this survey that for deep reflections (~10+ m) this traveltime can be approximated as the zero-offset traveltime

$$t_0 = \frac{2d}{v}, \tag{32}$$

where, d is the depth of the reflector and v is the EM wave velocity of the subsurface. For a potential maximum depth of investigation of 15m, and velocity ranging from $0.9\text{x}10^8$- $1.5\text{x}10^8$ m/s, traveltimes range from 200-300 ns respectively. Given that each trace occupies only several kilobytes of storage on the PulseEKKO PRO data logger, the time window for the cross-island transect was chosen to be 600 ns at the expense of only several hundred bytes per trace. This extended time window allowed for the collection of ample data so that any detectable signals from reflectors deeper than the envisioned maximum depth of investigation would not be lost.

The sampling interval for a survey is the rate, usually described in nanoseconds per sample, at which a given trace is recorded. To accurately reconstruct a band-limited continuous signal of a single frequency, f, the sampling rate, Δt, must satisfy,

$$\Delta t \leq \frac{1}{2f}, \tag{33}$$

again coming from the Shannon-Nyquist sampling theorem [*Shannon*, 1948]. Equation (33) can alternatively be arranged as,

$$f_N = \frac{1}{2\Delta t}, \tag{34}$$

where f_N is the maximum frequency that can be reconstructed with the given sampling rate, known as the Nyquist frequency. The minimum frequency signal that is able to be captured in a GPR trace is determined by the time window of acquisition, with one period of the signal being equal to the length of the trace. The choice of a 600 ns time window translates to a minimum recordable frequency of 2 MHz.

As mentioned previously, the antennas used in this study have a bandwidth that contains significantly powerful signals between 50-150 MHz. It is important to choose a sampling rate that gives a Nyquist frequency at least as high as the upper limit of this bandwidth to avoid temporal aliasing. Using Equation (33), the largest possible sampling rate permitted while allowing reconstruction of signals transmitted at 150 MHz is 1.67 ns/sample. For the cross-island transect a faster rate of 0.4 ns/sample was chosen. This rate is much more conservative as it gives a Nyquist frequency of 1 GHz. This choice did not appreciably impact acquisition speed and allowed for accurate capture of higher frequency signals required for effective discrimination between signal and noise during data processing.

The amount of stacking for a GPR transmitted signal is the number of traces that are recorded and summed at a given location within a survey. Since common-offset acquisition does not allow collection of gathers of traces such as in common-shot acquisition, the ability to increase signal to noise ratio (SNR) through a multi-fold stratagy is limited in this regard. However, GPR systems are able to transmit and record full waveforms at multiple times per second [*Annan*, 2003] allowing for recording of many traces at a single position in a survey. With a stationary TX and RX and under the assumption that the EM reflectivity of the subsurface is time-invariant, arrivals from subsurface reflectors will be constructive under summation of multiple recorded traces. If it is assumed that unwanted signals, hereafter classified as noise, are uncorrelated in time, the summation of such signals will be destructive. Therefore the SNR will increase as the stack number increases. However, signal-generated noise, such as unwanted errors in the transmitted signal, effects of improper recording, external radio signals, airwave reflections, etc. will not be removed via stacking, and must be removed with signal processing techniques. For the cross-island transect a stack of 16 was selected to allow for increased SNR while maintaining an acceptable speed of acquisition.

The length of the proposed survey line (4 km) necessitated the breaking of acquisition into multiple segments. This enabled the data acquisition to be paused between days of field work and allowed for monitoring of instrument drift and battery levels, assessment of any equipment malfunctions, and timely mitigation of operator errors. The length of

each segment was selected to be a maximum of 100 m, with some sections allowed to be shorter to address the above-mentioned acquisition issues.

A summary of the cross-island transect survey parameters as discussed above are listed in Table 2 below.

Cross-Island Transect Survey Parameters

Parameter	Value
Trace Spacing	20 cm
TX-RX Separation	1 m
Time Window	600 ns
Sampling Interval	0.4 ns/sample
Stacks	16
Line Segmentation (maximum length)	100 m

Table 2: List of survey parameters used in the cross-island GPR line.

Using the survey parameters in Table 2, 3900 m of continuous GPR data, collected in 50 individual segments, was acquired along the Bonaire bike trail shown in Figure 7b (red line indicates the location of the transect). The transect was traversed from west to east, over a period of 4 days with relative trace locations obtained using on-ground measuring tapes. Elevation data along this transect was obtained via the Google Maps satellite altimetry database. This database is derived from the Shuttle Radar Topography Mission (SRTM) dataset which has a spatial resolution of 1 arc sec (approximately 30 m) [*Farr*

et al., 2007]. This resolution was acceptable for the purposed of this survey as no topographic relief was observed to have periods shorter than 30 m.

4.2.2 Seru Grandi Survey

The Seru Grandi survey was conducted at the Seru Grandi outcrop on the northeastern portion of Bonaire within the Washington Slagbaai National Park (Figure 7a). Previous work by *Sulacia et al.* [2015] has shown that the outcrop consists of carbonates from two of the carbonate terraces occurring on the island, namely the 2nd and 3rd of these terraces. That work describes two depositional packages separated by an unconformity within the 2nd terrace strata (Figure 9), with the upper package consisting of heavily karstified boundstone-grainstones while the lower package contains largely un-karstified carbonate clinoforms geometries (Figure 10) having cyclical patterns of dolomitization [*Laya et al.*, 2017]. The goal of the Seru Grandi outcrop GPR survey was to provide subsurface imaging and evidence for the unconformity between the two aforementioned packages within the 2nd terrace strata, as well as the clinoform structures within the lower package.

South End of Seru Grandi

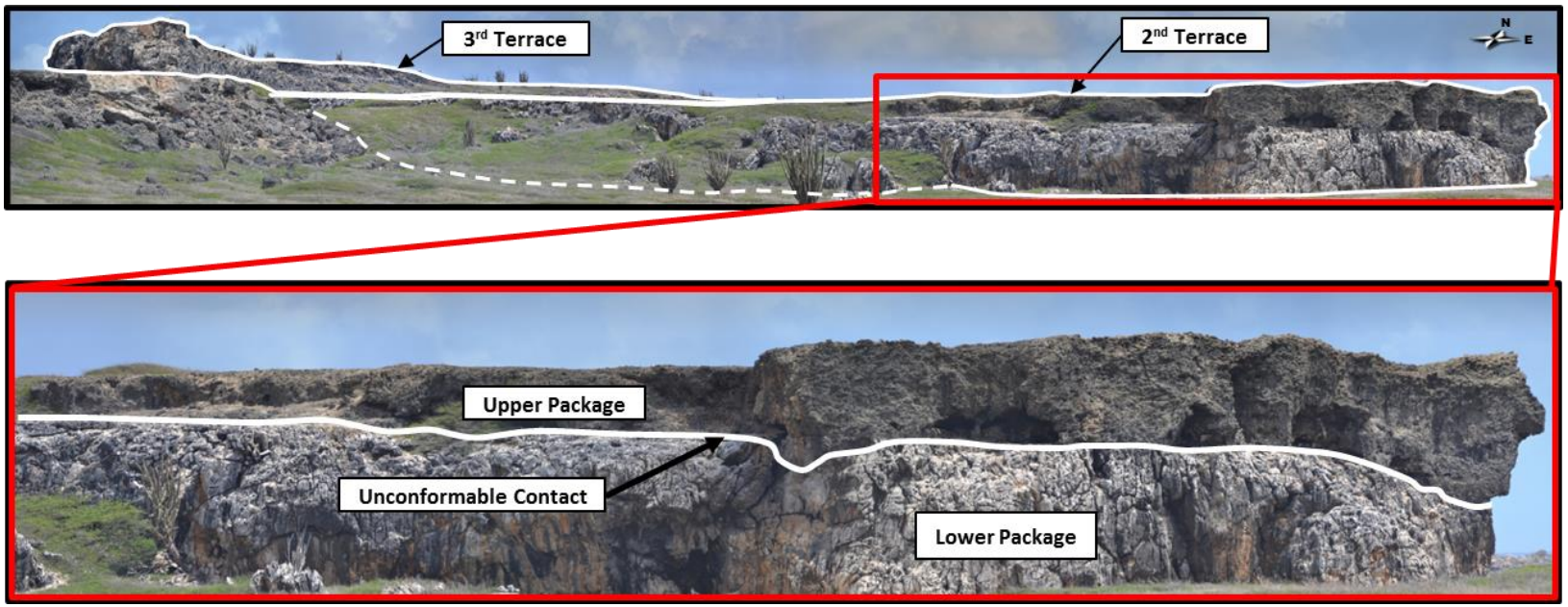

Figure 9: Panorama of southern end of Seru Grandi outcrop looking north-northwest. **(top)** Panoramic photo showing 3rd terrace strata overlying 2nd terrace strata. White lines indicate contacts (dashed where inferred). Units pictured at bottom-left are an isolated foreground outcrop not within the survey area. **(bottom)** Close up of outcrop panoramic indicating the upper and lower packages with the 2nd terrace strata.

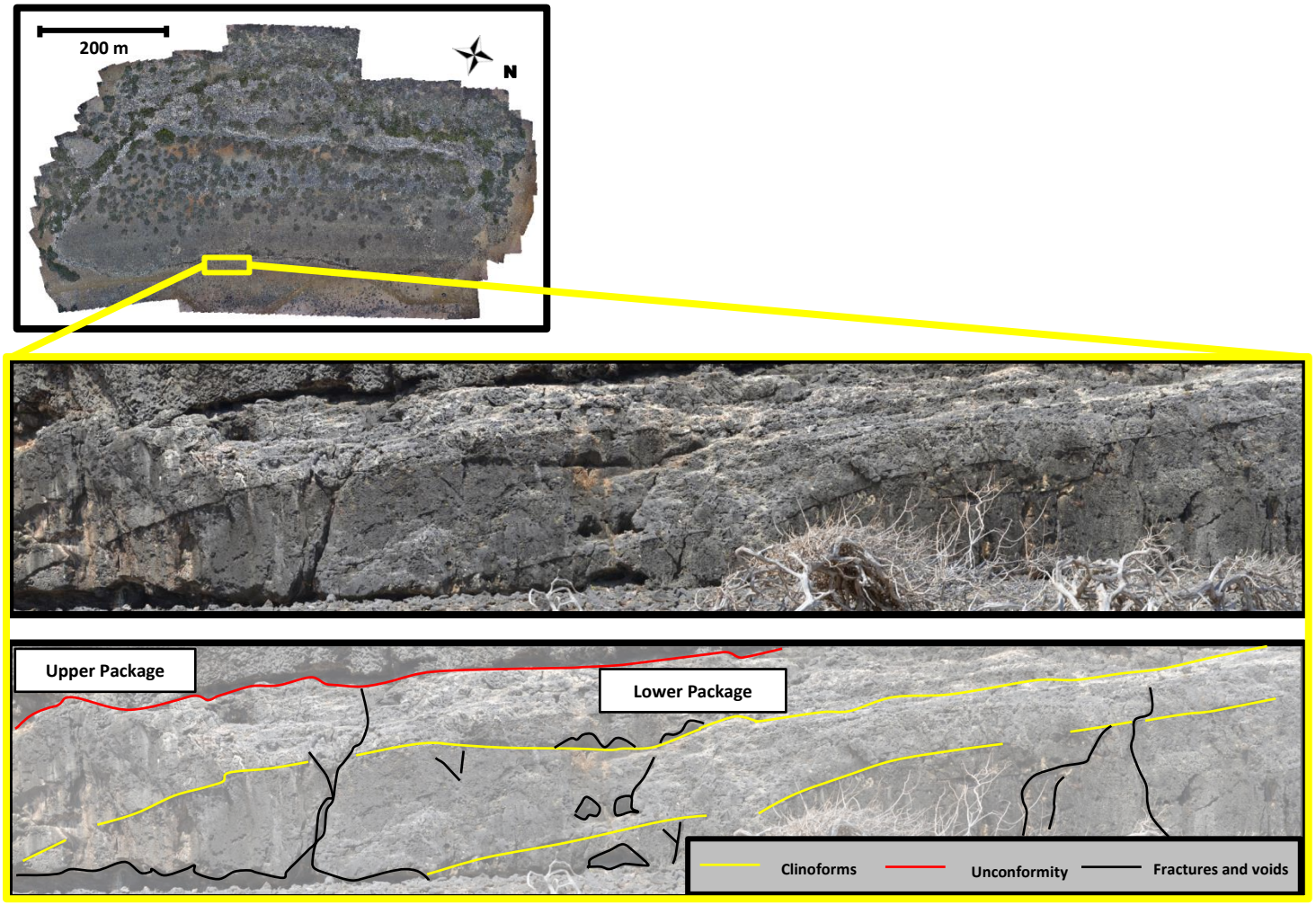

Figure 10: Clinoforms observed at the Seru Grandi outcrop. Well-preserved clinoform geometries observed in lower package.

Four separate GPR lines were traversed across the top of the outcrop. Three lines of GPR data were collected perpendicular to the face of the outcrop with one line running subparallel to the outcrop face. The locations of these lines can be seen in Figure 11a and b.

Locations of GPR Lines at Seru Grandi

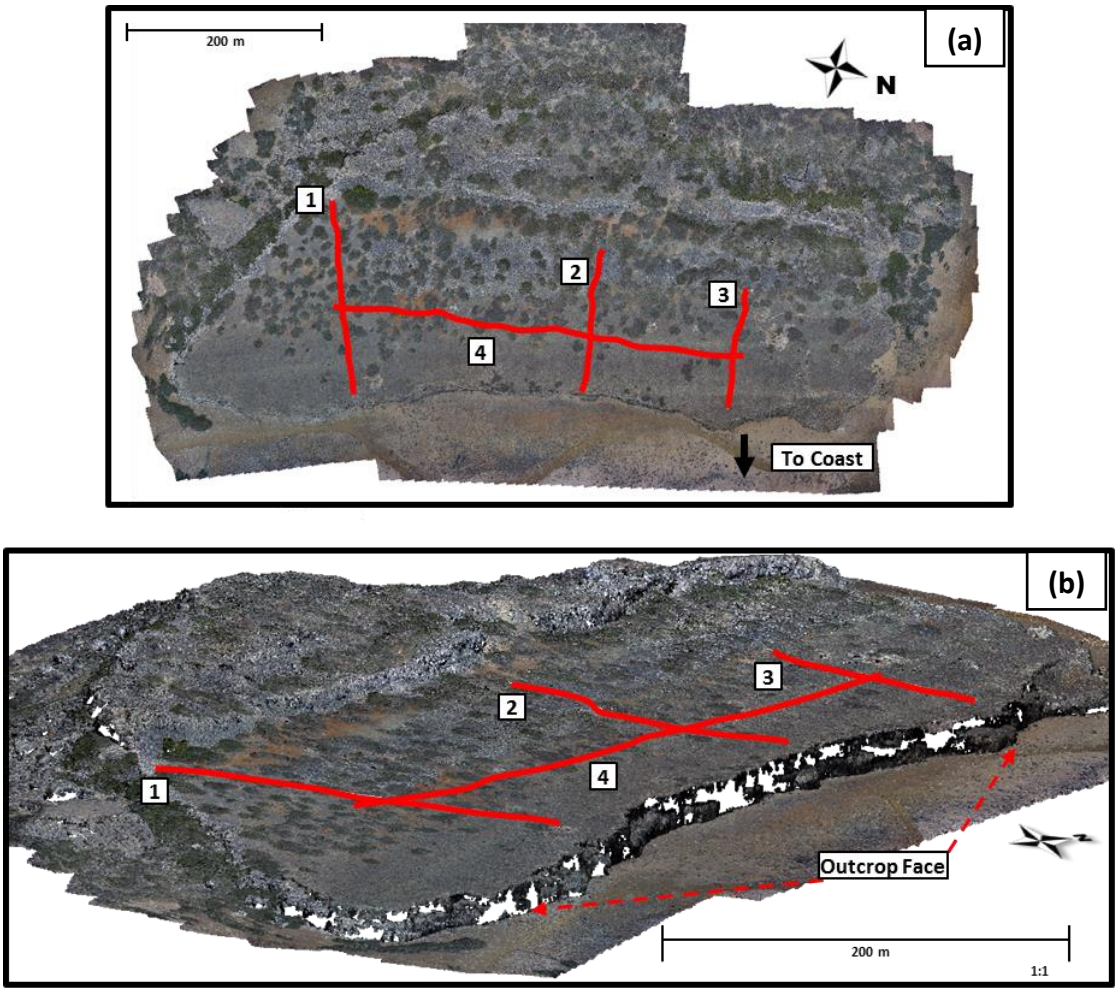

Figure 11: Maps showing GPR lines collected at Seru Grandi outcrop. **(a)** Plan view of Seru Grandi with GPR Lines 1-4 outlined in red. **(b)** Perspective view of Seru Grandi digital outcrop model with GPR Lines 1-4 outlines in red. Outcrop face indicated by red dashed arrows. White spaces in model indicate lack of point-cloud data.

Figure 11 above indicates the locations of the GPR lines (labeled 1-4) superimposed on a drone-based photogrammetry-derived digital outcrop model of Seru Grandi (from previous work by *Laya et al.* [2015]). The lengths of Lines 1-4 are respectively 200.0 m, 148.6 m, 122.0 m and 400.8 m. By designing the survey with several intersecting lines, the goal was to image the internal structure of the terrace from multiple perspectives in order to assemble them into a fence-diagram of sections, enabling 3D interpretation..

The GPR system specifications for this survey were the same as those used in the cross-island transect (Table 1), however, the 1000 V transmitter was unavailable for use during this field expedition so a substitute 400 V TX was used. The survey parameters used for the Seru Grandi survey were the same as those for the cross-island transect as well (Table 2), with the exception that the stack was increased from 16 to 32 in an attempt to increase SNR and potentially account for some of the decreased output power of the 400V TX compared to the 1000 V TX. Despite the increase in stack number, reflections were not discernable at as late of times as in the cross-island transect. Therefore, the time widow of acquisition was decreased to 400 ns in the Seru Grandi survey.

As previously mentioned, the upper package which comprises most of the top surface of the outcrop is heavily karstified, resulting in a field of sharp dissolution cracks, fissures, and even considerable sized voids (Figure 12a-c). In addition, numerous patches of low (< 1m in height) brush occur on top of the outcrop. These features posed considerable obstacles for data collection, as avoidance of near-surface dissolution features and brush

was incompatible with the goal of collecting straight, continuous lines of data. The end result was data collection in lines that were straight as possible, while avoiding any karstic features or large patches of brush. This was done with the understanding that the irregular terrain would have to be considered during data processing and interpretation. Position information for the lines was collected via tape measure as well as handheld-GPS (lateral precision of < 0.5 m but a vertical precision of only ~1 m), which would later be referenced to the high resolution digital model of the outcrop (having both lateral and vertical resolutions <10 cm).

Acquisition Challenges at Seru Grandi

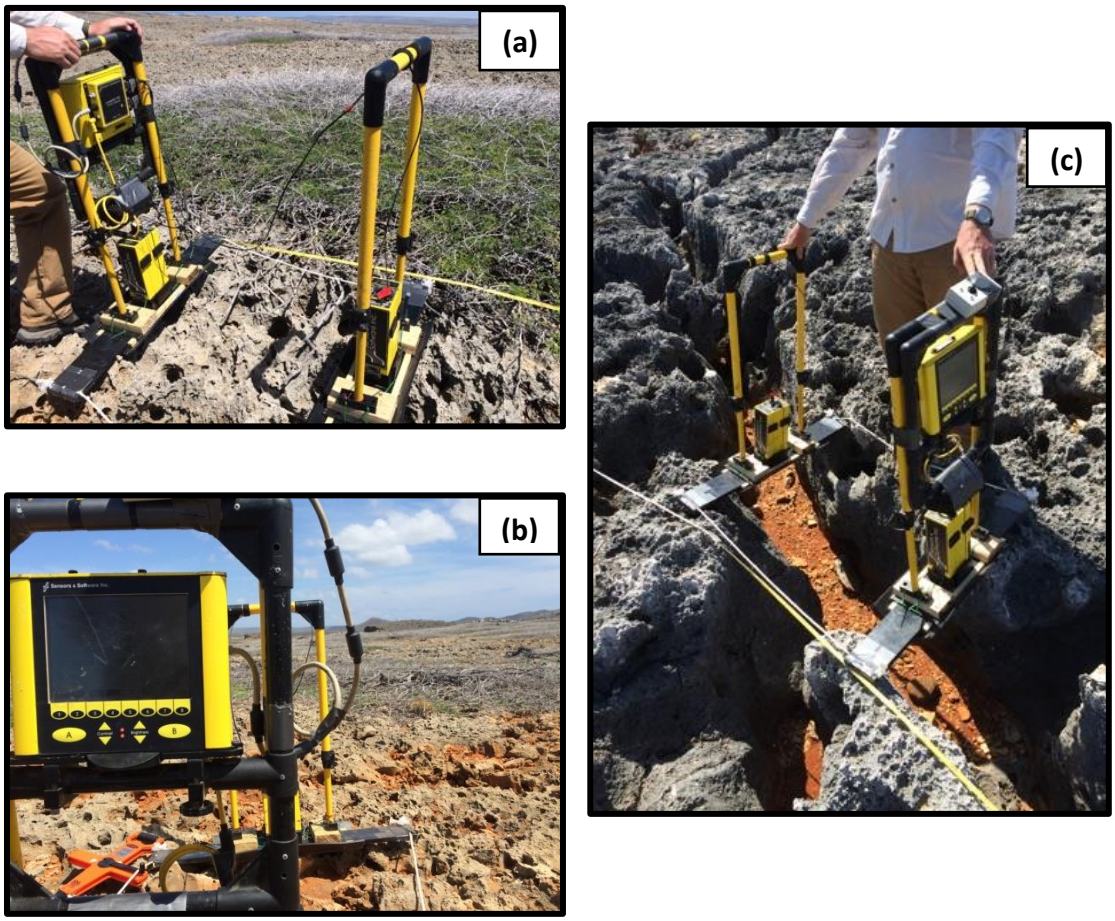

Figure 12: Photographs of the GPR system and the complexities atop the Seru Grandi outcrop. **(a)** Patch of low brush occurring on outcrop, and the karstified ground surface. **(b)** Pervasiveness of dissolution features on outcrop. **(c)** One of the large fissures (~50cm in width and ~1 m in depth) that was crossed during acquisition of line 3.

5. DATA PROCESSING

Before interpretation of the radar cross-sections collected on the island could be performed, the data were conditioned with multiple processing techniques. Preprocessing allowed for data organization and mitigation of unwanted noise. Then imaging techniques were applied to correctly position EM reflectors with the subsurface. Many of the processing techniques follow standard procedures for reflection-based geophysical surveys such as seismic [*Yilmaz*, 2001], however some special methods needed to be applied due to the nature of electromagnetic waves comprising GPR data [*Cassidy*, 2009b].

5.1 Cross-Island Transect

5.1.1 Preprocessing

The preprocessing techniques described below were largely performed using the EKKO_Project software package. This package was developed by Sensors and Software, the same manufacturers of the GPR equipment used in this study, and it contains various routines for editing and filtering the traces within a GPR cross-section.

5.1.1.1 Segment Concatenation

As mentioned, the cross–island transect collected across the Bonaire bike trail (Figure 7b) was acquired in 50 individual segments. The length of these segments varied and was dictated by in-field requirements, such as battery changes, and correction of instrument malfunctions, with none exceeding 100m in length (as discussed in Section

4.2.1). To create a single continuous line of data each of these segments was concatenated end-to-end with the adjacent sections as shown in Figure 13. This figure shows the complete unprocessed cross-island section.

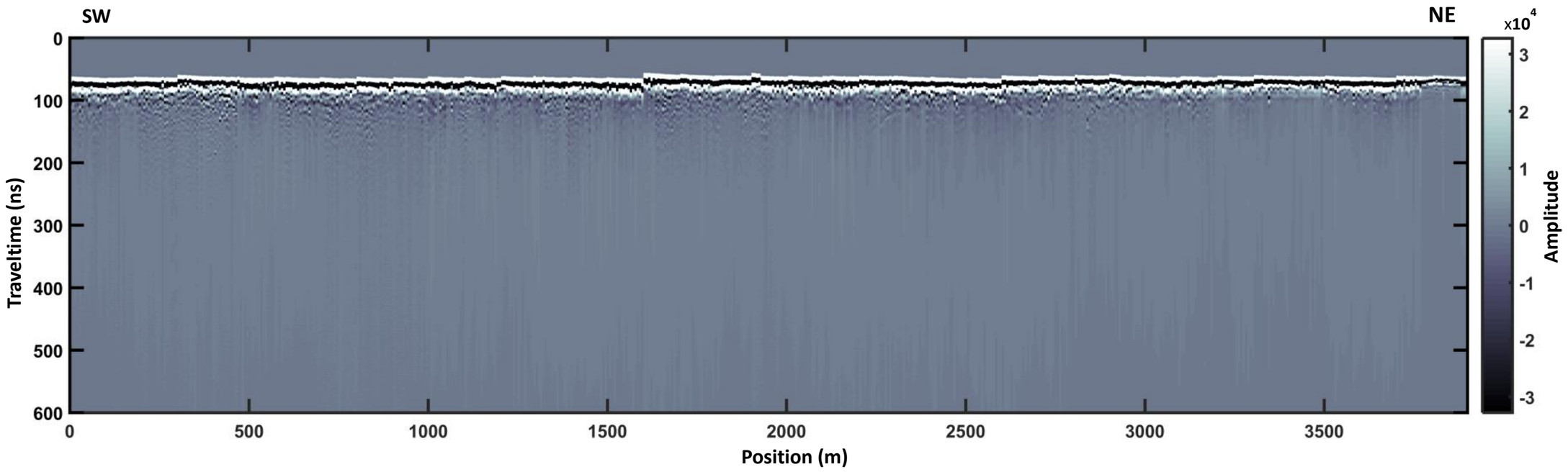

Figure 13: Full concatenation of unprocessed cross-island transect GPR segments oriented southwest to northeast along the bike trail. Left axis is in nanoseconds of two-way traveltime. Bottom axis is in meters along transect. Amplitude scale has been unaltered meaning it represents microvolts induced in the RX antenna.

5.1.1.2 First-Break Alignment

In Figure 13, the onset of recorded EM energy (known as the first-break) is not consistent in time across all of the traces in the section. The smooth variations in this time are due to the accruement of instrument timing issues between the TX and RX within a segment such as shifts in the fiber-optic cables connecting the TX, RX, and system control unit, and the sharper discrepancies are due to resetting of the delay between transmitting and recording times when the equipment was powered down between segments. To correct for these phenomena, the first-break is picked for each trace and then each trace is shifted so that the first-break of every trace aligns with the first-break of the any single trace, here chosen to be the first trace in the dataset. The EKKO_Project software determines the first-break by comparing the absolute amplitude of each consecutive sample in the signal to some predetermined threshold. When the threshold is exceeded, the first break is assigned to the exceeding sample. A schematic of the first-break picking and alignment process is shown in Figure 14a and b.

First-break Alignment Schematic

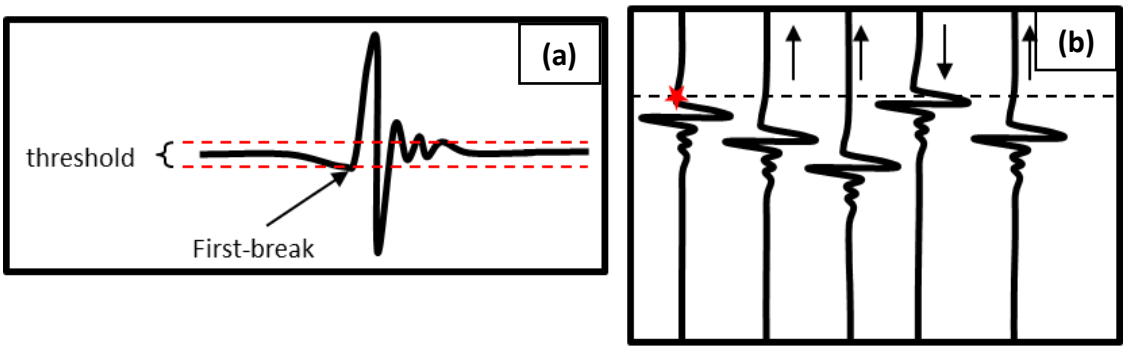

Figure 14: Cartoon describing first-break picking and alignment. **(a)** Illustration of picking the first-break for a trace at the first sample that exceeds some threshold amplitude range. **(b)** Showing shifting of traces to make first-breaks align with first-break of first trace (red star).

Using the process described above, the first-break was picked for each trace and then realigned along the cross-island transect section as seen in Figure 15. Note that although the first breaks for each trace have been aligned, there is still irregularities observed at the top of the section within the first arriving reflection. This arrival is not actually a reflection but the direct wave propagating through the air between the TX and RX. Small variations in the positon of the peaks of this arrival (on the order of serval nanoseconds) create the irregularities seen in Figure 15

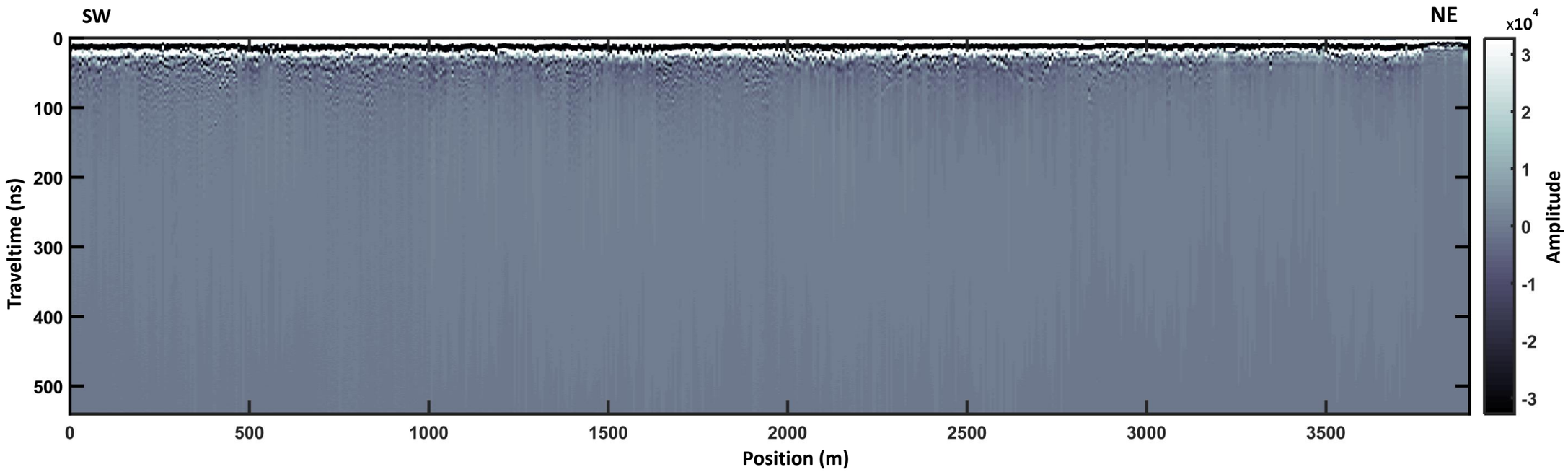

Figure 15: Cross-island transect after applying the first-break alignment process. Note that the region above the first-breaks has been cropped out of the section.

With the first break aligned for each trace, subsequent processing relying on this assumption was then able to be performed. In addition to aligning the first breaks for each trace across the transect, the zero-amplitude region above the first-break was cropped out of the section (i.e. muted) as seen in Figure 15.

5.1.1.3 De-wow

Ground penetrating radar signals often contain low-frequency signals that permeate the trace, often called the "wow" [*Annan*, 2009]. This is a low-frequency bias in the recorded signal [*Annan*, 1993]. Multiple theories about the cause of this signal distortion have been proposed. *Annan* [2003, 2009], suggest that inductive coupling between the TX and RX causes the wow. Others, such as *Gerlitz et al.* [1993], attribute the source of the wow to limitations by the electronic circuitry of the equipment to effectively record the large amplitude direct wave. Whichever the cause, the low-frequency bias of the wow obfuscates further interpretation and its removal is required.

Many methods exist to remove this unwanted signal in GPR traces. Several described by *Gerlitz et al.* [1993] include residual mean filtering, bandpass filtering, and residual median filtering. Both the mean and median residual filtering rely on subtracting a value from each sample (either a mean or median) that is computed from a moving window along the length of each trace. Bandpass filtering involves attempting to isolate and remove the low-frequency contamination in the frequency domain representation of each trace. The EKKO_Project software employs a residual mean filter (commonly called a

moving average filter) to remove the unwanted signal, or "de"-wow the traces [*Sensors and Software Inc.*, 2016]. For the Bonaire cross-island transect the length of the residual mean filter was selected at 1.33 times the transmitted pulse-width. The effects of the de-wow process can be seen for a single trace in Figure 12 and for the entire cross-island transect in Figure 17.

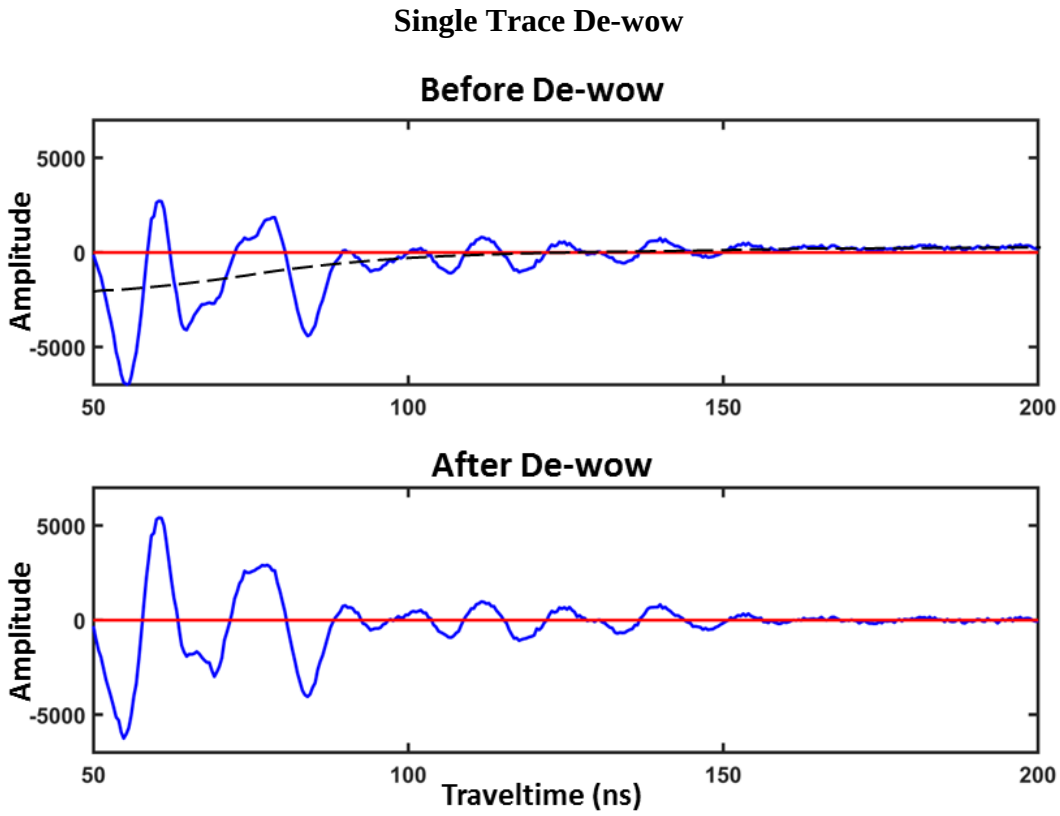

Figure 16: Effect of residual mean filter as a de-wowing filter. **(top)** Trace 50 from cross-island transect before filtering. Black dashed line illustrates the low frequency bias or wow. **(bottom)** Trace 50 after residual mean has been removed. Red lines indicate zero amplitude for reference.

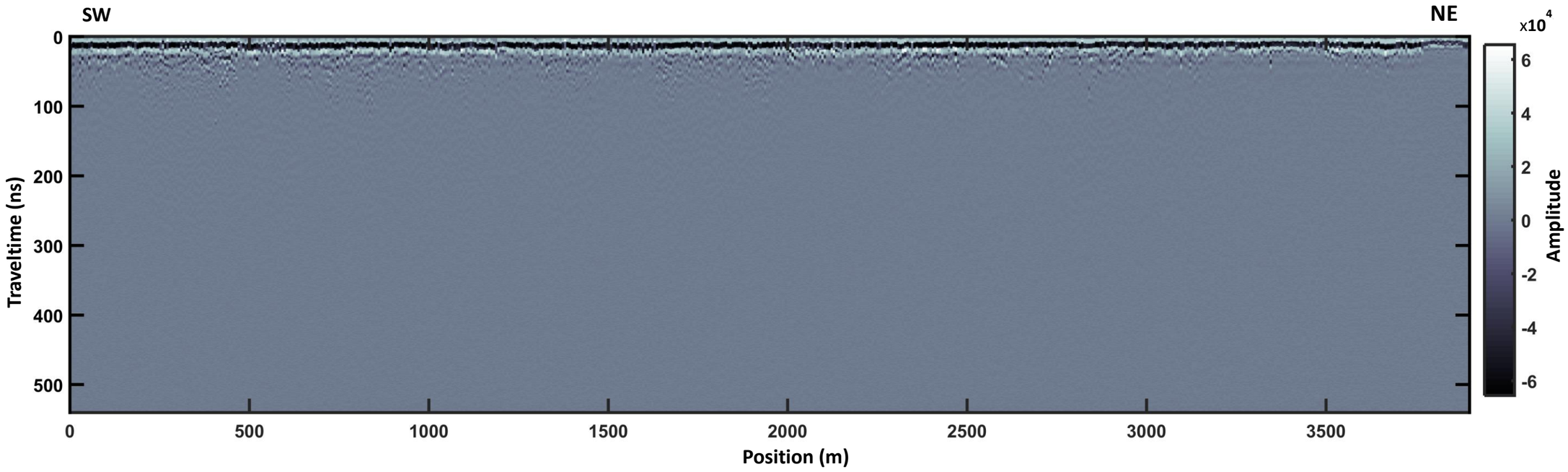

Figure 17: Cross-island transect after the low frequency wow has been removed.

In the top panel of Figure 16, the low frequency bias can be observed as a bulk shifting of amplitudes away from a line of zero mean (dashed line). After the de-wow filter was applied (Figure 16bottom panel), the bias is removed, and the trace has a zero-mean. The removal of the wow is important, because the low-frequency content affects the spectral content of the data, and the wow hinders interpretation due to the way it masks relative amplitudes along a trace. In Figure 17 the de-wow filter was applied to the entire cross-island transect. In comparing before (Figure 15) and after (Figure 17) de-wow filtering, it can be seen that the long period amplitude variations that make the data appear "washed-out" have been removed.

5.1.1.4 Background Subtraction

In GPR data, the direct arrival through the air between the TX and RX (air-wave), due to its large amplitude, often masks early time reflections. In addition, unwanted signal reverberation and/or coupling between the TX and RX, conventionally called ground-clutter or antenna ringing, can occur [*Everett*, 2013]. Both of these types of noise are observed as flat-lying reflections extending across a GPR section (observed in Figure 17). The air-wave is observed at the top of the section, with the ringing being observed extending further down into the section (see $x =$ 3250-3750 m, $t =$25-75 ns Figure 17). To remove this noise a background subtraction filter was applied. Background subtraction is the process of removing an average computed from a laterally moving window for each sample in each trace. The width of the window determines the lateral extent of features that can be removed, and in general features whose lateral extent is

greater than or equal to the width of the window are well removed [*Sensors and Software Inc.*, 2016]. The window used in the background subtraction applied here is the Nuttall-defined Blackman-Harris style window [*Nuttall*, 1981] shown in Figure 18, which weights traces at the edges of the window less than those at the center. The effect is a smoother removal of noise as opposed to a sharp-edged rectangular window.

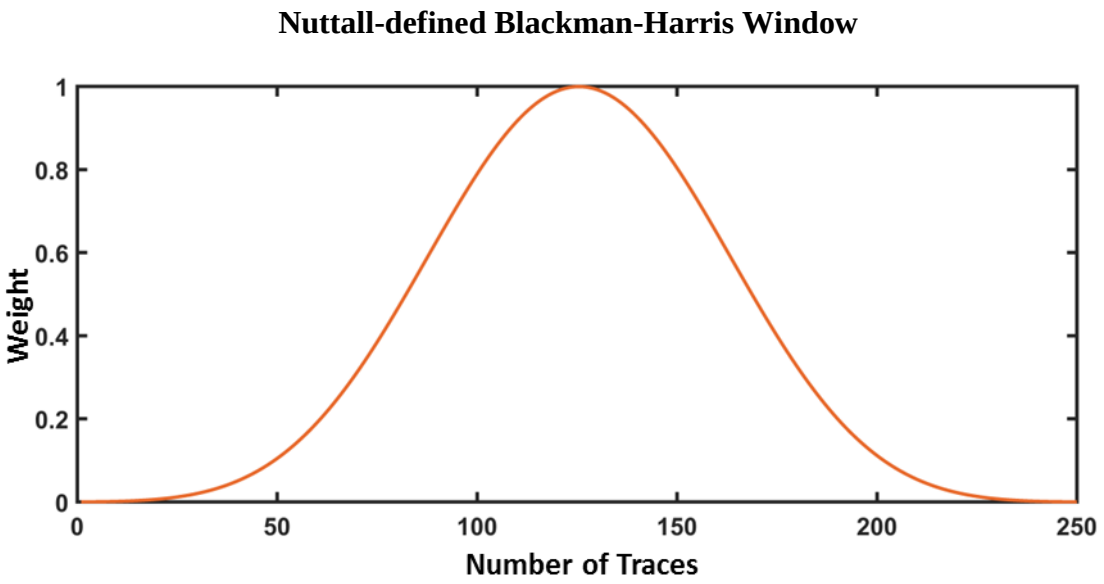

Figure 18: Nuttall-defined Blackman-Harris window used in background subtraction. Height of curve represents weight given to each trace when computing the average within the window.

One issue with the background subtraction process is that if flat lying reflections of interest exist in the data, they too will be removed along with the ground-clutter [*Everett*, 2013]. This issue was mitigated in two ways for the Bonaire cross-island transect. First, the background subtraction was applied to the dataset before correcting the data to align

with the topographic surface of acquisition. With the data uncorrected for topography, geologically flat reflections are no longer flat, but mirror the topography, and any observed horizontal signals can be attributed to the ringing/ground clutter. Second, the window length was chosen to be relatively large at 250 traces (equating to 50 m spatially) so that in regions where the acquisition surface was flat, the signatures of truly flat geologic reflectors would not be removed. The effect of applying this background subtraction to the cross-island transect is shown in Figure 19.

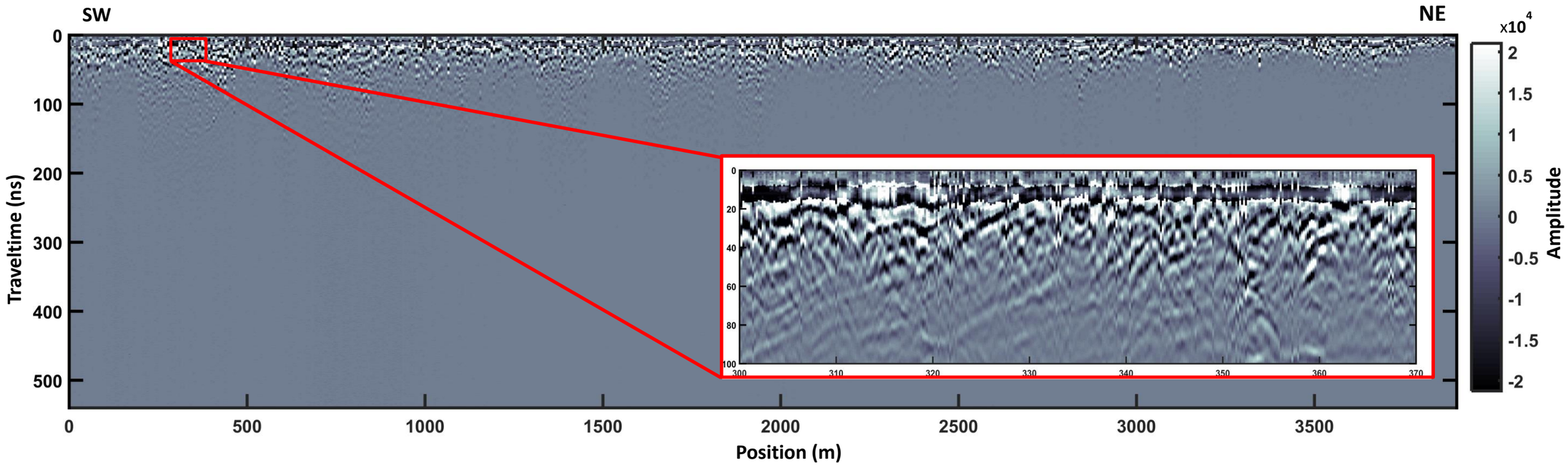

Figure 19: Background subtraction applied to cross-island transect. Amplitudes have been clipped to 99% based on occurrence and centered about zero for display. Inset section showing artifacts of background subtraction.

As is shown in Figure 19, the background subtraction removed much of the noise due to the air-wave and aforementioned ground-clutter. It must be noted that the background subtraction reduces the mean amplitudes across the section, therefore Figure 19 is displayed with amplitudes first clipped to only display the bottom 99% of amplitudes, thus mitigating the distortion of the colorscale by large spurious amplitudes.

Although the background subtraction removed unwanted noise, artifacts from the process can be seen. The inset section in Figure 19 displays in detail an amplitude striping artifact across the top of the section. If the amplitude of the air-wave was identical for each trace in the section, it would be completely removed using the background subtraction. However, given that the amplitude striping artifact occurs as a remnant of the air-wave, this implies that the air-wave has minor yet significant trace-to-trace variations. This results in the low-frequency amplitude variation seen in the early-time arrivals that mirrors the original air wave pulse. This artifact can be mitigated though frequency filtering as discussed in the next section, 5.1.1.5.

5.1.1.5 Frequency Filtering

To better understand periodic types of noise existing in the dataset, such as the low frequency artifacts of the background subtraction, or residual TX-RX reverberations, the average frequency spectrum of all the traces in the data can be computed. This is done via the classical discrete Fourier transform, which describes a sampled time series as the summation of complex-valued sine and cosine basis functions of variable frequency. The

coefficients of each of the basis functions in this representation contain a real part, Re, and an imaginary part, Im, with the amplitude, A, defined as,

$$A = \sqrt{Re^2 + Im^2}, \tag{35}$$

and the phase, ϕ, defined as,

$$\phi = tan^{-1}\left[\frac{Im}{Re}\right], \tag{36}$$

for each frequency component in the time series [*Bracewell*, 1986]. An average was taken of the amplitudes of the Fourier transform for each trace in the cross-island transect to create the average amplitude spectrum shown in Figure 20a.

From the discussion in Section 4.2.1 about the frequency content of the EM waves radiated by the transmitter, it is expected that signals resulting from geologic reflections will fall largely within the 50-150 MHz frequency range defining the antenna bandwidth. As signals produced by the transmitter outside this bandwidth have comparatively low amplitude, high amplitude signals recorded at frequencies outside the bandwidth can largely be considered unwanted noise. Figure 20a shows high amplitudes occurring between 45 and 155 MHz which fall within the theoretical bandwidth of the GPR system and are expected to be due to primary reflections of EM energy. Above 155 MHz,

moderate to low amplitude frequencies are observed which may be due to high-frequency systematic noise caused by instrumentation bias. Below 45 Hz, a small peak is observed at frequencies between 5-15 MHz. This is likely due to the artifacts of the background subtraction and potential remnants of the low-frequency wow, and is considered low-frequency noise.

To remove the effects of both the high-and low frequency noise in the time series representation of the dataset, the data can be filtered in its Fourier domain representation. A bandpass filter was designed with a low cutoff frequency of 15 MHz, a low-pass frequency 45 MHz, a high-pass frequency of 155Hz and a high-cutoff frequency of 185Hz. The 15 MHz and 185 Hz cutoff frequencies where chosen conservatively to avoid removing geologic reflection signals that occur at the margins of the antenna bandwidth. The EKKO_Project software implements bandpass filters with a cosine tapered boxcar function between the frequency pass and cutoff bands [*Sensors and Software Inc.*, 2016]. The cosine taper avoids sharp truncations so as to minimize ringing in the time domain after filtering, known as Gibbs phenomenon. The amplitude spectrum of the filter used here is shown in Figure 20b.

The filtering process multiplies the frequency response of the filter with the Fourier transform (both real and imaginary parts) of each trace in the GPR section. The resulting amplitude spectrum after filtering is shown in Figure 20c. As can be seen, the

frequencies above and below the cutoffs were smoothly brought to zero, while leaving the high amplitude frequencies within the 45-155 MHz range unaltered.

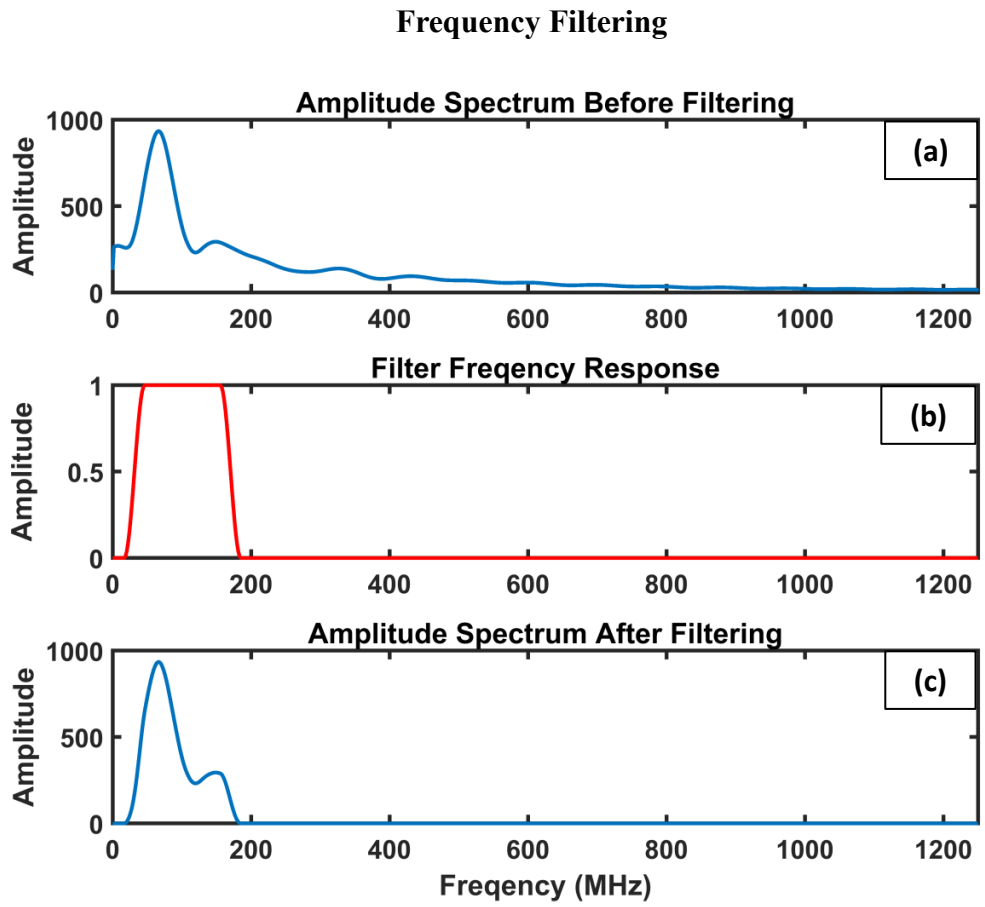

Figure 20: Amplitude spectrums of data and filter. **(a)** Average amplitude spectrum of cross-island transect before frequency filtering. **(b)** Frequency response of cosine tapered boxcar filter. **(c)** Average amplitude spectrum of cross-island transect after filtering with filter in **(b)**.

To return the dataset to the time domain representation, an inverse discrete Fourier transform is applied to each trace. The effect of the filtering process on a single trace within the dataset is shown in Figure 21.

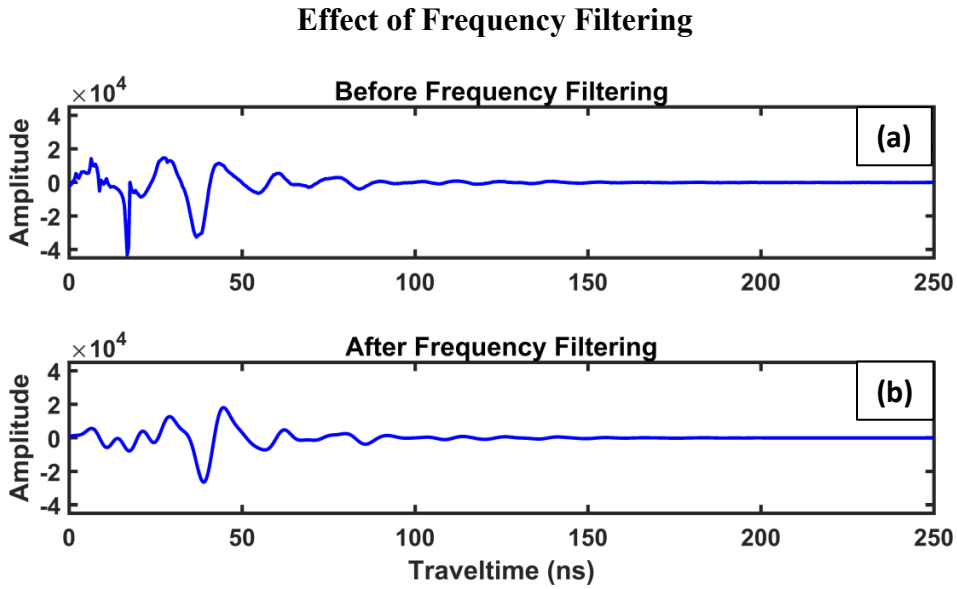

Figure 21: Effect of frequency filtering. Showing filtering application to first 250 ns of trace 50 in the cross-island transect. **(a)** Trace before frequency filtering applied. **(b)** Trace after frequency filtering applied.

The small-scale irregularities observed at early times in Figure 21a are the high-frequency noise components of the data, as observed in Figure 20a, and the more broadly varying bias in those early time amplitudes reflects the low-frequency noise seen in Figure 20a that was attributed to the background subtraction artifacts. After the application of the frequency filter in Figure 20b to the trace in Figure 21a, both the high-frequency irregularities and the low-frequency bias have been well removed from the trace. Although small distortions to the shape (i.e. phase [*Yilmaz*, 2001]) of the reflections can be observed after filtering, the locations of the peaks and troughs of each reflection remain fixed, which is important for subsequent interpretation. The result after

applying the frequency filtering to the entire cross-island transect is shown in Figure 22 below.

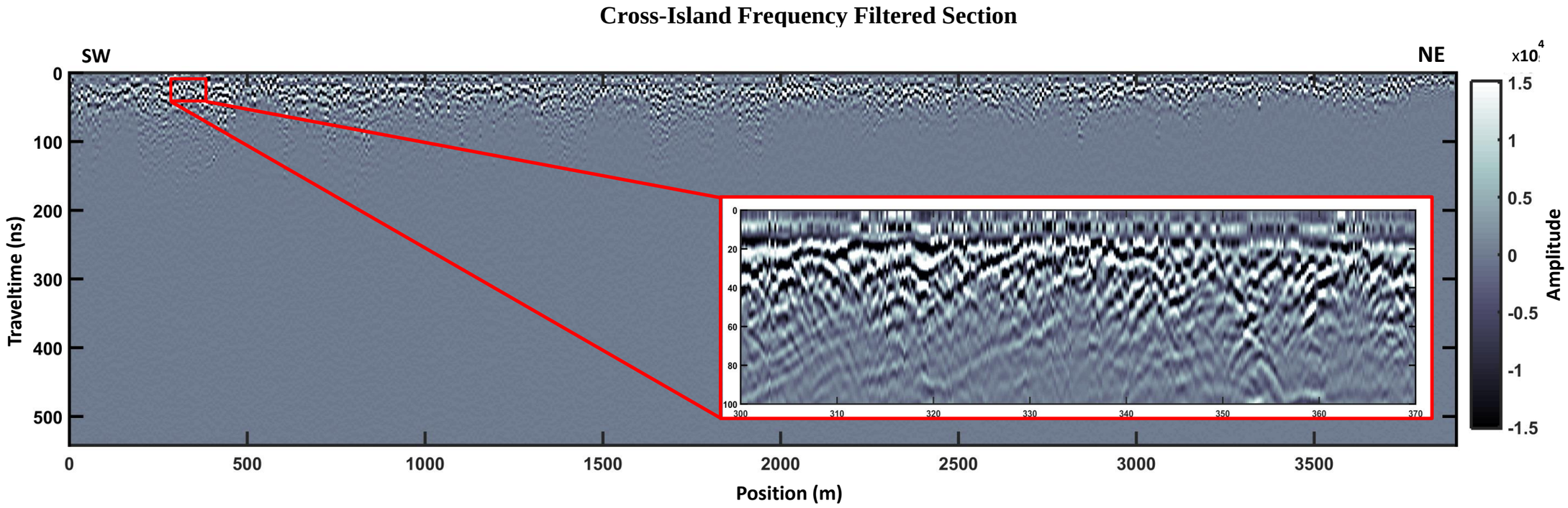

Figure 22: Cross-island transect after frequency filtering. Amplitudes have been clipped to 99% based on occurrence and centered about zero for display. Inset section showing suppression of artifacts of background subtraction.

The filtering applied to the dataset can improves the clarity of the image, especially at early times. The inset axis in Figure 22 shows that the low-frequency noise introduced by the background subtraction has been largely mitigated, although not removed completely.

5.1.2 Imaging

At this point in the processing workflow, the effects of noise have been largely mitigated, and the arrivals in each trace are considered to be the result of EM waves interacting with subsurface geologic features. However, this side-by-side arrangement of GPR traces collected along a transect does not necessarily produce a realistic image of the subsurface. Given that the topography of the acquisition surface is not flat, corrections must be made to account for the terrain effect on the data. In addition, interplay between the propagating EM energy and the acquisition geometry return the *response* of the subsurface to the EM wavefield rather than an image of the subsurface itself. Migration techniques must therefore be employed to move reflections to the spatial location of their corresponding reflector. Such processing techniques largely fall outside the ability of the EKKO_Project software. Therefore the methods discussed in this section on imaging were implemented using MATLAB, a data analysis and scripting computer language.

5.1.2.1 Topographic Correction

As mentioned in Section 4.2.1 elevation data along the cross-island transect was obtained via the Google Maps satellite altimetry database which comes from the 30 m resolution SRTM dataset. Topographic variations along the cross-island transect were not observed to have frequencies exceeding this resolution, and it was therefore determined that the SRTM derived elevation data was adequate for the purposes of correcting for the topographic changes along the transect. These elevations were then interpolated to give elevations at every trace (every 0.2m) along the line (Figure 23)

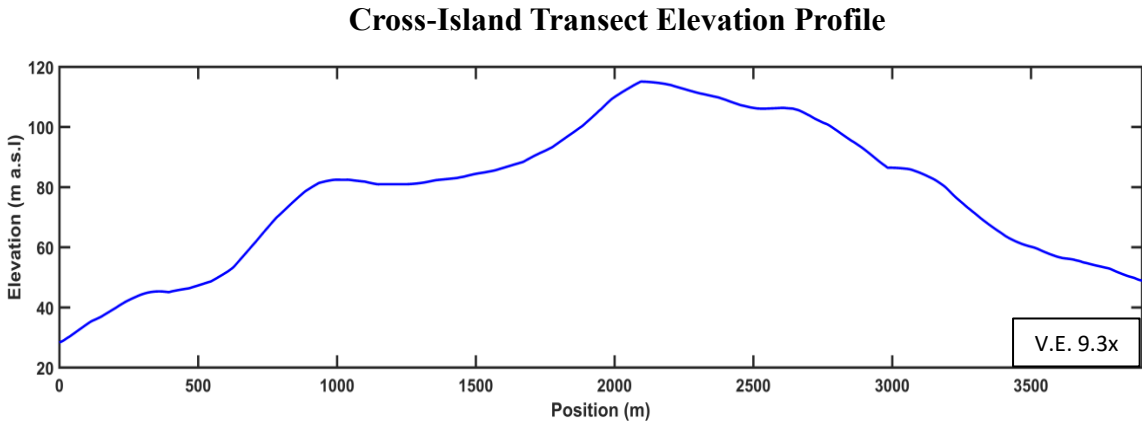

Figure 23: Elevation data (in meters above sea level) along cross-island transect, interpolated to 0.2 m trace spacing. Vertical exaggeration 9.6.

To correct for the differences in elevation between traces, each trace is shifted in time to its correct elevation using Equation (26). This method is similar to those used in static correction of seismic data [*Yilmaz*, 2001], where a constant subsurface velocity is used. It must be noted that topographic effects perpendicular to the plane of the bike trail are

ignored in this correction. However, efforts were made during acquisition to keep the TX and RX from tilting out-of-plane so it is expected that such effects are negligible. For the cross-island transect an estimated $1x10^8$ m/s was used to convert elevation to traveltime, and the resulting corrected section is shown in Figure 24.

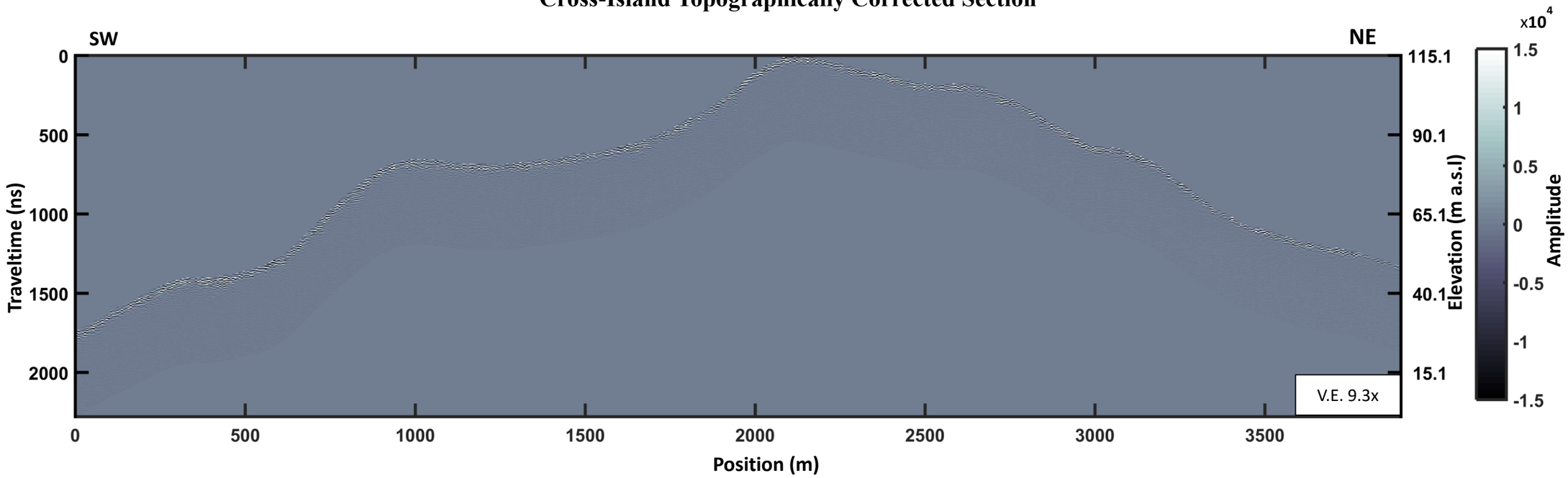

Figure 24: Topographic correction applied to preprocessed cross-island transect. Right axis in meters above sea level. Constant velocity of $1.0x10^8$ m/s used. Vertical exaggeration 9.3

5.1.2.2 Gain

Although the use of gain is discussed at this point in the imaging process, it must be noted that gain should not be applied (save for visualization purposes) until the data have been finally processed. This allows for the preservation of relative amplitude information throughout the data processing. Therefore the migration process discussed in the subsequent section was performed on un-gained data.

From the discussions on EM wave attenuation, amplitudes decreases intrinsically with traveltime. This can be observed in the previous cross-island transect sections shown. In order to better visualize reflections at later times, a scaling of the amplitudes, or gain, can be applied. There are many types of gains that are useful for GPR data ranging from constant valued to automatic [*Cassidy*, 2009b]. Two types of gain, power-law and automatic gain control (AGC) were individually used in this study to aid in the interpretation of the cross-island transect.

Power-law gain applies a time varying gain function that attempts to compensate for the effects of attenuation due to geometrical spreading [*Yilmaz*, 2001]. The simplest, and one that is frequently used in seismic reflection studies, is the t^2 power-law gain [*Clarbout*, 1985] where amplitudes are scaled according to the square of their traveltime. The gain function used in this thesis is similar and has the form,

$$g(t) = \alpha t^{\beta} + 1, \tag{37}$$

where α is some user-defined scaling factor, with units $1/s^{\beta}$, and β is a user-defined exponent. The gained trace, $s_g(t)$, is then simply the multiplication of the original trace, $s(t)$, by the gain function,

$$s_g(t) = s(t)g(t). \tag{38}$$

The benefit of functionally defined gains such as Equation (37), is that relative amplitudes between reflections along a given trace as well as those between traces are preserved [*Cassidy*, 2009b]. This power-law gain was applied to the traces in the topographically corrected section beginning at the first break and ending after a user specified time window. After the end of the time window, an exponential decay was appended to the gain function to smoothly bring the gain back to unity to make an aesthetically pleasing truncation to the application of the gain. This is done so as to avoid amplification of artifacts and noise beyond the interpretable depth in the GPR data. An example of this gain applied to a single trace using $\alpha = 1$ s^{-2}, $\beta = 2$, and a time window of 300 ns is shown in Figure 25.

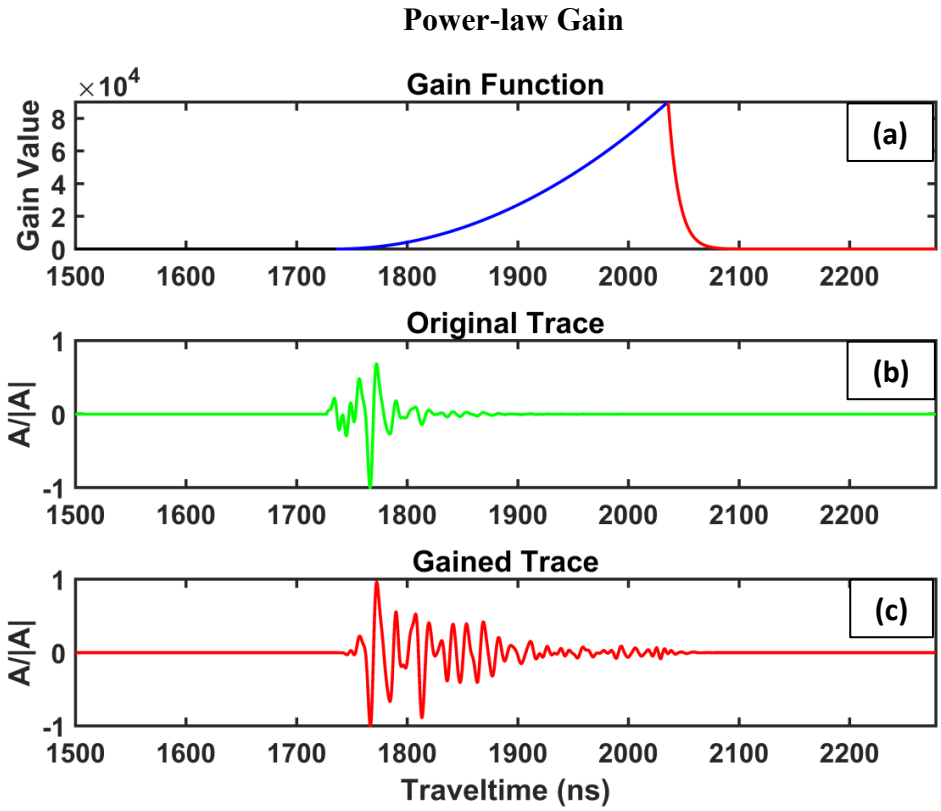

Figure 25: Power-law gain function applied to trace 50 in cross-island transect. **(a)** Gain function with $\boldsymbol{\alpha = 1}$, $\boldsymbol{\beta = 2}$, and a time window of 300 ns. Black is region before first break where no gain is applied, blue indicates gain application window, while red indicates ramping down of gain at end of application window. **(b)** Trace before gain. **(c)** Trace after application of gain. All trace amplitudes normalized to unity.

AGC is not a functional gain but rather an adaptive gain based on the average amplitude within a defined time window compared to some desired amplitude [*Yilmaz*, 2001]. For the AGC implemented in this study the desired amplitude was chosen to be the maximum amplitude in each trace, $s(i) : i = 1 \ldots n$, and thus the AGC as a function of sample was defined as:

$$g(i) = \frac{\max(\{s(1), \ldots, s(n)\})}{\frac{1}{N}\sum_{k=i-\frac{N}{2}}^{i+\frac{N}{2}} |s(k)|}, \tag{39}$$

where N is the number of samples in the AGC window. However, if $g(i)$ becomes larger than some user defined maximum gain value, $g(i)$ is set to that value. An example of this AGC applied to the same trace shown in Figure 25 is shown in Figure 26, where N was chosen to be 7, the maximum gain was 100, and the time window was 300 ns.

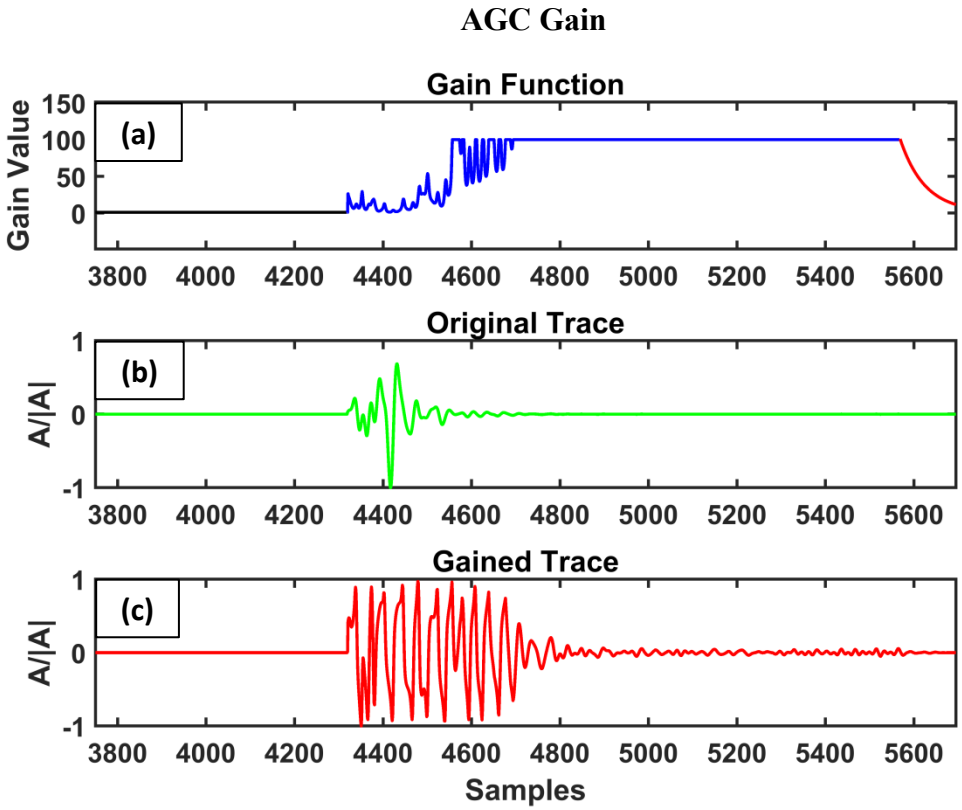

Figure 26: Automatic gain control applied to trace 50 of the cross-island transect. **(a)** Gain function with $\boldsymbol{N = 7}$, maximum gain of 100, and a time window of 300 ns. Black is region before first break where no gain is applied, blue indicates gain application window, while red indicates ramping down of gain at end of application window. **(b)** Trace before gain. **(c)** Trace after application of gain. All trace amplitudes normalized to unity.

Similarly to the power-law gain, a smooth ramp-down at the end of the time window was appended to the gain function. As can be seen, the effect of AGC is to bring all amplitudes up to a near-maximum level within a desired time window. The use of appropriate maximum gain value is essential to avoid magnifying small amplitudes below the depth of investigation. A drawback of AGC is that relative amplitude information both along a trace and compared to adjacent traces is lost in the process.

The same parameters as described above for both the power-law and AGC gains were applied across the cross-island transect. Figure 27 compares the effects of each gain on the data.

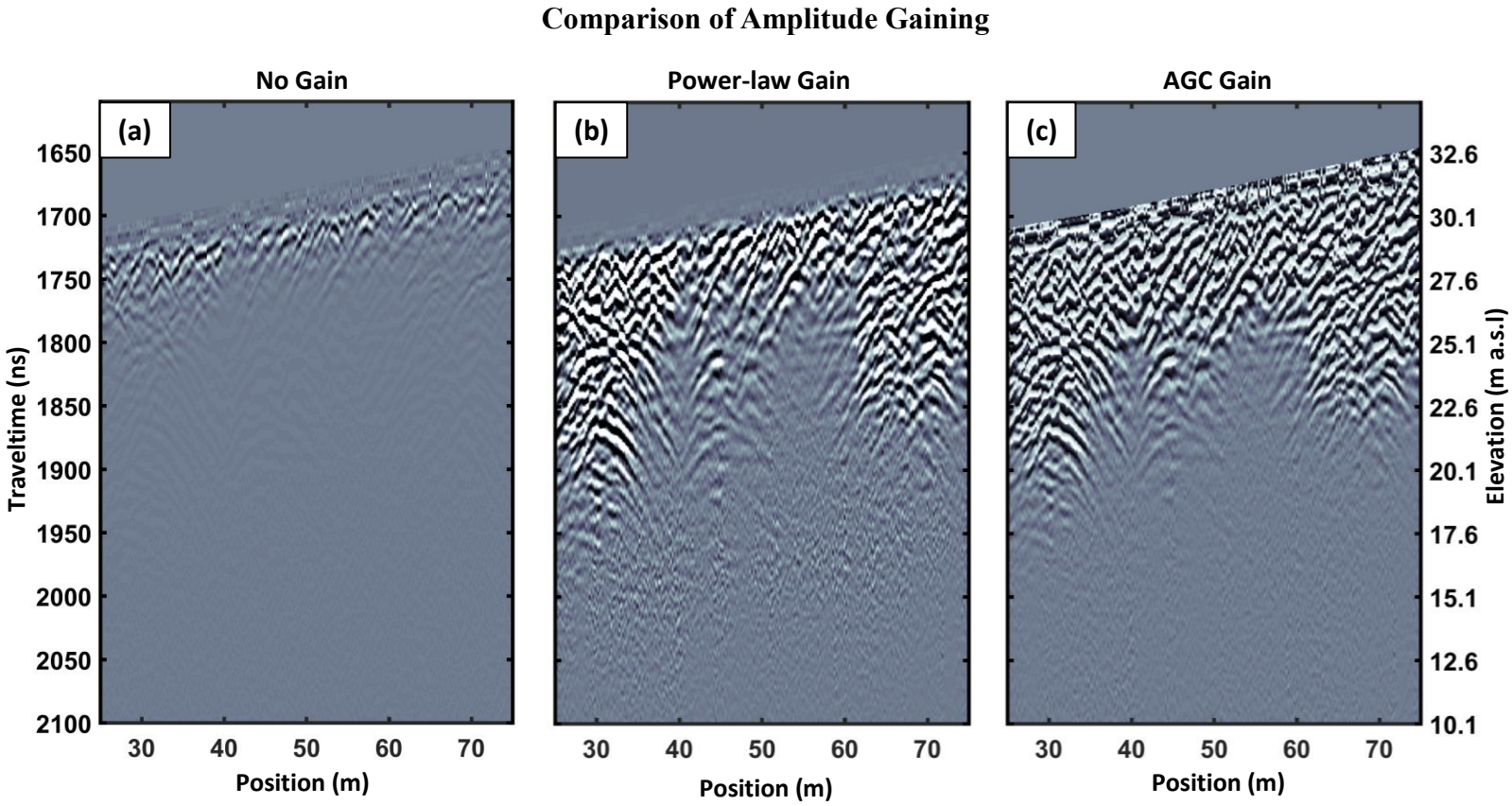

Figure 27: Comparison of gaining to cross island transect from 25-75 m along profile and traveltimes 1610-2100 ns. All figures at 3x vertical exaggeration. **(a)** No gain applied. **(b)** Power-law gain. **(c)** AGC gain.

Figure 27 shows that both gain functions allow for better visualization of deeper reflections within the data. As discussed, the power-law gain preserves the relative amplitudes of reflections, while the AGC does not. An example of this is the very low amplitudes observable at the surface in the power-law gained data. This is a result of the background subtraction largely removing the TX-RX direct wave. However, these low amplitudes prevent interpretation of the section at very early times, and the amplitude equalization performed during the AGC gaining makes these early time reflections (between t= 1625 and 1725 ns in Figure 27) more apparent. In addition the AGC gain highlights other geometrical features that are difficult to distinguish in the power-law gained section, such as those occurring at ~40 m in Figure 27b where relative amplitudes are low.

5.1.2.3 Migration

An in-depth discussion on the details of migration is outside the scope of this study. However, as migration is an important tool for creating interpretable images of the subsurface, and as special considerations must be taken when migrating GPR data, this section will provide a high-level overview of the motivations and process of migration.

When performing a GPR survey, the EM energy travels from the transmitter to a reflector where it is scattered. Some of that energy travels back up to the receiver and is recorded. Even though the position of a reflector in the subsurface is fixed by the geology, the traveltime for an EM wave to the reflector varies with position along a

transect. The result is that a collection of GPR traces above a reflector represents the response of the subsurface to both the EM energy and the acquisition geometry. This phenomena has been well studied and documented in the realm of exploration seismology [*Clarbout*, 1985; *Yilmaz*, 2001], and the principles can be applied to EM wave propagation under assumptions of far-field wave-fronts [*Cassidy*, 2009b] from an isotropic point source, that behave similarly to acoustic and elastic waves. More accurate representations of EM wave propagation in GPR must take into account the radiation pattern of the antenna [*Annan*, 1973; *Engheta et al.*, 1982].

A point reflector is here defines as having a radius of curvature smaller than the wavelength of the incident EM wavefield. For such point reflectors in the subsurface (known as diffractors), the traveltime curve that is recorded for a zero-offset survey traces out a hyperbola. The apex of this hyperbola is centered above the diffractor, as that is the location where the traveltime from source-receiver is the shortest. Figure 28 illustrates this concept by showing the raypaths and associated arrivals from an EM wavefield traveling from the TX-RX to the diffractor and back.

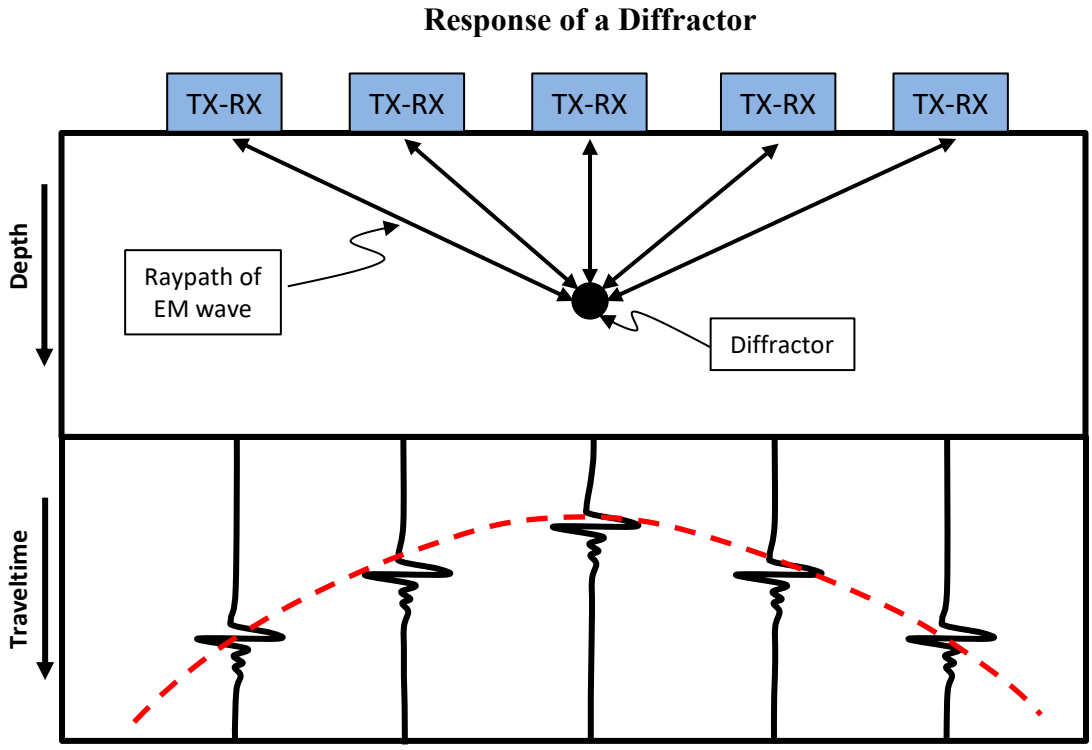

Figure 28: Cartoon describing zero-offset response of a diffractor. The reflected arrival at each trace location is a portion of a hyperbola.

Recall that the zero-offset assumption is valid for the cross-island transect due to the small TX-RX offset of 1 m compared to the envisioned depth of investigation of < 10m. Huygens principle, as restated by *Yilmaz*, [2001], says that these diffraction hyperbolae can be thought of as the arrivals from a so-called secondary source producing spherical wave-fronts located at the diffractor. In this manner, continuous reflectors can be thought of as being composed of many point diffractors, and the superposition of the wave-fields coming from these secondary sources is the reflection recorded at the

surface [*Yilmaz*, 2001]. Examples from *Yilmaz* [2001] and *Clarbout* [1985] are shown below for a horizontal and dipping reflector respectively.

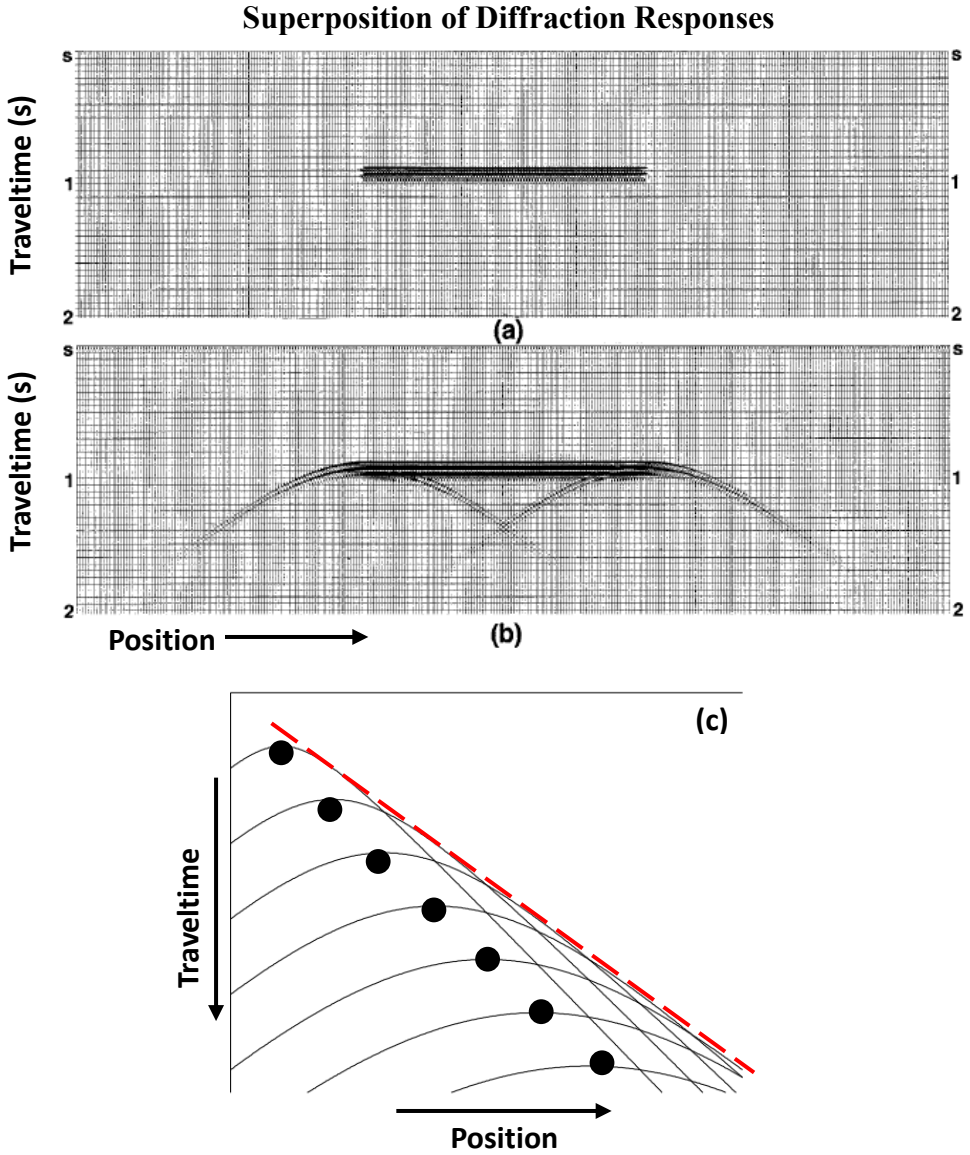

Figure 29: Describing reflections as a superposition of diffraction hyperbolas (modified after [*Yilmaz*, 2001] and [*Clarbout*, 1985]). **(a)** Horizontal continuum of diffractors. **(b)** Superposition of diffractions creates a reflection. From *Yilmaz* [2001]. **(c)** Discrete number of diffractors (black dots) describing a dipping reflector. Hyperbolas superimpose to produce the reflection outlined by red-dashed line. Modified after *Clarbout* [1985].

Figure 29a and b shows that, in this model, the horizontal reflection arrives coincident with the location of the line of diffractors. Yet hyperbolic, "diffraction-tails" are observed due to the discontinuous edges of the reflector (Figure 29a and b). For the case of the diffractors describing a dipping reflector (Figure 29c), the superposition of the hyperbolas produces a reflection (red line) that is both longer and dipping shallower than the true reflector (black dots).

The process of migration involves taking the energy recorded by the receivers and moving it to its correct spatial location. So, after migration, diffraction hyperbolae will be collapsed to points and dipping reflectors will be shortened and steepened [*Yilmaz*, 2001]. There a large number of migration algorithms available to perform this process, and there even exist some that account for the discrepancies in propagation between seismic (scalar) and EM (vector) waves [*Cassidy*, 2009b] as well as source signature effects. However one of the simplest migration methods to idealize and implement is hyperbolic summation. This process sums together recorded data along diffraction curves defined as (after [*Dujardin and Bano*, 2013])

$$t_s(x) = \sqrt{t_0^2 + \frac{4(x - x_d)^2}{v^2}}, \tag{40}$$

where $t_s(x)$ is the traveltime of the hyperbola recorded at receiver position x, t_0 is the vertical two-way traveltime to the diffraction point located at (x_d, z_d), and v is the

average or RMS subsurface velocity. Algorithms that implement what is known as Kirchhoff migration perform this hyperbolic summation while at the same time accounting for amplitude phase, spherical spreading, and wavelet phase along the summation curve [*Yilmaz*, 2001]. Kirchhoff migration was developed from the far-field portion of an integral solution to the scalar wave equation in seismology [*Schneider*, 1978].

Most classical migration schemes, including simple hyperbolic summation and complete Kirchhoff migration, are performed from a flat datum. This is reflected by the absence of z, the elevation of the receiver, when computing the hyperbolic traveltime curve in equation (40). Yet the response of a diffractor recorded on a non-horizontal surface is no longer a hyperbola. The shape is modified by the elevation changes along the surface of acquisition [*Dujardin and Bano*, 2013]. This effect is shown in Figure 30 for an idealized zero-offset case.

Distortion of Diffraction Hyperbola due to Topography

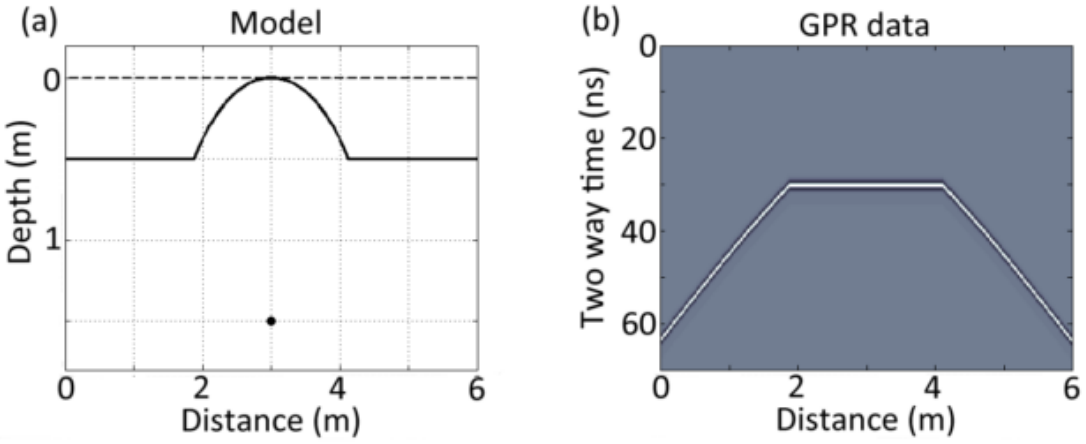

Figure 30: Synthetic example of effect of topography on response of a diffractor for GPR data, taken from [*Dujardin and Bano*, 2013]. **(a)** Model with topography indicated by black line, and diffractor as black point. Dashed line as reference to z=0 m. **(b)** Synthetic response of diffractor collected on topographic surface indicated in **(a)**.

Traditionally, corrections for elevation, as discussed in Section 5.1.2.1, are performed prior to migration to account for the distortion seen in Figure 30. In most cases of seismic exploration, the relief of the acquisition surface versus the depth of reflections renders static elevation corrections appropriate for returning diffraction curves to hyperbolas [*Lehmann and Green*, 2000]. However in cases of extreme topography this static correction is insufficient, and work by *Wiggins* [1984] showed that topographic effects could be accounted for by modifying the summation curve in Kirchhoff migrations. In the case of GPR, the depth to reflections is often less than or equal to the relative changes in elevation along a line. Therefore even relatively small topographic variation causes errors in the traditional approach of elevation corrections followed by

migration [*Lehmann et al.*, 1998; *Dujardin and Bano*, 2013]. This necessitates accounting for topography during migration of GPR data, and the resulting modification to the summation curve in Equation (40) gives

$$t_s(x) = \sqrt{t_0^2 + 4\frac{(x - x_d)^2 + (-z_0)^2}{v^2} - 4\frac{t_0(z(x) - z_0)}{v}}, \tag{41}$$

where $z(x)$ is the elevation of the acquisition surface at position z, and z_0 is the elevation of the migration datum. A detailed derivation of Equation (41) is given in [*Dujardin and Bano,* 2013]. For simplicity z_0 is often defined as 0 m with all topographic variation along a prolife existing below this datum, i.e. z_0 is the highest point along the profile.

Using Equation (41) and following the algorithm described in [*Dujardin and Bano*, 2013] a topographic hyperbolic summation migration routine was implemented in MATLAB. This algorithm not only sums data along topographically modified hyperbolas but it also accounts for amplitude changes along the summation curve due to oblique incidence [*Yilmaz*, 2001]. Since the migration internally corrects the data for effects of topography, the preprocessed dataset shown in Figure 22 was used as input to the algorithm rather than the topographically corrected section in Figure 24.

Accurate migration results depend on knowledge of the subsurface velocity. Given that only fixed offset data were collected on Bonaire, velocity structure cannot be determined via traditional velocity analysis methods such as semblance and NMO stacking [*Yilmaz*, 2001]. As a result, optimal migration velocity was determined by iterative attempts at migration while varying the velocity. A good migration velocity will collapse hyperbolic diffractions without causing overmigration visible by semi-elliptical, concave-upward, artifacts [*Yilmaz*, 2001]. Previous studies have shown insignificant variation in average velocity with depth [*Forte et al.*, 2012] and little improvement to imaging from using more complex velocity models [*Menezes et al.*, 2016] for GPR surveys in limestone lithologies. Therefore, three constant migration velocities, 0.9×10^8 m/s, 1.0×10^8 m/s, and 1.1×10^8 m/s, were tested at multiple locations along the cross island transect. These tests were looking to find the velocity that best collapsed diffraction hyperbolas and tails observed in topographically corrected data.

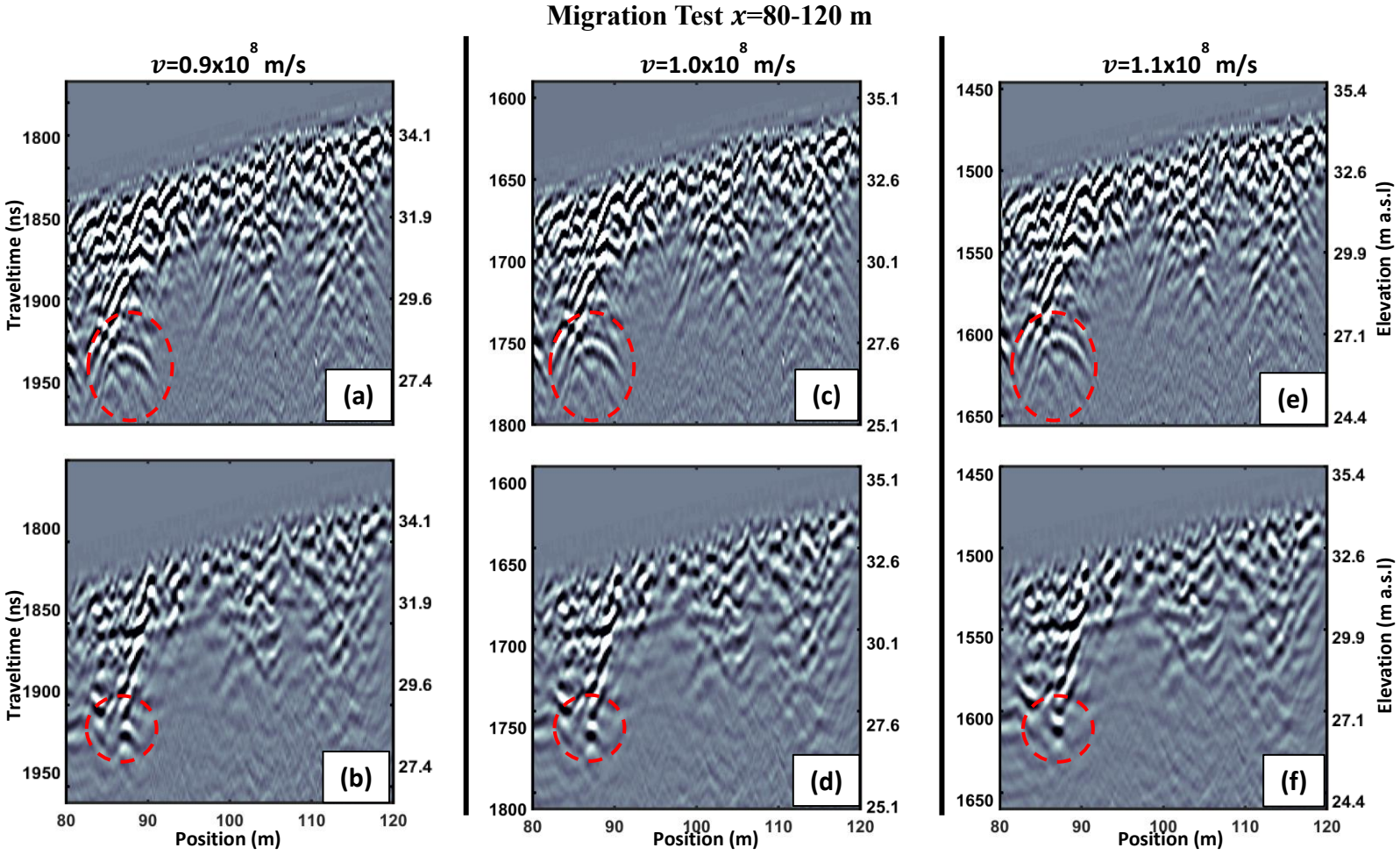

Figure 31: Topographic correction but no migration (top panels) versus topographic migration (bottom panels) at x=80-120. **(a-b)** v=0.9x10^8 m/s **(c-d)** v=1.0x10^8 m/s **(e-f)** v=1.1x10^8 m/s. Ovals indicate diffractions of interest. Power-law gain.

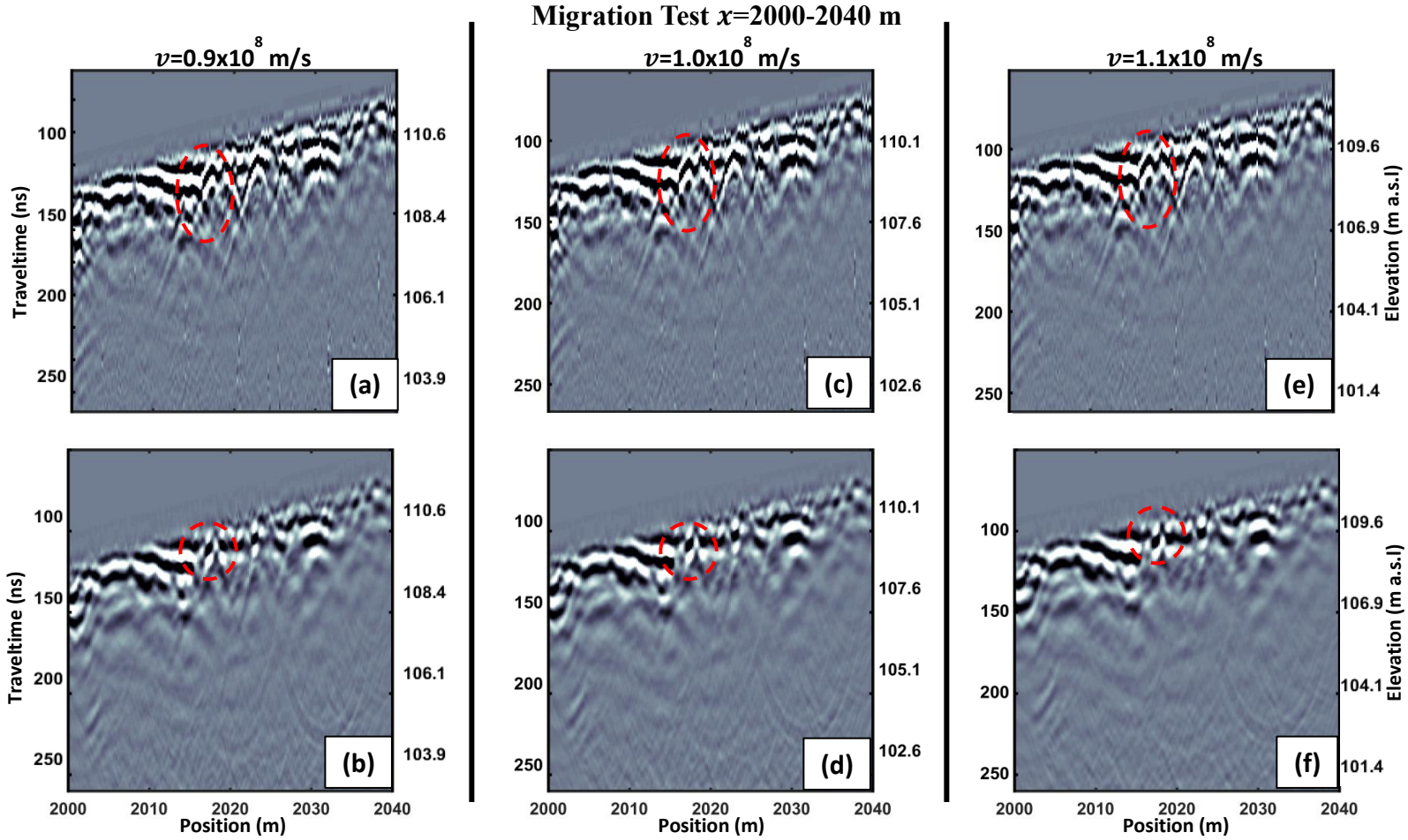

Figure 32: Topographic correction but no migration (top panels) versus topographic migration (bottom panels) at x=2000-2040. **(a-b)** v=0.9x10^8 m/s **(c-d)** v=1.0x10^8 m/s **(e-f)** v=1.1x10^8 m/s. Ovals indicate diffractions of interest. Power-law gain.

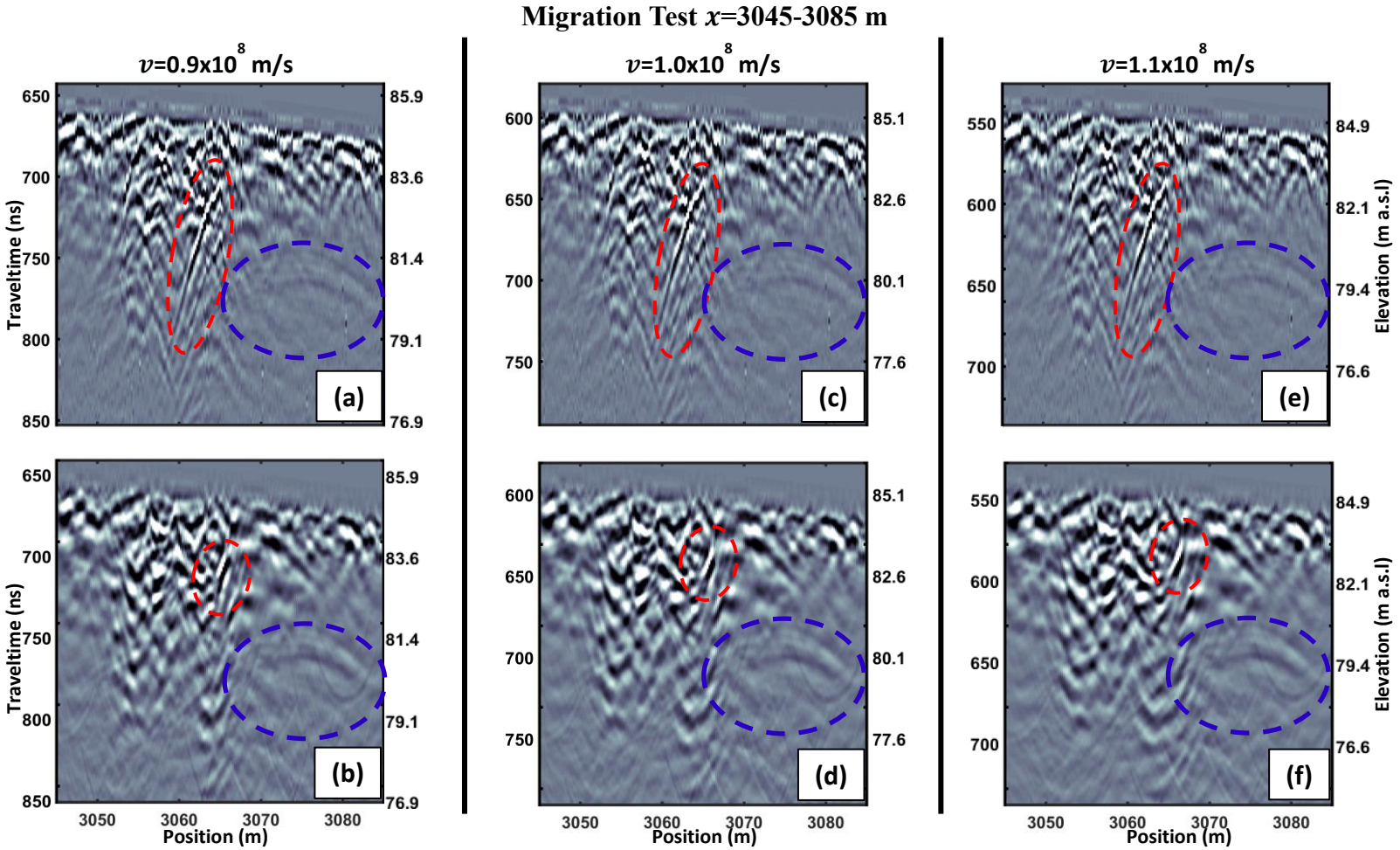

Figure 33: Topographic correction but no migration (top panels) versus topographic migration (bottom panels) at x=3045-3085. **(a-b)** v=0.9x10^8 m/s **(c-d)** v=1.0x10^8 m/s **(e-f)** v=1.1x10^8 m/s. Ovals indicate diffractions of interest. Power-law gain.

In each of the panels in Figures 31- 33 a power-law gain using the parameters chosen in Section 5.1.2.2 was applied for visualization purposes. In examining the above tests, the effects of changing velocity are subtle, however the diffractions and diffraction tails outlined by the red ovals show how well each velocity migrated the data. It was observed in general that a velocity of $0.9x10^8$ m/s did not collapse diffractions completely (red ovals Figure 31b and Figure 33b). Similarly, a migration velocity of $1.1x10^8$ m/s caused overmigration of diffractions seen by the upturning of reflections near the edge of the diffractor in the migrated sections (panel (f) of Figures 26-28). The migration velocity of $1.0x10^8$ m/s collapsed diffraction hyperbolas well while infrequently causing overmigration artifacts, thus providing the best imaging of the three velocities tested

It is important to note that some diffraction hyperbolae were not collapsed at any of the migration velocities in the above tests. An example of this is highlighted by the blue ovals in Figure 33. In the unmigrated sections of Figure 33 this hyperbola is observed to be considerably broader than many neighboring diffractions. From the discussion of diffraction hyperbolae, this implies that the EM energy traveled a fast velocity (close to the speed of EM waves in air in fact) between the TX-RX and the diffractor for the broad hyperbola compared to a slower velocity for the the more narrow ones. Given that the antennas used in this survey were unshielded, EM energy was radiated into the air as well as into the subsurface. Reflections off of tree branches, or the prevalent cactus branches along the bike trail, would produce the observed broad diffraction hyperbolae.

Since the migration velocities used in the tests were all much slower than that of EM waves in air (~$3.0x10^8$ m/s) these hyperbolae were not collapsed. As such these "air-reflections" represent unwanted noise that was not removed during the preprocessing stage and require caution to avoid mis-interpretation. However, these features are mainly observed below the interpretable depth in the GPR data and therefore are easily identifiable. It is likely that such features occur throughout the dataset, yet because they have low amplitudes due to the preferential propagation of EM energy into the subsurface [*Annan,* 1973; *Engheta et al.,* 1982] much of these signals are masked by the higher amplitude subsurface reflections. Therefore the air-wave diffractions are only visible where few other signals are coincident, such as below the depth of investigation.

Figures 34-45 show the results of the migration using the best performing migration velocity of $1.0x10^8$ m/s along the full cross-island transect. So as to better show the complete characteristics of the data, both power-law gained and AGC gained data are displayed.

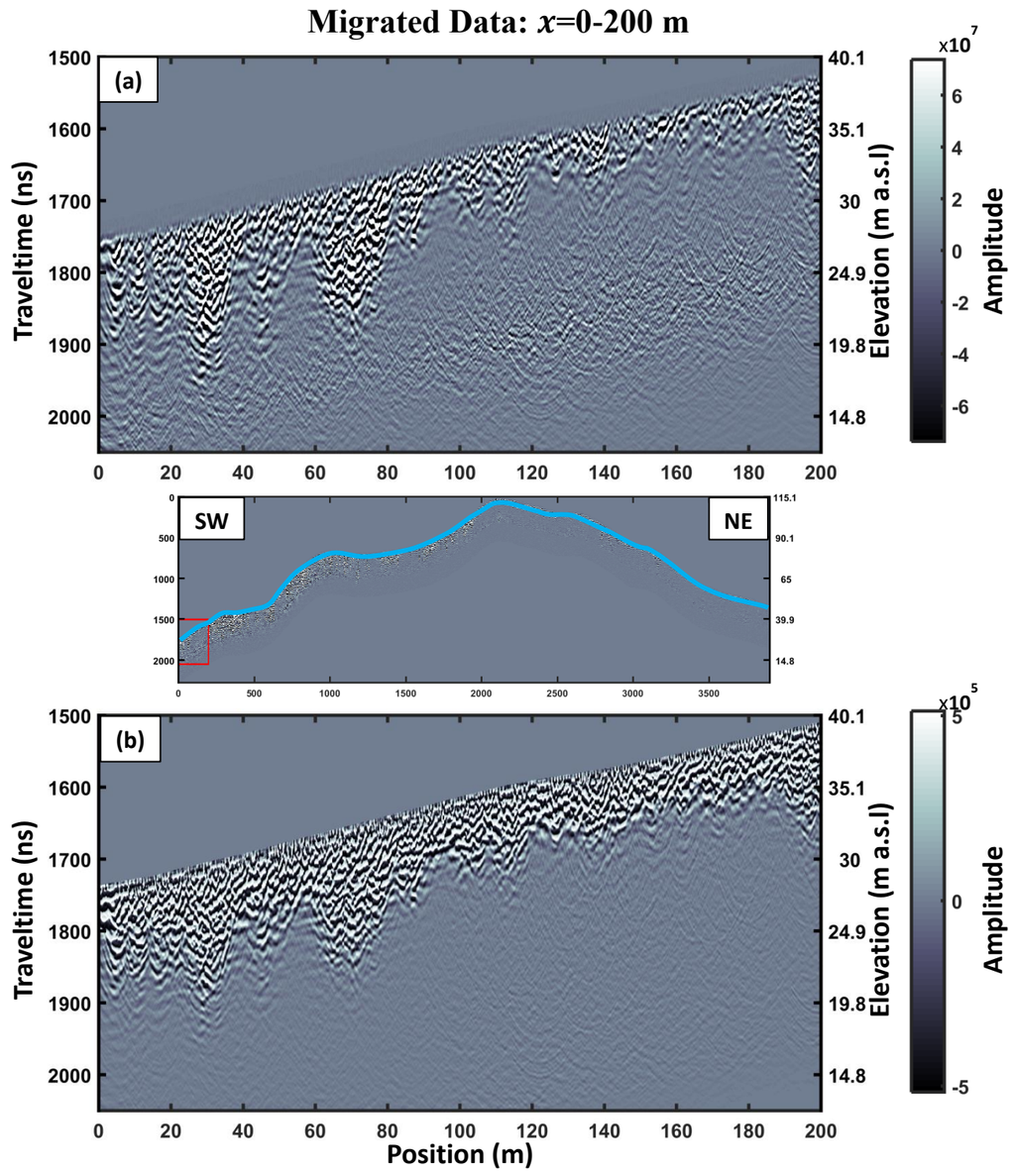

Figure 34: Topographically migrated cross-island transect, x=0-200 m. **(a)** Power-law gained data. **(b)** AGC gained data. Locator map in center showing location of section (red box) in relation to entire line (cyan line). Vertical exaggeration of sections, 4x. Vertical exaggeration of locator map, 9.3x.

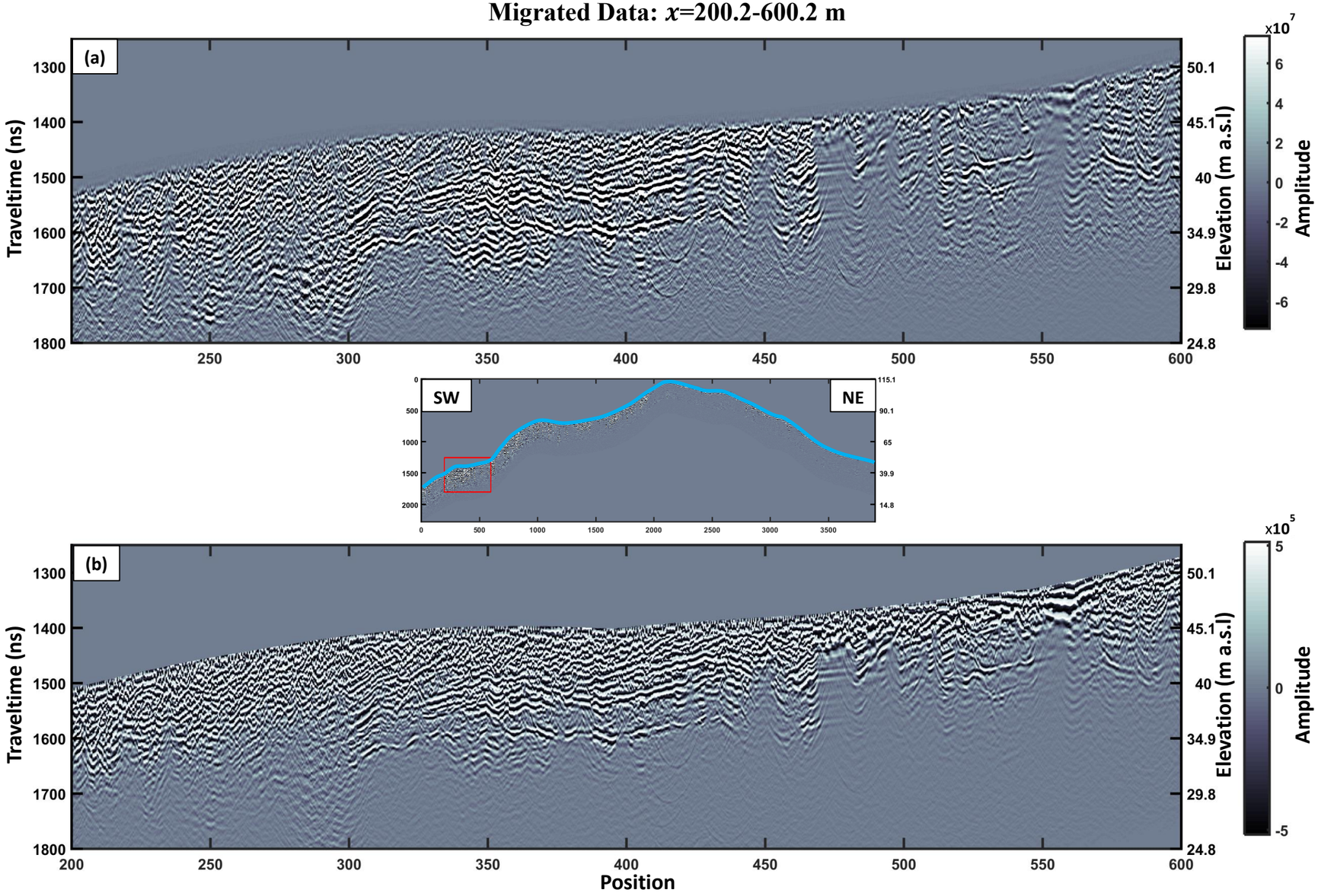

Figure 35: Topographically migrated cross-island transect, x=200.2-600.2 m. **(a)** Power-law gained data. **(b)** AGC gained data. Locator map in center showing location of section (red box) in relation to entire line (cyan line).Vertical exaggeration of sections, 4x. Vertical exaggeration of locator map, 9.3x.

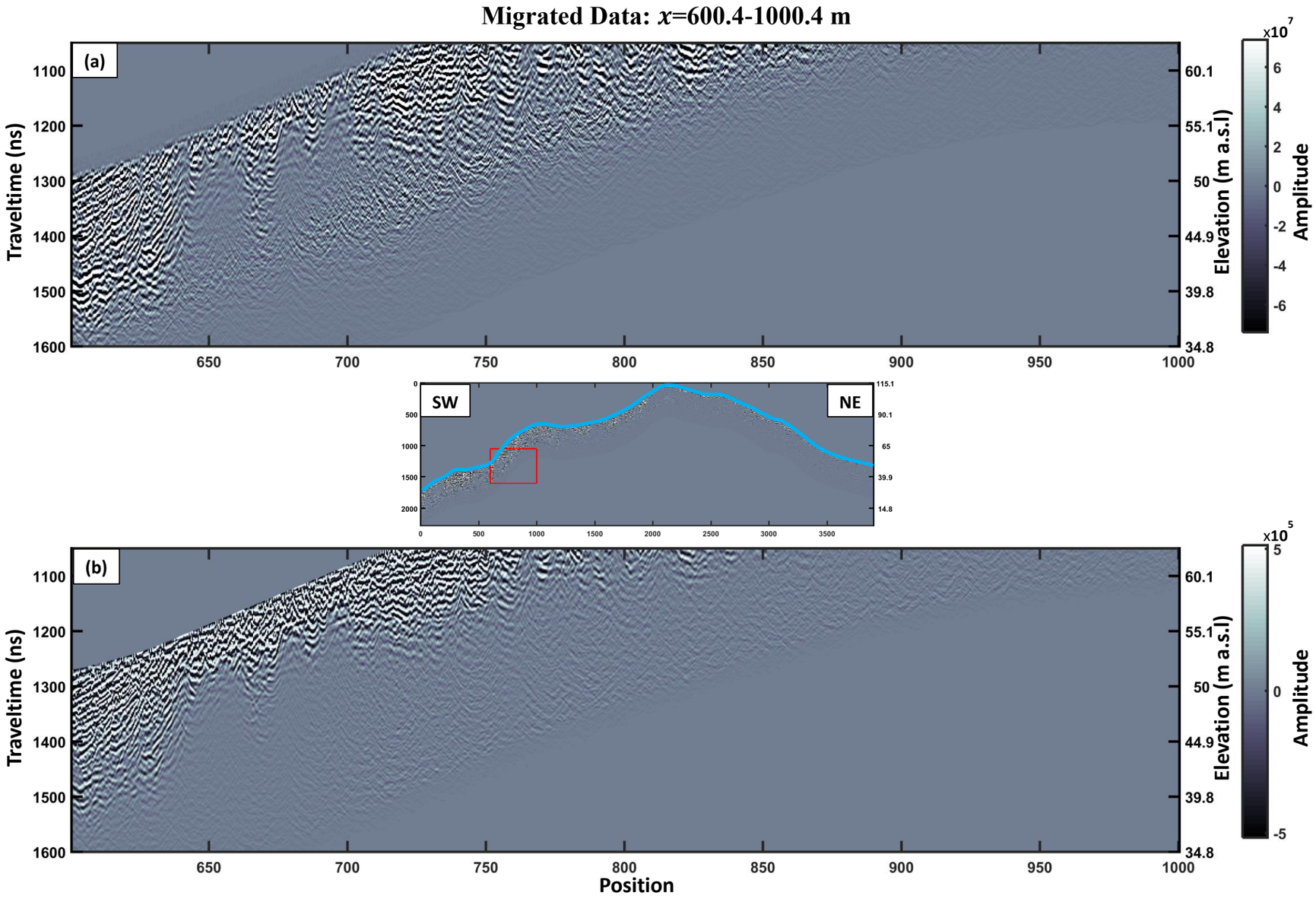

Figure 36: Topographically migrated cross-island transect, ***x***=600.4-1000.4 m. **(a)** Power-law gained data. **(b)** AGC gained data. Locator map in center showing location of section (red box) in relation to entire line (cyan line).Vertical exaggeration of sections, 4x. Vertical exaggeration of locator map, 9.3x.

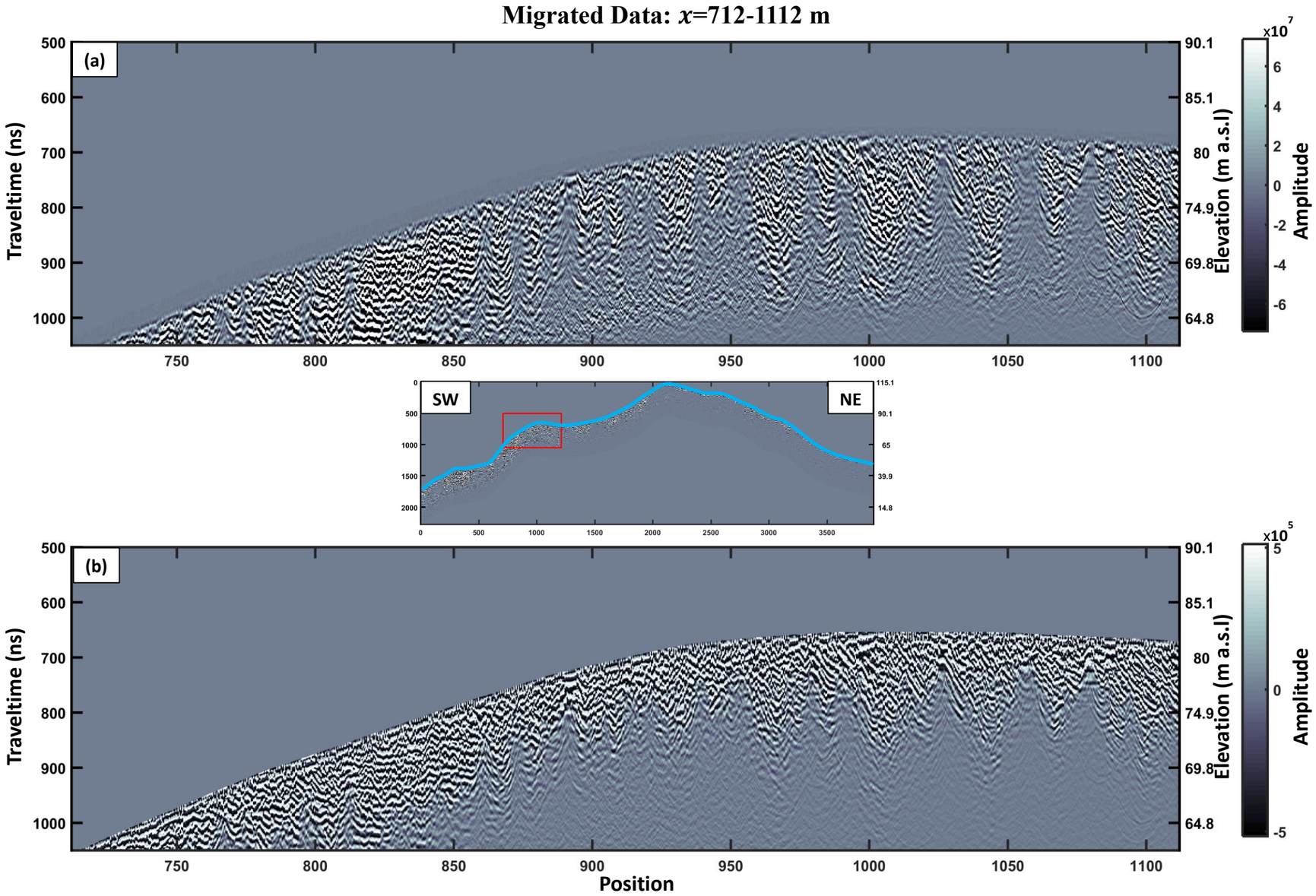

Figure 37: Topographically migrated cross-island transect, x=712-1112 m. **(a)** Power-law gained data. **(b)** AGC gained data. Locator map in center showing location of section (red box) in relation to entire line (cyan line).Vertical exaggeration of sections, 4x. Vertical exaggeration of locator map, 9.3x.

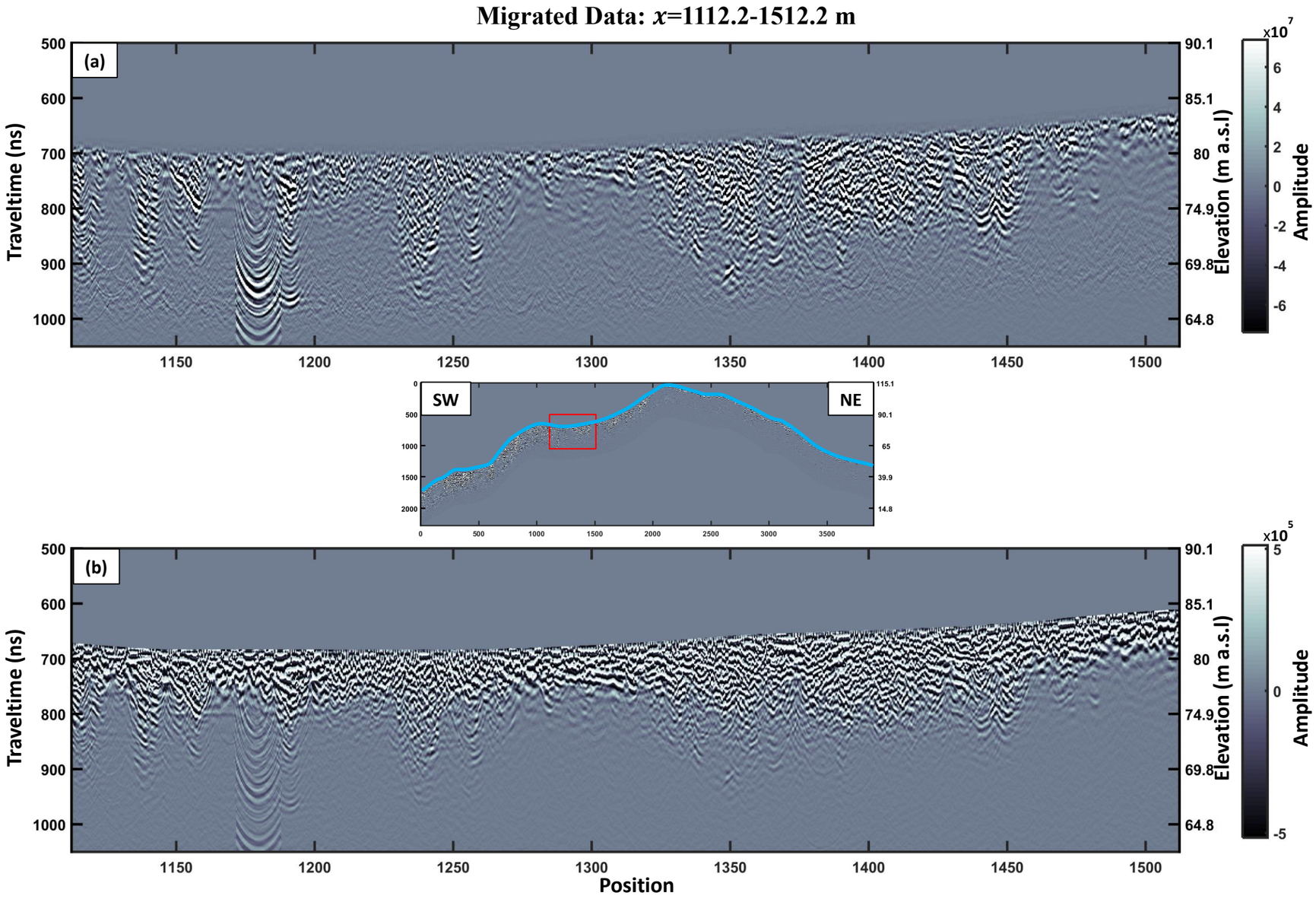

Figure 38: Topographically migrated cross-island transect, ***x***=1112.2-1512.2 m. **(a)** Power-law gained data. **(b)** AGC gained data. Locator map in center showing location of section (red box) in relation to entire line (cyan line).Vertical exaggeration of sections, 4x. Vertical exaggeration of locator map, 9.3x.

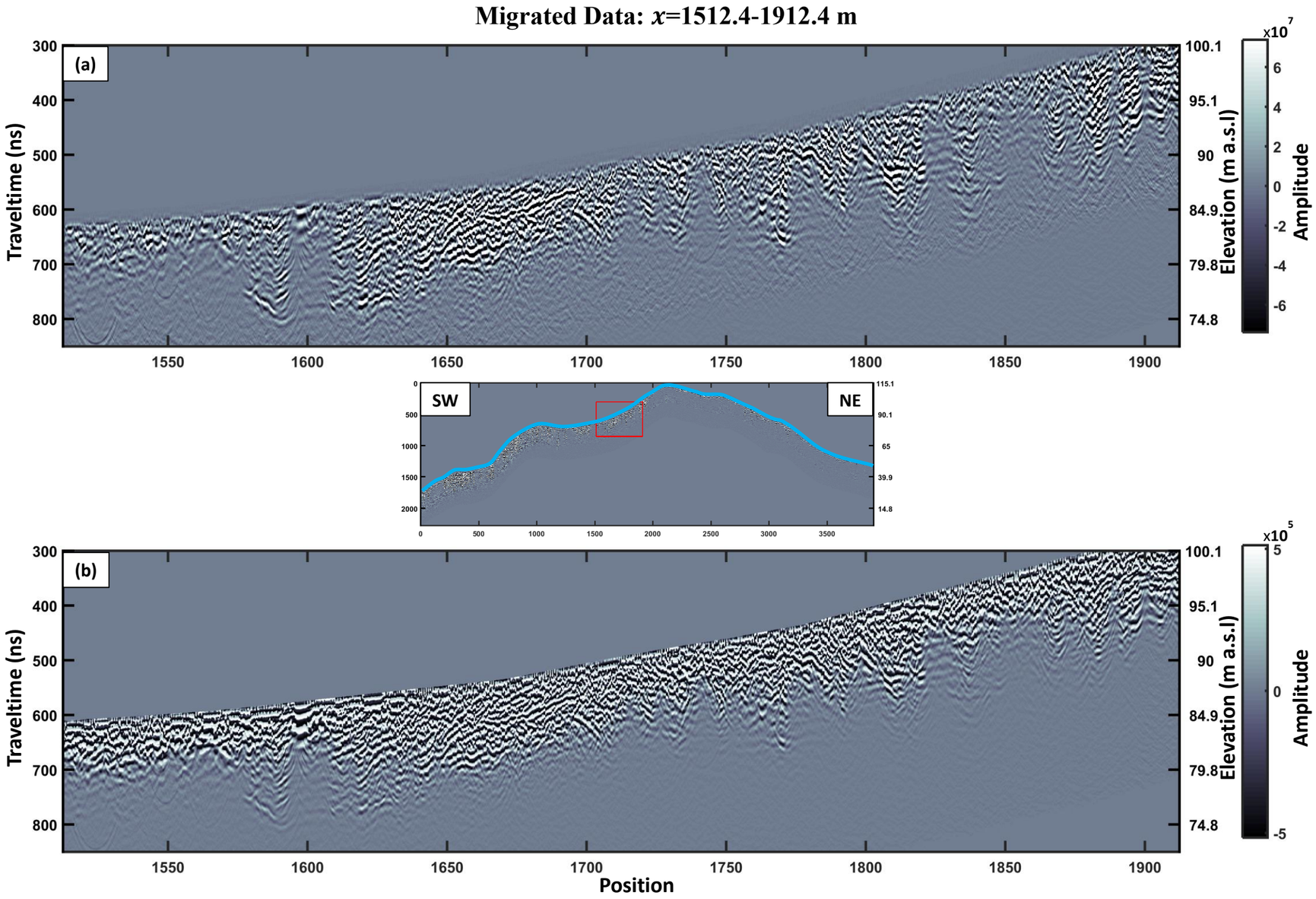

Figure 39: Topographically migrated cross-island transect, ***x***=1512.4.2-1912.4 m. **(a)** Power-law gained data. **(b)** AGC gained data. Locator map in center showing location of section (red box) in relation to entire line (cyan line).Vertical exaggeration of sections, 4x. Vertical exaggeration of locator map, 9.3x.

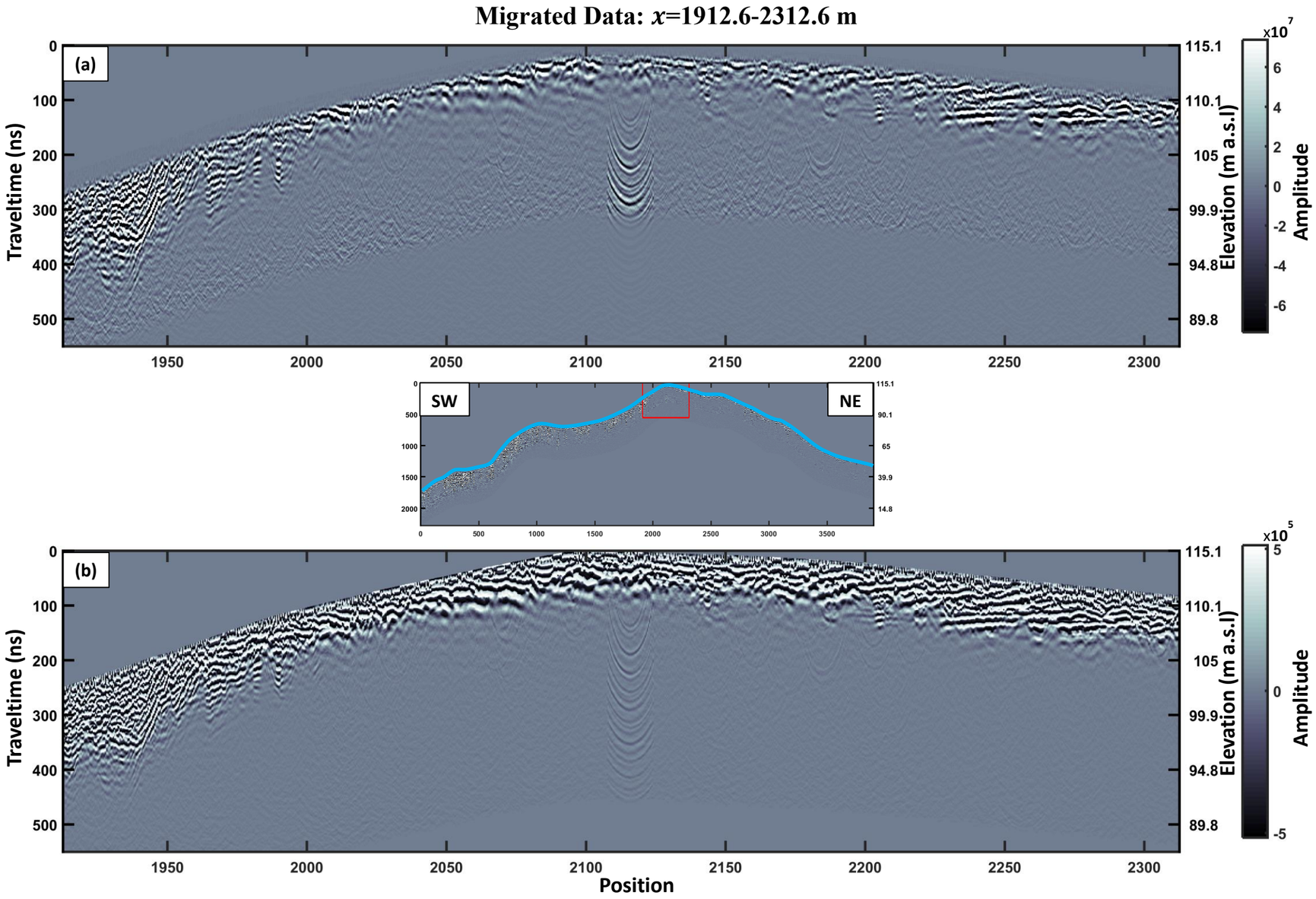

Figure 40: Topographically migrated cross-island transect, ***x***=1912.6.4.2-2312.6 m. **(a)** Power-law gained data. **(b)** AGC gained data. Locator map in center showing location of section (red box) in relation to entire line (cyan line).Vertical exaggeration of sections, 4x. Vertical exaggeration of locator map, 9.3x.

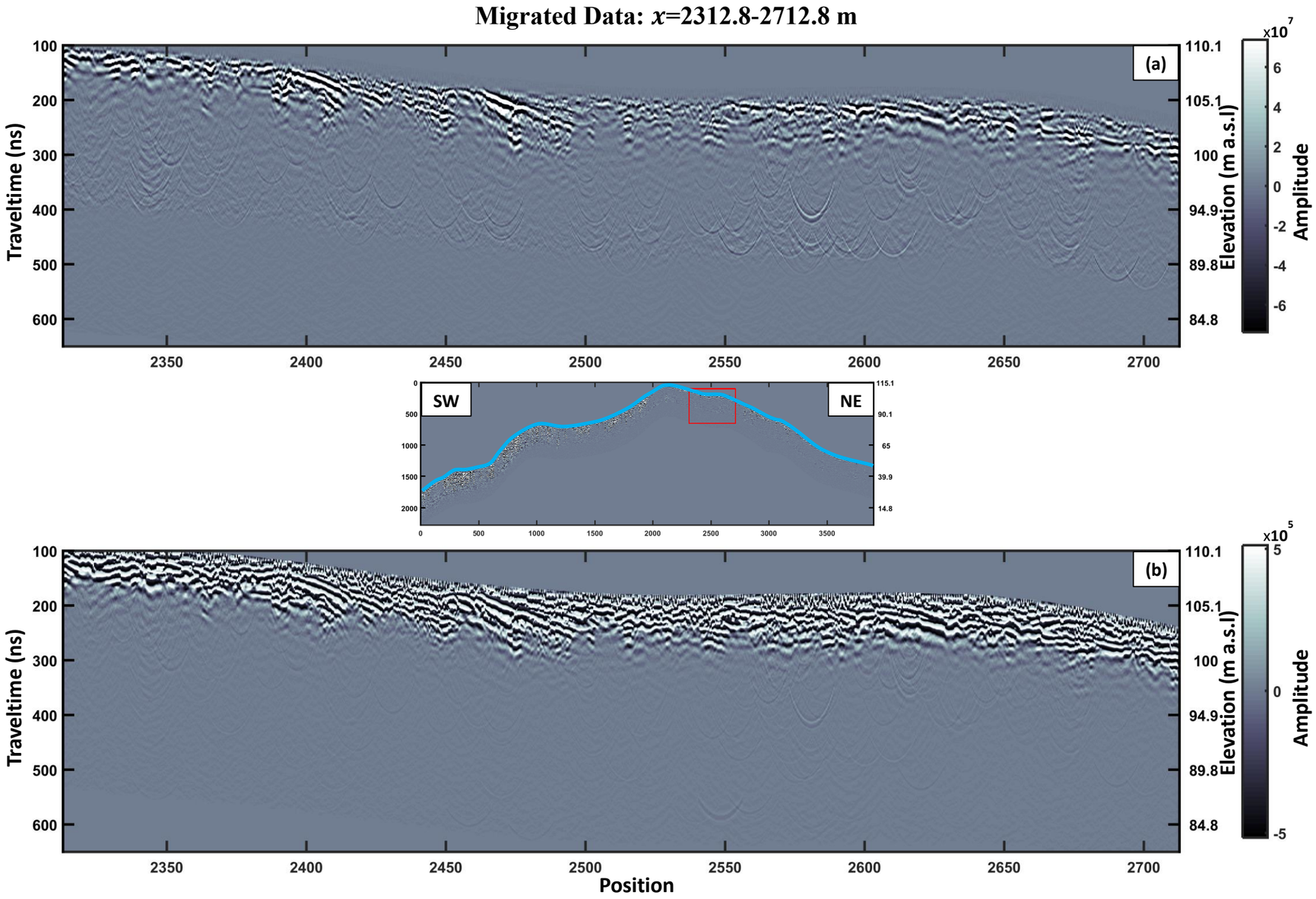

Figure 41: Topographically migrated cross-island transect, ***x***=2312.8.4.2-2712.8 m. **(a)** Power-law gained data. **(b)** AGC gained data. Locator map in center showing location of section (red box) in relation to entire line (cyan line).Vertical exaggeration of sections, 4x. Vertical exaggeration of locator map, 9.3x.

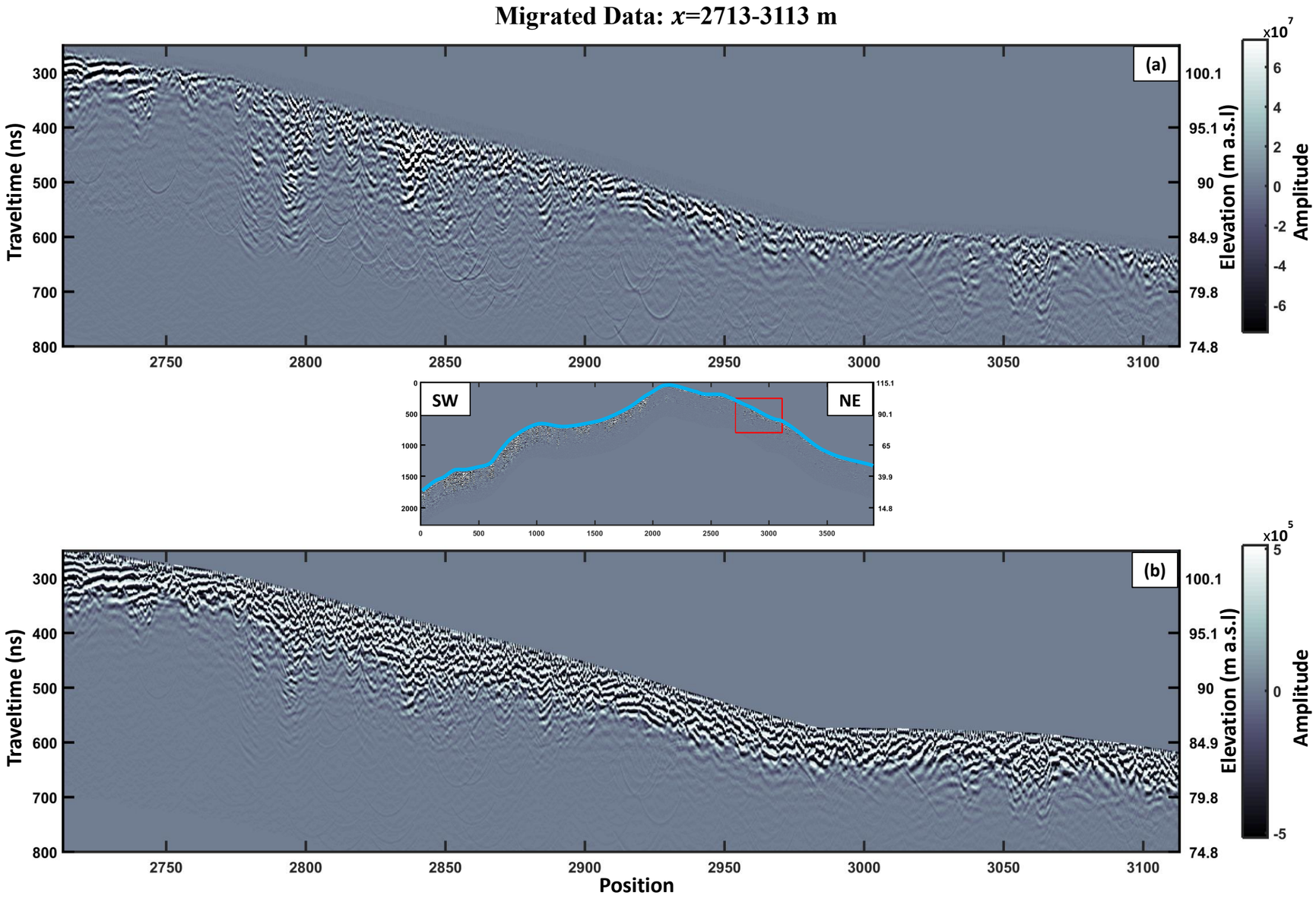

Figure 42: Topographically migrated cross-island transect, x=2713-3113 m. **(a)** Power-law gained data. **(b)** AGC gained data. Locator map in center showing location of section (red box) in relation to entire line (cyan line).Vertical exaggeration of sections, 4x. Vertical exaggeration of locator map, 9.3x.

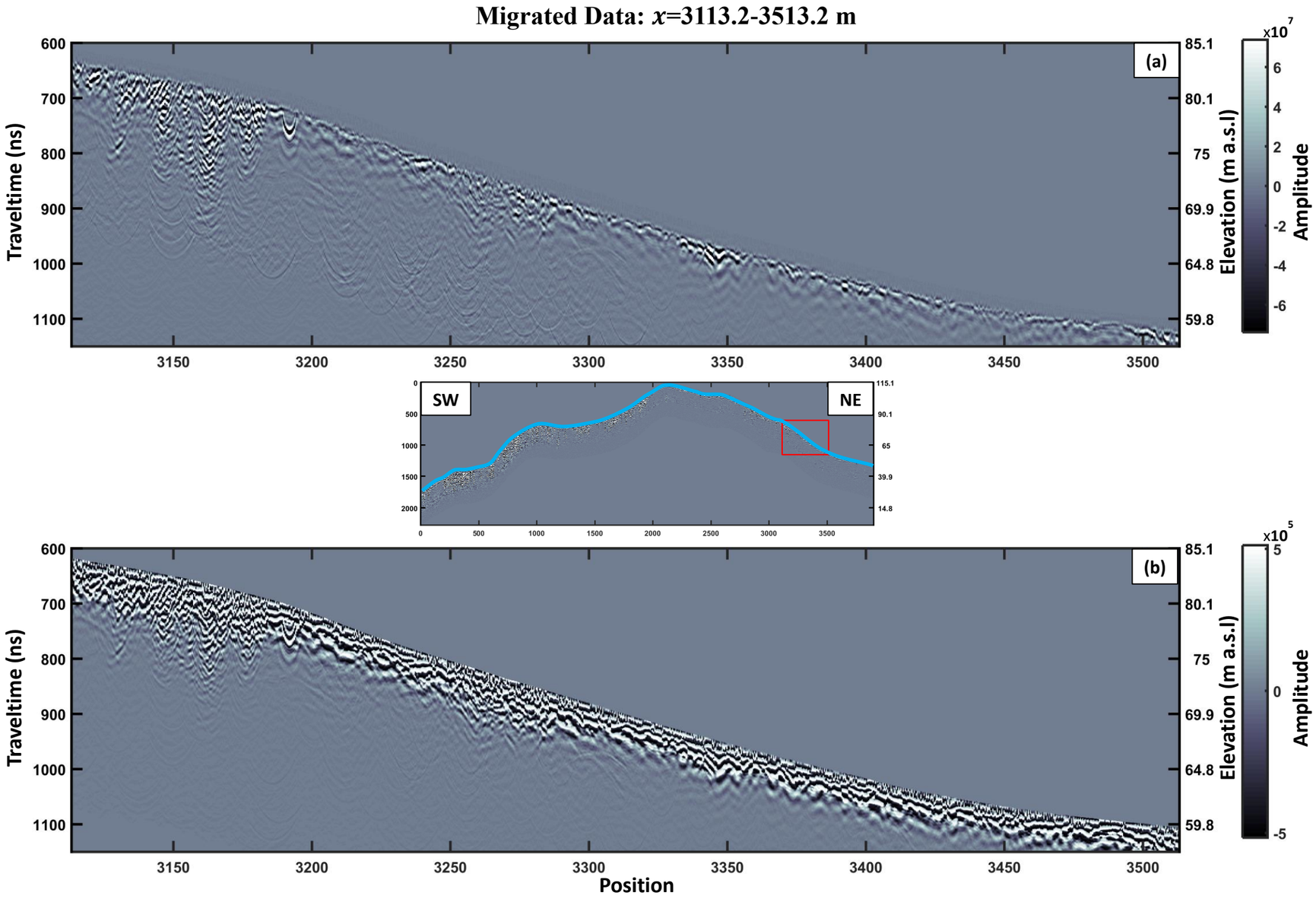

Figure 43: Topographically migrated cross-island transect, ***x***=3131.2-3513.2 m. **(a)** Power-law gained data. **(b)** AGC gained data. Locator map in center showing location of section (red box) in relation to entire line (cyan line).Vertical exaggeration of sections, 4x. Vertical exaggeration of locator map, 9.3x.

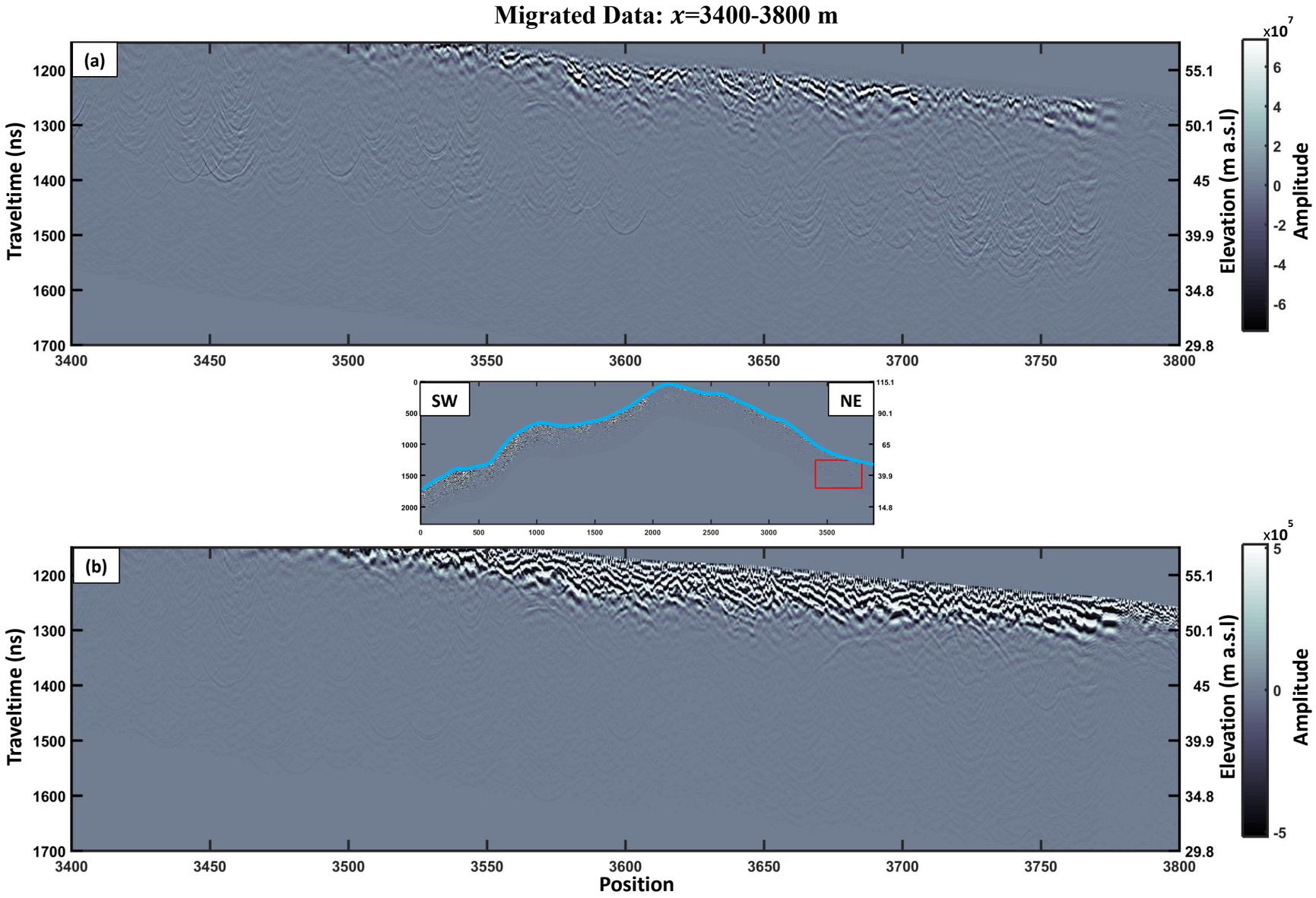

Figure 44: Topographically migrated cross-island transect, ***x***=3400-3800 m. **(a)** Power-law gained data. **(b)** AGC gained data. Locator map in center showing location of section (red box) in relation to entire line (cyan line).Vertical exaggeration of sections, 4x. Vertical exaggeration of locator map, 9.3x.

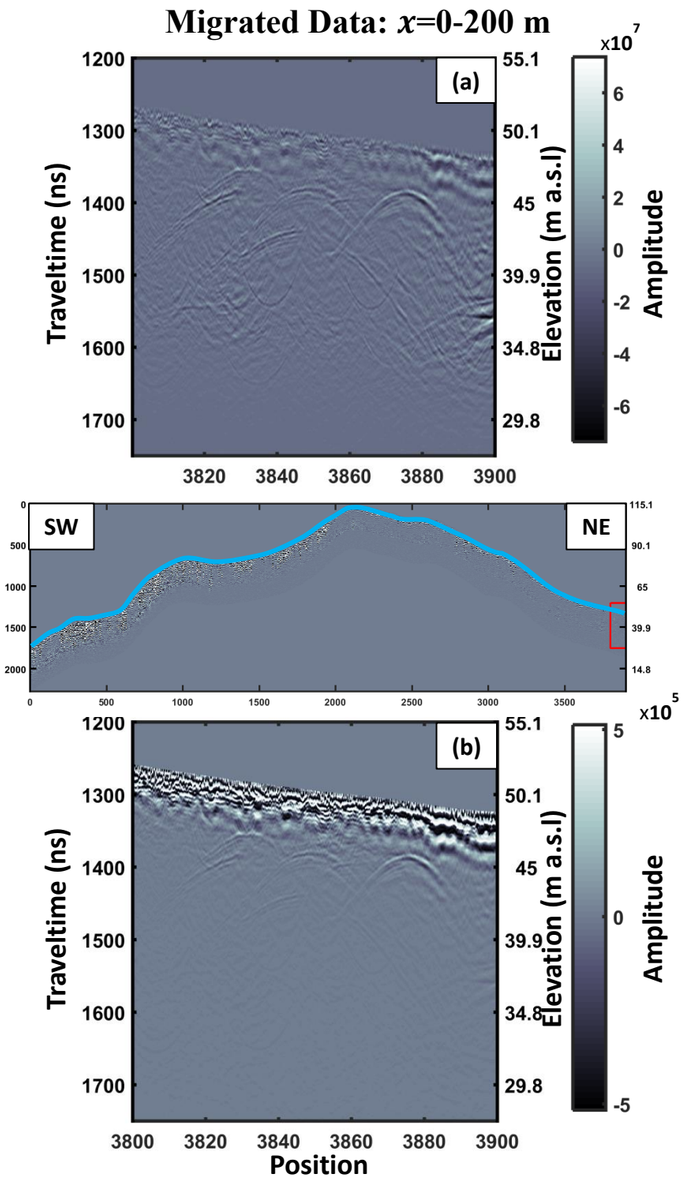

Figure 45: Topographically migrated cross-island transect, x=3800-3900 m. **(a)** Power-law gained data. **(b)** AGC gained data. Locator map in center showing location of section (red box) in relation to entire line (cyan line).Vertical exaggeration of sections, 4x. Vertical exaggeration of locator map, 9.

Examination of the migrated data shows that the greatest depths of penetration occur on the southwest portion of the transect. In this region coherent reflections are observed up to 15 m below the surface. However at the top of the line (Figure 40), and then down the northeast side, the depths of penetration are much shallower. In some places reflections are not observable past 1-2 m. Poor ground coupling on irregular surfaces along the transect may be the cause for such trends. Changes in geology including scattering caused by fractures, or high contrast interfaces could also affect the depth of penetration, and the implications of such will be discussed in Section 6. It must be noted that equipment errors are likely the cause of the drastically low amplitudes and inconsistent signal character observed from 3750-3900m along the line (Figure 44 and Figure 45). The abrupt change in amplitudes could have been caused by poor electrical connections between the TX and the antenna. In addition, there are several of the previously mentioned air-reflections with broad hyperbolas in this portion of the line. They are more easily observable due to the lack of subsurface reflections observed. Yet in general, artifacts due to migration are generally insignificant across the line. The most noticeable of which is the migration response of the specked "white-noise" seen in the unmigrated sections (Figure 31 and Figure 33). Although migration collapses hyperbolas to points, the impulse (point) response for migration is a semi-ellipse [*Yilmaz*, 2001]. Therefore where random-like signal noise occurs, the migration algorithm creates semicircular artifacts. A prominent example of this is in Figure 40 where a noisy trace in the unmigrated section produced the inverted hyperbolas seen after migration. A detailed look at this portion of the data is shown in Figure 46.

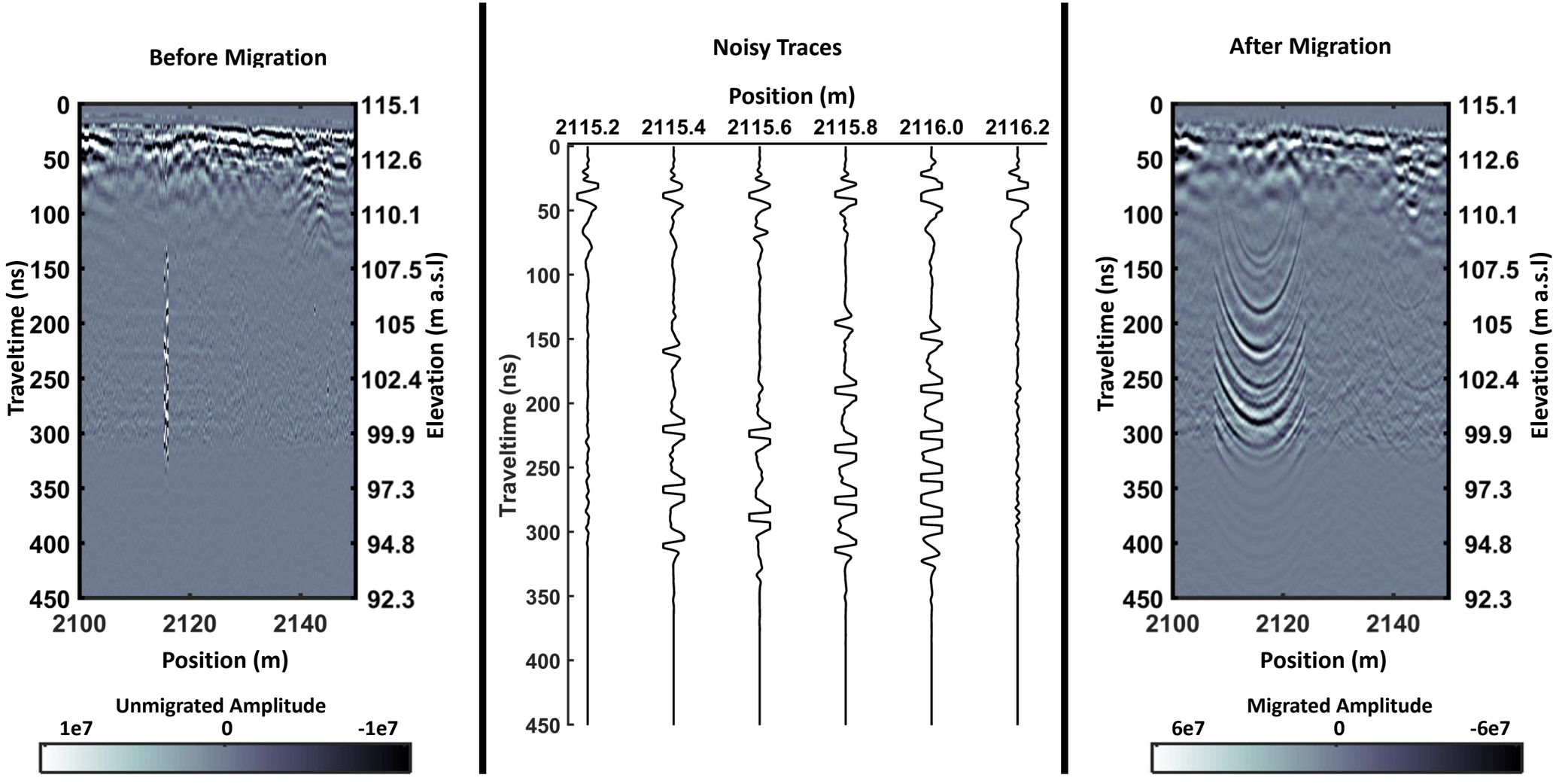

Figure 46: Example of migration artifacts. **(left)** Unmigrated portion of cross-island transect from x =2100-2150 showing noisy traces. **(middle)** Trace plot showing noisy traces bounded by non-noisy traces. **(right)** Migrated portion of cross-island transect from x =2100-2150 showing migration artifacts resulting from noisy traces.

5.2 Seru Grandi Survey

The processing of the GPR lines collected at Seru Grandi followed the same processing steps outlined in Section 5.1. The data were pre-processed with first break realignment, de-wow, background subtraction, and frequency filtering. The data were then migrated with the topographic hyperbolic summation algorithm. The topography dataset that was used in the migration was extracted from the previously mentioned high-resolution point cloud model of the Seru Grandi outcrop [*Laya et al.*, 2015]. An example of the topographic profile extracted from the point cloud model for Line 1 is shown in Figure 47.

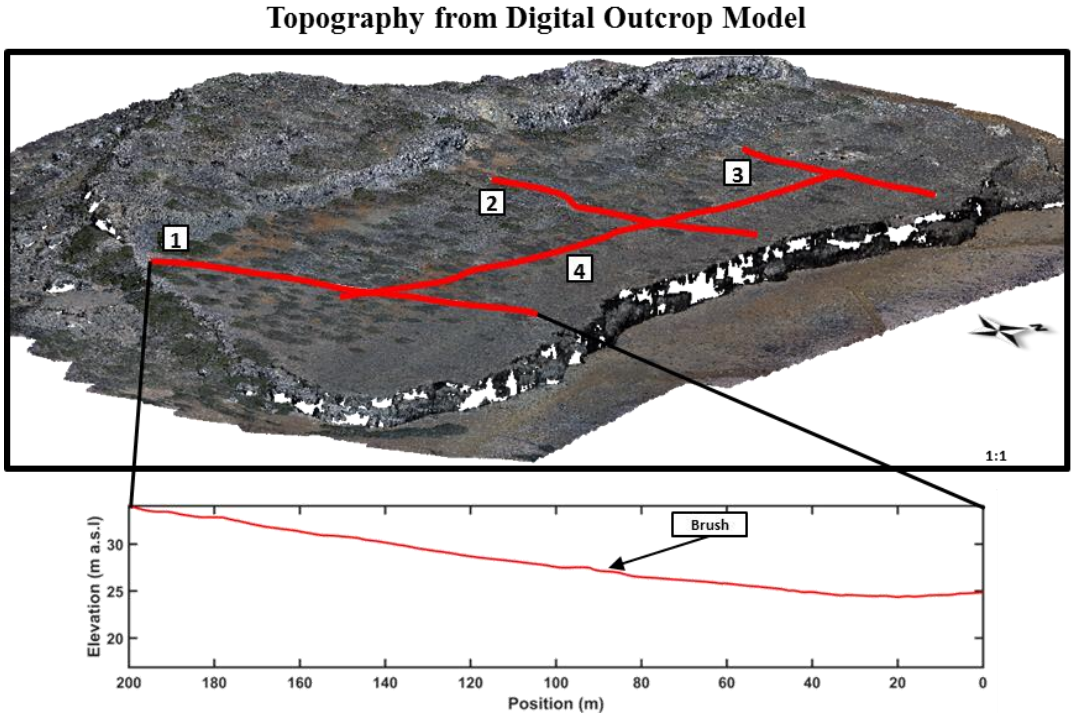

Figure 47: Showing extraction of topography data for Line 1 from point cloud model of Seru Grandi.

The high resolution of the digital outcrop model allowed for accurate characterization of small scale topography variations, on the order of tens of centimeters, across the lines. An example is shown in Figure 47 where a patch of low brush that was crossed during collection of Line 1 is observable in the topography data.

Migration velocity tests for the Seru Grandi survey showed that the same velocity of $1.0x10^8$ m/s used in the cross-island transect accurately collapsed observed diffractions. Although this velocity produced the most interpretable migrated images, it does not necessary represent the true subsurface velocity if the outcrop. A more detailed velocity analysis, likely requiring modeling and even tomographic inversions, would be required to obtain a true representation of the subsurface velocity structure, which is outside the scope of this study. After migration, power-law gain and AGC gain were separately applied to each line in order to be able to visualize deeper reflections in the sections. The final processed Lines 1-4 are shown below in Figures 48-51. The amplitudes for the power-law gained sections have been clipped to an equal scale so that relative amplitudes can be compared between lines. Note that lines 1-3 are being viewed while looking south, while line 4 is being viewed while looking east.

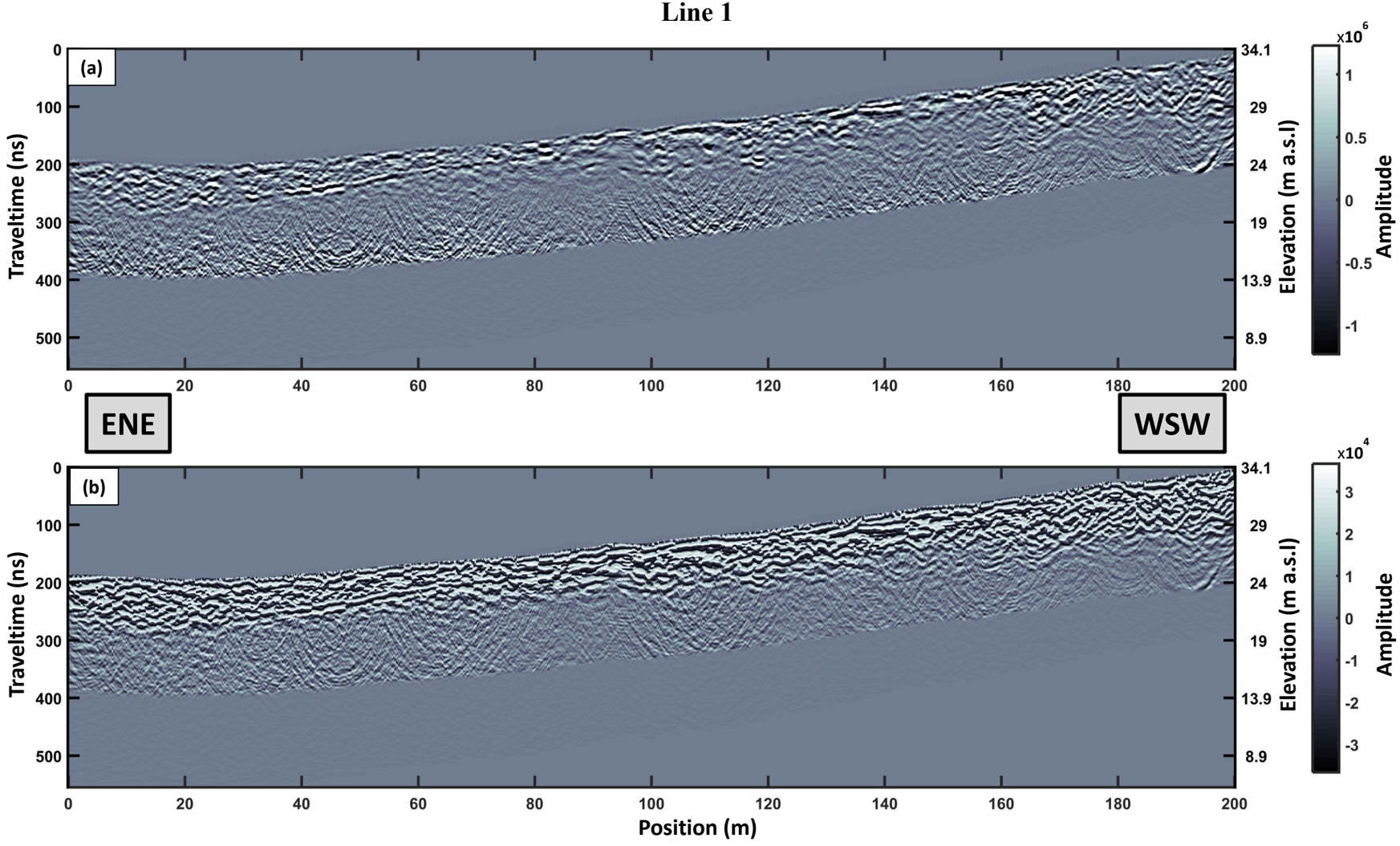

Figure 48: Seru Grandi survey fully processed Line 1. **(a)** Power-law gained data. **(b)** AGC gained data. Vertical exaggeration 2x.

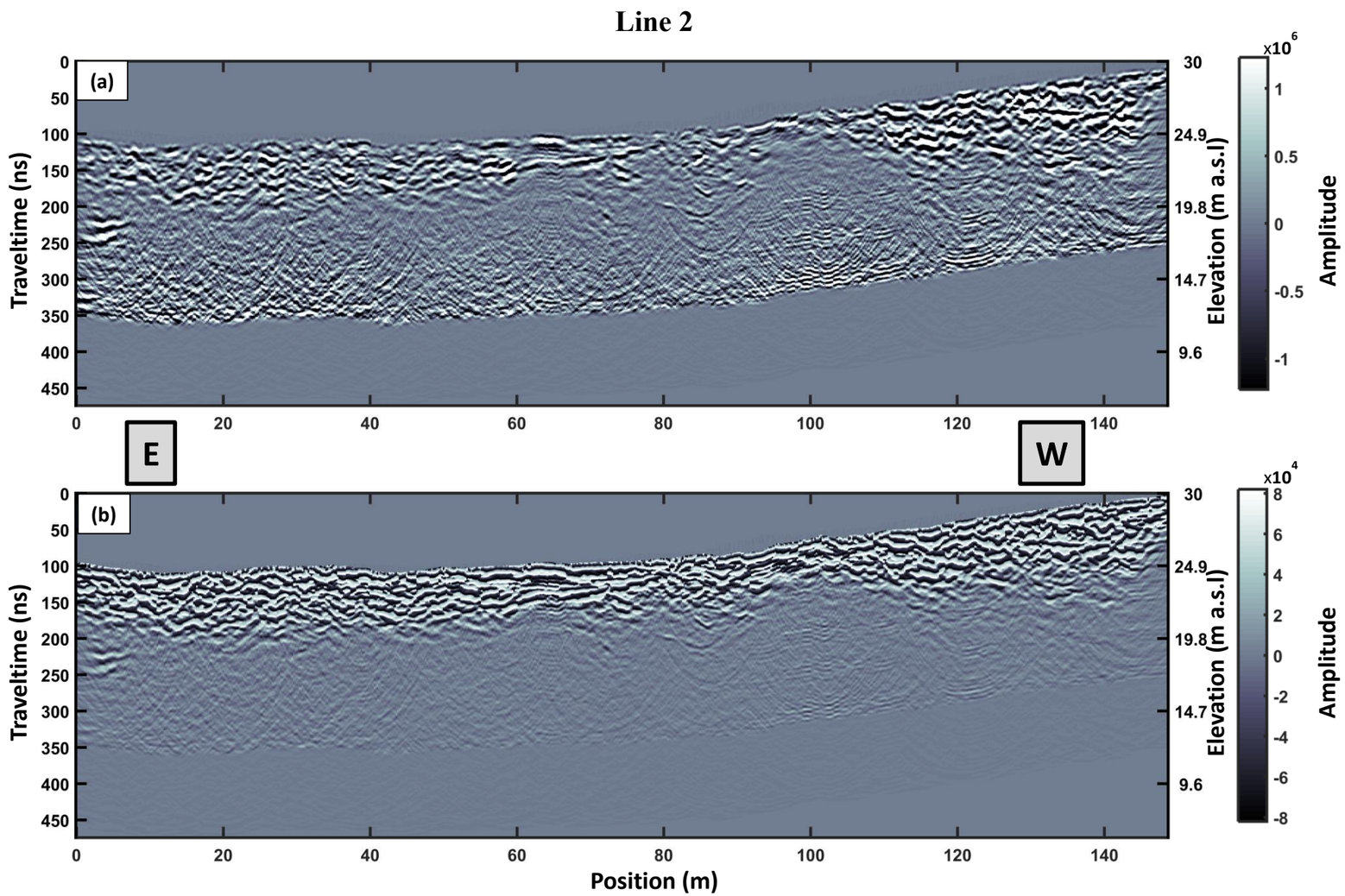

Figure 49: Seru Grandi survey fully processed Line 2. **(a)** Power-law gained data. **(b)** AGC gained data. Vertical exaggeration 2x.

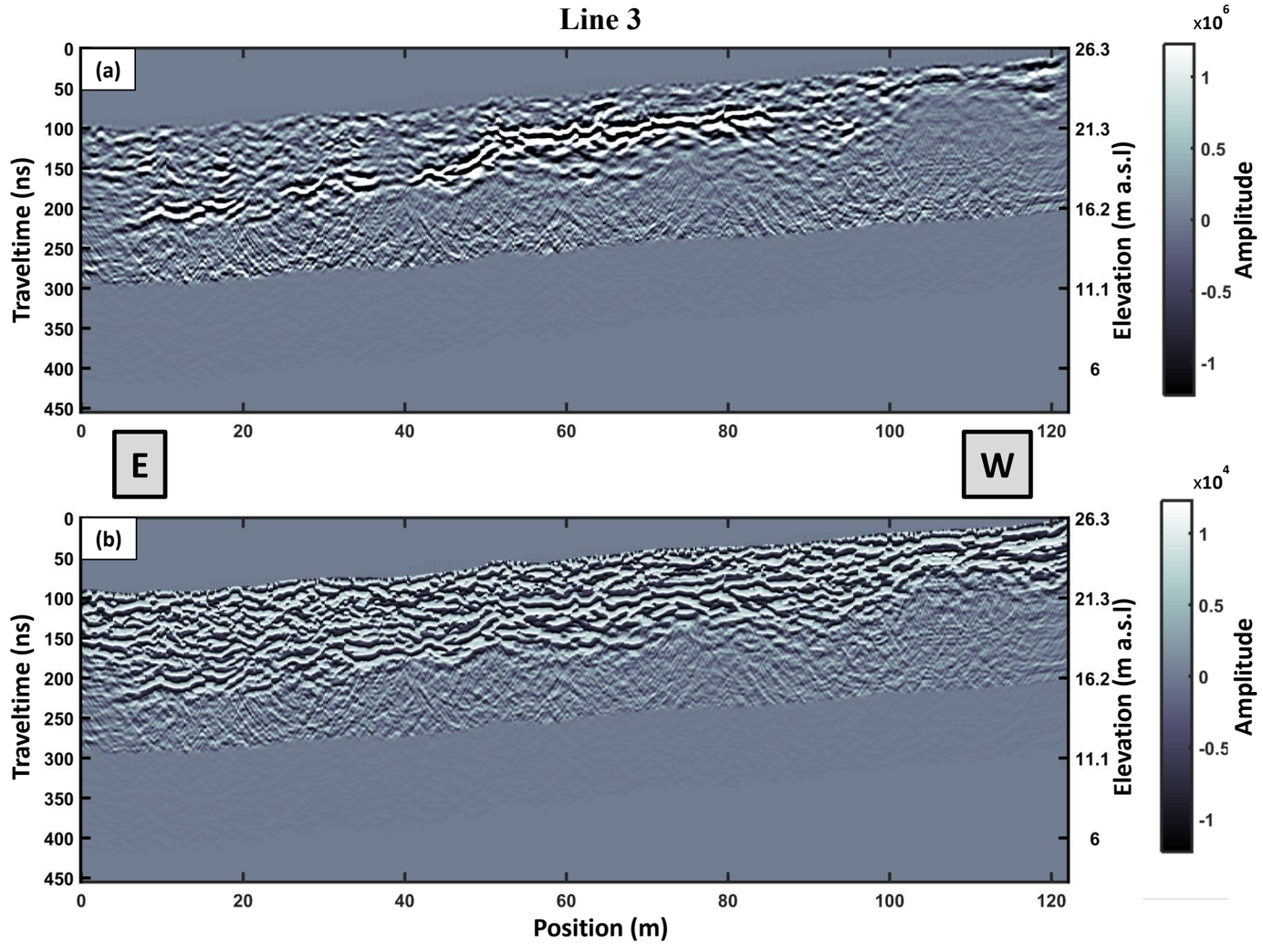

Figure 50: Seru Grandi survey fully processed Line 3. **(a)** Power-law gained data. **(b)** AGC gained data. Vertical exaggeration 2x.

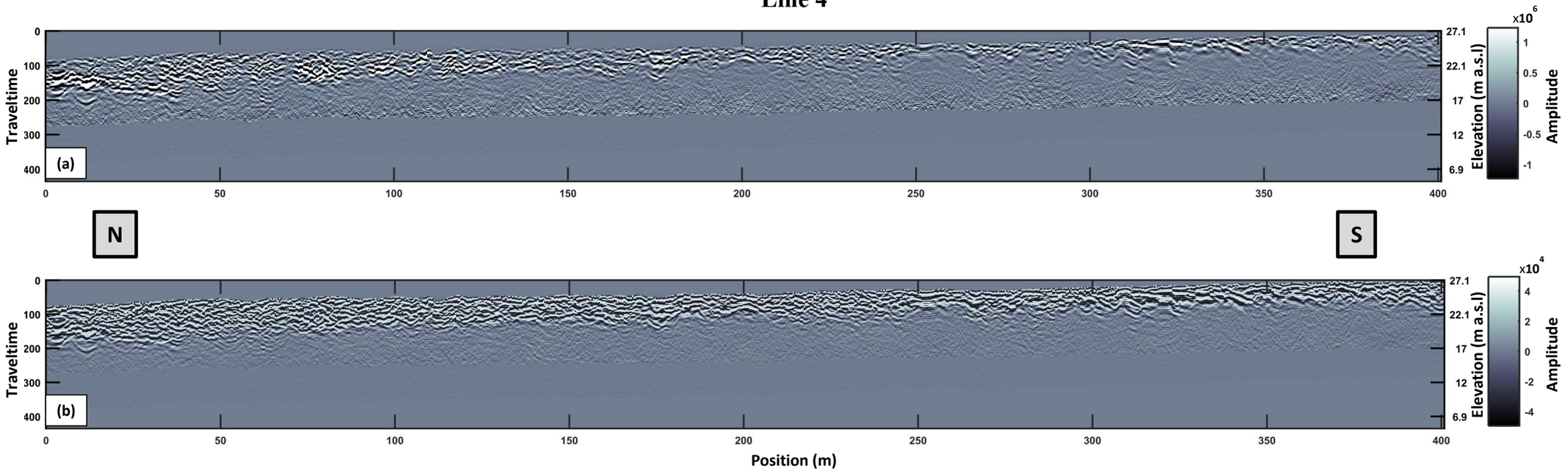

Figure 51: Seru Grandi survey fully processed Line 4. **(a)** Power-law gained data. **(b)** AGC gained data. Vertical exaggeration 2x

From Figures 48-51 it is immediately clear that the depth of investigation for the Seru Grandi survey is considerably less than much of the cross-island transect. Here distinguishable reflectors are only observed up to 6 m below the surface. While lithologic differences could account for this decrease in depth of investigation at Seru Grandi, it is likely that lack of transmitter power is the cause. Recall that the Seru Grandi survey was performed using a 400 V transmitter as the 1000 V transmitter was unavailable. Lithologic controls on variable signal penetration depth within the Seru Grandi lines will be discussed further in Section 6. Similarly to the cross-island transect, migration artifacts are minimal. Observable migration responses of random noise similar to those observed in the cross-island transect (Figure 46) are visible only below where primary subsurface reflections can be confidently identified in the sections (see x =0-80 m, t =300-350 ns Figure 48). Note that the sharp cutoff in amplitudes at later times in the above figures indicates the end of the application window for the respective gain functions. The sections were not gained to end of the full 400 ns time window so as to avoid further amplification of late time migration artifacts.

To visualize the spatial relationships between each transect Lines 1-4 were plotted in three-dimensions as a fence diagram in Figure 52. As the digital outcrop model is georeferenced, the lines shown below are located at their true real-world UTM coordinates.

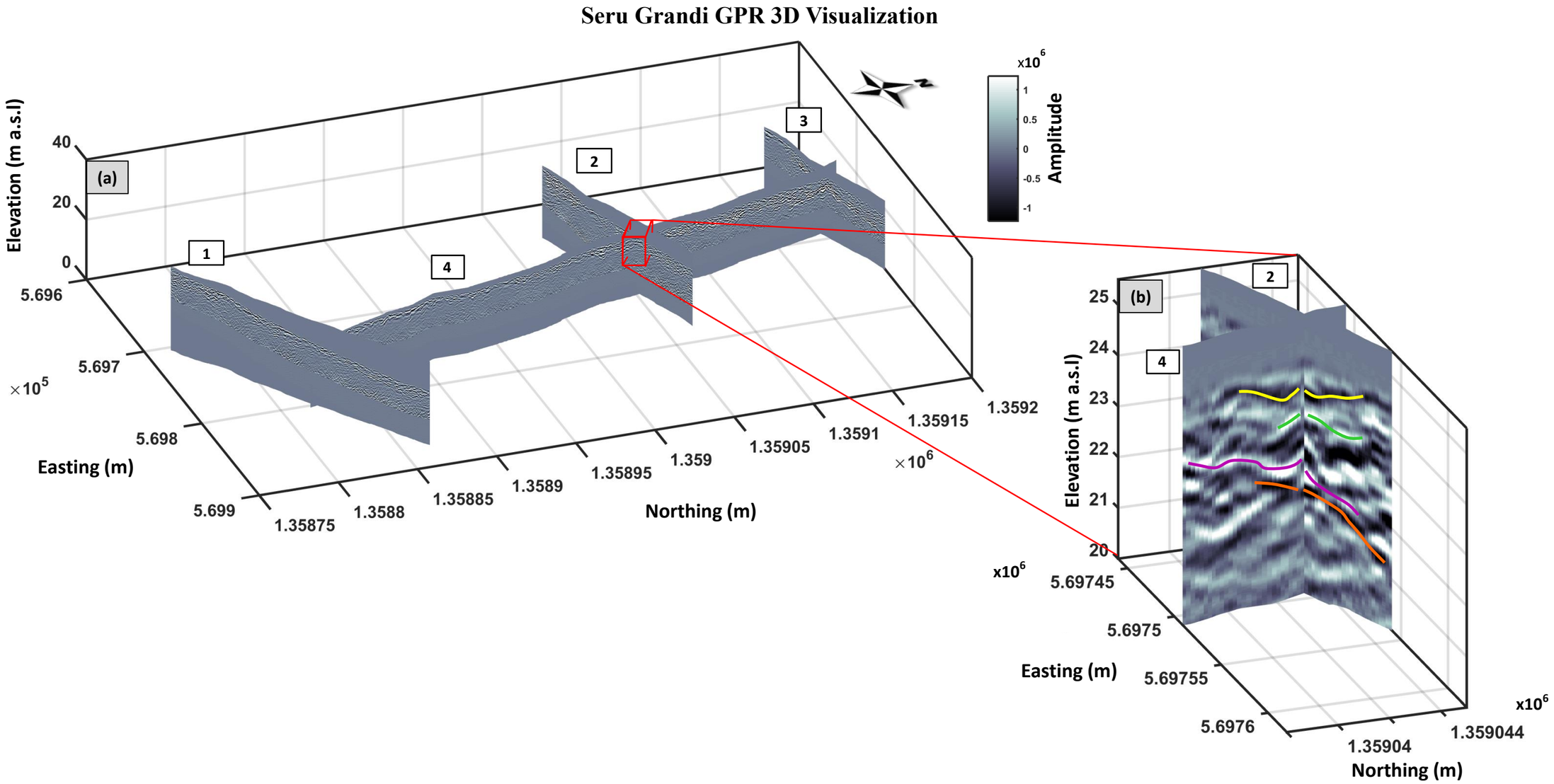

Figure 52: Fence diagram of Seru Grandi GPR survey lines. Vertical exaggeration 2x. **(a)** Visualization of all 4 lines. **(b)** Close-up of intersection between Lines 2 and 4 showing good ties between reflections (indicated by yellow, green, magenta, and orange lines).

Figure 46 shows that the ties between the lines are generally good (Figure 52b) with only minor discrepancies which are on the order of the theoretical vertical resolution (~10-20 cm as computed in Section 4.2.1).

6. INTERPRETATION

One of the goals of this thesis is to use the subsurface information gained from the GPR data collected on Bonaire to better understand the geology and the processes of the island's evolution. The final processed GPR lines for both the cross-island transect as well as the Seru Grandi survey show many features that can be interpreted to facilitate understanding of geological processes. To aid in this interpretation, multiple methods were used including numerical classification of GPR images as well as three-dimensional subsurface visualization.

6.1 Cross-Island Transect

The cross-island transect produced a large volume of high-resolution data. When analyzing such a large dataset it is important to maintain confidence and consistency in interpretations along the line. Traditional manual methods of observation and interpretation provide a qualitative approach to identification of radar facies [*Neal*, 2004] and interpretation of geologic features. To increase the confidence in interpretation along the cross-island transect, and to provide a more quantitative approach to interpretation, a method of k-means clustering of image structure tensors was developed. This method, described below, segments a GPR image based on the local orientation of reflections. In so doing, the relative geometries of sets of reflections can be quantitatively compared. This provides confidence in interpreting large datasets such as the cross-island transect where manual discrimination of reflector orientations is subjective and may be time consuming.

6.1.1 K-means Clustering of Structure Tensors

A description of the method developed for GPR image classification based on k-means clustering of structure tensors is broken down into several parts here. First is an overview of structure tensors and their computation for the data acquired along the cross-island transect. A brief review of k-means clustering then follows. Then, the adaptation of k-means clustering for structure tensors is discussed, along with observations about some important characteristics of the algorithm. Finally the results of the application of this method performed on the cross-island transect are presented and discussed.

6.1.1.1 Structure Tensors

Structure tensors are matrices that represent textural information about an image. Their original formulation derives from the gradient square-tensor, G, [*Van Vliet and Verbeek*, 1995] having the form,

$$G = \nabla u(x,y)\nabla u(x,y)^T = \begin{bmatrix} \left(\frac{\partial u}{\partial x}\right)^2 & \left(\frac{\partial u}{\partial x}\right)\left(\frac{\partial u}{\partial y}\right) \\ \left(\frac{\partial u}{\partial y}\right)\left(\frac{\partial u}{\partial x}\right) & \left(\frac{\partial u}{\partial y}\right)^2 \end{bmatrix}, \tag{42}$$

where $u(x,y)$ represents the some scalar value (color, intensity, etc.) for a point (or pixel) in an image at location(x,y). *Weickert* [1995] shows that G is insensitive to noise in the image at a local scale, denoted here as σ_1, if the image point, $u(x,y)$, is replaced

with its smoothed version, $u_{\sigma_1}(x,y)$. The smoothing can be achieved by convolution with a Gaussian [*Weickert*, 1995] or identically, the gradient vector $\nabla u(x,y)$ can be computed by convolution of $u(x,y)$ with the derivatives of a Gaussian [*Hale*, 2006] to give $\nabla u_{\sigma_1}(x,y)$. The outer product of these nose-reduced gradients gives the noise-reduced gradient square tensor G_{σ_1}.

G_{σ_1} gives gradient information at a specific image point, but the structure tensor provides gradient information over a larger scale [*Van Vliet and Verbeek*, 1995; *Weickert*, 1995; *Fehmers and Höcker*, 2003], denoted here as σ_2. The structure tensor, S, is derived by averaging the elements of G_{σ_1} over σ_2,

$$S(x,y) = \bar{G}_{\sigma_1} = \begin{bmatrix} \overline{\left(\frac{\partial u_{\sigma_1}}{\partial x}\right)^2} & \overline{\left(\frac{\partial u_{\sigma_1}}{\partial x}\right)\left(\frac{\partial u_{\sigma_1}}{\partial y}\right)} \\ \overline{\left(\frac{\partial u_{\sigma_1}}{\partial y}\right)\left(\frac{\partial u_{\sigma_1}}{\partial x}\right)} & \overline{\left(\frac{\partial u_{\sigma_1}}{\partial y}\right)^2} \end{bmatrix}, \tag{43}$$

where $\bar{}$ represents the averaging operation.

The eigen-decomposition of tensor S can be written as,

$$S = \lambda_u \boldsymbol{u}\boldsymbol{u}^T + \lambda_v \boldsymbol{v}\boldsymbol{v}^T, \tag{44}$$

where $\boldsymbol{u}$ and $\boldsymbol{v}$ are the eigen-vectors and λ_u and λ_v are the eigenvalues defined such that $\lambda_u \geq \lambda_v \geq 0$ [*Hale*, 2009]. It can be shown that these eigenvectors of S are orthonormal ($\boldsymbol{u}^T\boldsymbol{u} = \boldsymbol{v}^T\boldsymbol{v} = 1$), [*Weickert*, 1995] with $\boldsymbol{u}$ pointing in the direction of maximum image gradient and $\boldsymbol{v}$ pointing in the direction of minimum image gradient [*Van Vliet and Verbeek*, 1995; *Hale*, 2009].

In addition to the above description of the directionality of the eigenvectors, it is possible to define both the linearity, λ_1 (notation after [*Hale*, 2009]),

$$\lambda_1(x, y) = (\lambda_u - \lambda_v)/\lambda_u\,, \tag{45}$$

and isotropy, λ_0,

$$\lambda_0(x, y) = \lambda_v/\lambda_u\,, \tag{46}$$

for a structure tensor S at an image location (x, y). Again using the notation provided by *Hale*, [2009] linearity and isotropy are defined such that $\lambda_1 + \lambda_0 = 1$. For a given image point, $u(x, y)$, structure tensors with higher linearity indicate that orientations at the scale of σ_2 are more consistent than those with lower linearity (and therefore higher isotropy) [*Van Vliet and Verbeek*, 1995], which tend to exhibit scattered orientations.

For images that are produced by geophysical surveys involving reflected source wavelets such as seismic and GPR, gradients in signal amplitude are generally highest perpendicular to reflections within the image and lowest paralleling reflections. Given that these reflections define the structural geometries of the image (and potentially the geology of interest), for a structure tensor S, the eigenvector $\boldsymbol{u}$ is a *structure-perpendicular* vector and eigenvector $\boldsymbol{v}$ is a *structure-parallel* vector. In seismic imaging these eigenvectors and values have been used to develop structure-oriented filtering [*Fehmers and Höcker*, 2003; *Hale*, 2009] and attributes [*Hale*, 2009]. In the method described here it is the structure-parallel vectors that will be used as a basis for classifying sets of reflectors comprising the GPR image.

Structure tensors and their corresponding structure-parallel vectors were computed for an arbitrary portion of the cross-island transect GPR. Following the method described by *Hale* [2009], image gradients were computed with Gaussian derivative filters, and averaging of the gradient–square tensor was computed with Gaussian smoothing filters. The standard deviation for the Gaussian derivative filters was defined as the same local scale σ_1, with filter dimensions $(3\sigma_1 \times 3\sigma_1)$. That is, each dimension of the filter is three times the size of the local scale, σ_1. Similarly, the Gaussian smoothing filter had standard deviation σ_2, with filter dimensions $(3\sigma_2 \times 3\sigma_2)$. Examples of these filters are shown in Figure 53.

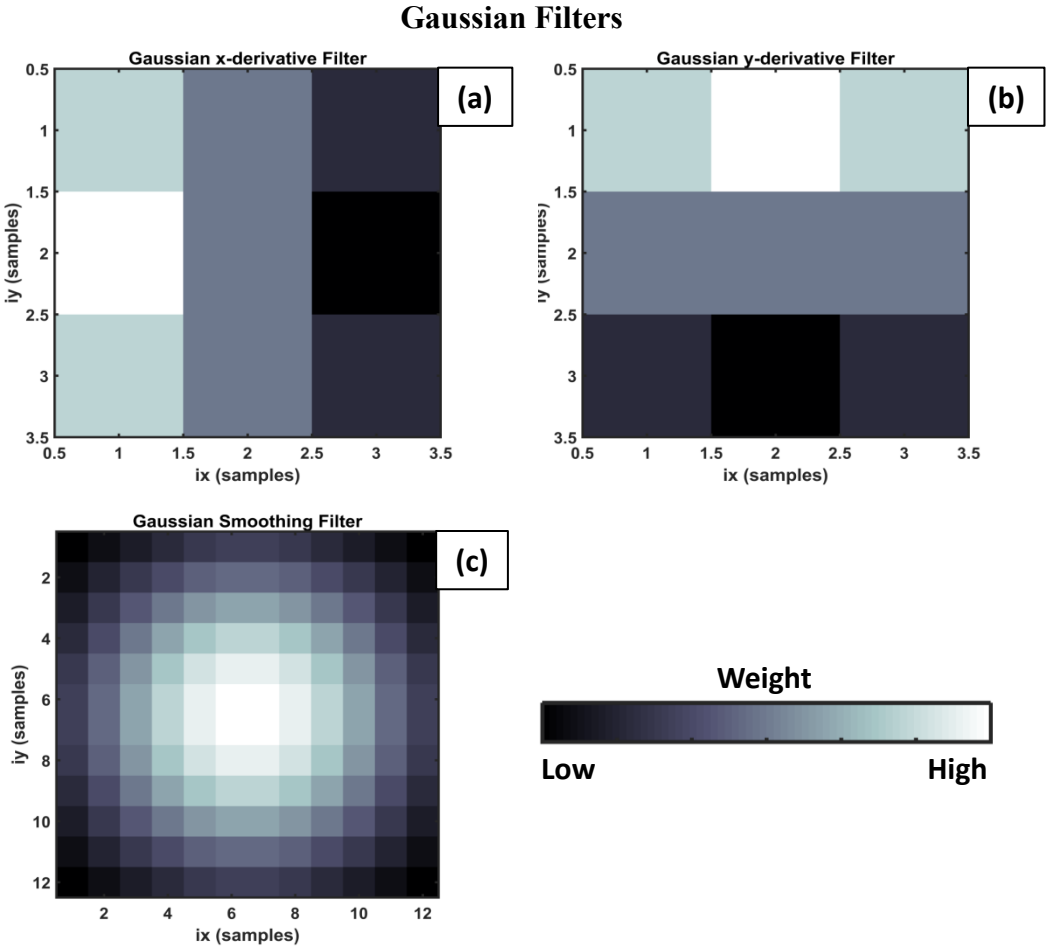

Figure 53: Example of Gaussian filters used in creation of structure tensors. **(a)** Gaussian x-derivative filter $\boldsymbol{\sigma_1 = 1}$. **(b)** Gaussian y-derivative filter $\boldsymbol{\sigma_1 = 1}$. **(c)** Gaussian smoothing filter $\boldsymbol{\sigma_2 = 4}$.

Given that structure-parallel vectors are sensitive to local changes in gradient, relative amplitude changes along a reflector will affect their orientation. From the power-law gained cross-island transect, where relative amplitudes are preserved (Figures 34a-45a), it is observed that amplitudes can vary dramatically along a given reflector. However, when the data are AGC gained (Figures 34b-45b) these relative amplitudes are lost and

only the structural aspects of the reflections remain. To simplify further analysis and to remove effects of local amplitude variation, computation of structure tensors and subsequent analysis was performed only on the AGC-gained data.

Multiple tests were performed while keeping the local scale fixed at $\sigma_1 = 1$ and varying σ_2. Experiments were performed on values of σ_2 ranging from 1-24 pixels. The goal was to find a value of σ_2 that established a good characterization of the general orientations of reflections while remaining insensitive to smaller-scale variations. Three examples from these tests for σ_2=4, 10, and 24 are respectively shown in Figures 54-56.

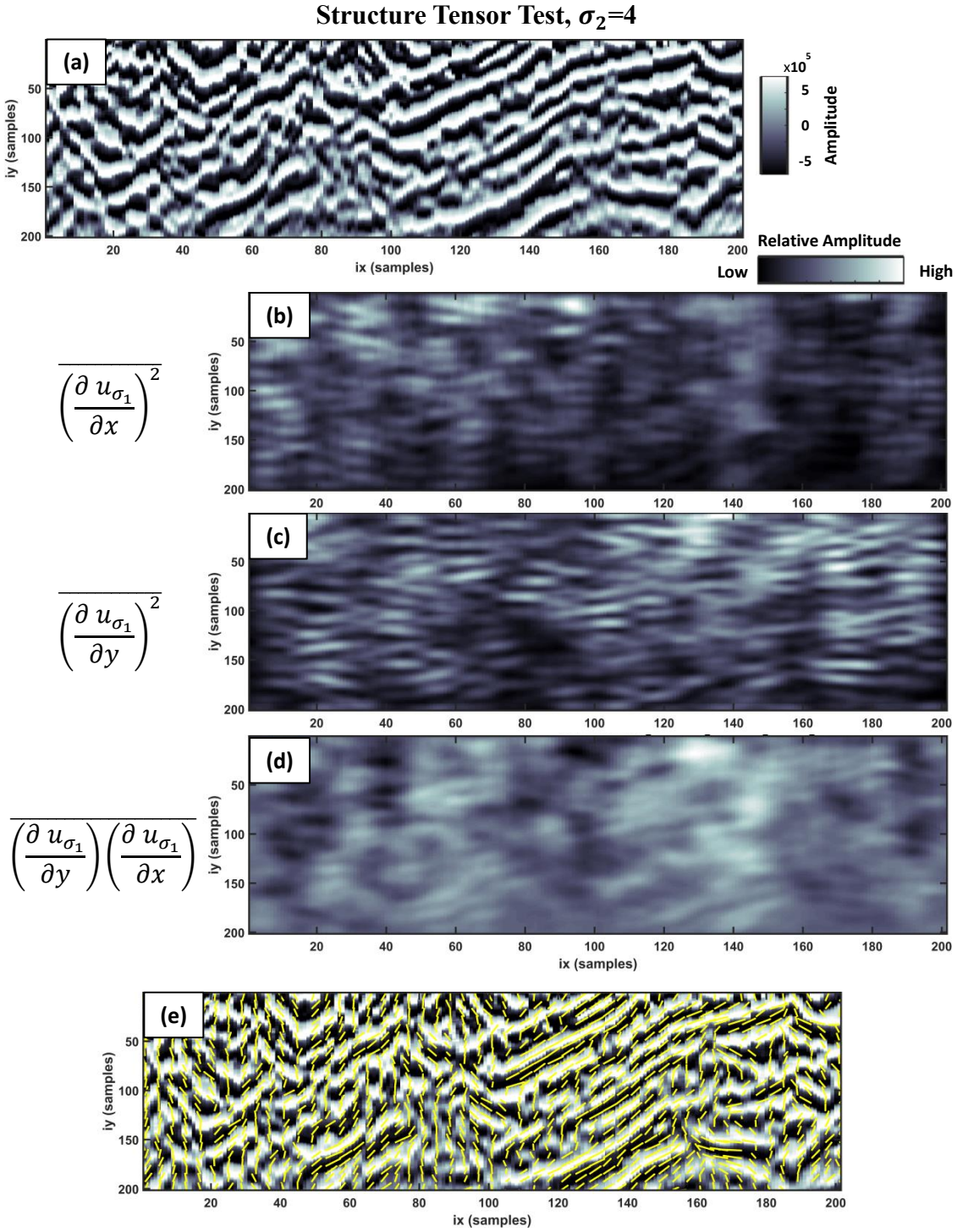

Figure 54: Structure tensor computation with σ_2=4. **(a)** Arbitrary portion of AGC gained cross-island transect. Note both axes are in image samples. **(b-d)** The relevant element of the structure tensor computed at every point in **(a)**. **(e)** Structure-parallel vector field overlain on **(a)**. Vectors have been scaled by linearity and exaggerated 10x.

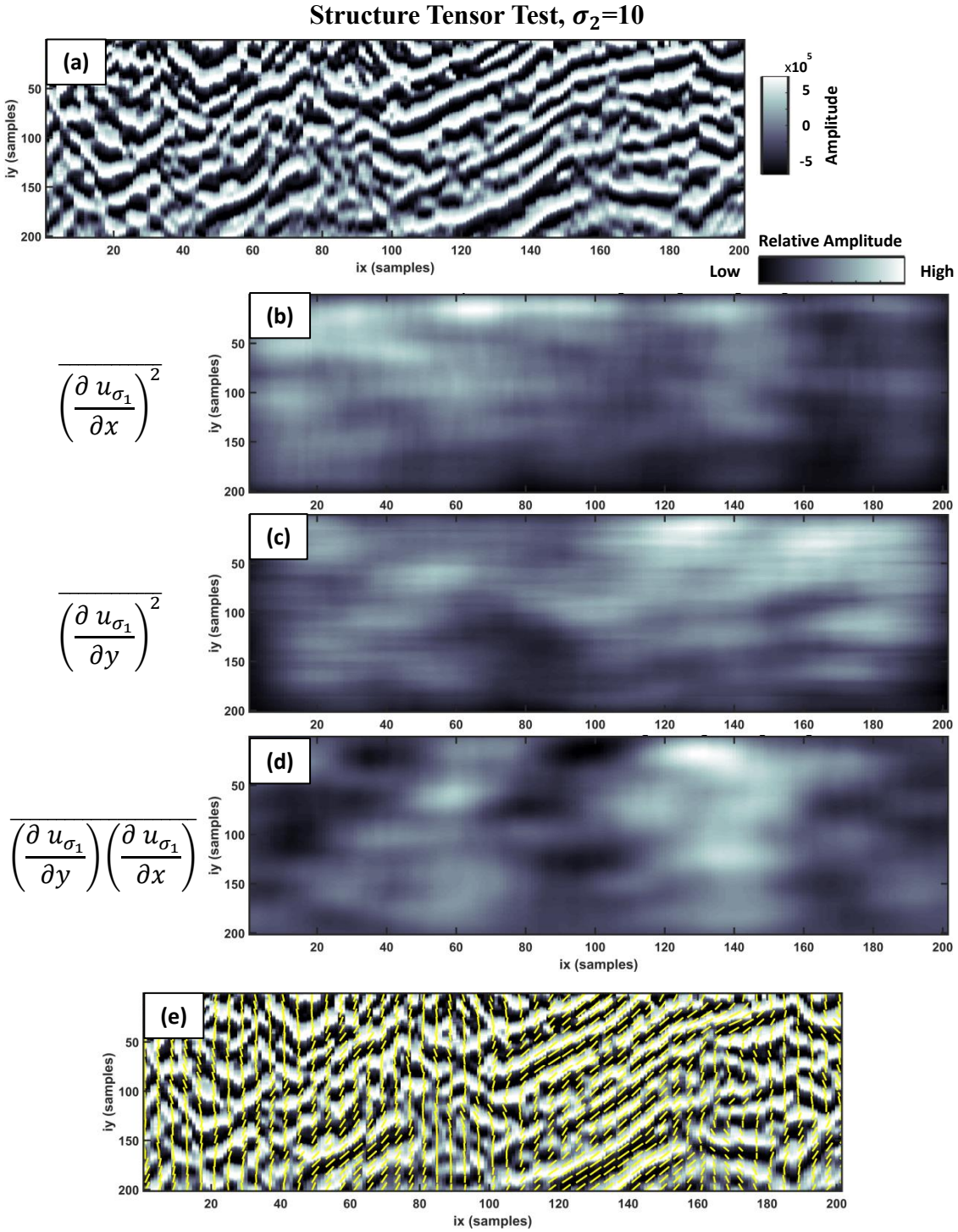

Figure 55: Structure tensor computation with σ_2=10. **(a)** Arbitrary portion of AGC gained cross-island transect. Note both axes are in image samples. **(b-d)** The relevant element of the structure tensor computed at every point in **(a)**. **(e)** Structure-parallel vector field overlain on **(a)**. Vectors have been scaled by linearity and exaggerated 10x.

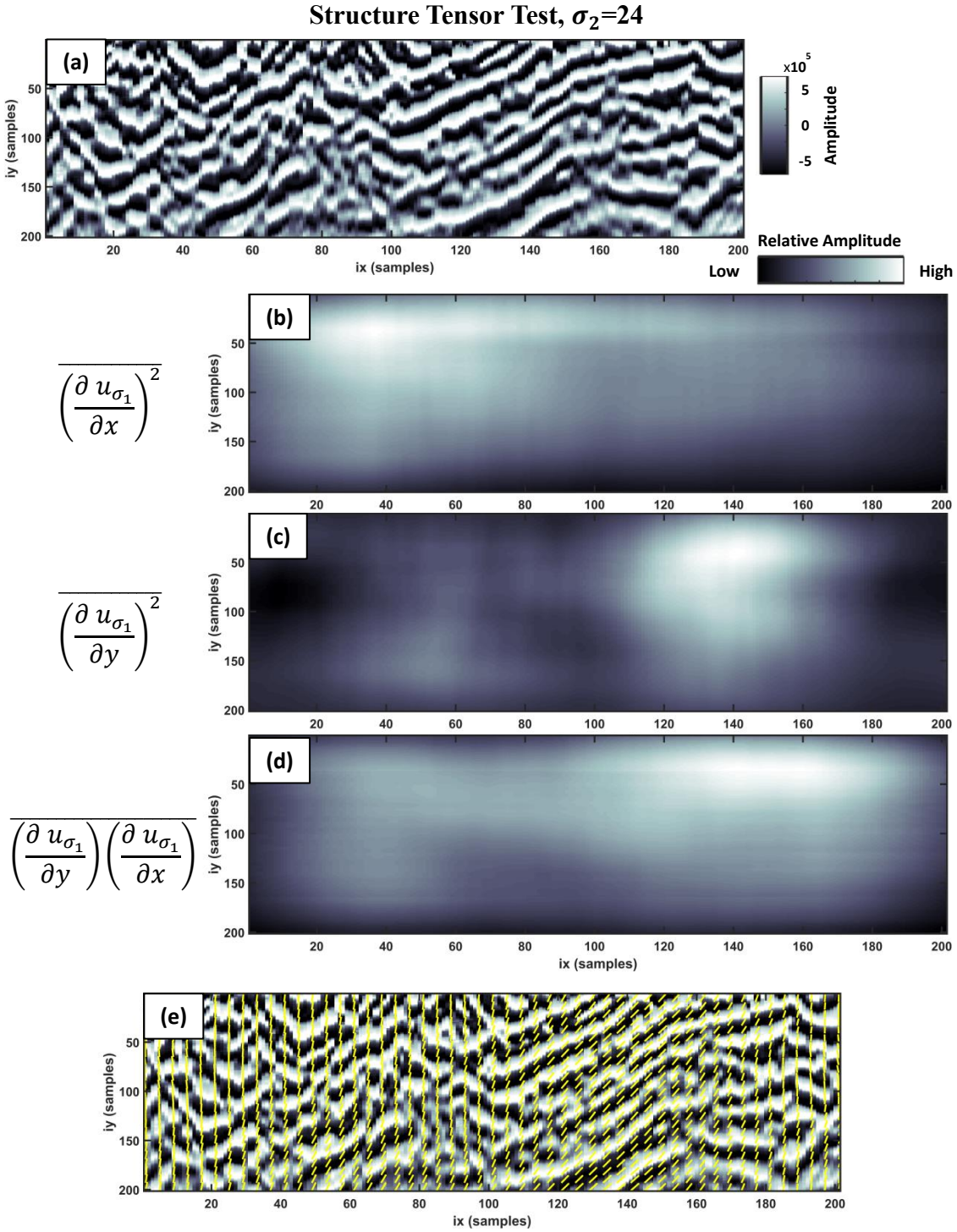

Figure 56: Structure tensor computation with σ_2=24. **(a)** Arbitrary portion of AGC gained cross-island transect. Note both axes are in image samples. **(b-d)** The relevant element of the structure tensor computed at every point in **(a)**. **(e)** Structure-parallel vector field overlain on **(a)**. Vectors have been scaled by linearity and exaggerated 10x

The above figures show the effects of changing the averaging scale, σ_2, when computing structure tensors and structure-parallel vectors. Note when computing structure-parallel vectors, their lengths have been scaled by the linearity parameter λ_1. This emphasizes regions of more consistent local orientation.

Figures 54-56 show that as the averaging scale increases, the orientations of the structure-parallel vectors become less sensitive to local variations and begin to describe more general trends. The reflections shown in Figures 54-56 extend over a spatial scale of ~4 m vertically and ~40m laterally. Considering the estimates of vertical resolution for the GPR data in this study to be on the order of tens of centimeters, and that significant geologic features of carbonate platforms are not expected to laterally vary on the order of less multiple tens of meters [*Lucia*, 2007], the subset of data shown in panel (e) of Figures 54-56 roughly represents the smallest spatial scale of interest for the cross-island transect. It is therefore necessary to have a value of σ_2 that describes the broad trends in reflector orientation at this spatial scale. When σ_2=4, very detailed orientations of reflections are visible in the structure-parallel vector field overlay (Figure 54e). This averaging scale would likely be appropriate for structure-oriented filters as described by *Fehmers and Höcker* [2003] and [*Hale*, 2009]. However, the detailed characterization of orientations with σ_2=4 is unnecessary for this study and amounts to noise within the broader trends or reflector orientation. Yet with σ_2=24 (Figure 56), even distinctive features are not well represented in the structure-parallel vector field. At this averaging scale, too much local information has been lost during the Gaussian smoothing. But

with σ_2=10, the structure-parallel vector field describes broad trends while smaller-scale variations have been averaged out. This level of detail is regarded as pertinent to this study and therefore σ_2 was set at 10 for subsequent structure-tensor calculations.

6.1.1.2 k-means Clustering

In its simplest form, k-means is a method for organizing a set of N vectors into k groups. This process was discussed by *MacQueen* [1967] as a method for partitioning data into groups that have low within-group variance and consequently high intra-group variance. The algorithm, outlined in Table 3, compares each vector comprising a dataset to the average, or mean, values of non-overlapping subsets of data belonging to a specified number of clusters. Each vector is then assigned to the nearest cluster. After each vector has been assigned to a cluster, a new cluster mean is computed from the vector assigned to each cluster. Each vector in the dataset is then re-compared to the new cluster means and reassigned as appropriate. This process repeats until some threshold regarding the stability of the clusters is reached.

***k*-means Clustering Algorithm**

Given a set of *N* vectors:

(1) Initially choose *k* vectors that represent the mean-vectors of *k* clusters

(2) For each vector in *N*, compute the distance to each mean-vector, μ, in *k*

(3) Assign the vector to the cluster whose mean-vector is closest

(4) After all vectors in *N* have been assigned, compute the new mean-vectors of each cluster

(5) Repeat (2)-(4) until the mean-vectors do not change significantly between iterations

Table 3: The basic flow of the k-means clustering algorithm, after description by *Steinley* [2006].

In segmentation of images, each vector in N is associated with a pixel in the image. Definitions for these vectors are often pixel color (RGB, CYMK, etc.), measures of intensity, or texture. In step (2) of the k-means algorithm given above, the distance metric used to compare vectors is not defined but it is often a simple Euclidean distance [*Steinley*, 2006; *Jain*, 2010] representing a norm of the difference between the vectors. The exit criterion (step (5)) can take multiple forms as well. A "zero-change requirement" allows termination of the algorithm only when vectors cannot be moved between clusters [*Steinley*, 2006]. A more forgiving condition would be one in which the

change in cluster means between successive iterations falls below some predetermined tolerance. For an image of pixel size $N = p \times q$ the k-means algorithm states that each pixel must be traverse in turn, meaning that the distance computation between a vector and a mean must be computed $(p)(q)(k)$ times for each iteration of the algorithm. Conventionally this is expressed in terms of algorithm complexity as $O(N)$, which means that the number of computations for the k-means image segmentation algorithm is "on the order of" the number of pixels in the image, N.

Table 3 shows that this algorithm is relatively straightforward and involves simple mathematical operations of means, distances, and relative changes. Yet despite its prominent use and success [*Jain,* 2010], there are several limitations associated with k-means clustering that must be considered.

First is that the initial means of each cluster must be assigned prior to beginning the algorithm. Such choices, given that they are the first set of means to which each vector in the dataset is compared, influence the resulting clusters. In his synthesis paper on k-means, *Steinley* [2006] describes some of the many methods that have been presented for initial mean assignment. He lists heuristic methods such as user-defined initial means and random initial assignment. In addition, he mentions deterministic methods that choose initial means based on other data metrics such as density distance [*Astrahan,* 1970] and results from hierarchal agglomerative clustering [*Milligan,* 1980]. It is

therefore important to consider the effects of the manner by which initial means are assigned when performing k-means clustering.

Second, k-means implicitly is a minimization of the sum of squared distances, SSD, over all clusters,

$$SSD = \sum_{i=1}^{k} \sum_{\boldsymbol{x}_j \in C_i} \left\| \boldsymbol{x}_j - \boldsymbol{\mu}_i \right\|^2, \tag{47}$$

where $\boldsymbol{x}_j$ is the j^{th} vector assigned to the i^{th} cluster, C_i, whose mean-vector is $\boldsymbol{\mu}_i$ (notation after [*Jain*, 2010]). However, k-means clustering does not guarantee convergence to a global minimum of Equation (47) [*MacQueen*, 1967; *Steinley*, 2006; *Jain*, 2010]. So if global minimization of total cluster "error" is necessary when performing a clustering, k-means should not be relied upon.

For the purpose of GPR image classification based on structure-parallel vectors, the k-means algorithm was chosen primarily for its simplicity and adaptability. In regard to the aforementioned short-comings of k-means clustering, the utility of the clustering results as a GPR interpretation aid was considered. Initial mean assignment can be used to advantage their adherence to *a-priori* geologic observations, and a global minimization of cluster within-cluster variance is not required for the clustering to remain useful in aiding subsurface interpretation.

6.1.1.3 Adaption of k-means for Structure-Parallel Vector Fields

A structure-parallel vector computed from amplitudes at a given GPR image point describes the orientation of a reflection averaged over the scale σ_2. Yet geologic features that are of interest of this study, such as clinoforms, karstic features, gradational changes in dipping beds, etc. contain multiple orientations. These multiple orientations are not well described by simply extending this averaging process to larger scales. Therefore instead of performing k-means clustering through observation of each individual vector in the structure-parallel vector field, local neighborhoods (hereafter referred to as "patches") of vectors are instead compared in a modified k-means algorithm. Using the notation from Equation (47), a given patch of structure-parallel vectors is defined as a three-dimensional matrix, $\boldsymbol{X}$, with dimensions $n \times m \times 2$, where X_1 is a matrix containing the first elements in each of the associated structure-parallel vectors, and X_2 is a matrix containing the second elements in the vectors. Visually, an example of a 3×3 patch of structure-parallel vectors is shown in Figure 57.

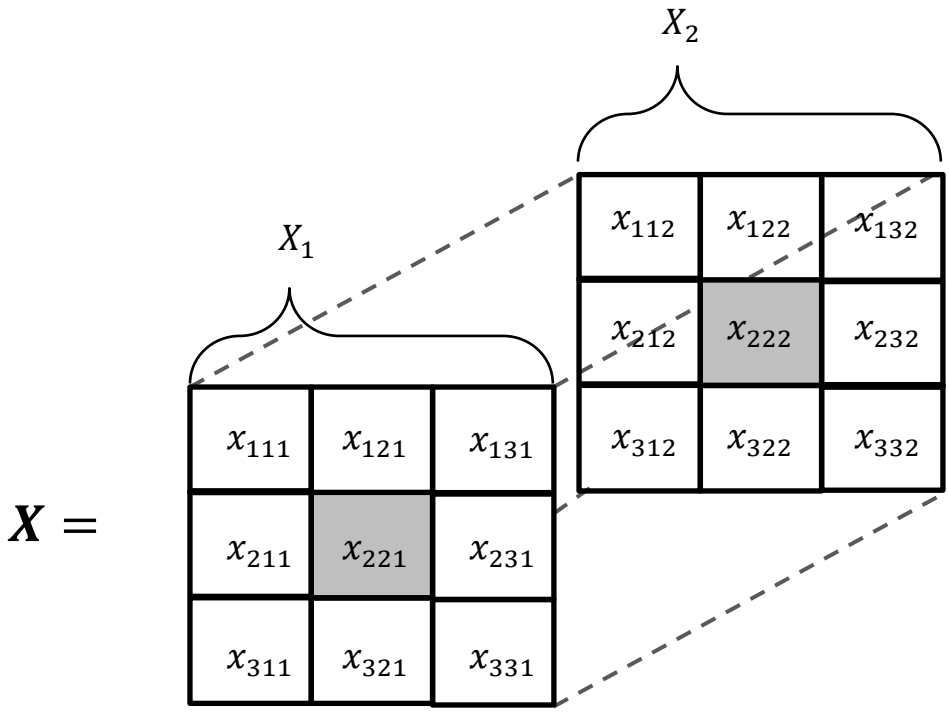

Figure 57: Visual diagram of an example 3×3 patch of structure-parallel vectors, $\boldsymbol{X}$, centered on vector $\boldsymbol{x_{22}}$ indicated by gray box.

Each patch is centered on an individual image point, and therefore the complexity of the k-means algorithm remains $O(N)$.

By recasting the vectors in a traditional k-means algorithm as patches of structure-parallel vectors, a new way of computing a measure of closeness (step (2-3) in Table 3) between these new "vectors" must be developed. In two-dimensions, such as the space of GPR sections, a Euclidian norm of the difference between two vectors defines the distance, and therefore closeness, between them. Similarly, a matrix of such norms

defines the element-wise distance between two matrices of vectors (such as the patches described here). Comparison of such matrices of Euclidean norms via relational operators requires further reduction in dimensionality. This can be accomplished by a matrix norm. The norm chosen here is what is known as the $L_{2,1}$-norm which represents the sum of the Euclidean norms of a the columns of a matrix. This norm can be written as,

$$\|A\|_{2,1} = \sum_{i=1}^{n} \left(\sum_{j=1}^{m} a_{ij}^2 \right)^{1/2}, \tag{48}$$

for a matrix A of size $n \times m$. The $L_{2,1}$-norm has been shown to be a robust as effects of data outliers are mitigated [*Cai et al.*, 2013; *Du et al.*, 2015].

Here, the measure of distance, D, between two patches of structure-parallel vectors, $\boldsymbol{X}$ and $\boldsymbol{M}$, is defined as the $L_{2,1}$-norm of the matrix of element-wise Euclidean norms between, $\boldsymbol{X}$ and $\boldsymbol{M}$,

$$D(\boldsymbol{X}, \boldsymbol{M}) = \left\| \left(\sum_{l=1}^{2} (X_l - M_l)^{\circ 2} \right)^{\circ 1/2} \right\|_{2,1}, \tag{49}$$

where the expression inside the double bars describes a matrix of Euclidean norms between the vectors associated with patches $\boldsymbol{X}$ and $\boldsymbol{M}$. The computation of these

element-wise Euclidean norms is facilitated by the use of the Hadamard power operator, $^{\circ}$, [*Reams,* 1999]. Hadamard power operators act on the elements of a matrix rather than on a matrix as a whole. For example, a matrix A squared by a Hadamard power operator, $A^{\circ 2}$, is simply the matrix A with each of its elements squared as opposed to the product of A with itself.

The other adaptation to the traditional k-means algorithm in Table 3 is the exit criterion (step 5). Given that the means of each cluster are now patches of structure-parallel vectors, comparison of the means can be done using the operation defined in Equation (49). For this method, the change in a given mean, $\boldsymbol{M}$, between iterations $n-1$ and n is a measure of the relative error between $\boldsymbol{M}_{n-1}$ and $\boldsymbol{M}_n$ [*Golub and Van Loan*, 1996],

$$\frac{D(\boldsymbol{M}_{n-1}, \boldsymbol{M}_n)}{D(\boldsymbol{M}_n)} \tag{50}$$

with D being defined as in Equation (49). Note that for the denominator of (50), this distance metric operates on a single patch as a norm. The use of relative error means that this metric is independent of the number of individual structure-parallel vectors in $\boldsymbol{M}$.

Now the modified k-means algorithm terminates when the maximum change in the patches representing the means across all clusters,

$$\Delta(n)_{max} = \max\left\{\frac{D\left(\boldsymbol{M}_{i,n-1}, \boldsymbol{M}_{i,n}\right)}{D\left(\boldsymbol{M}_{i,n}\right)}, \ldots, \frac{D\left(\boldsymbol{M}_{k,n-1}, \boldsymbol{M}_{k,n}\right)}{D\left(\boldsymbol{M}_{k,n}\right)}\right\}, \tag{51}$$

falls below some tolerance. Here, $\boldsymbol{M}_{i,n}$ is the patch representing the mean of cluster i for $i = 1, \ldots, k$ at iteration n. The tolerance at which to allow the algorithm to terminate should be small enough that the orientations of vectors within the patches representing the means of each cluster are not significantly different between successive iterations.

With the previous considerations, the modified method for k-means clustering of patches of structure-parallel vectors can be described as shown in Table 4.

Modified k-means Clustering Algorithm

Given a field of N structure-parallel vectors:

(1) Initially choose k patches of vectors of size $n \times m$ that each represent a mean-patch, M, of k clusters

(2) For each vector, x, in N, compute the distance between a patch of $n \times m$ vectors, X, centered on x, to each mean-patch in k using Equation (45)

(3) Assign x to the cluster whose mean-patch is closest to X

(4) After all vectors in N have been assigned, compute the new mean-patch of each cluster

(5) Iterate (2)-(4) until the maximum change across all cluster means, $\Delta(n)_{max}$ (as per Equation (47)), falls below some tolerance

Table 4: The modified k-means clustering algorithm for structure-parallel vector fields.

This algorithm was implemented in MATLAB and run using the Texas A&M High Performance Research Computing cluster, Ada. A detailed analysis of algorithm optimization is not the focus of this thesis, but currently the algorithm has a serial implementation and runs on a single node. Further work towards parallelization would therefore greatly improve performance.

6.1.1.4 Observations from the Modified k-means Clustering Applied to GPR Data

From the previous section it is evident that several parameters must be chosen in the clustering algorithm; namely patch size, number of clusters, and initial cluster means. This section summarizes testing variations of these parameters. The results suggest appropriate parameter choices for clustering the entire cross-island transect. The tests shown here were performed on a small subset of the cross-island dataset from x =200-600 m (Figure 58). Recall that the data have been AGC-gained to remove from the clustering results the effect of amplitude variation along reflections.

Subset of Cross-Island Transect for Clustering Tests:
***x*=200-600 m**

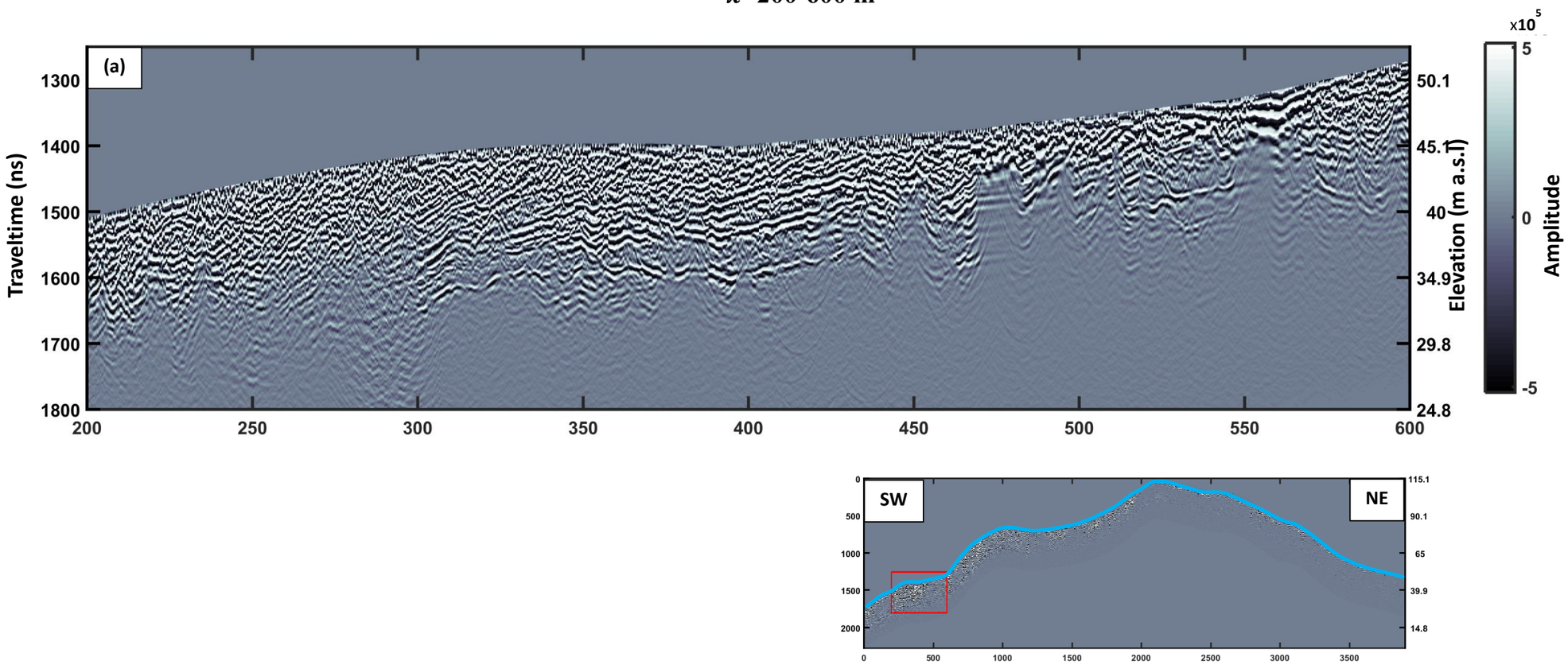

Figure 58: Portion of cross-island transect from $\boldsymbol{x}$ =200-600 m to be using in k-means clustering tests. Locator map at bottom right

The first tests performed involved varying the size of the patch of structure-parallel vectors used in the new k-means algorithm. For these tests the number of clusters, k, was fixed at 5 and the initial means were randomly selected from within the GPR section shown in Figure 58. A tolerance of less than 0.05 was required for the largest change in cluster means (Equation (51)) before the algorithm terminated. The goal was to understand the effect of patch size on the clustering results, and to find a patch size that would classify features at the previously mentioned scale of interest (~1-10 m in vertical extent and ~10-100 m in lateral extent) into single clusters.

To visualize the results of each clustering, a color that represents the cluster assignment for each pixel was semi-transparently overlain on the GPR data, so as to build up a color-coded image of the clustering results. Examples of four such overlays for patch sizes of [5×5], [21×21], [51×51], and [201x201] pixels are shown in Figure 59 below.

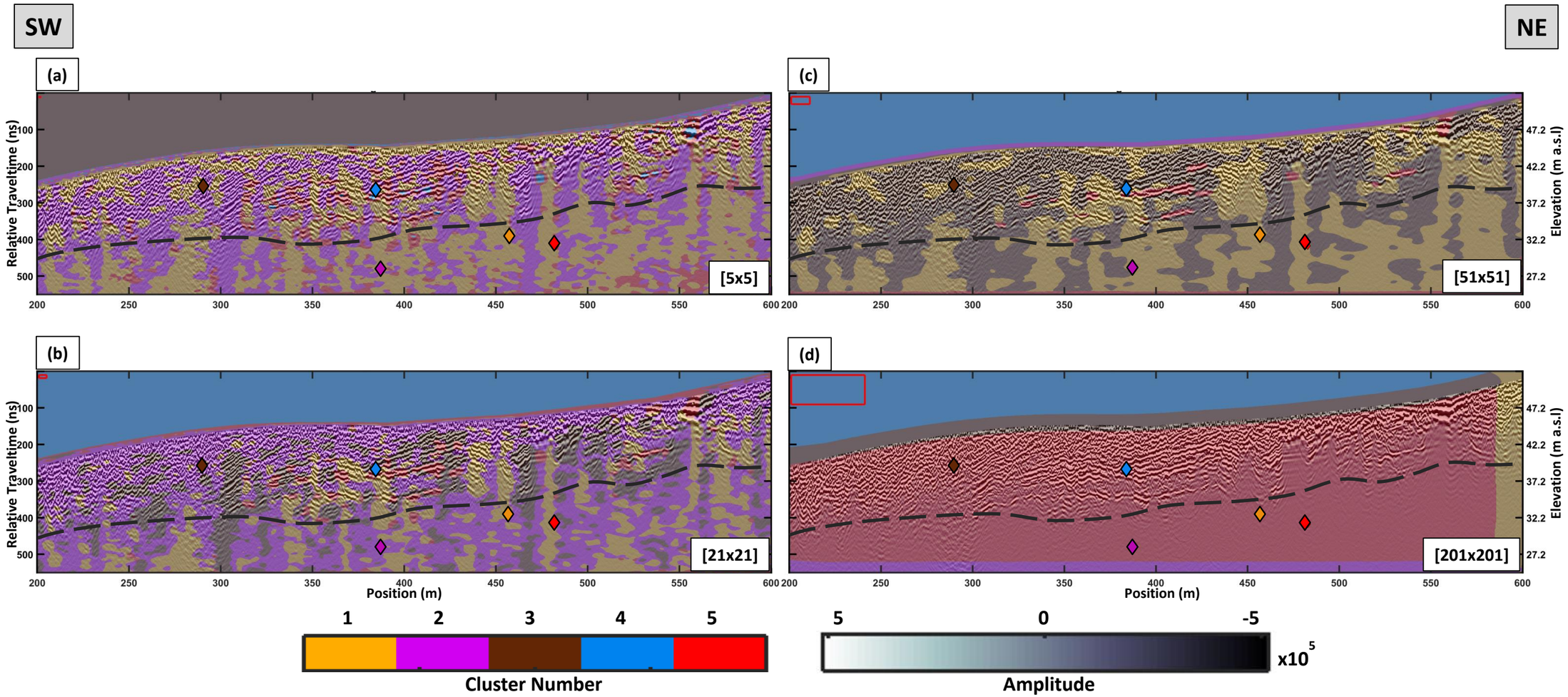

Figure 59: Tests on varying patch size. Depth of investigation indicated by dashed gray line. Red box in top left of panels indicates size of patch. Colored diamonds indicate locations of initial mean patches. **(a)** 5×5 patch size. **(b)** 21×21 patch size. **(c)** 51×51 patch size. **(d)** 201×201 patch size. Vertical exaggeration 4x.

Note that in Figure 59 above, the respective patches (indicated by the red boxes in the upper left of each panel) do not appear to be square despite being square in pixels. This is because, for the GPR data, there are more samples in the vertical direction (time/depth) than there are in the horizontal direction at this vertical exaggeration.

It is apparent that as the patch size increases, the clusters become larger and tend to classify more broad-scale features. For patch size [5×5] (Figure 59a) larger features, such as the more-continuous southwesterly dipping reflections between 350-450m, become discontinuously clustered due to the relatively minor changes in orientation along these reflectors. In contrast, when the patch size was set to [201×201] Figure 59d only the most expansive features in the image become separated into individual clusters. This includes the bounding edges of the image, and the only other clustering in this example involves the regions of zero-amplitudes above the earth's surface and non-zero GPR amplitudes in the subsurface. Neither the [5×5] nor the [201×201] patch sizes produced clusters that are on the scale of features of interest. However, the [21×21] and the [51×51] patch size tests gives results that are more useful. Here the patch sizes are large enough that features are permitted to have multiple orientations without being classified into multiple clusters. Yet the patch sizes are not so large that features that are visually distinguishable within the GPR reflections are not distinguishable by the clustering algorithm.

Note that an interpreted depth of penetration has also been indicated by the dashed black line on each of the panels in Figure 59. Below this depth, confidence is low in identifying clear reflectors due to decreases in SNR. In this region migration artifacts are the major data feature, and the clustering in this region is highly variable but most likely does not represent true earth structure. For this reason the quality of clustering results were assessed only above the depth of investigation.

A second set of tests were performed to explore the effect of changing the number of clusters, k, on the resulting classification. In these tests, patch size was fixed at [51×51] pixels. In these tests k was varied from 2 to 11. The initial cluster means were chosen at random from within the GPR data subsection. So as focus on the effect of adding additional clusters, the initial means between tests were retained with only a single new random mean being chosen as k increased. For example, the test for k=7 had one new initial mean while retaining the 6 initial means chosen for k=6, which had one new initial mean while retaining the 5 initial means chosen for k=5, and so on. Examples of these tests for k =2, 4, 7, and 11 are shown in Figure 60.

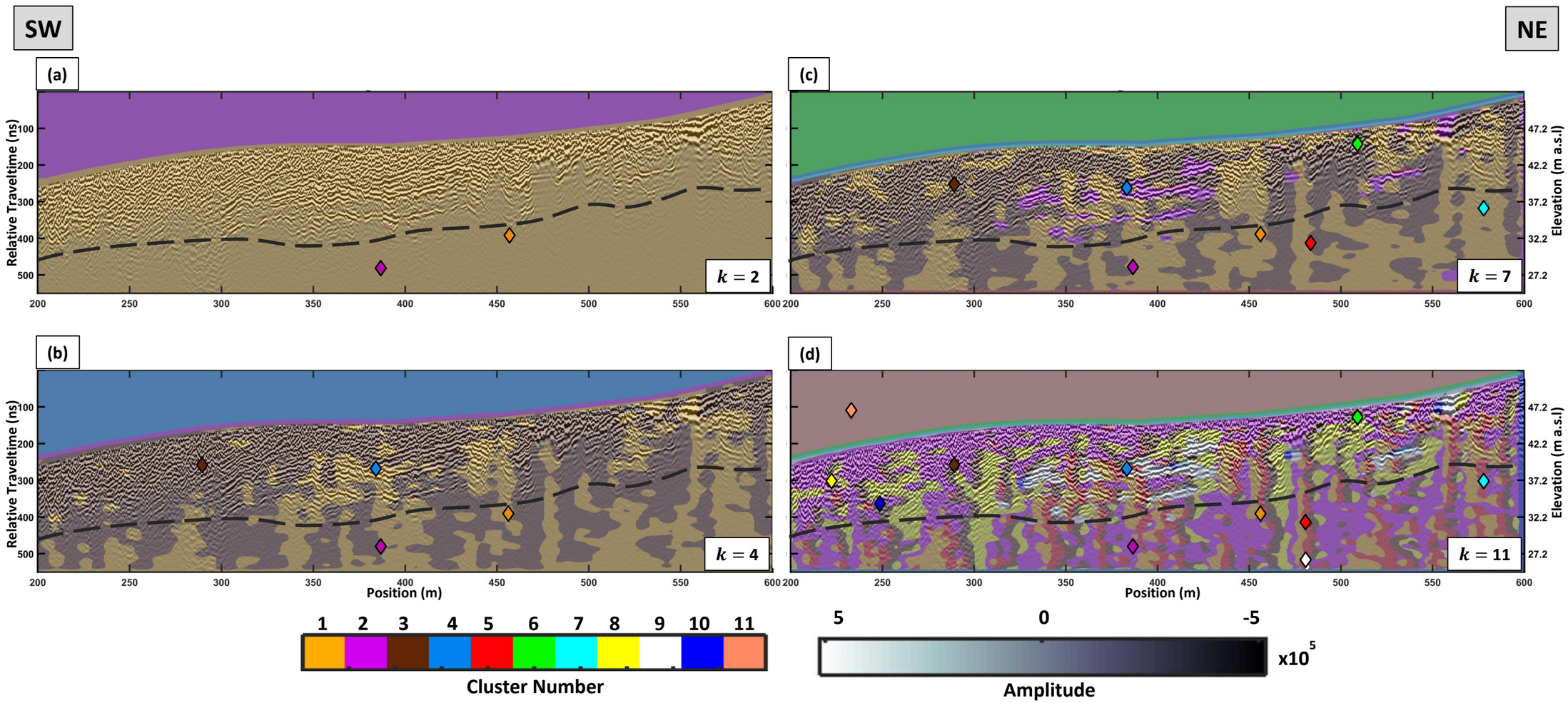

Figure 60: Tests on varying the number of clusters. Depth of investigation indicated by dashed gray line. Diamonds indicate locations of initial mean patches. **(a)** k =2. **(b)** k =4. **(c)** k =7. **(d)** k =11. Vertical exaggeration 4x.

Figure 60a shows the clustering results for the case $k = 2$. Here the clustering is too sparse, and only the difference between zero-amplitudes and GPR amplitudes can be distinguished. Yet when k was set to 11 (Figure 60d), features in the GPR data tend to be dissected. Here, the large number of clusters resulted in prominent features being broken up into multiple clusters that separate only subtly different orientations. Intermediate ranges for k (Figure 60b-c) reveal clusters that define specific features but allow some variability within a cluster. The trends observed in these tests are similar to those for patch size shown in Figure 59. However, the range of patch size describes the size of features than can be classified into a single cluster, whereas the value of k describes how specific the orientations of features within that cluster are.

The sum of within-cluster distances, conventionally referred to as within cluster error, was computed by inserting Equation (49) into Equation (47). This error was examined as a function of k (Figure 61) to see if an "optimal" number of clusters could be determined quantitatively for the subset of the cross-island transect tested here.

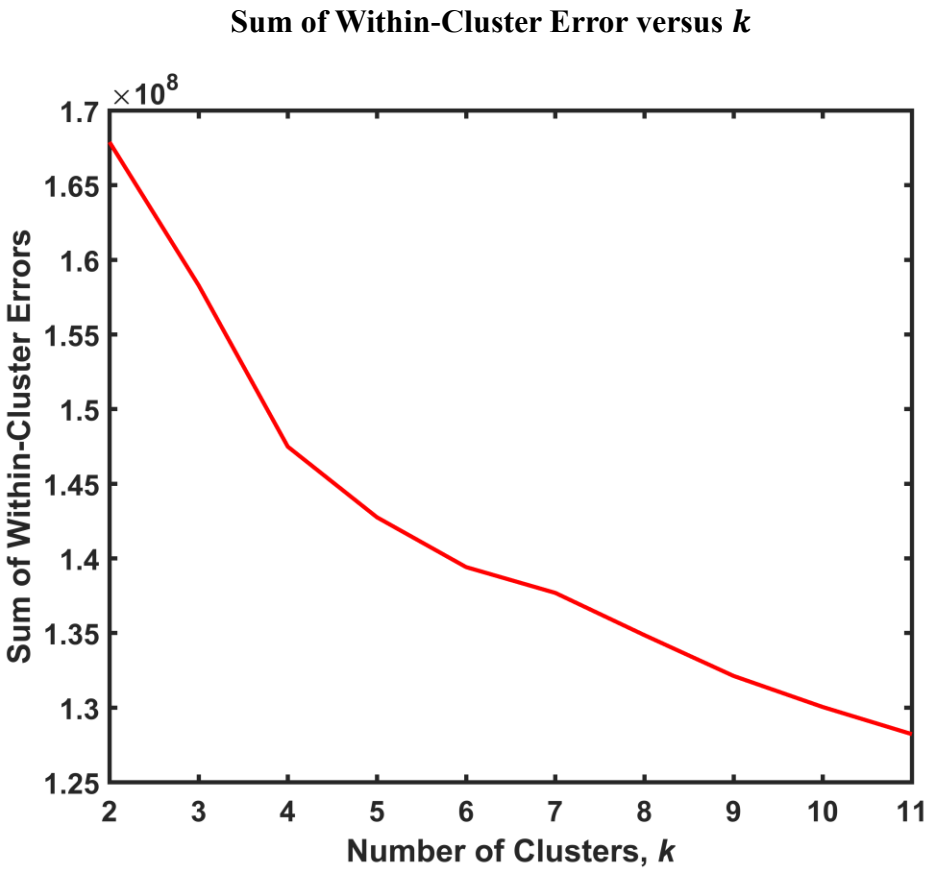

Figure 61: Measure of total clustering error as a function of number of clusters.

Figure 61 shows that total error decreases quickly as k increases from 2-4, then decreases at a slower rate for larger values of k. The "kink" in Figure 61 observed at $k = 4$ suggest that this value of k may be "optimal" in terms of total error, as it is the point where additional increases in k provide less significant reduction in total error compared to previous increases in k. However, this point does not necessarily reflect an appropriate number of clusters when considering the goal of segmenting the GPR reflections into features at the scale of interest for this study. From the tests on number

of clusters in Figure 60, it was observed that for values of k=4,7, and 11 clusters existed that characterized the major image-scale features such as the bounding edges of the image and the earth's surface contrast previously mentioned. This suggests that these features are significantly distinct to warrant their own clusters at even though k may be large. It is not coincidence that four clusters can be used to describe the zero-amplitude region above the surface, the surface/subsurface contact, the bottom edge of the image, and the right edge of the image. As such, once k has increased to a value of 4, additional increases in k serve to refine the clustering by segmenting parts of GPR reflections. Therefore, even though the measurement of total error versus number of clusters does not serve as a useful tool for finding the optimal number of clusters when segmenting the test GPR image, it summaries some of the observations from the cluster number tests. It confirms quantitatively that there are 4 highly significant features in the image, and that, although significant to aiding geological interpretation, additional clusters do not dramatically reduce the total within-cluster error.

It is important to mention the rate of convergence of the algorithm described here. For both the patch size and cluster number tests described above, the maximum change in cluster mean, Δ_{max}, was recorded at each iteration, n. Examining graphs of these values (Figure 62) gives insights into how quickly, or slowly, the method converges to the predetermined tolerance (here set at 0.05) for cluster stability.

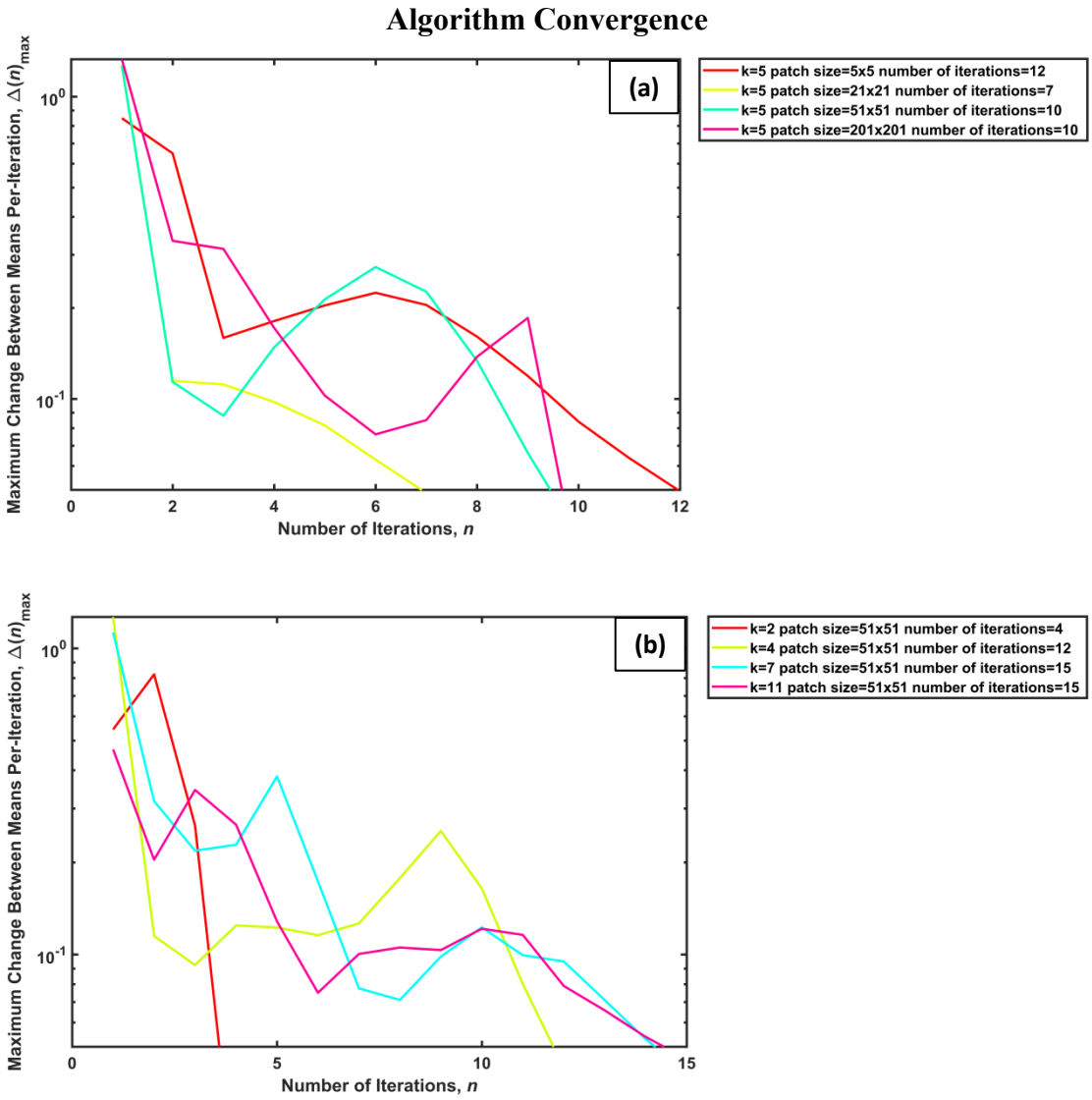

Figure 62: Convergence rate of ***k***-means clustering of structure-parallel vectors. **(a)** Maximum change between means per-iteration for patch size tests in Figure 59. **(b)** Maximum change between means per-iteration for cluster number tests in Figure 60.

As previously mentioned, *k*-means clustering algorithms are not global minimizers of the sum of within-cluster error (Equation (47)), although they do implicitly seek a local minimum of the function. However, *k*-means algorithms explicitly seek a predefined

minimum value related to cluster stability. For the modified k-means algorithm described here, this is the maximum change between cluster means per-iteration as defined in Equation (51). From Figure 62, it is observed that this value is not necessarily monotonically decreasing as a function of iteration. Given the random starting cluster means of both the patch size (Figure 62a) and cluster number tests (Figure 62b), cluster means stabilized quickly at early iterations, but at later iterations, increased in instability before again stabilized to reach the specified tolerance level. Some tests even showed multiple cycles of stability change (k=7 and 11 in Figure 62b). Each test performed in this study reached the set tolerance level (0.05), and none were observed to go into infinite loops where cluster stability constantly fluctuated. Further tests would be required to determine the theoretical limit for the tolerance of cluster stability. One explanation for the fluctuating stability of the cluster means may be closely spaced (in terms of between-patch distance as in Equation (49)) groups of structure-parallel vector patches occurring in the GPR image. Surrounding these groups may be regions of non-too-distant outliers. The mean of a cluster will be drawn to a group of patches quickly at early iterations (the initial sharp increase in stability of cluster means Figure 62). Yet, neighboring outliers may force the cluster mean out of stability until it reaches a significantly isolated group of patches where subsequent iterations cannot place outliers within a cluster to force the mean out of stability.

The last tests performed were designed to assess the effect of user-defined initial cluster means versus their random assignment. For all previous tests, random initial means have

been used. It can be seen however, that these assignments can fall below the depth of investigation. In addition, the cluster number tests show that image-scale, non-geological features such as edges are nearly always present as clusters despite the addition of new random initial means.

Using the previous patch size of [51×51] and choosing k=7, user-defined initial means were selected and the resulting clustering was compared to the results of random initial means (Figure 63 below).

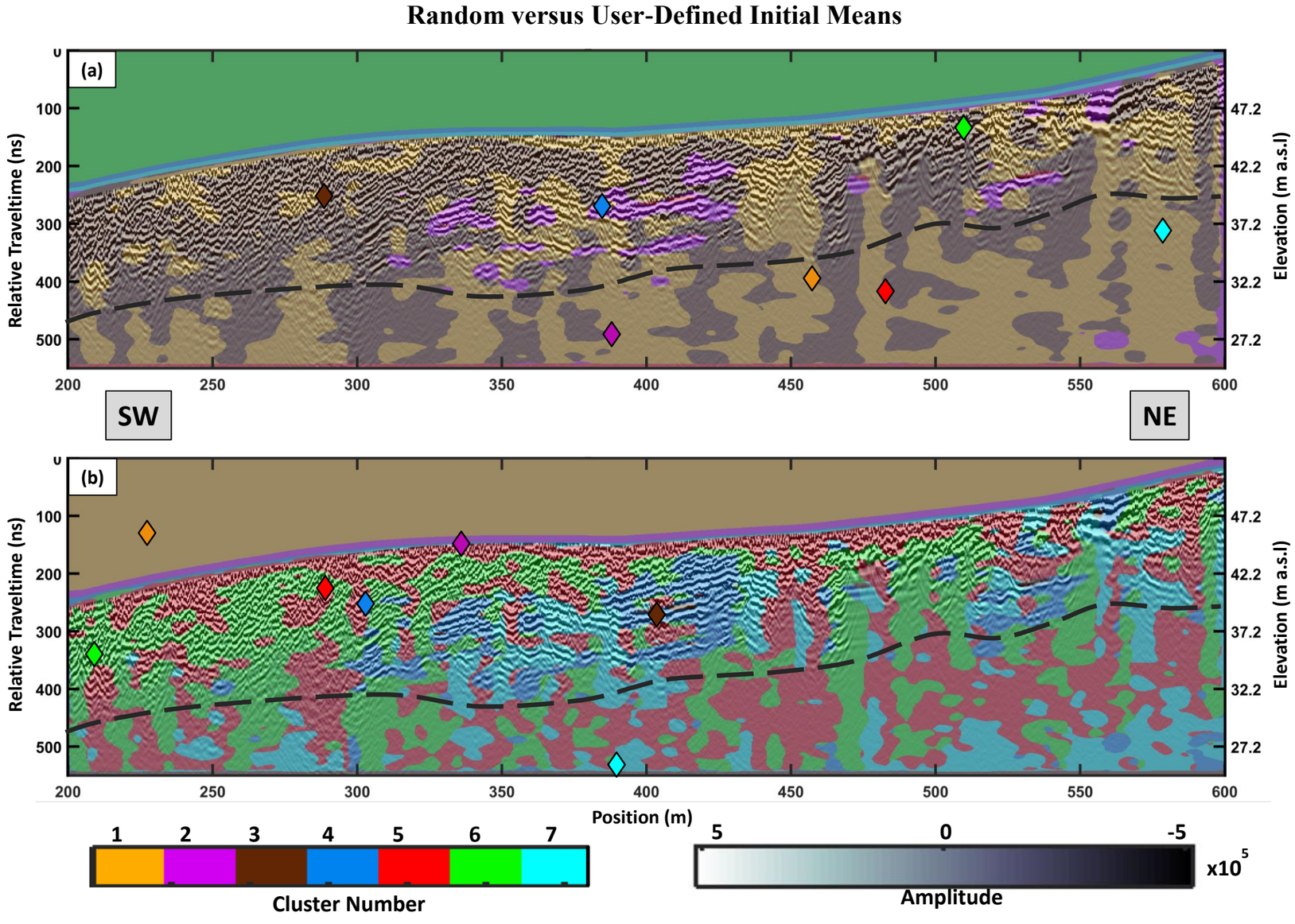

Figure 63: Comparison of randomly selected versus user-defined initial means. Depth of investigation indicated by dashed gray line. Diamonds indicate locations of initial mean patches. **(a)** Clustering results with random initial means for patch size 51×51 and $\boldsymbol{k}$ =7. **(b)** User-defined initial means for patch size 51×51 and $\boldsymbol{k}$ =7. Vertical exaggeration 4x.

As is shown in Figure 63b, initial means were chosen within the zero-amplitude region (orange diamond), at the surface subsurface contact (purple diamond), and along the long bottom edge of the image (cyan diamond). This was done to facilitate the segmentation of these major features early in the clustering process. Then four additional means were chosen within the GPR data to try and guide remainder of the segmentation process. The choices for these initial means were within: regions of steeply dipping features (green diamond), shallowly dipping features (brown diamond), complex reflections (red diamond), and intermediately dipping reflections (blue diamond). The choices for these initial means were guided by the criterion that each distinctive region should have an initial mean associated with it. The resulting clustering did segment the image into many of the features chosen in the initial means; however the final assignments do not necessarily correlate to the initial choices. For example, cluster 3 characterizes the thin edge along the bottom of the image despite its initial mean being chosen within the region of shallowly dipping reflections. Instead cluster 4 classifies those shallow southwesterly reflections. In addition, cluster 7, which characterizes the very gently northwest dipping reflections in Figure 63b did not have an initial mean that was located with the region of those reflections. Although the cluster numbers are different, comparing the results of the user-defined initial means to the randomly selected initial means shows that cluster geometries are similar. The largest difference is that the user-defined initial means test avoids the use of two clusters to characterize the surface subsurface contact and instead reserves on of these clusters to segment the GPR reflection into an additional group.

To gain additional insight into the effect of user-defined means, a convergence rate plot, similar to Figure 62 was created showing the maximum change between cluster means per-iteration, $\Delta(n)_{max}$, (Figure 64 below).

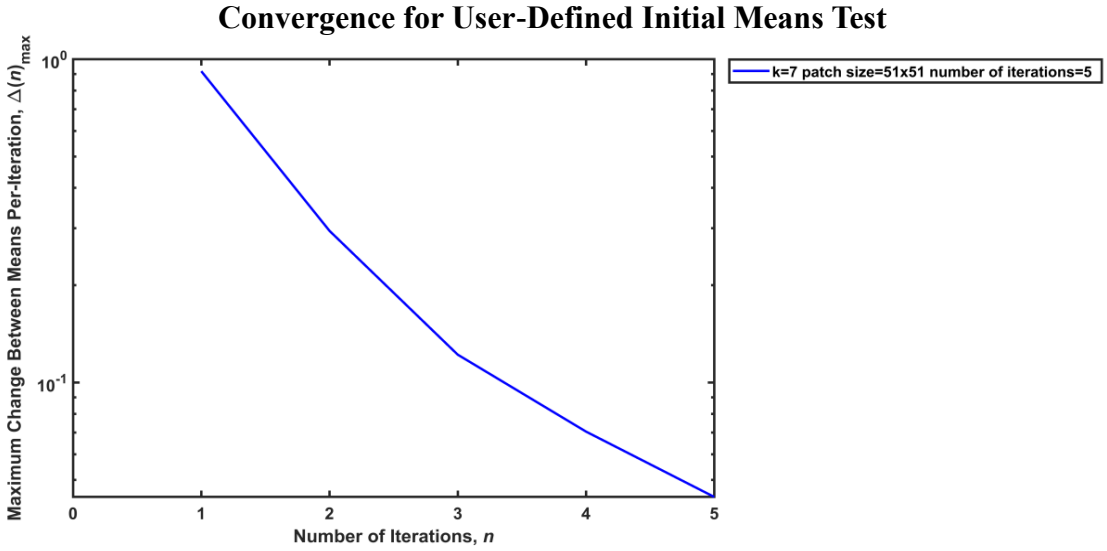

Figure 64: Convergence rate for user-defined initial means test

The convergence plot in Figure 64 shows that only 5 iterations were required to reach the predefined 0.05 tolerance for cluster stability in the user-defined initial means test. In contrast, 15 iterations were required for the test with randomly selected initial means, where both the patch size and k were the same (magenta curve in Figure 62b). Also, the convergence curve for the user-defined initial means test is strictly decreasing as opposed to the fluctuations seen in previous test results. These observations suggest that by manual selection of the initial means using a-priori knowledge of image features and

potentially geologic information, causes the k-means clustering of structure-parallel vectors to be more efficient.

The previously described tests of the modified k-menas algorithm provide information on the meaning and significance of the various parameters required in the method. The patch size test showed, as is intuitive, that the size of the patch of structure-parallel vectors should reflect the scale of features that are to be clustered in the GPR image. By varying the number of clusters, k, it was discovered that fewer clusters resulted in greater variety of features associated with each cluster, opposed to a larger number of clusters having less variability. Lastly, user-defined initial means were shown to allow prior information to more efficiently guide the clustering assignments.

6.1.1.5 Clustering Applied to Full Cross-Island Transect

The knowledge gained from the previous tests was acquired based on a small subsection of the cross-island transect. Structure-parallel vectors were next created for the entire cross-island transect and then clustered using the modified k-means method. A summary of the parameters chosen for this clustering is shown in Table 5.

Parameters for *k*-means Clustering of Cross-Island Transect

Parameter	Value	
Structure Tensors		
Gaussian Derivative	Radius=σ_1=1	Filter dimensions= $[3\sigma_1 \times 3\sigma_1]$
Gaussian Smoothing	Radius=σ_1=10	Filter dimensions= $[3\sigma_2 \times 3\sigma_2]$
Scale structure-parallel vectors by linearity, λ_1,	Yes	
***k*-means Clustering**		
Patch Size	[51×51] pixels	
Number of Clusters	k =8	
Initial-means selection method	User-defined	

Table 5: List of parameters used in the ***k***-means clustering of structure-parallel vectors along the cross-island transect.

Figure 65 shows the results of this clustering applied to the full cross-island transect, along with the locations of the initial cluster means. Figures 66-77 show a multi-figure panoramic of the clustering results at the same intervals and vertical exaggeration as the migrated images Figures 34-45.

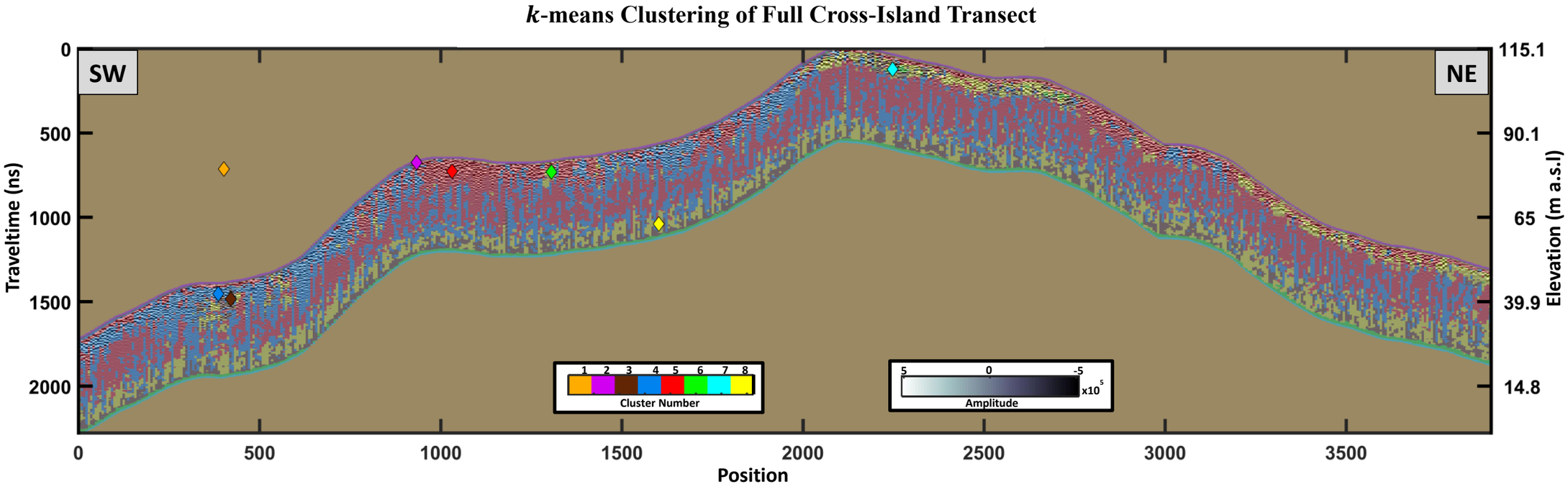

Figure 65: ***k***- means clustering of full cross-island transect. Colored diamonds represent locations of user-defined initial means. Two close-up sections show the detailed clustering assignments.

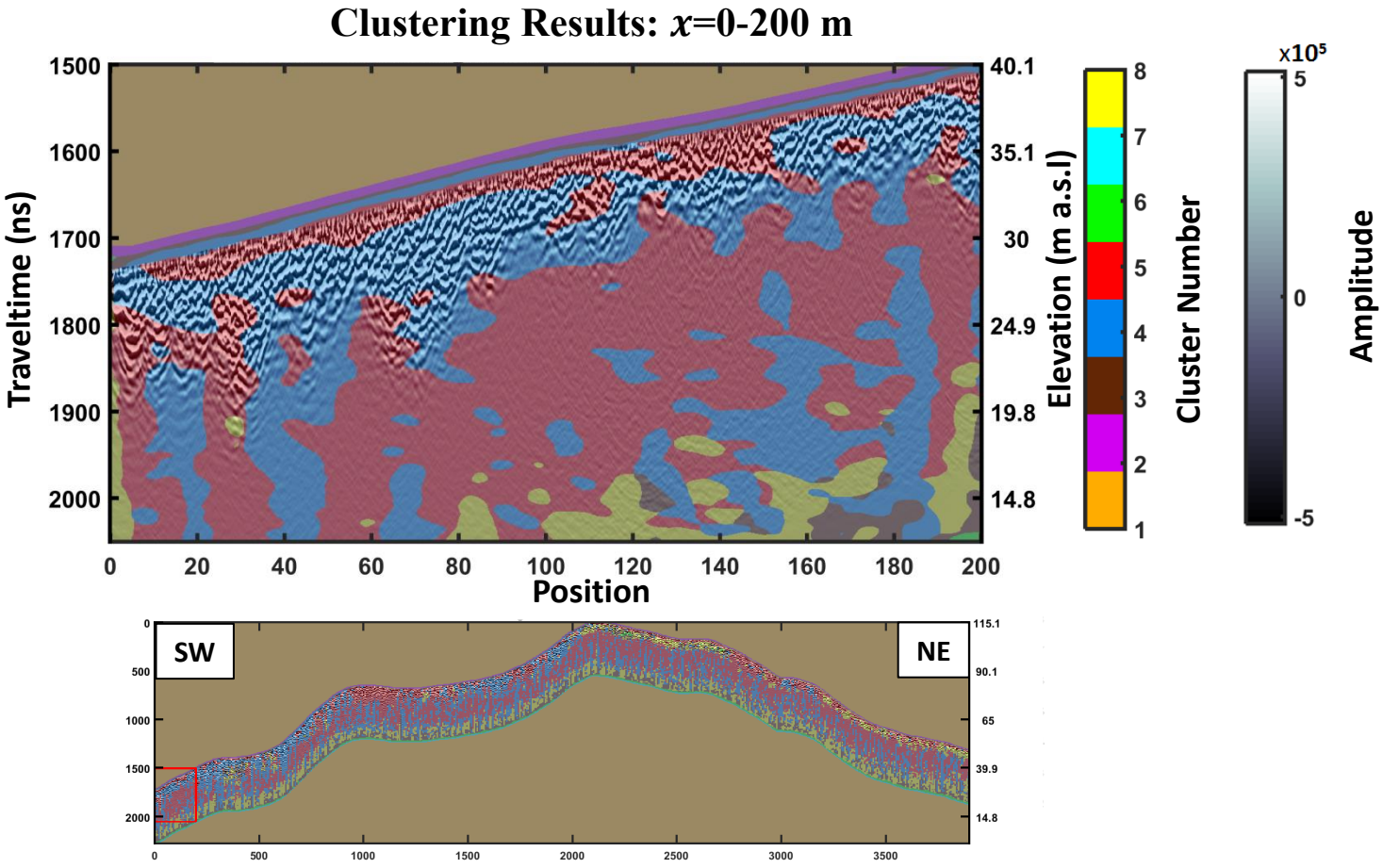

Figure 66: Clustering results: x=0-200 m. Vertical exaggeration 4x. Locator map on showing section displayed indicated by red box.

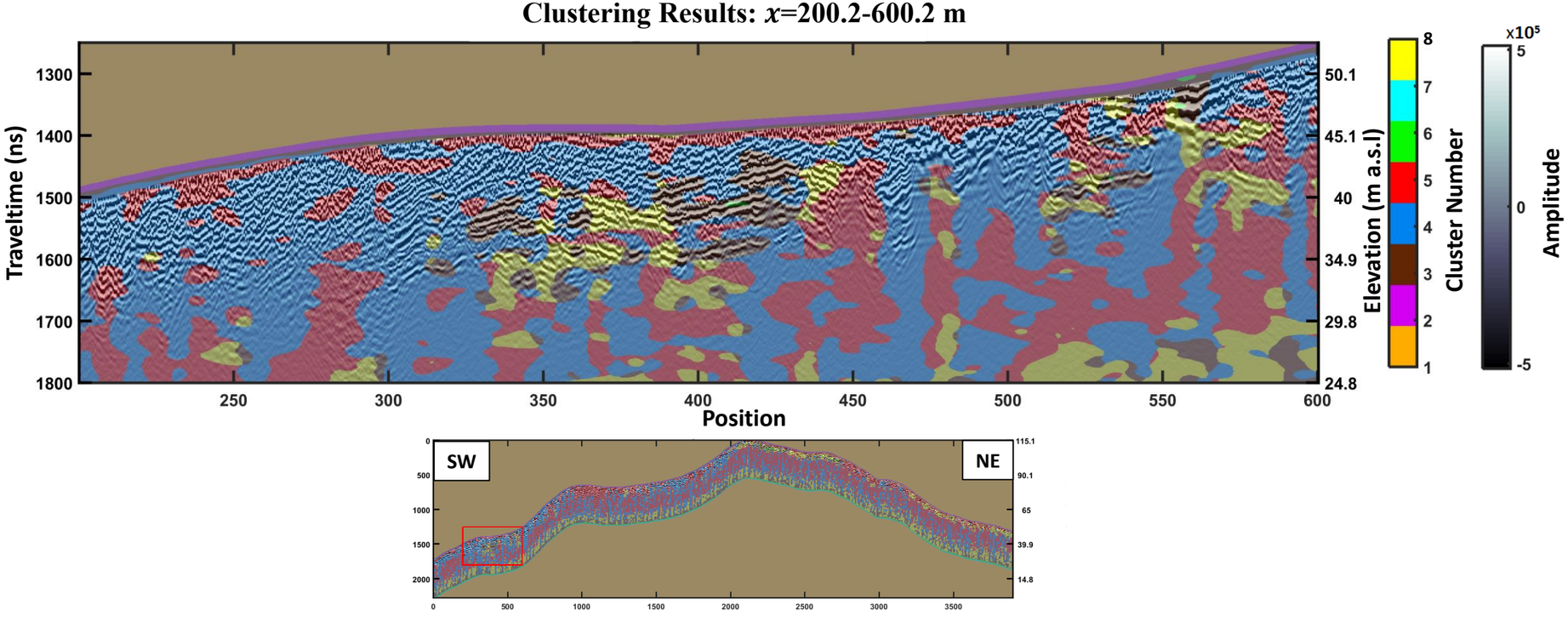

Figure 67: Clustering results: x=200.2-600.2 m. Vertical exaggeration 4x. Locator map on showing section displayed indicated by red box.

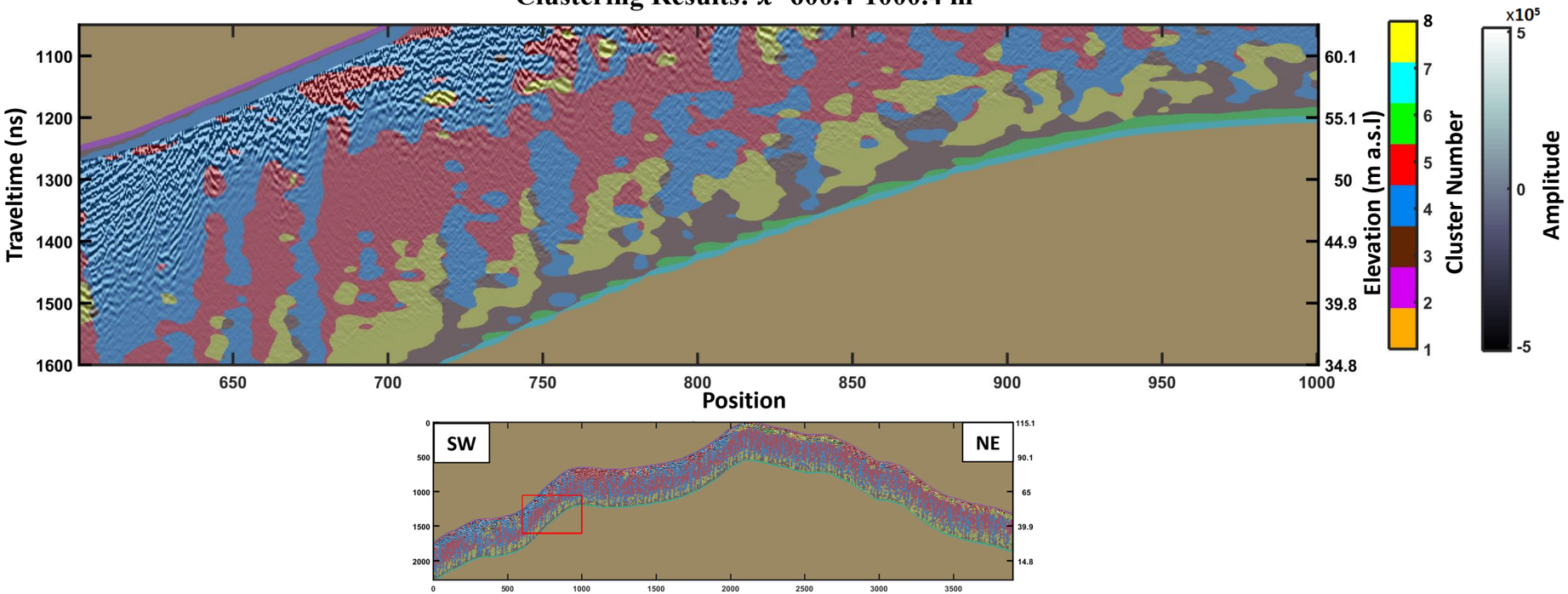

Figure 68: Clustering results: x=600.4-1000.4 m. Vertical exaggeration 4x. Locator map on showing section displayed indicated by red box.

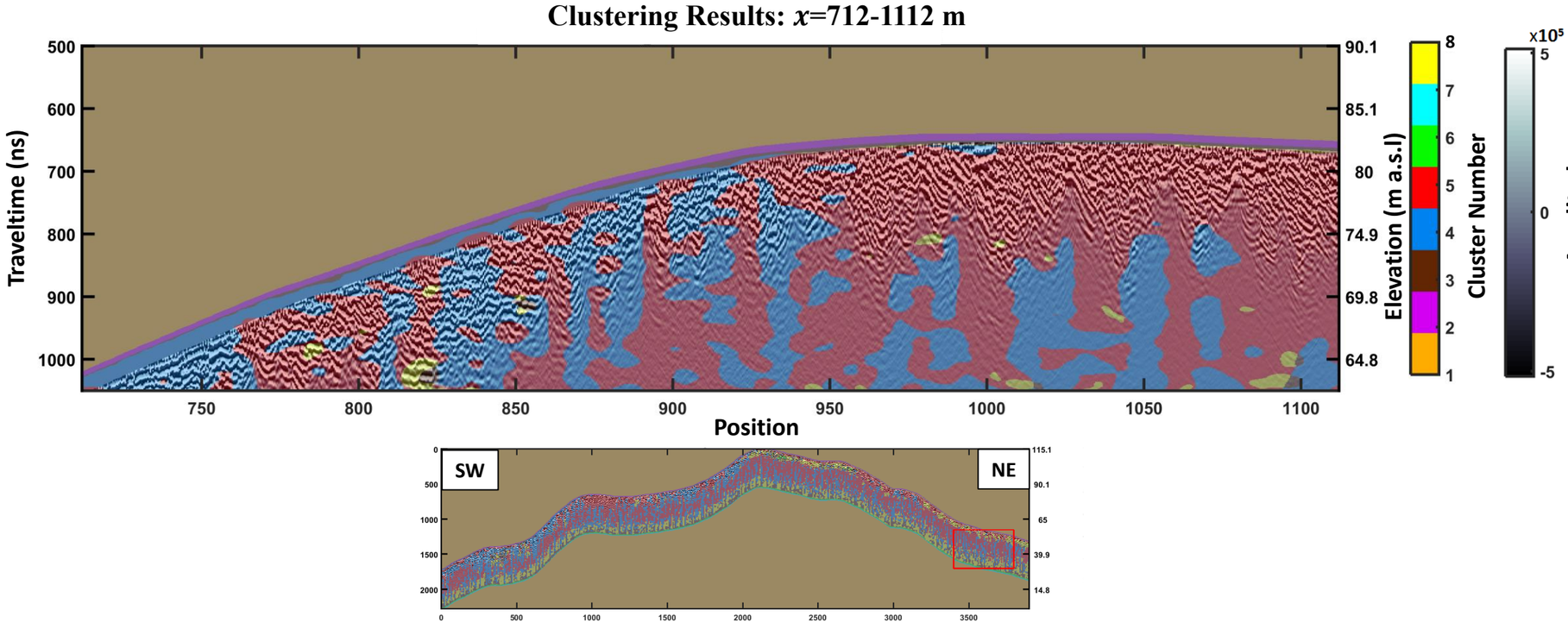

Figure 69: Clustering results: x=712-1112 m. Vertical exaggeration 4x. Locator map on showing section displayed indicated by red box.

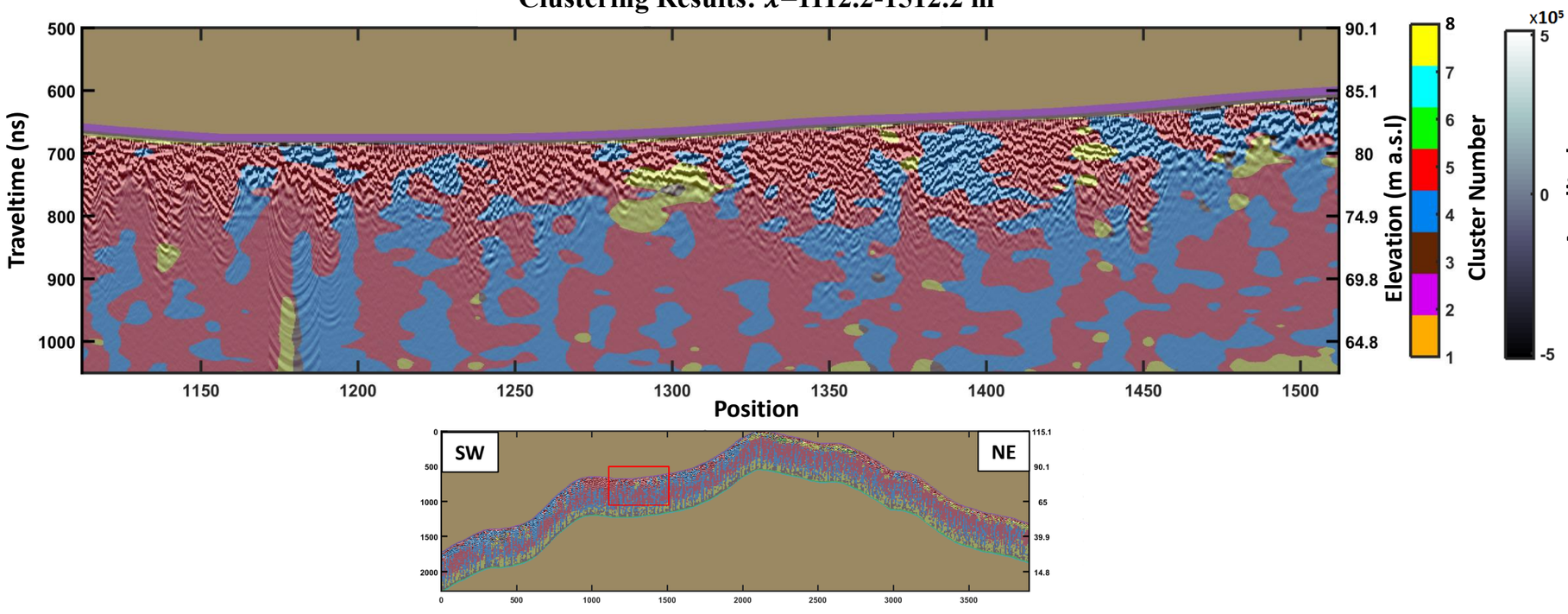

Figure 70: Clustering results: x=1112.2-1512.2 m. Vertical exaggeration 4x. Locator map on showing section displayed indicated by red box.

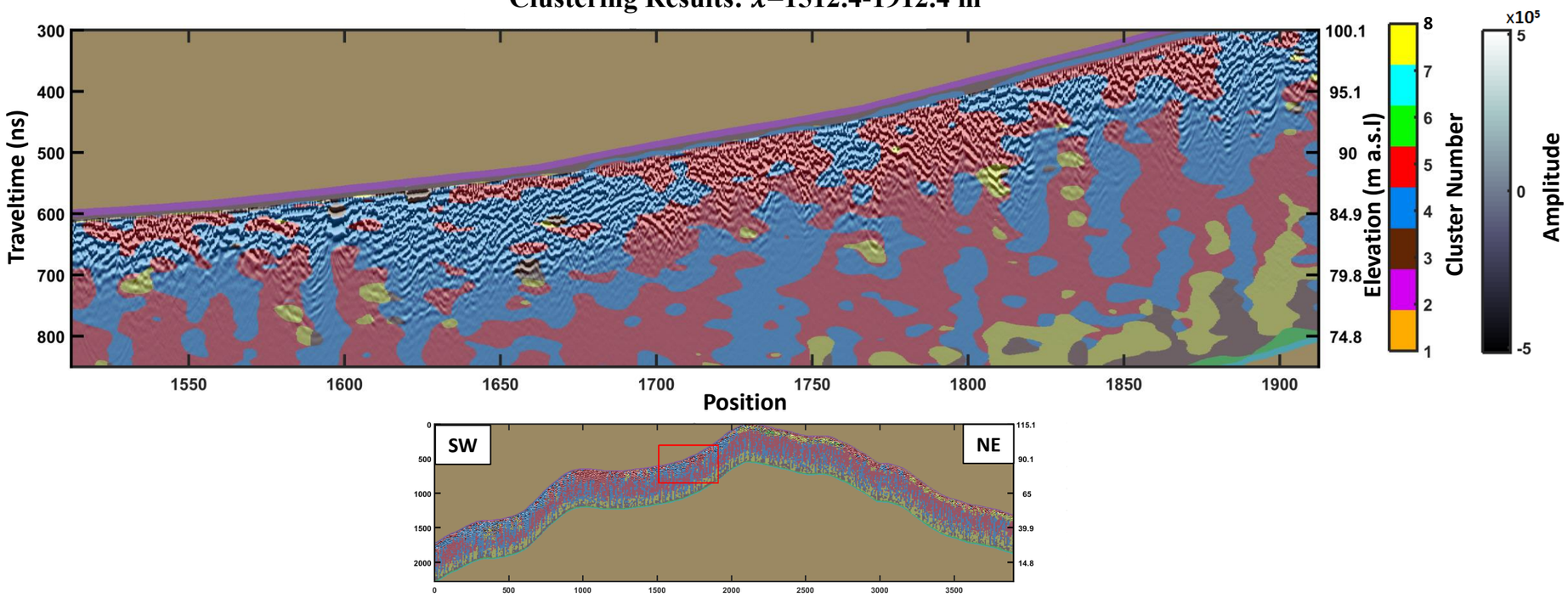

Figure 71: Clustering results: x=1512.4-1912.4 m. Vertical exaggeration 4x. Locator map on showing section displayed indicated by red box.

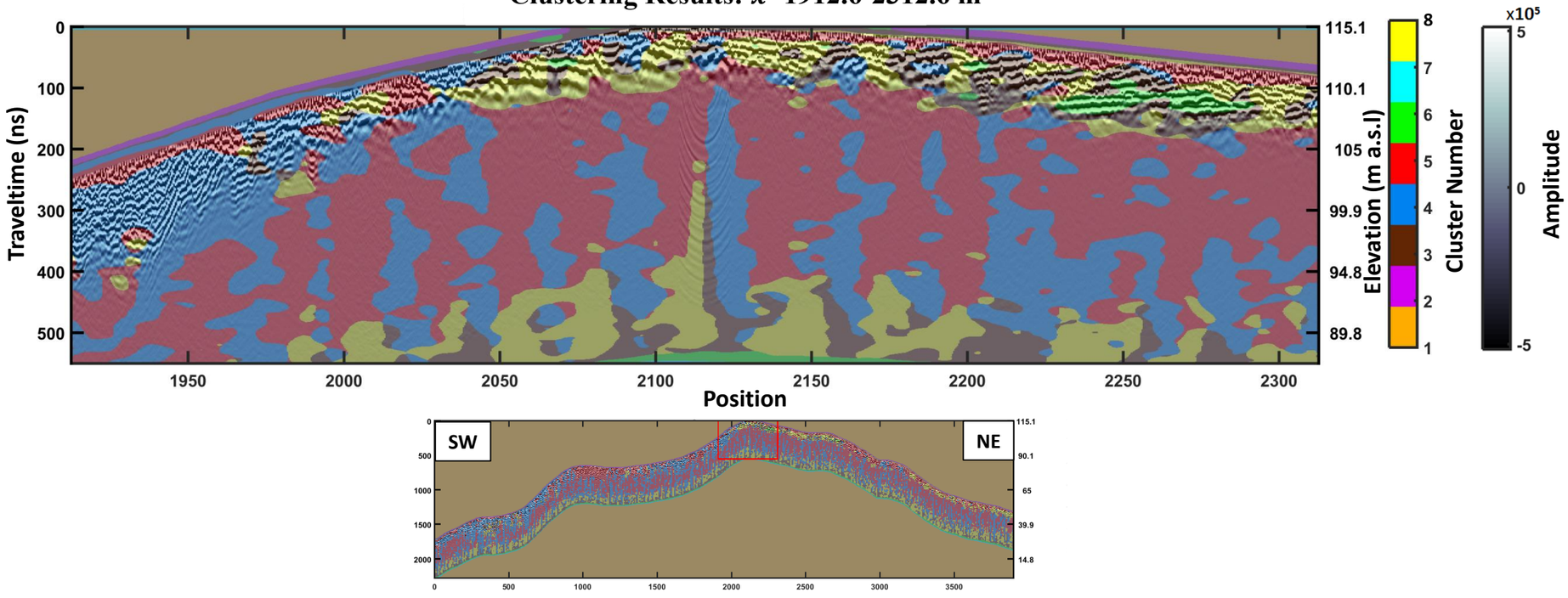

Figure 72: Clustering results: x=1912.6-2312.6 m. Vertical exaggeration 4x. Locator map on showing section displayed indicated by red box.

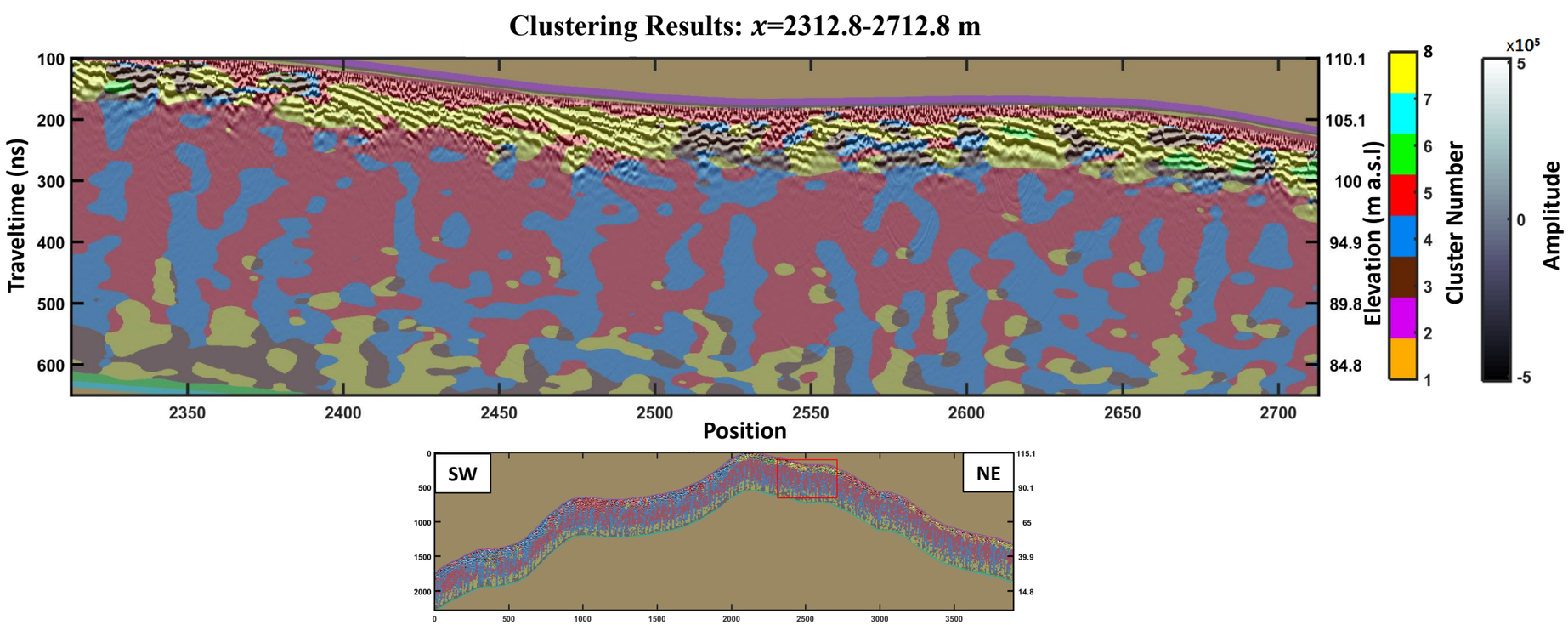

Figure 73: Clustering results: x=2312.8-2712.8 m. Vertical exaggeration 4x. Locator map on showing section displayed indicated by red box.

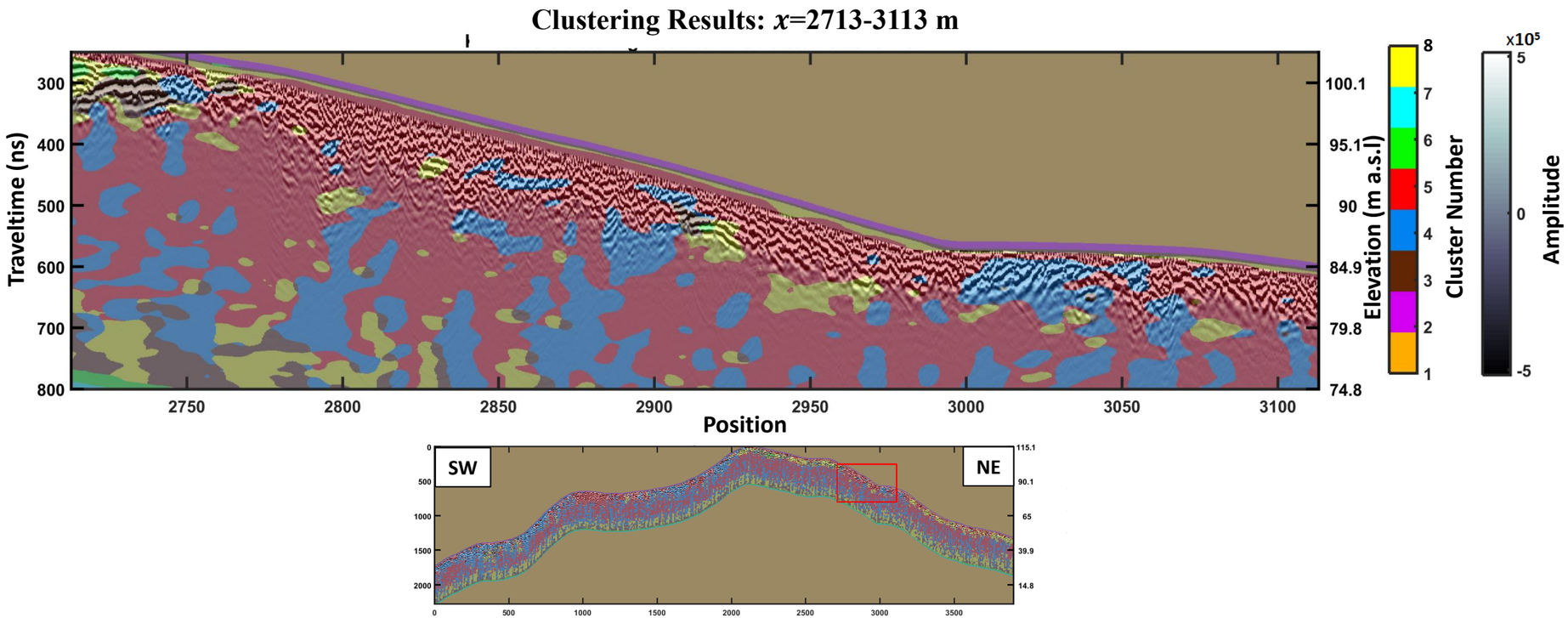

Figure 74: Clustering results: x=2713-3113 m. Vertical exaggeration 4x. Locator map on showing section displayed indicated by red box.

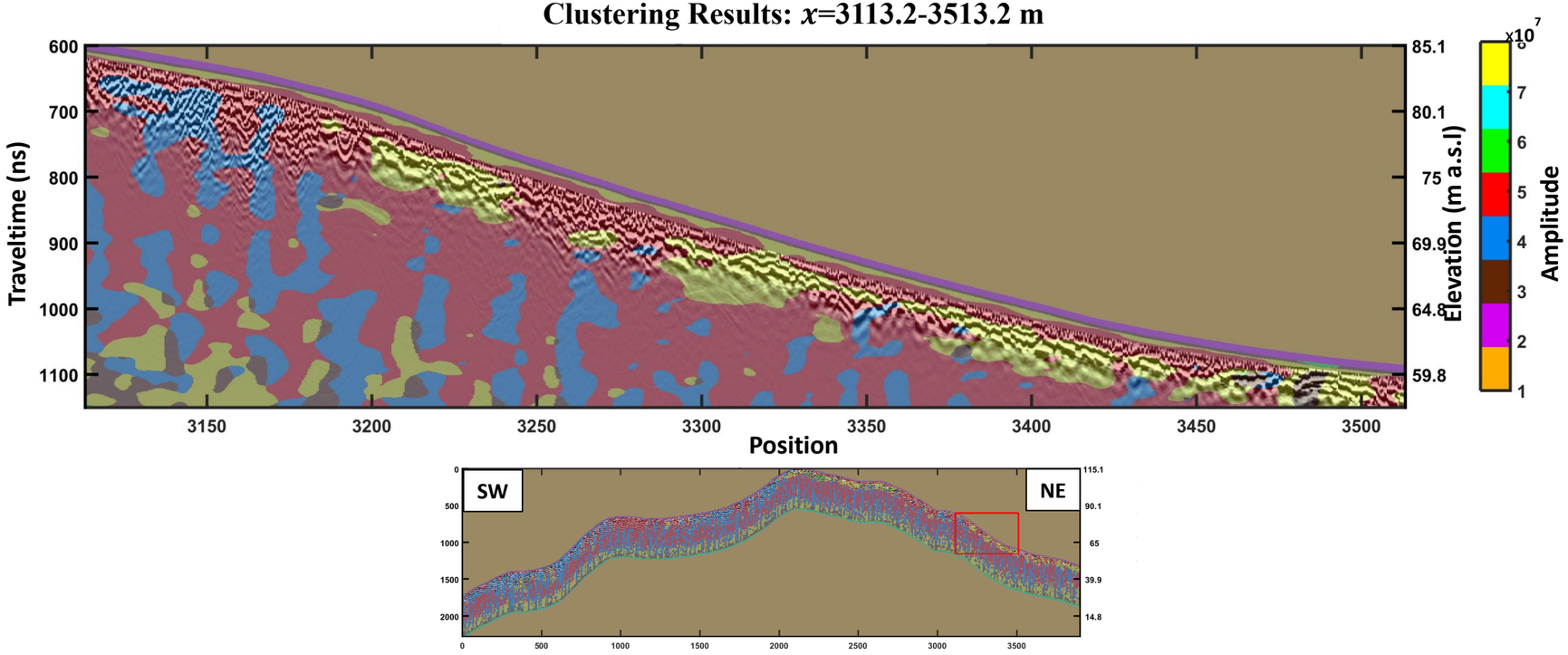

Figure 75: Clustering results: x=3113-3513.2 m. Vertical exaggeration 4x. Locator map on showing section displayed indicated by red box.

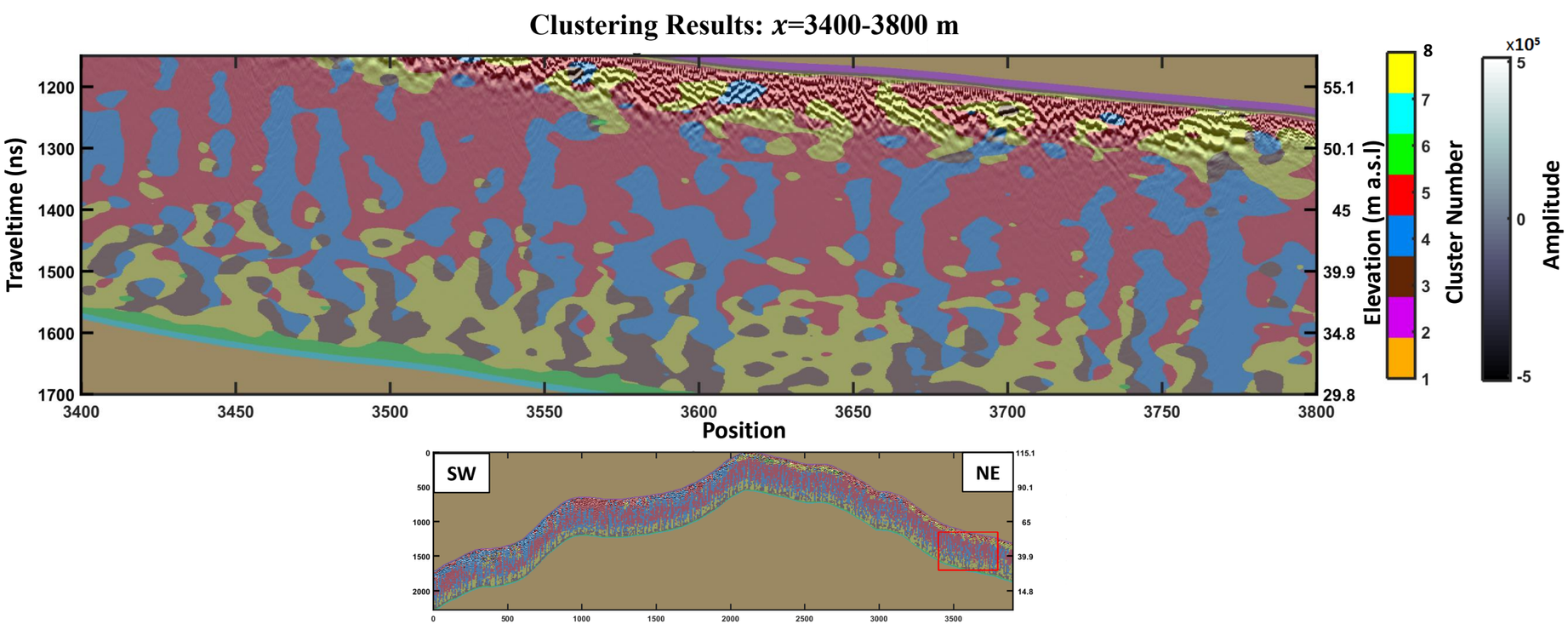

Figure 76: Clustering results: x=3400-3800 m. Vertical exaggeration 4x. Locator map on showing section displayed indicated by red box.

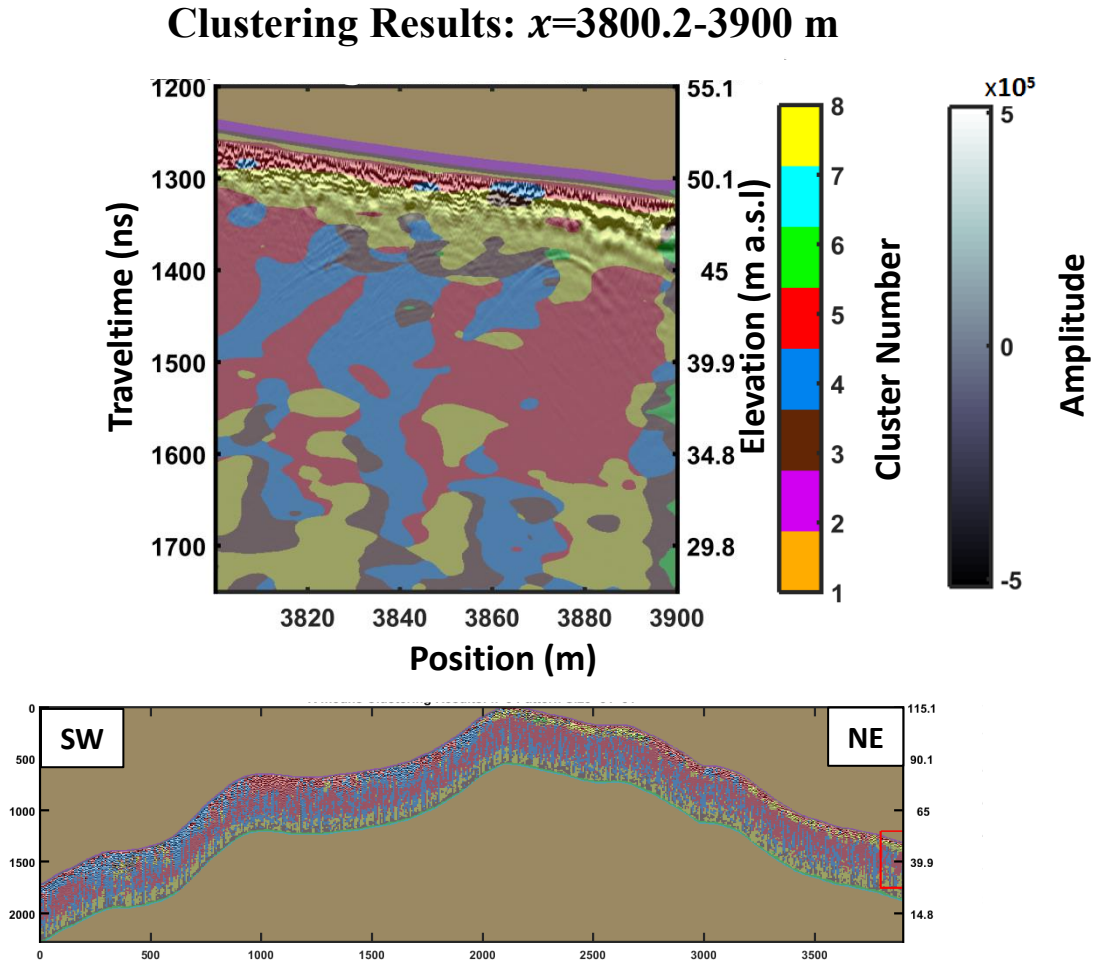

Figure 77: Clustering results: x=3800.2-3900 m. Vertical exaggeration 4x. Locator map on showing section displayed indicated by red box

The locations of initial means 1, 2, and 8 were chosen so as to account for the major image features that were not related to the GPR reflections, including both the upper and lower edges of the data, as well as the zero amplitude regions that have been inserted as padding due to the topographic migration. The remaining initial means were chosen within regions of GPR features that were considered to be significant across the line. The initial mean for cluster 3 was centered among reflections that dip shallowly to the southeast, whereas clusters 4 and 5 were chosen in regions of more steeply dipping reflections to the southwest and northeast respectively. The initial means for clusters 6 and 8 were chosen where reflections were horizontal or very shallowly dipping with orientations either to the southwest or to the northeast. Similarly to the small-scale tests, it transpired that the locations of these initial mean assignments were not necessary included in their respective clusters in the end result. Nevertheless, Figures 66-77 show that the clustering classifies features that are on the scale of interest (10s to 100s of meters in extent) for this study, with enough allowable within-cluster variability that similar features are associated with the same clusters across the line.

A detailed description of each of the clusters follows. The descriptions in this section serve to define the characteristics of the features assigned to each cluster. Interpretations and observations about distributions of features within each cluster as related to radar facies are discussed in Section 6.1.2. In addition to the following qualitative descriptions, dip-histograms for each cluster were created. These plots (Figures 78-85) show the number of structure-parallel vectors falling within a bin representing a given

range of dips for each cluster. The dips in these histograms represent actual apparent dips as the length of each vector component was converted from image samples to meters prior to the dip calculation. In addition to binning the vectors by dip, each bin was then color-coded according to the average linearity of the vectors in that bin. Recall that each structure-parallel vector was scaled by the linearity parameter, λ_1, which ranges from 0 to 1. This scaling was done during the structure-tensor generation process. Vectors with larger associated values of linearity describe more consistent local orientations, and with their length scaled by this value, they are preferentially weighted when computing the "distance" between patches of vectors as per Equation (49). Therefore vectors with higher average linearity for a given range of dips represent the more continuous and consistent reflectors in the cross-island transect.

Cluster 1: This cluster contains vectors associated with the zero amplitude regions of the image (Figure 78c). Dips for these vectors are almost exclusively zero (Figure 78a) with zero linearity as well. This occurs due the image being constant-valued above and below the GRP data and therefore all gradients are zero. Only several hundred vectors have dips above zero (here between 5-10 degrees). Due to the high linearity of these non-horizontal vectors, they may be associated with pre-first arrival artifacts of the data processing creating a distinct edge in the data.

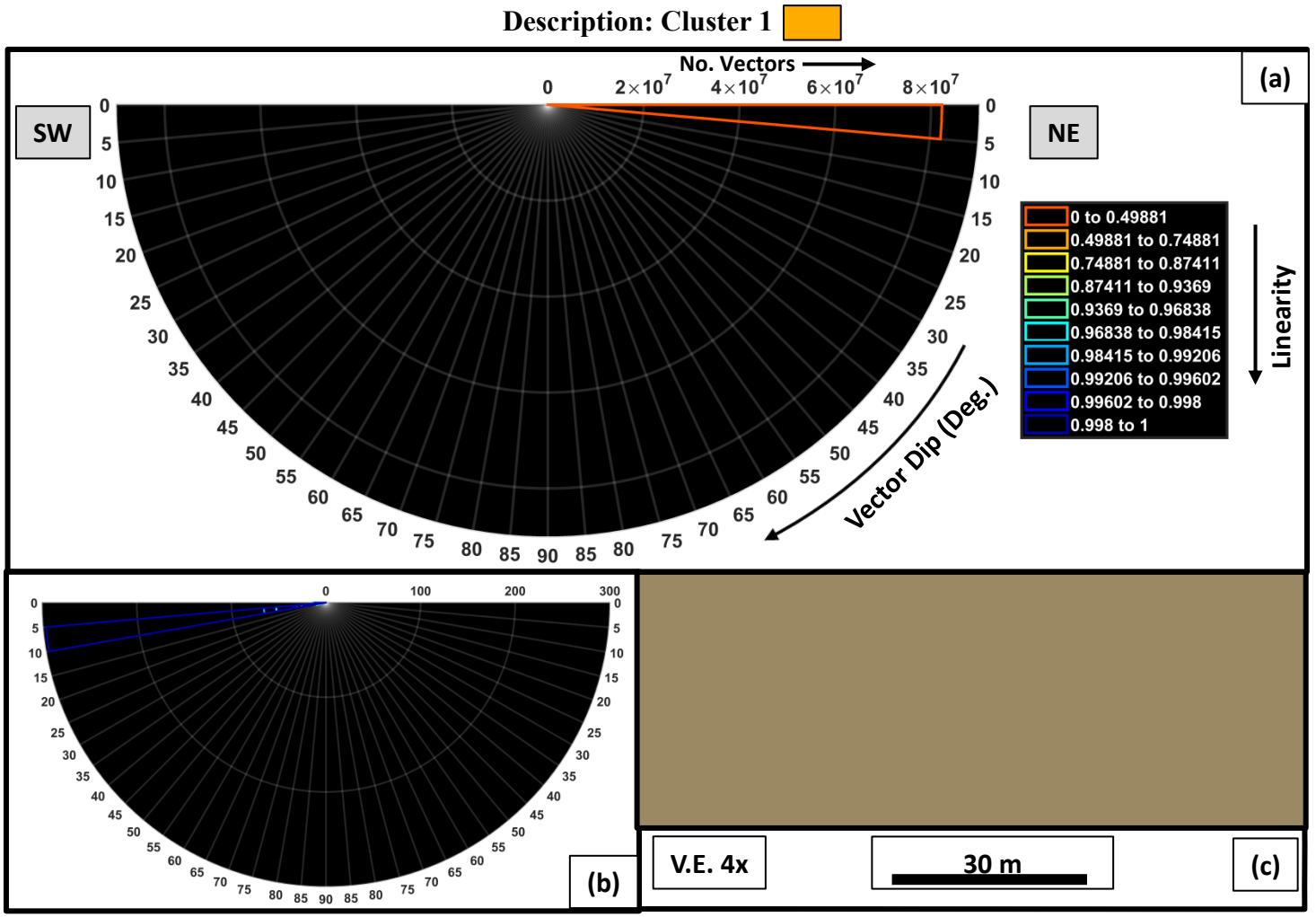

Figure 78: Dip-histogram of vectors in cluster 1 along with example of cluster 1 from Figure 65. **(a)** Linearity colored dip-histogram of vectors in cluster 1. **(b)** Dip-histogram with only linearities ≥ 0.87 displayed. **(c)** Example of cluster 1 features.

Cluster 2: This cluster characterizes the upper boundary of the GPR data along the surface of acquisition (Figure 79c). Similarly to cluster 1, the dips for most vectors in this cluster are zero with zero linearity (Figure 79a). When looking at the subset of vectors with linearities ≥ 0.87 (Figure 79b), dips are nearly horizontal as well, with few vectors having dips greater than 5-10 degrees. These vectors with non-zero linearities can be attributed to pre-first arrival amplitudes in the data, likely caused by data processing artifacts.

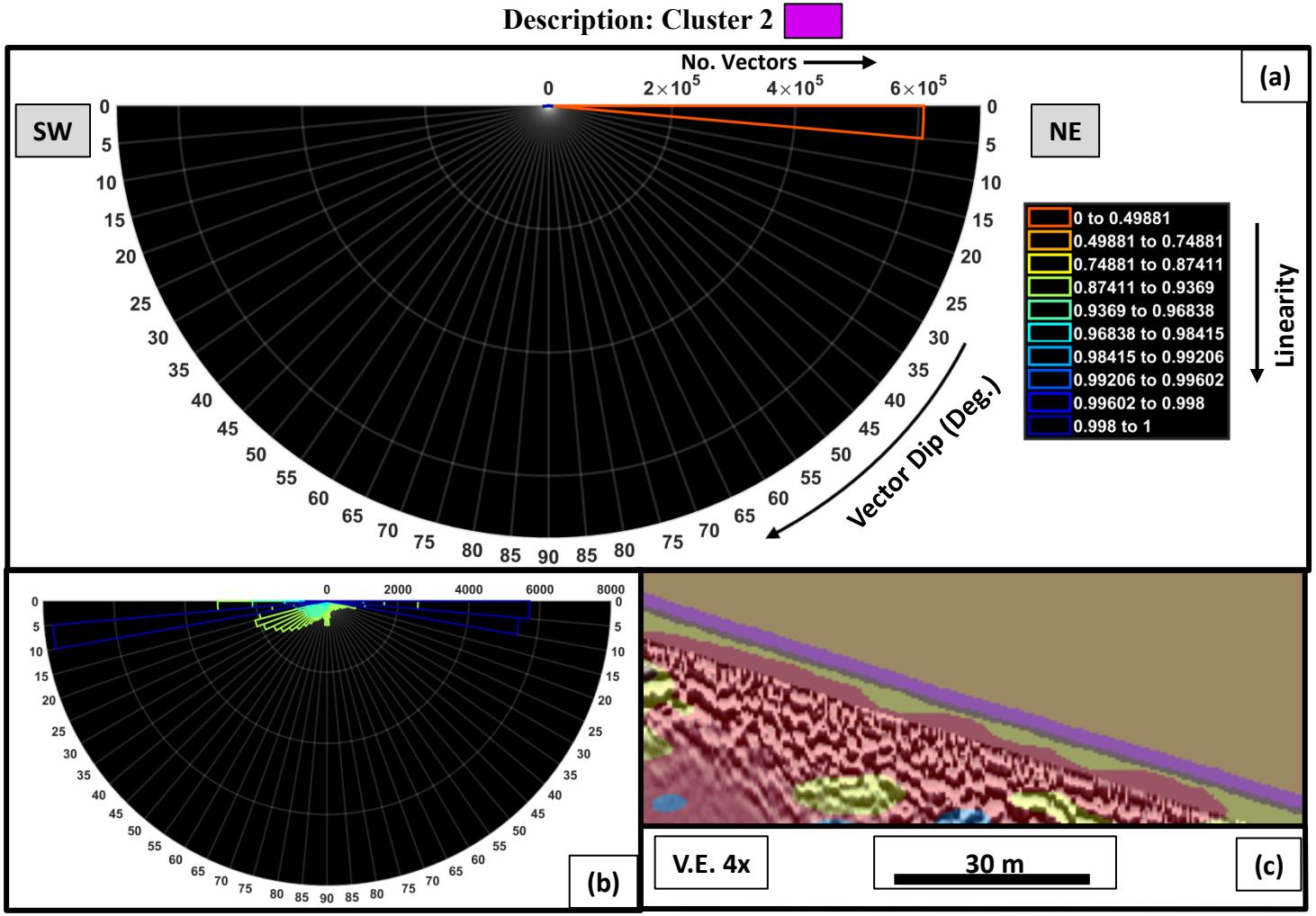

Figure 79: Dip-histogram of vectors in cluster 2 along with example of cluster 2 from Figure 65. **(a)** Linearity colored dip-histogram of vectors in cluster 2. **(b)** Dip-histogram with only linearities ≥ 0.87 displayed. **(c)** Example of cluster 2 features.

Cluster 3: This cluster classifies relatively low-angle, southwest dipping, reflections in the cross-island transect. Figure 80a shows that this cluster encompasses a range of dips between 5 and 90 degrees, with some dips even being to the northwest. The majority of the vectors have linearities less than 0.75 which suggests that these features do not produce sharp gradients in the image causing local orientations to be less consistent. This can be observed in Figure 80c where examples of reflectors in this cluster are broader and more diffuse compared to neighboring reflections, such as those classified by cluster 4 in blue. Also, these reflectors show a hummocky and irregular character which accounts for the large range of dips shown in Figure 80a. When looking at vectors with high linearities ($\lambda_1 \geq 0.87$ in Figure 80b), a bimodal distribution is observed. Many of these high-linearity vectors have dips between 5 and 15 degrees, which correlates with the large-scale orientation of the features in this cluster. The other significant group of dips shown in Figure 80b is nearly vertical ($90^\circ \pm 5^\circ$). These dips match with the near vertical dips of the fine scale irregularities and discontinuities along the reflectors in this cluster (Figure 80c).

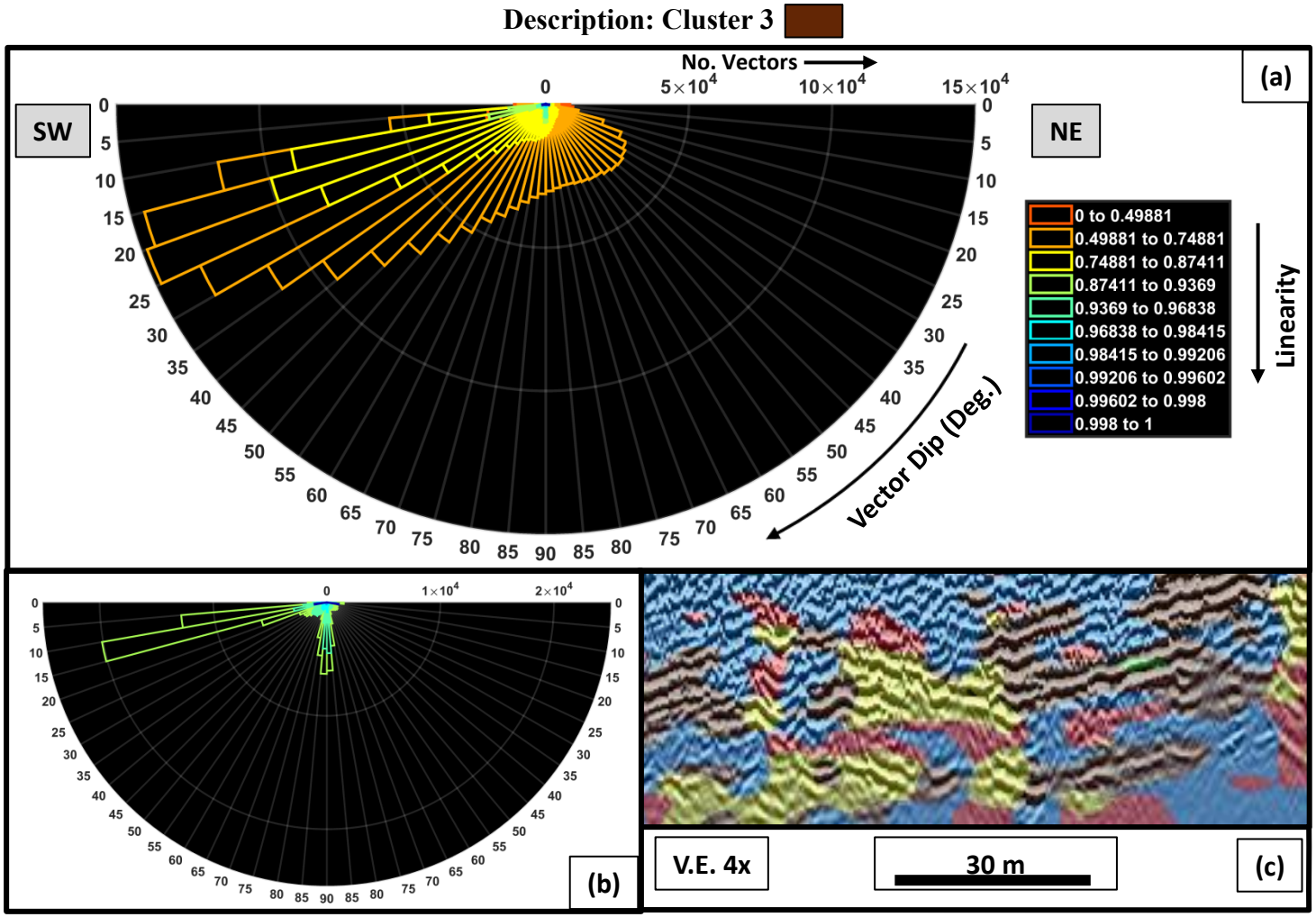

Figure 80: Dip-histogram of vectors in cluster 3 along with example of cluster 3 from Figure 65. **(a)** Linearity colored dip-histogram of vectors in cluster 3. **(b)** Dip-histogram with only linearities ≥ 0.87 displayed. **(c)** Example of cluster 3 features.

Cluster 4: Cluster 4 classifies reflectors that are more steeply dipping to the southwest (Figure 81c) than those in cluster 3. The dip histogram in Figure 81a shows that most orientations for vectors in this cluster are distributed between 20 and 60 degrees. Linearities are shown to be comparatively high, with no vectors falling below $\lambda_1 = 0.74$. For the vectors with the most consistent local orientations ($\lambda_1 \geq 0.87$ in Figure 81b), dips are more narrowly distributed, with most of these vector falling between 45 and 25 degrees. Manually measured dips of continuous reflectors in assigned to this cluster show dips between 20-30 degrees. This is correlated with the dips of vectors in Figure 81b having linearities above 0.97, and therefore provides evidence that the more continuous reflectors in the section are characterized by the vectors with the highest linearities. The comparatively high overall linearities and narrow dip distribution implies that features in cluster 4 are consistently oriented within the cluster.

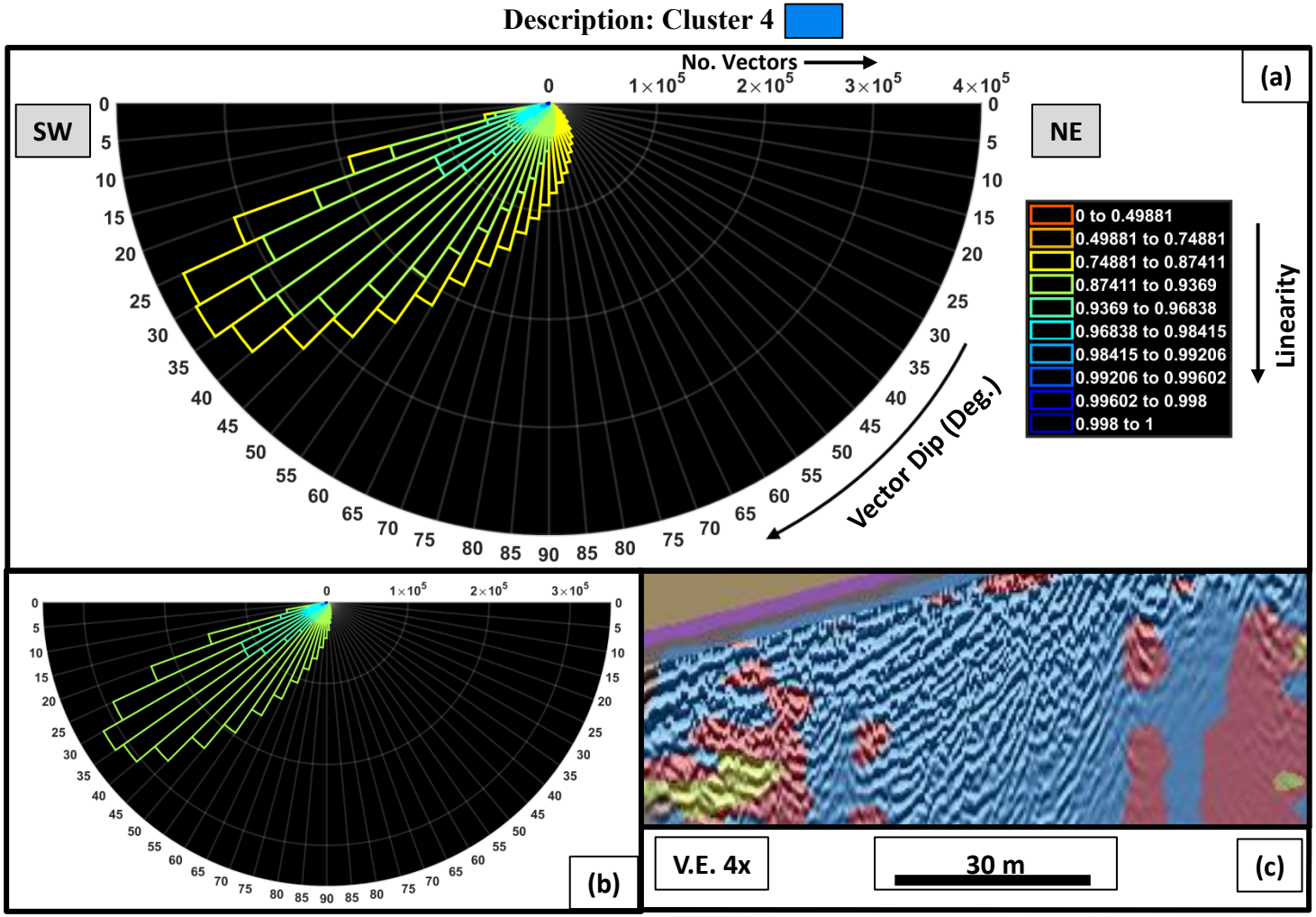

Figure 81: Dip-histogram of vectors in cluster 4 along with example of cluster 4 from Figure 65. **(a)** Linearity colored dip-histogram of vectors in cluster 4. **(b)** Dip-histogram with only linearities ≥ 0.87 displayed. **(c)** Example of cluster 4 features.

Cluster 5: This cluster identifies reflections that are dipping steeply to the northeast. Many of the features in this cluster are essentially 90˚ rotations of those in cluster 3. However, this cluster also contains regions of more complex reflectors, especially near the top of the GPR traces, which have near vertical orientations. These features can be seen at the top of Figure 82c. Further evidence for the classification of these high-angle complex reflectors is the dip-histogram in Figure 82a. Here many of the vectors are shown to have dips falling within the same 20 to 60 degree range as cluster 4, however the distribution in Figure 82a is broader and encompasses dips that are up to 90 degrees as well. The linearities of vectors in this cluster are also high, with the majority falling above 0.87. This illustrates the fact that both the high-angle complex reflections and the more continuous northeast dipping reflections in this cluster produce high gradients in the image, thereby increasing the consistency of local orientations.

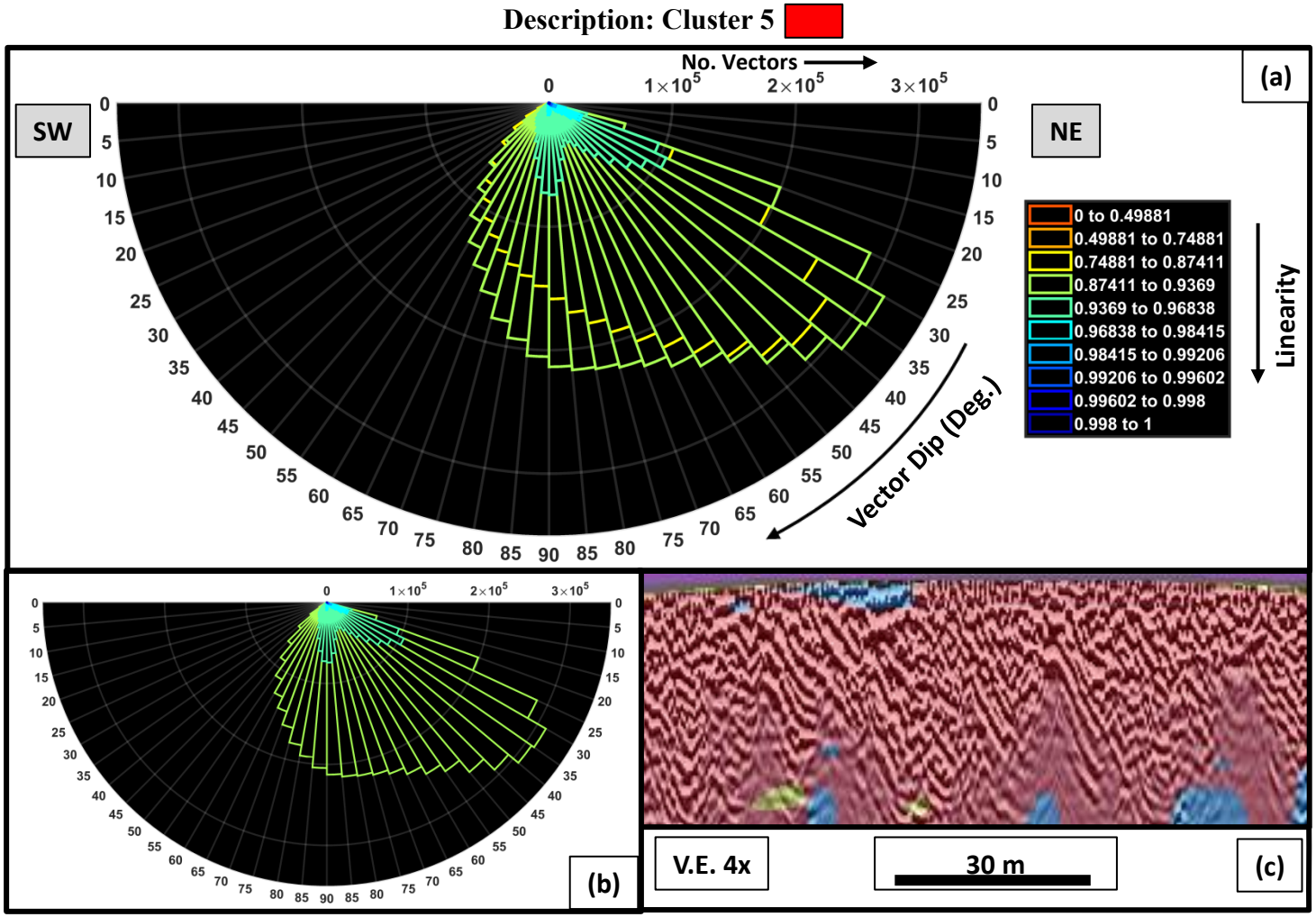

Figure 82: Dip-histogram of vectors in cluster 5 along with example of cluster 5 from Figure 65. **(a)** Linearity colored dip-histogram of vectors in cluster 5. **(b)** Dip-histogram with only linearities ≥ 0.87 displayed. **(c)** Example of cluster 5 features.

Cluster 6: From Figure 83c it is evident that GPR reflections in this cluster are near-horizontal compared to surrounding reflections. The dip-histogram in Figure 83a shows that the majority of the vectors in this cluster have low linearities (rarely exceeding $\lambda_1 = 0.74$). This is likely due to the fact that the majority of vectors it in this cluster exist near the bottom edge of the GPR data (Figure 65 and Figure 84c), with few residing within the GPR reflections themselves. At the bottom of the data, low-amplitude migration artifacts are characterized by very broad semi-ellipse shapes that consequently have near horizontal orientations. Given that they are low-amplitude compared to the GPR data, image gradients due to these features are also low, resulting in low linearities. Looking at vectors in this cluster where linearities are higher (Figure 83b) dips are less than than 10 degrees. This correlates well with the sub-horizontal GPR reflections in Figure 83c that are associated with this cluster.

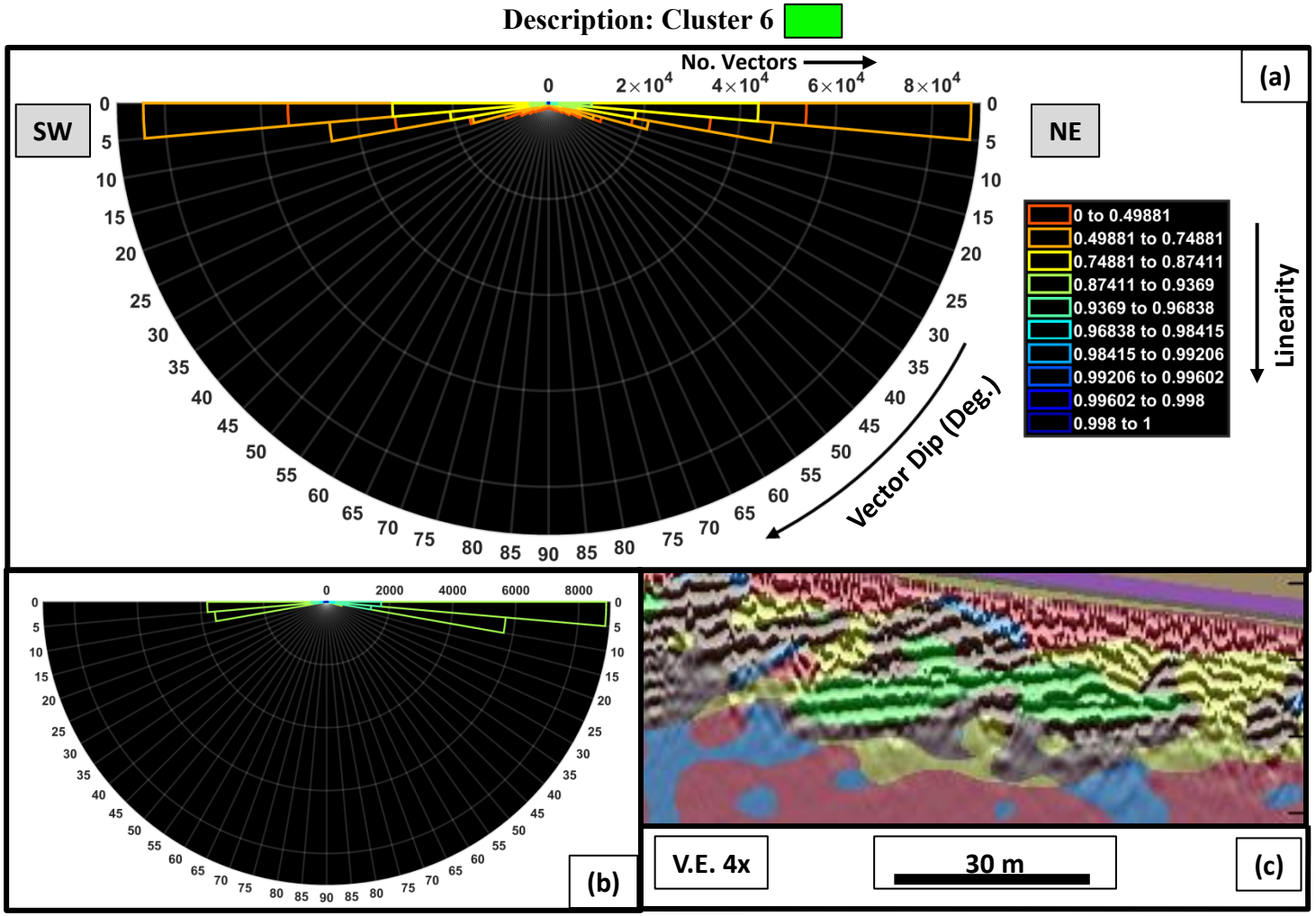

Figure 83: Dip-histogram of vectors in cluster 6 along with example of cluster 6 from Figure 65. **(a)** Linearity colored dip-histogram of vectors in cluster 6. **(b)** Dip-histogram with only linearities ≥ 0.87 displayed. **(c)** Example of cluster 6 features.

Cluster 7: Cluster 7 is the complementary cluster to cluster 2. Here this cluster characterizes vectors associated with the bottom edge of the GPR data (Figure 84c). Similarly to cluster 2, the dips of these vectors are largely zero with zero linearity (Figure 84a). Dips with higher linearity (Figure 84b) also show low dips, and in contrast to cluster 3, no dips exceed 5 degrees. This is possibly due to the fact that the data are truncated after the recording time window, causing a relatively sharp and horizontal edge, which would produce the high linearity, low-dip vectors.

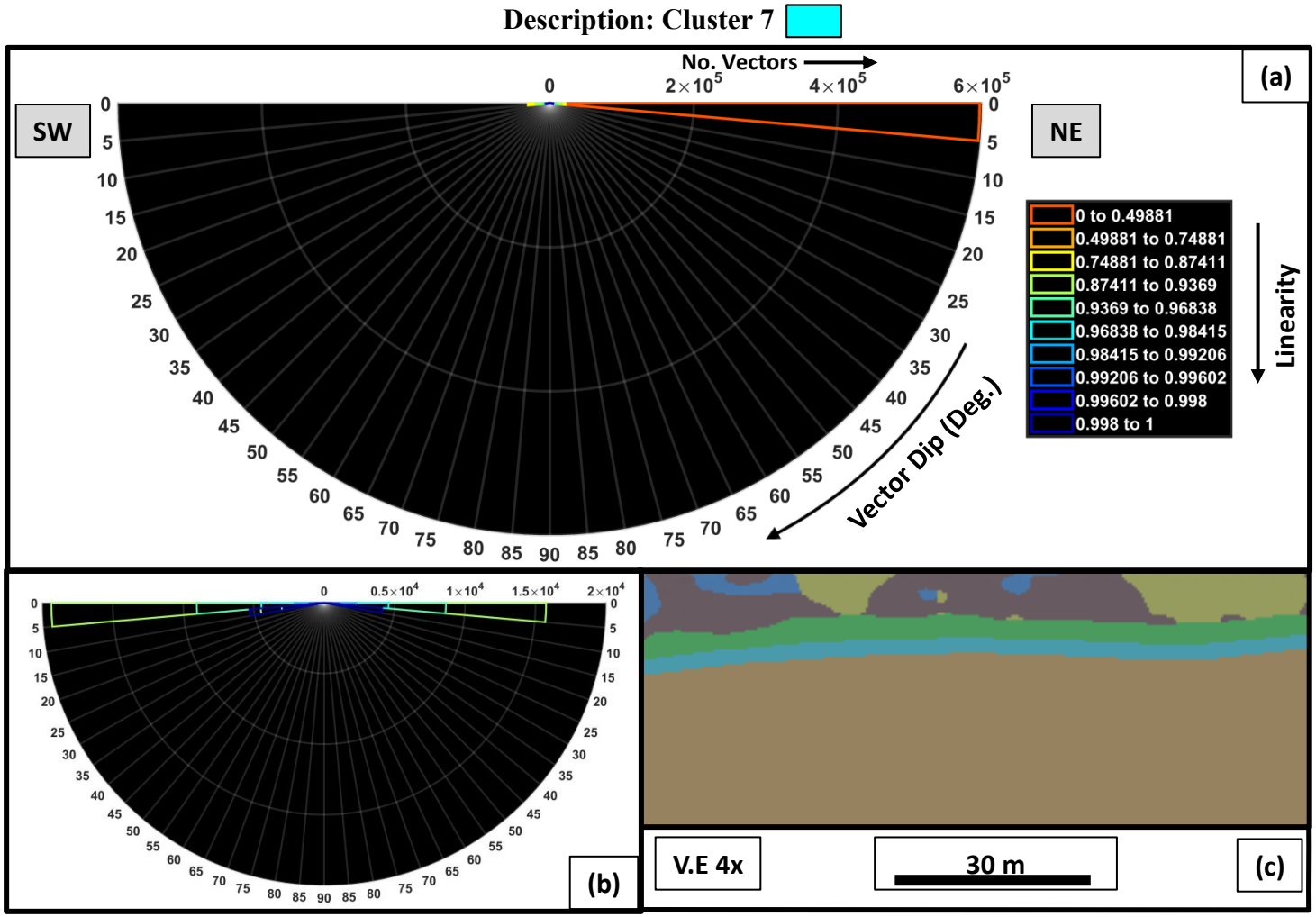

Figure 84: Dip-histogram of vectors in cluster 7 along with example of cluster 7 from Figure 65. **(a)** Linearity colored dip-histogram of vectors in cluster 7. **(b)** Dip-histogram with only linearities ≥ 0.87 displayed. **(c)** Example of cluster 7 features.

Cluster 8: This cluster contains vectors associated with comparatively low-angle northeast dipping reflections (Figure 85c). These reflections can be seen to be laterally continuous and contain less of the fine scale reflector irregularities seen in cluster 3, although some can be observed (Figure 85c) The dip-histogram in Figure 85a shows the narrowest distribution of dips for any cluster within the cross-island transect, with most dips ranging from 10-35 degrees. Similarly to cluster 3, the majority of linearities for vectors in this cluster fall below the 0.87-0.94 range, which illustrates the more diffuse character of the reflections, thereby creating smaller gradients, as seen in Figure 85c. Looking at those linearities that exceed 0.87 (Figure 85b), the dip distribution further narrows to a range of 10-25 degrees. This suggests that the better-defined reflectors have shallower dips than other reflections in this cluster.

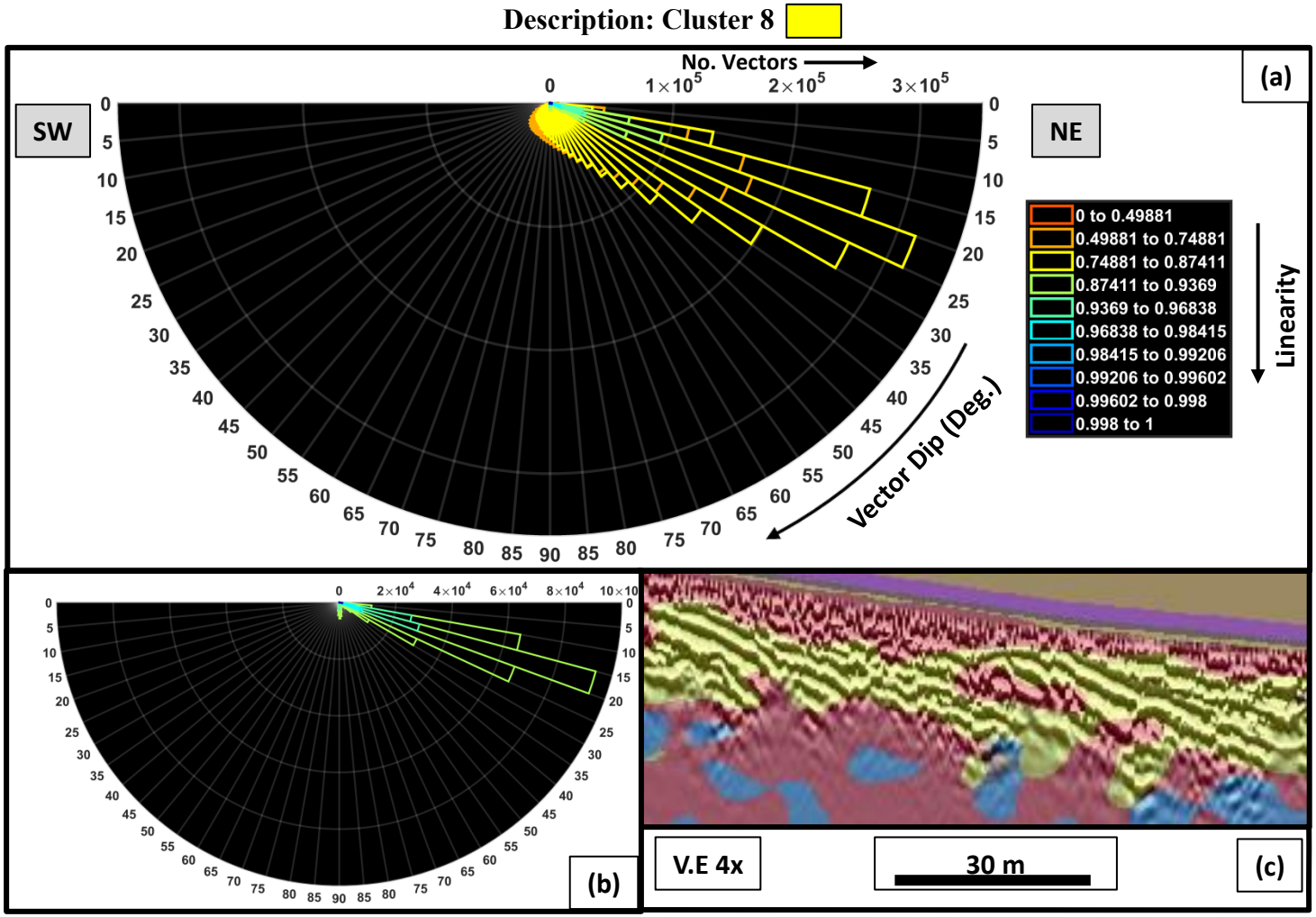

Figure 85: Dip-histogram of vectors in cluster 8 along with example of cluster 8 from Figure 65. **(a)** Linearity colored dip-histogram of vectors in cluster 8. **(b)** Dip-histogram with only linearities ≥ 0.87 displayed. **(c)** Example of cluster 8 features.

The description of the clusters in this section has focused only on the characteristics of the clustering assignments as related to the GPR reflections. Clustering assignments made in the region below the depth of investigation predominantly reflects the geometries of migration artifacts. The low-linearities of such vectors, as mentioned previously, made them less significant in the clustering assignments (per Equation (49)).

6.1.2 Radar Facies

From the previous results of the k-means clustering, the clusters that are associated with the informative parts of the GPR image, i.e. radar reflections (specifically clusters 3, 4, 5, 6 and 8) can be used to describe a set of radar facies [*Neal*, 2004]. However, it must be noted that the clustering assignments do not completely determine radar facies. Some reflections with multiple orientations along their length are observed to span multiple clustering assignments. It is therefore important to also use amplitude information and relationships between reflections to define radar facies. With these considerations, six radar facies, labeled R1-R6, were identified. A summary list of these radar facies is shown in Table 6. Descriptions of the various facies include information about reflection dip, amplitude, shape, and relationships between reflections. Reflection shape and relationships between reflections are described using terminology from seismic stratigraphic analysis [*Mitchum et al.*, 1977; *Vail*, 1987].

Radar Facies Summary

Facies	Description	Primary Clusters	Associated Clusters	Example
R1	Parallel to sub-parallel hummocky reflections with high amplitudes. Generally continuous with dips 0 -15˚ to SW.	3,4 and 8	5	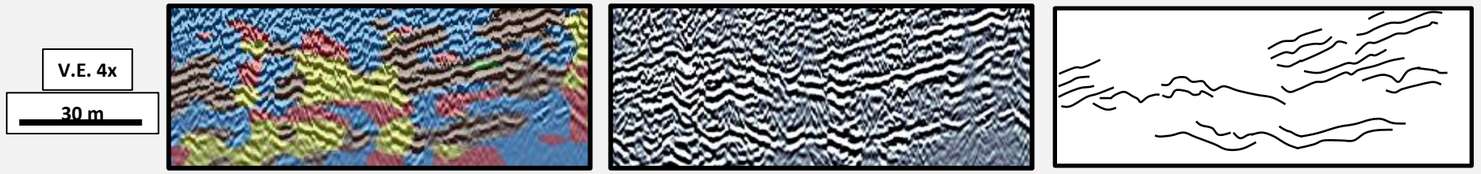
R2	High angle (20-40˚ to SW), narrow subparallel to divergent reflections. High amplitude. Sometimes with lower amplitudes and less continuity.	4	5	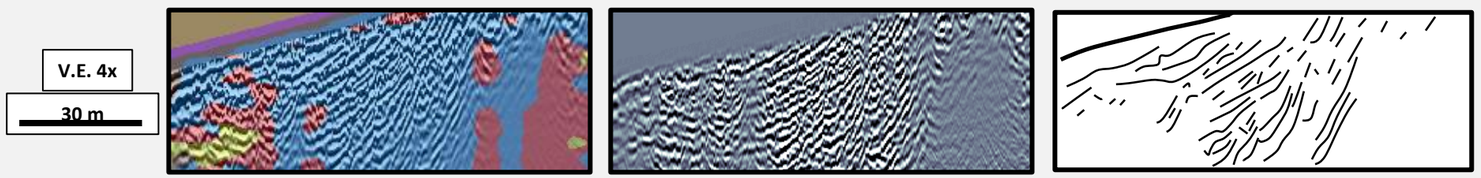
R3	High angle (25-45˚ to NE), frequently discontinuous, with moderate amplitudes. Local regions display more chaotic shapes.	5	4	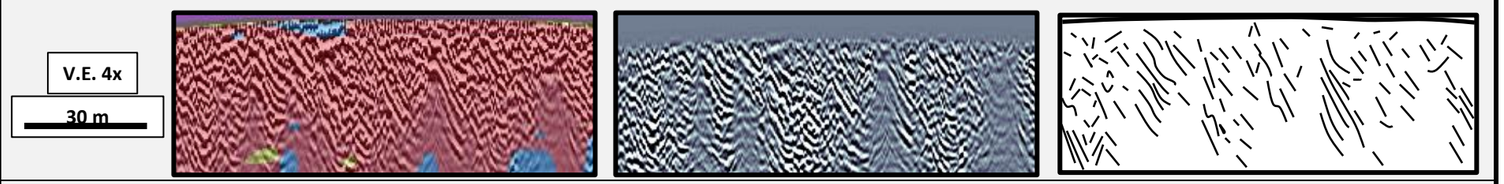
R4	Sigmoidal and subparallel reflections, having very high amplitudes. Sometimes showing offlap patterns. Generally continuous with dips 5-25˚ to NE.	8 and 5	3	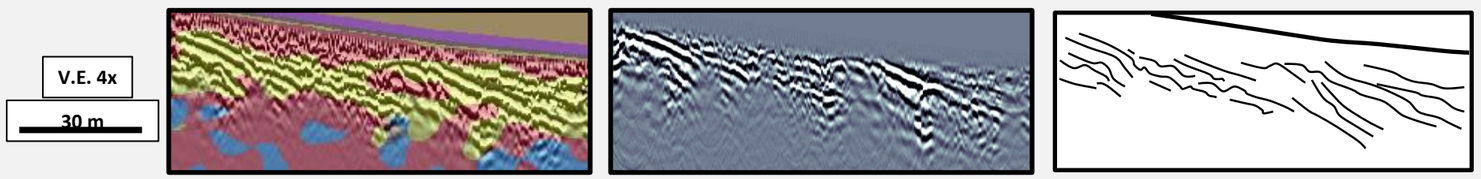

Table 6: Radar facies summary. Descriptions of each of the four radar facies identified in the cross island transect along with the clusters that define the geometries of the facies. Also, examples are shown of the clustering results, power-law gained radar amplitudes, and resulting line-drawing for each of the radar facies types.

Facies	Description	Primary Clusters	Associated Clusters	Example
R5	Near-horizontal (0-15˚) parallel to subparallel reflections. Generally very high amplitude and laterally continuous.	6,3, and 8	None	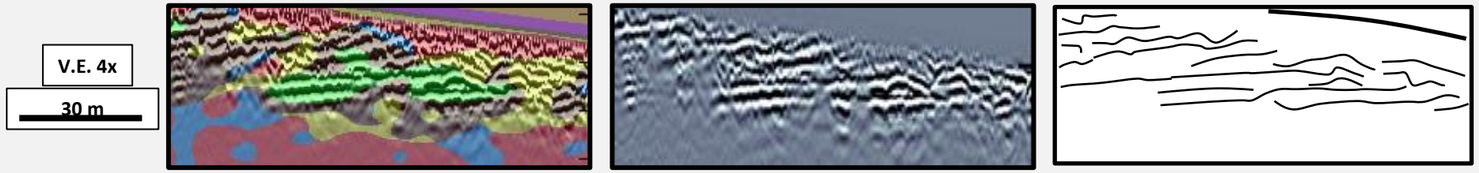
R6	Highly discontinuous high angle (>45˚) reflections. Parallel to subparallel at very local scales, bordering on chaotic. Typically have low to moderate amplitudes	4 and 5	None	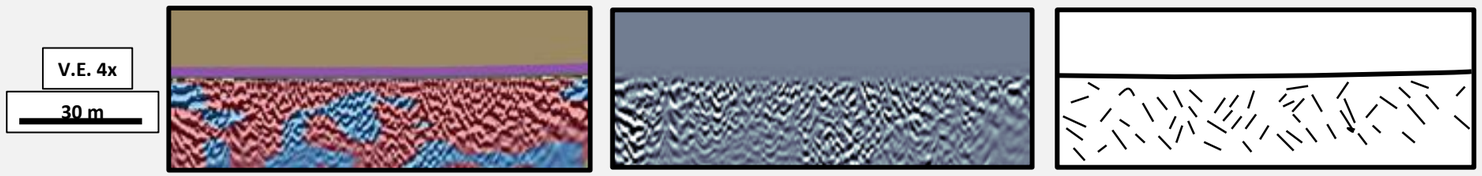

Table 6: Continued.

R1 Description: The reflections in this radar facies are largely shallowly dipping to the southwest with dips between 0-20˚. Reflection shapes are typically parallel to subparallel with small scale hummocky irregularities. The more continuous reflections in this facies are generally broad in width and have high amplitude. R1 is primarily characterized by clusters 3, 4, and 8 from the *k*-means clustering. Reflections with low-angle (<10 degrees) southwest dips are classified by cluster 3, areas of flat to northeast dips, are classified by cluster 8, and the more complex areas with locally steep dips are classified by cluster 4. Within these, small patches of complex reflections showing steep northeast dips are classified by the cluster 5. This cluster is deemed an "associated" cluster because it often occurs within the radar facies as a minor constituent of isolated features.

R2 Description: R2 contains reflections that are more steeply dipping to the southwest than those in R1. From the *k*-means clustering results, R2 contains primarily the more continuous reflectors classified by cluster 4. Dips of these reflectors range from 20-40˚ as observed in Figure 81. Reflectors are typically narrow, with high amplitudes, and reflection patterns are mostly subparallel to oblique. Small patches of discontinuous reflections with southwest dips classified by cluster 5 also exist within this facies. These more complex regions usually have comparatively lower amplitudes.

R3 Description: This radar facies characterizes reflections that dip steeply to the northeast (25-45˚). Reflections are narrow and generally high amplitude in R3, as in R2. However, features in R3 are significantly more discontinuous than those in R2, with a

larger fraction of complex regions. The more continuous reflections associated with cluster 5 from the *k*-means classification make up the majority of R3. Yet similarly to R2, isolated patches of low amplitude reflectors with opposing dips to the southwest (classified by cluster 4) also occur within this facies.

R4 Description: R4 consists of laterally continuous reflections that dip gently to the northeast. These reflectors typically exhibit sigmoidal to sub-parallel patterns, with some reflectors showing a progradational patterns as well. This facies is mainly classified by cluster 8 in the cross-island transect. Where reflectors in this facies are nearly flat lying or dipping slightly southwest, these portions are classified by cluster 3, and where reflections become more discontinuous and complex, these areas are classified by cluster 5. Local-scale reflector character is irregular and hummocky like R1, and reflection width is broader than either R2 or R3.

R5 Description: This radar facies is composed of horizontal to sub-horizontal reflections (dips no greater than 10 degrees). Patterns are generally parallel to subparallel, and amplitudes are high compared to surrounding reflections. As the dips for this facies are near horizontal, classification by clusters 3, 6, and 8 occurs as each of these clusters classifies some portion of horizontal or near-horizontal dips. Similarly to other shallowly dipping reflections (such as those in radar facies R1 and R4) the reflections in R5 have broad widths.

R6 Description: This facies describes highly discontinuous groups of reflectors. Dips of these reflectors are very high compared to other facies (often greater than 45 degrees), and therefore are classified by either cluster 4 or 5 depending if dips are either toward the southwest or northeast. Reflectors in this facies are parallel to subparallel at scales of less than 5 m, but appear chaotically organized at larger scales. This facies tends to be low to moderate in amplitude, as observed by the power-law gained example of reflectors in this facies from Table 6.

To facilitate geological interpretation of the radar data, facies R1-R6 were mapped along the cross-island transect. Figures 86-89 show the distribution of these facies at four locations along the line which provide representative examples for the spatial distribution and geometry of the various radar facies.

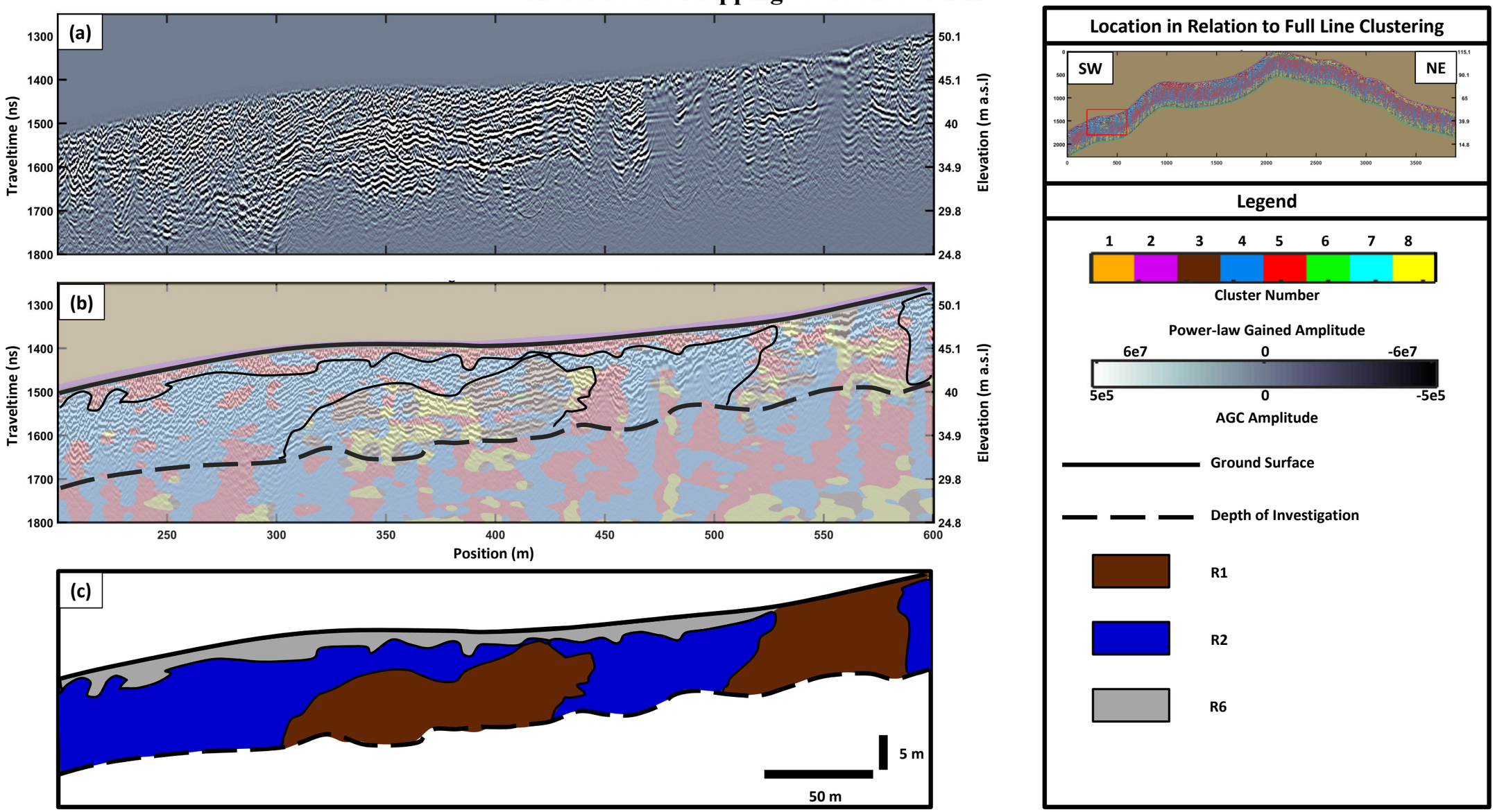

Figure 86: Radar facies mapping x=200.2-600.2 m. **(a)** Power-law gained GPR section. **(b)** Clustering results with facies boundaries outlined. **(c)** Cross-section showing radar facies distribution.

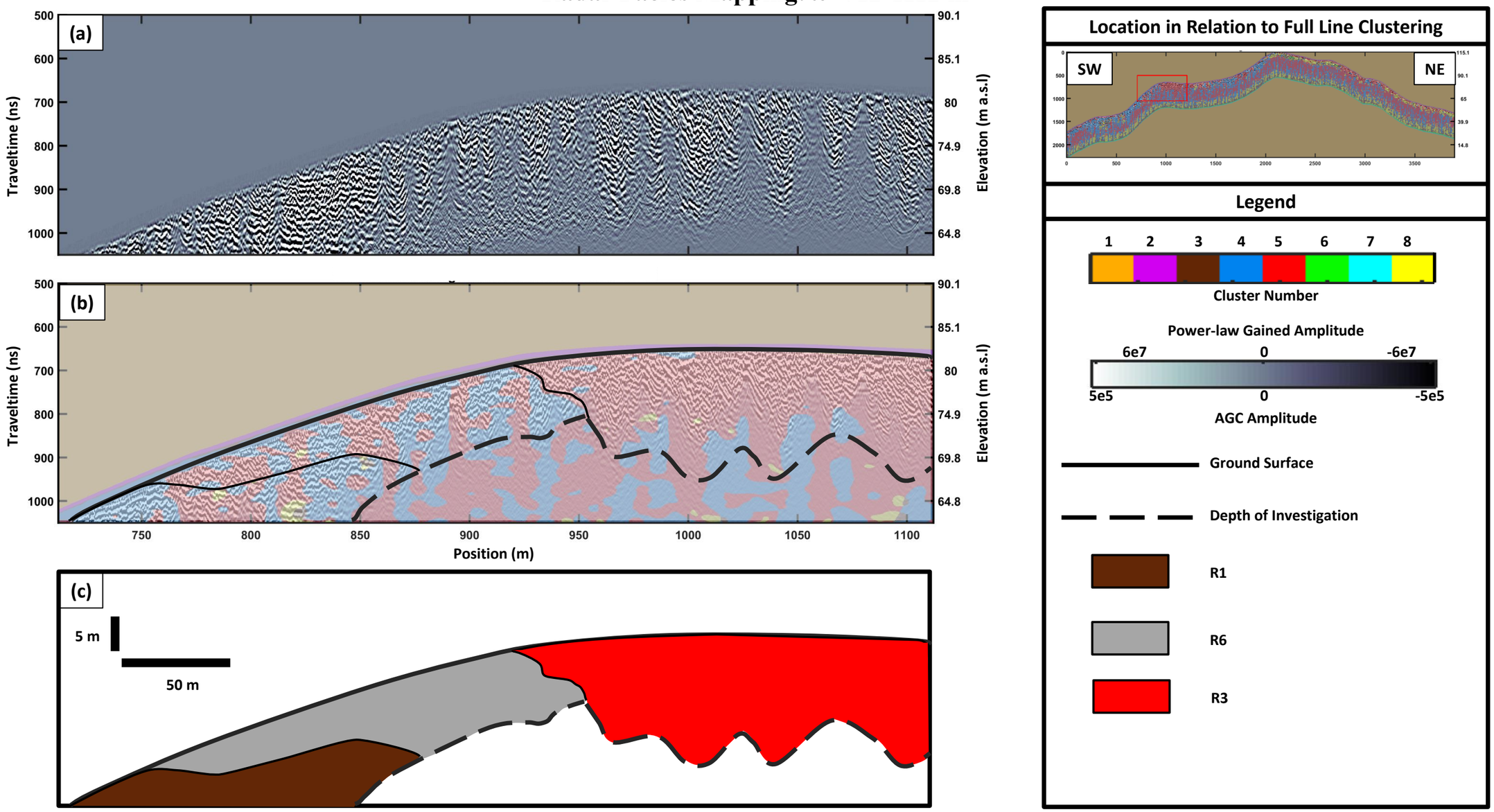

Figure 87: Radar facies mapping x=712-1112 m. **(a)** Power-law gained GPR section. **(b)** Clustering results with facies boundaries outlined. **(c)** Cross-section showing radar facies distribution.

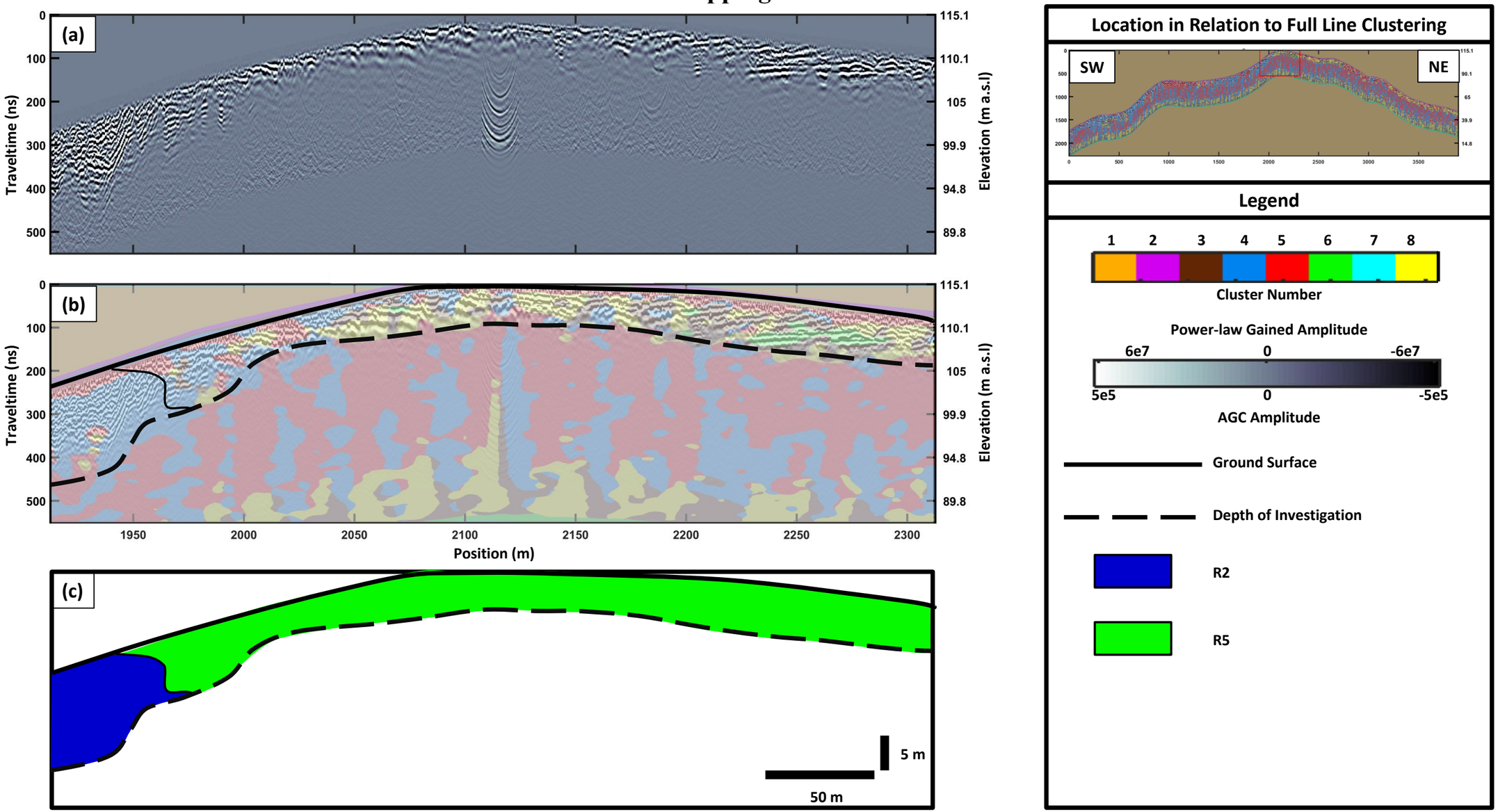

Figure 88: Radar facies mapping x=1912.6-2312.6 m. **(a)** Power-law gained GPR section. **(b)** Clustering results with facies boundaries outlined. **(c)** Cross-section showing radar facies distribution.

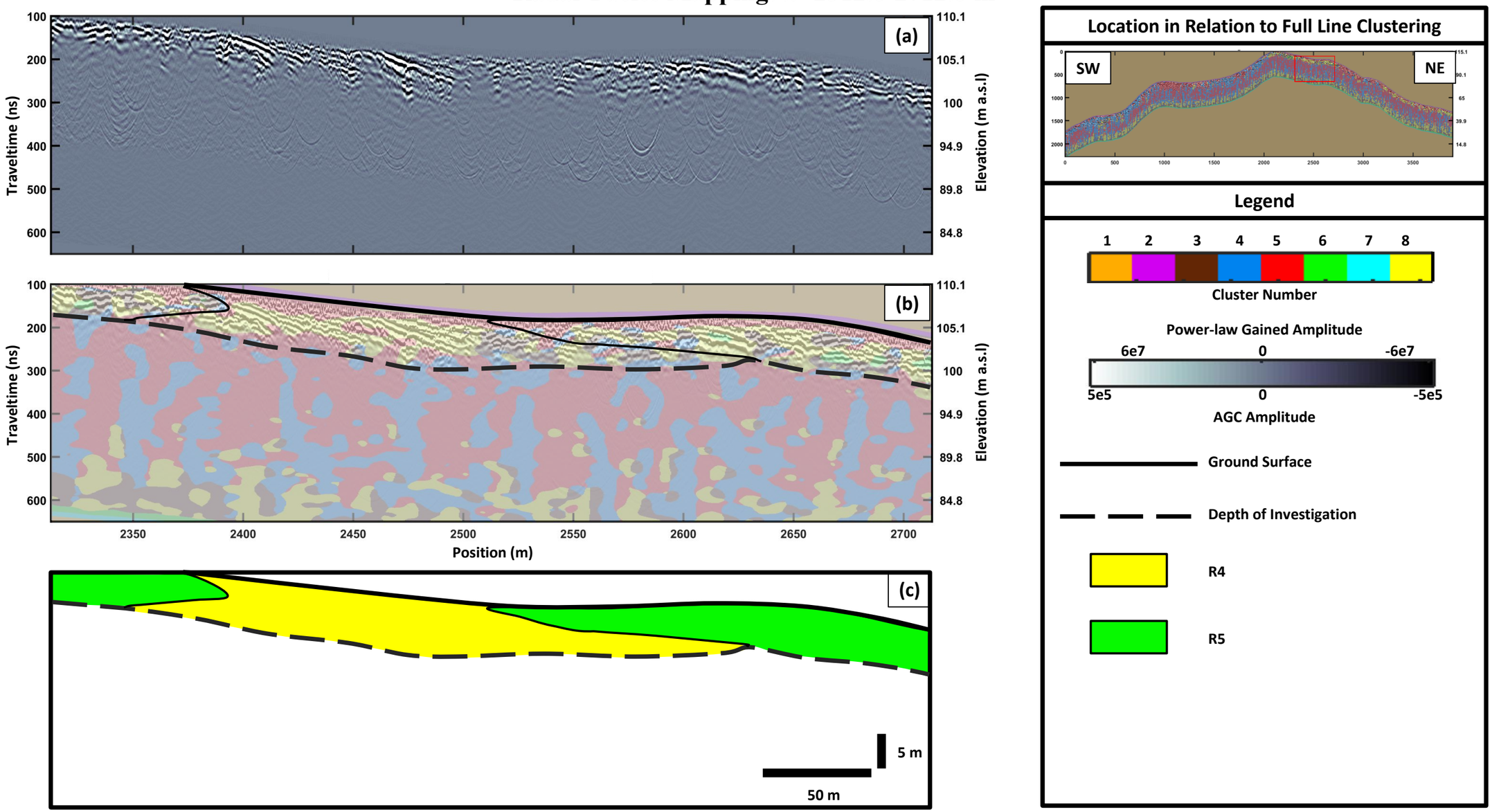

Figure 89: Radar facies mapping x=2312.8-2712.8 m. **(a)** Power-law gained GPR section. **(b)** Clustering results with facies boundaries outlined. **(c)** Cross-section showing radar facies distribution.

Using the previous descriptions of the radar faces and the mapping of these facies across the transect (Figures 86-89), interpretations of the geologic basis for each of the radar facies were made as follows:

R1 Interpretation: R1 was observed to exclusively occur on southwest portion of the transect. R1 occurs discontinuously and interspaced with steeper reflectors associated with R2. The low-angle parallel to subparallel orientations of reflections in R1 suggests sediments deposited in relatively low-energy environments, such as those dominated by subtidal currents below the storm wave base [*Lucia*, 2007]. These low-energy environments have been observed to be dominated by calcareous muds and occur on leeward sides of carbonate platforms [*Lucia*, 2007].

R2 Interpretation: R2 also occurs on the southwest portion of the cross-island transect. The higher angle of the reflectors in R2 compared to R1 implies that the sediments, whose internal discontinuities between beds cause the GPR reflections observed here, were deposited in higher energy environments, such as southwest facing shoreface to foreshore slopes that were subject wave action [*Lucia*, 2007]. Similar radar patterns were observed by *Jorry and Biévre*, [2011] in work done in the Paris basin where the patterns were attributed to bioclastic packstone/grainstone progradational units. A similar interpretation of interpretation of R2 here correlates well with surface geology observations by [*Sulaica*, 2015], where grainstone/packstone sediments were mapped along the far southwest portion of the bike trail.

R3 Interpretation: R3 is found in a wide continuous section at ~1000 m along the cross island transect, and also at a smaller section at ~2000 m. Similarly to R2, the high angle reflections in R3 suggest sediments deposited in higher-energy conditions. However, the reflectors are more discontinuous than those in R2 and therefore likely do not represent analogous northeast shoreface to foreshore deposits. Reflector geometries similar to those in R3 were observed and interpreted in work by *Asprion and Aigner,* [2000] to occur adjacent to carbonate mound buildups. The attribution of R3 to similar buildup-flanking deposits along the bike trail of Bonaire may account for the short and discontinuous nature of the reflectors in this facies.

R4 Interpretation: This radar facies occurs on the northeast side of the cross-island transect in relatively continuous segments between 2300-3900 m along the line. The sigmoidal shapes of the reflectors in R4 are characteristic of clinoforms created from outer-shelf and slope deposits [*Lucia*, 2007]. These geometries have been observed at multiple locations on the island. A comparison of R4 in the cross-island transect to interpreted clinoforms at an outcrop north of the bike trail is shown in Figure 90.

R4 Compared to Outcrop Observations

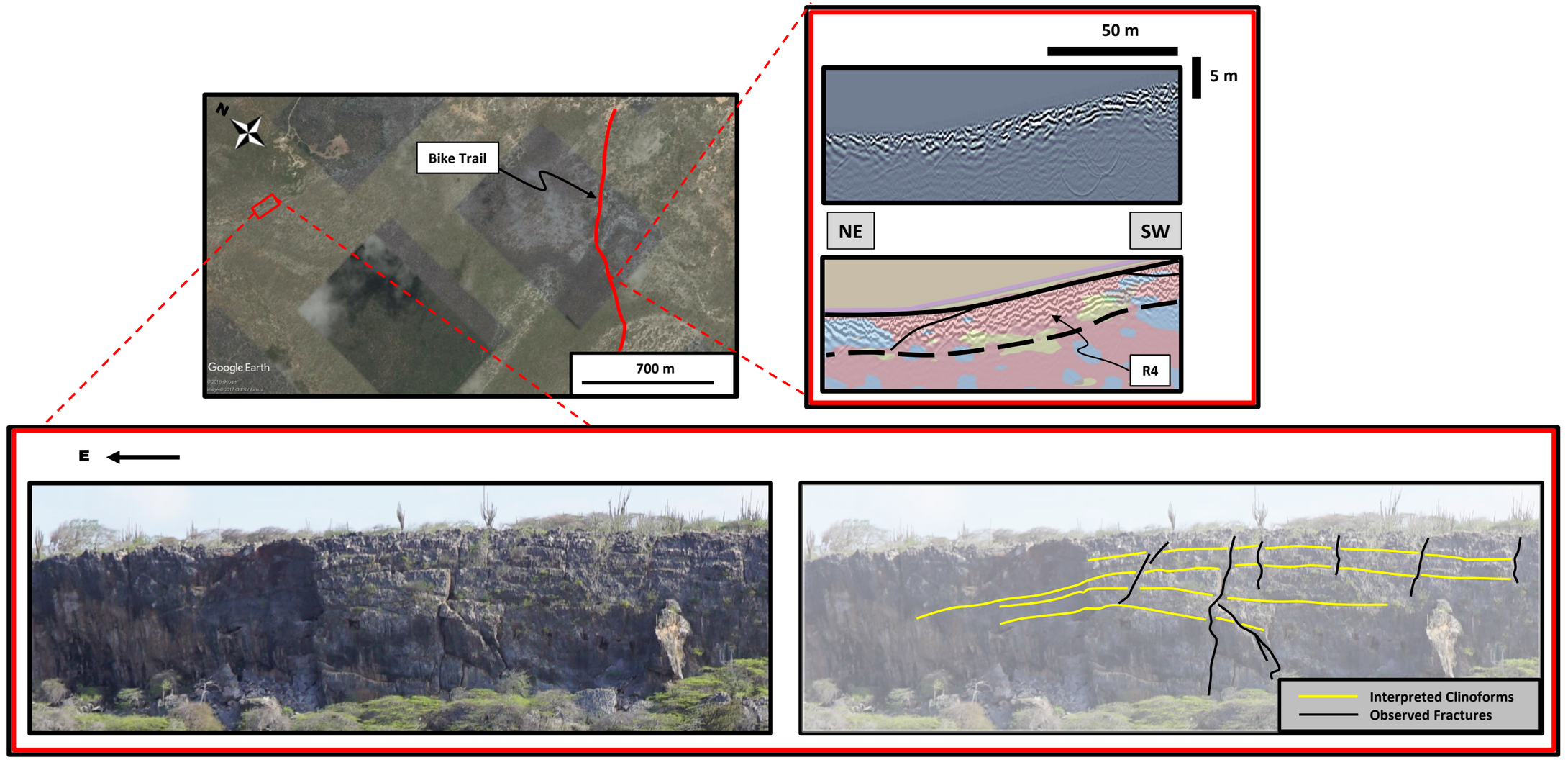

Figure 90: R4 compared to outcrop observations. **(top right)** Interpretation of R4 along northeast side of cross island transect. **(bottom)** Interpreted clinoform geometries in drone-based outcrop photo as well as observed fractures. **(top left)** Map showing location of Bonaire bike trail and respective locations for GPR segment and outcrop photo.

The geometries of the clinoforms (yellow lines) interpreted from a previously acquired drone-based outcrop photo (Figure 90 bottom) compare well with those contained in R4. In addition, near-vertical fractures cross-cutting clinoform traces were observed, as shown in the outcrop photo (black lines). If similar fracture styles occur in the subsurface along the bike trail, it would account for the sometimes discontinuous nature of R4. These discontinuities in reflector shape produce gradients in the GPR image that are strong and are often oriented vertical or near vertical, causing which classification by cluster 5 in the *k*-means clustering.

R5 interpretation: R5 occurs at two locations (shown in Figure 88 and Figure 89) at the top of the cross island transect, with this facies essentially "capping" the top of the bike trail. The low-angle reflections of R5 seem to suggest low-energy environments of deposition; however, *Sulaica* [2015] has mapped eolianite deposits at the same locations where R5 are found in the GPR data. These deposits are described as containing high angle cross-bedding derived from windblown sediments [*de Buisonjé*, 1974], thereby defining a high energy environment of deposition. Given that the estimated vertical resolution for the GPR data in the cross-transect is on the order of tens of cm, it is likely that individual high-angle foresets within these fine-grained sediments are too small to be resolved. Instead, what is likely being imaged are the lower-order bounding surfaces within sediment packages that have much shallower dips [*Brookfield*, 1977], resulting in the low-angle character of R5.

R6 Interpretation: The high angle, discontinuous to chaotic reflections observed in R6 are not readily attributable to specific aspects of carbonate platform geology. Meteoric weathering is the major cause of the karst on Bonaire as rainwater causes dissolution of the minerals comprising the limestones, leaving voids and other near-surface irregularities. These irregularities cause scattering of EM waves, which result in complex radar returns being recorded. It is therefore interpreted that the reflections characterizing R6 represent local regions where karstification is significant, and obscures interpretation of original depositional environments.

6.1.3 Synthesis and Implications

Figure 91 below shows a generalized radar facies map across the entire cross-island transect. This cross-section summarizes the information derived from the interpreted radar facies, and also includes locations and corresponding lithologies of hand-drilled core samples previously collected along the bike trail [*Sulaica*, 2015].

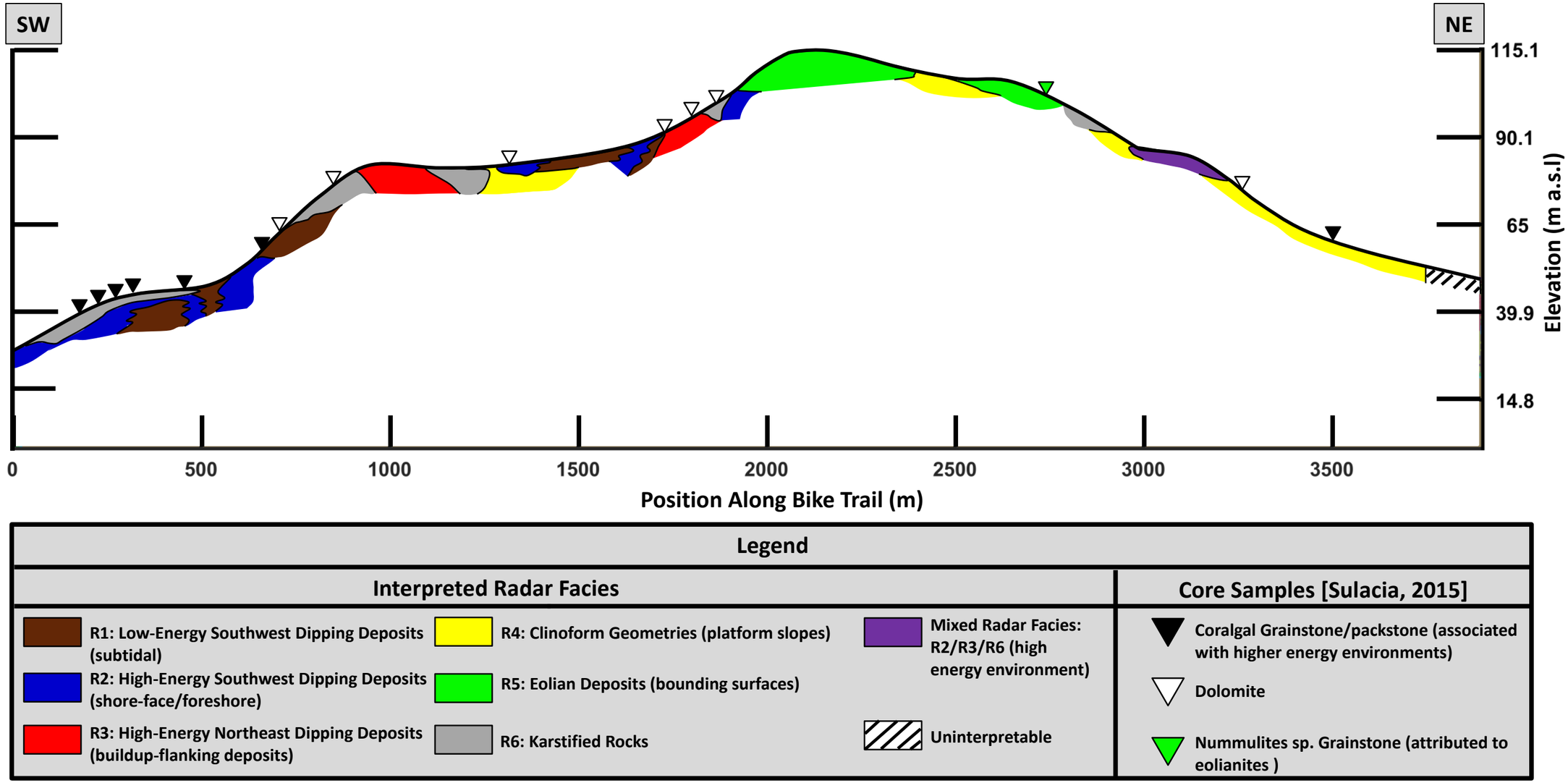

Figure 91: Interpreted cross-island transect. Mapping of radar faces with locations of previously collected [*Sulaica*, 2015] core samples down in colored triangles.

The above interpretations lead to several important observations and conclusions relating to the geology along the Bonaire bike trail:

(1) Figure 91 displays multiple regions showing transitions between low-and high energy southwest dipping deposits mapped as R1 and R2 respectfully. These occur on the southwest portion of the transect between 0 and 800 m. These alternating packages may represent depositional responses to sea-level fluctuations causing shoreface deposits to migrate either landward or seaward [*Lucia*, 2007]. The interpretations of R2 are supported by observations of coralgal grainstone/packstones occurring at similar locations along the bike trail which were attributed to high-energy deposits by *Sulaica* [2015].

(2) The occurrence of the large body of high-angle northeast dipping deposits mapped as R3 at ~1000 m in Figure 91 accompanied by lower angle deposits between 1000-1200 m suggests a carbonate buildup (now masked by the karstification interpreted by R6 at 900-1000 m) with flanking deposits (those mapped as R3) transitioning into a low-energy lagoon (regions mapped as R4 and R1). Observations of dolomitized rocks occurring at these locations [*Sulaica*, 2015] (white triangles Figure 91) support the idea of a lagoon where hypersaline waters may have contributed to dolomite creation [*Deffeyes et al.*, 1965].

(3) The interpreted eolianite deposits of R5 occurring along the bike trail are confined to the highest portions of the transect (2000-2700 m Figure 91). These observations match spatially with the occurrence of *Nummulites sp*. occurring in samples which *Sulaica* [2015] identified as being the primary grain constituent of the eolianite sediments identified by previous workers [*Bandoian and Murray*, 1974; *de Buisonjé*, 1974]. The GPR data and interpretation in Figure 91 serves to provide subsurface support for interpretations of these eolian derived sediments.

(4) The majority of the northwestern portion of the cross-island transect consist of radar facies R4, which has been interpreted here as slope deposits producing clinoform geometries. This mapping supports multiple observations of clinoforms occurring on the northern side of the island (Figure 90 and [*Laya et al.*, 2017]). These geometries are in contrast to the interpreted subtidal to shoreface transition sequences mapped in the southwestern portion of the cross-island transect, and imply differing controls on the structural evolution of the island between the northeast and southwest. In addition, a small section of mixed geometries containing facies R2, R3, and R6 is observed between 3000 m and 3200 m within the larger region of clinoforms. Here alternating patterns of southwest and northeast steep dipping deposits indicate a high-energy environment. The alternating orientations of reflectors observed at these locations (see Figures 74-75) may be due to remnants of carbonate buildups similar to those observed in GPR data by *Jorry and Biévre* [2011].

6.2 Seru Grandi

Interpretation for the Seru Grandi GPR data was focused on identifying and mapping features related to geometries associated with the two previously described sedimentary packages that comprise the outcrop. The general character of many of the reflections evident on the four GPR lines is complex and discontinuous with few spatially contiguous patterns or trends among reflections. Given this observation, reflection classification using the k-means clustering of structure-parallel vectors was not carried out on the Seru Grandi data. Furthermore, the Seri Grandi dataset covers a much smaller area compared to the cross-island transect, and as the survey lines encounter few changes in lithology, at such scales numerical image classification methods such as k-means clustering were not expected to provide a significant increase in confidence of interpretation compared to manual methods.

6.2.1 Reflection Observations and Two-Dimensional Mapping

Despite many of the reflections being complex, several relatively continuous and generally high-amplitude reflections were observed along the Seru Grandi lines. In particular, a distinct high-amplitude, east-dipping reflection was observed in Lines 1-3. This feature, along with other distinctive reflections were mapped on the power-law-gained Seru Grandi sections from Lines 1-3, as shown below.

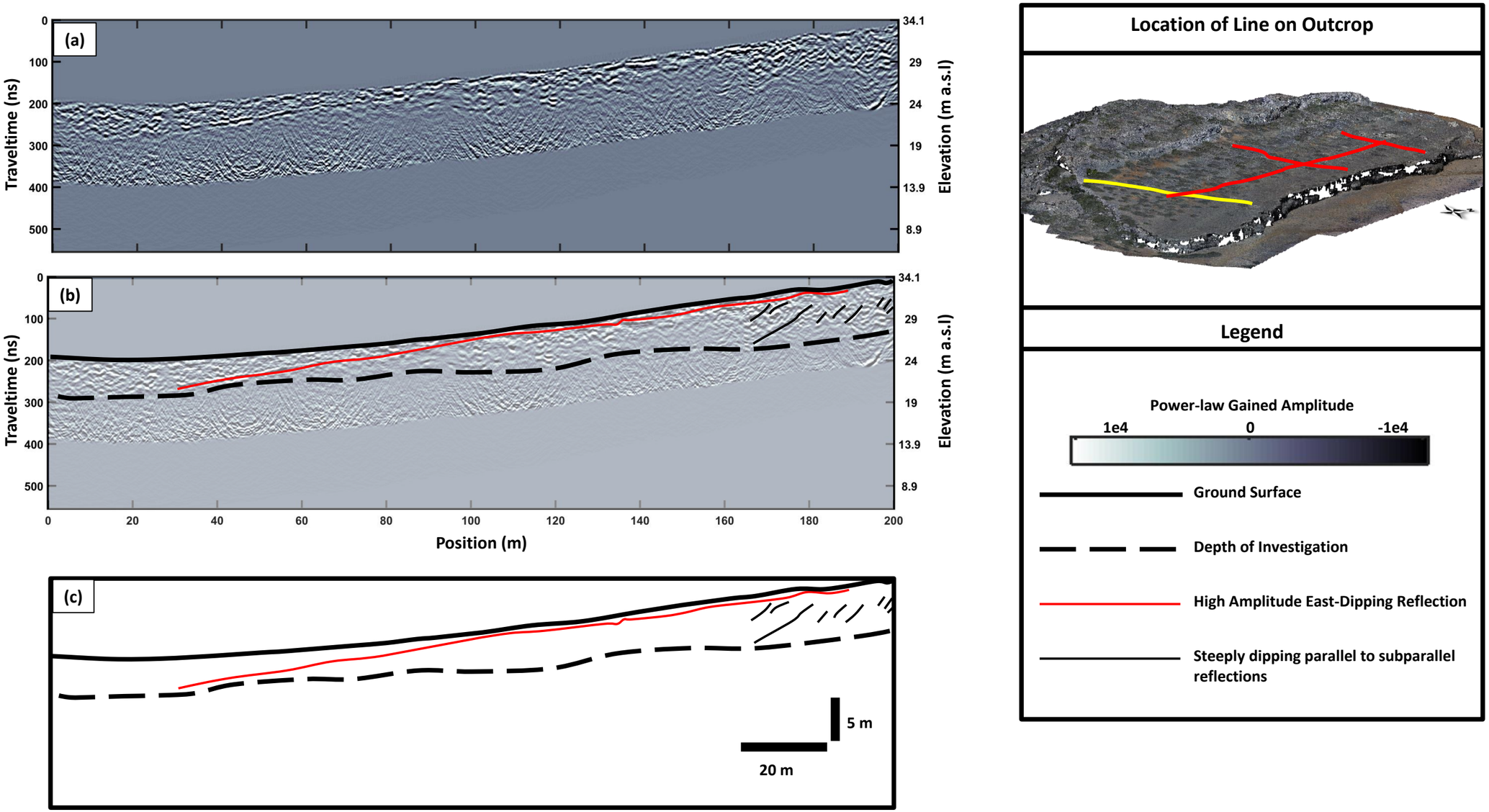

Figure 92: Reflection mapping Line 1. **(a)** Power- law gained Line 1. **(b)** Mapping overlay on GPR data. **(c)** Line-drawing showing observed reflection geometries.

Reflection Mapping Line 2

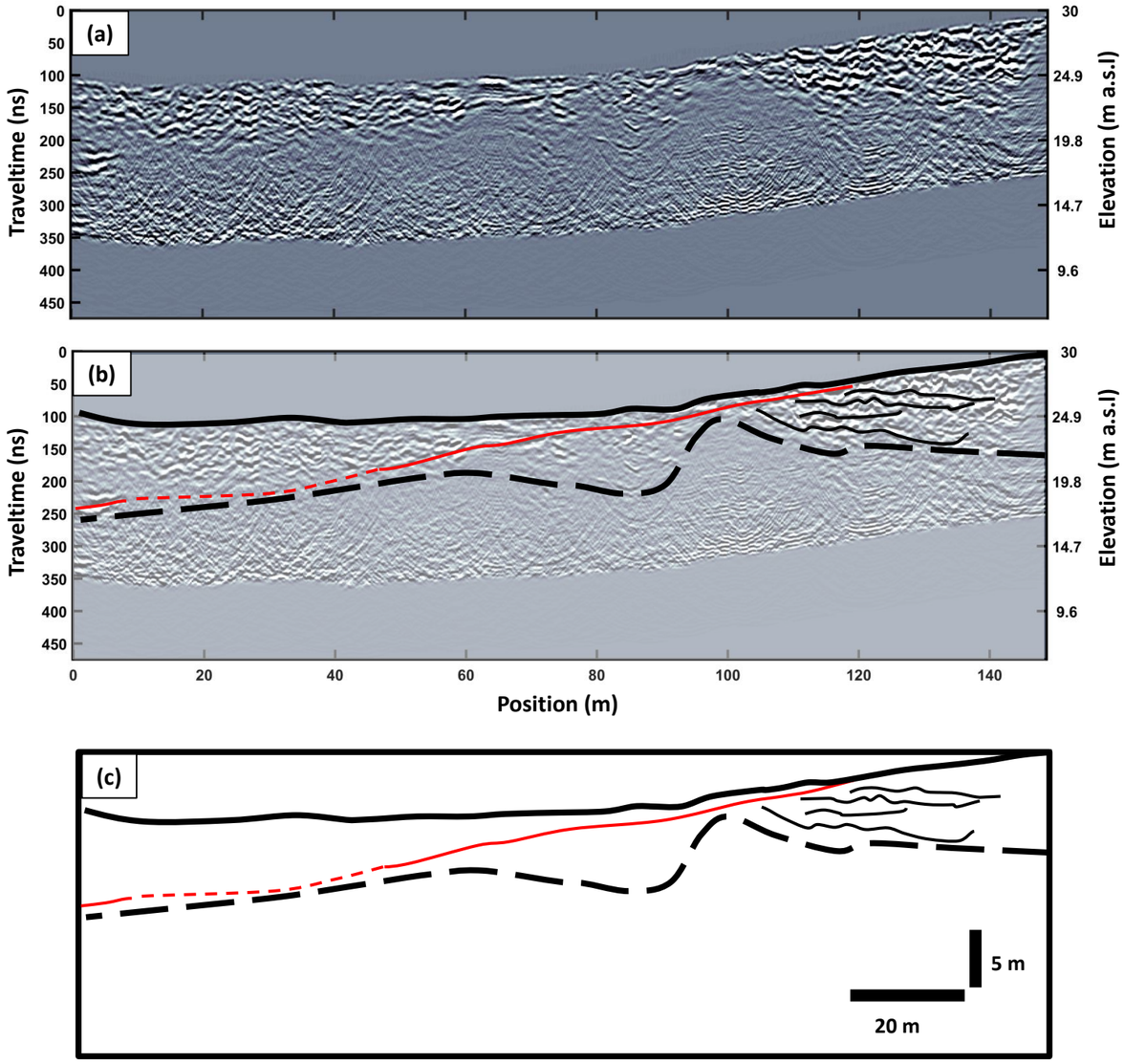

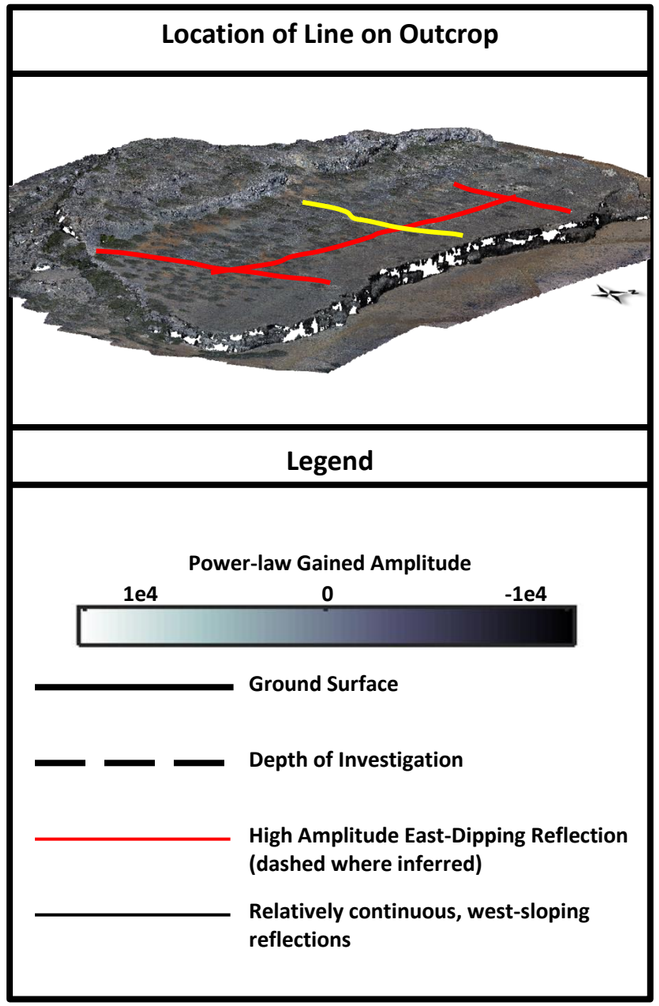

Figure 93: Reflection mapping Line 2. **(a)** Power- law gained Line 2. (b) Mapping overlay on GPR data. **(c)** Line-drawing showing observed reflection geometries.

Reflection Mapping Line 3

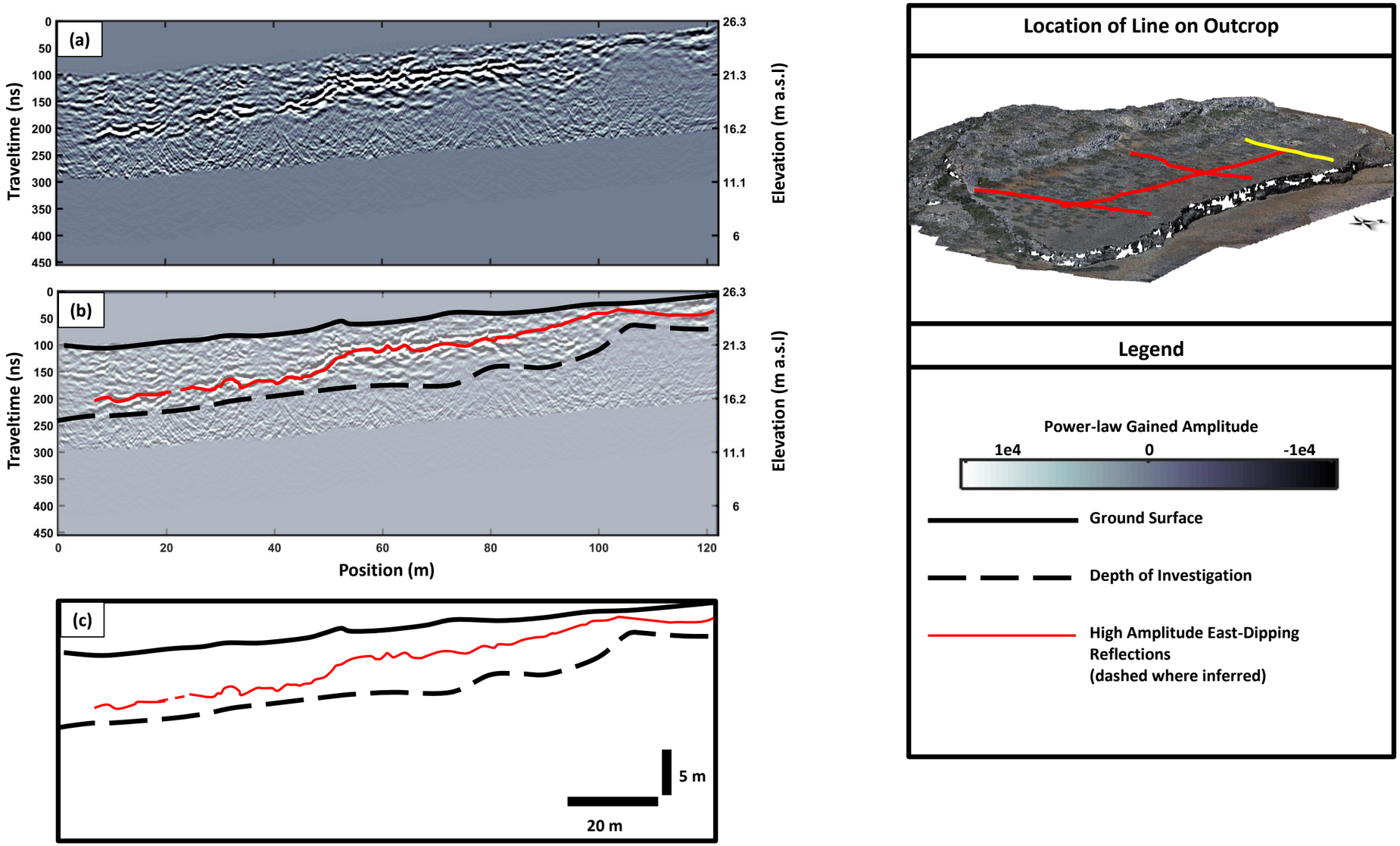

Figure 94: Reflection mapping Line 3. **(a)** Power- law gained Line 3. **(b)** Mapping overlay on GPR data. **(c)** Line-drawing showing observed reflection geometries.

The above-mentioned high-amplitude reflector was readily apparent in all three cliff-face-perpendicular lines as shown in Figure 92-94. It was detected in the very shallow near-surface or even at the ground surface in the higher topographic portions of the lines, and was seen to increase with depth at lower elevations in the transects. This variation in depth to the reflection occurs because its dip of is greater than that of the topographic surface. In both Line 1 and Line 2, the reflection was generally thin in width and linear in shape. However in Line 3, the reflection is broad in width and more irregular and contorted in shape. In addition, the highest amplitudes for this reflection were observed in Line 3.

The depth of investigation in Lines 1-3 can be seen to mimic the first-order shape of the east-dipping reflection. Interpretations of both Lines 1 and 2 show that penetration depths are the shallowest when the east-dipping reflection is closest to the ground surface. Penetration is observed to increase as the reflection deepens farther to the east or where the reflection comes into contact with the surface on the west-side of the lines.

Evidence of the previously described high-amplitude, east-dipping reflection was not immediately apparent in Line 4 (see Figure 95a). Given the observations of the dip of this reflection on the other lines, Line 4 should be aligned parallel to the strike of the reflector. Moreover, the consistent depths at which the reflection occurs in Lines 1-3 suggests little, if any, dip would be expected along the Line 4 direction. However, by

identifying locations where the reflection, as interpreted in Lines 1-3, intersected Line 4, an itermittent trace of the feature could be made as shown in Figure 95b.

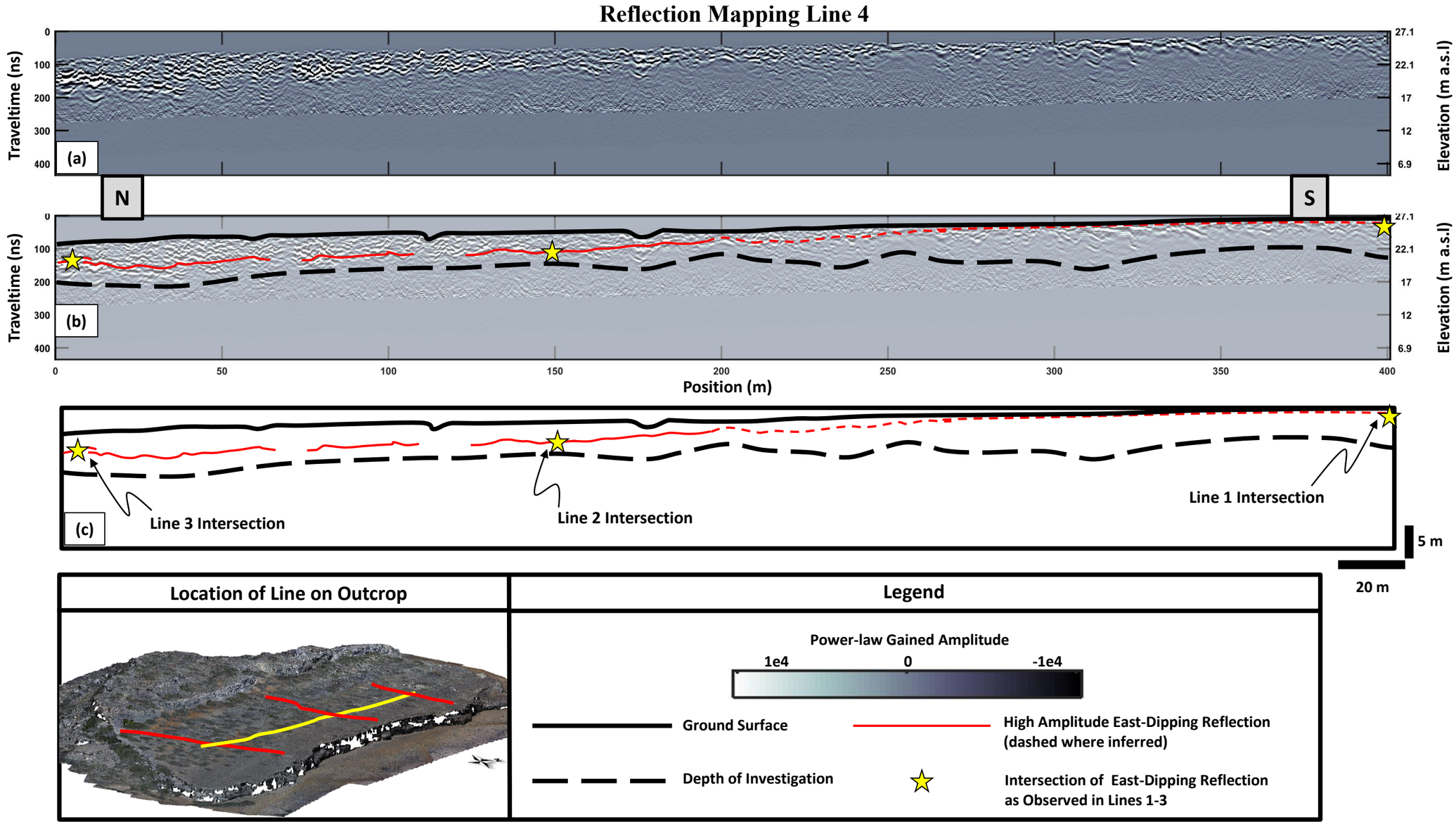

Figure 95: Reflection mapping Line 4. **(a)** Power- law gained Line 4. **(b)** Mapping overlay on GPR data. **(c)** Line-drawing showing observed reflection geometries.

The same high-amplitude, east-dipping continuous reflection observed in Lines 1-3 is shown to be more discontinuous in Line 4 (Figure 95). However, the relative amplitude changes along the reflection are more easily observable when viewed oblique to dip as in Line 4. On the far north side of the line, amplitudes are very high as is observed in Line 3, and when moving south, the amplitude of the observed reflection decreases. Also, the gentle incline of the mapped reflection in Figure 95 suggests that there is not only an east component to the reflection dip but a north component as well. Beginning at x=200m in Line 4, the depth of the high amplitude reflection becomes shallow and more difficult distinguish. This coupled with the observed depth at which the reflection in Line 1 intersects Line 4 motivates an indirect interpretation that the reflection lies very close to or at the Earth's surface from x=300 m to the end of Line 4.

In addition to the prominent northeast-dipping reflection observed in Lines 1-4, regions of more concordant reflections (as opposed to the pervasive discordant geometries) were observed along small sections of the lines. In the cliff-face perpendicular lines (1-3), parallel to sub-parallel reflections were observed at depth in the regions of higher topography. In Line 1 these reflections are discontinuous but they exhibit local patterns showing relatively steep eastward dips. In contrast, similar locations in Line 2 show more continuous reflections that dip shallowly to the southwest. Penetration depths for Line 3 in such higher relative topographies are very shallow and, as a consequence, few signals can be distinguished beyond 1 m depth. So, further observations of the reflection types readily seen in Lines 1 and 2 could not be made in Line 3.

At the southern end of Line 4, where the high amplitude reflection parallels the surface, other reflections that dip southward can be seen extending deeper into the section. Mapped observations of these geometries are shown in Figure 96 (yellow lines).

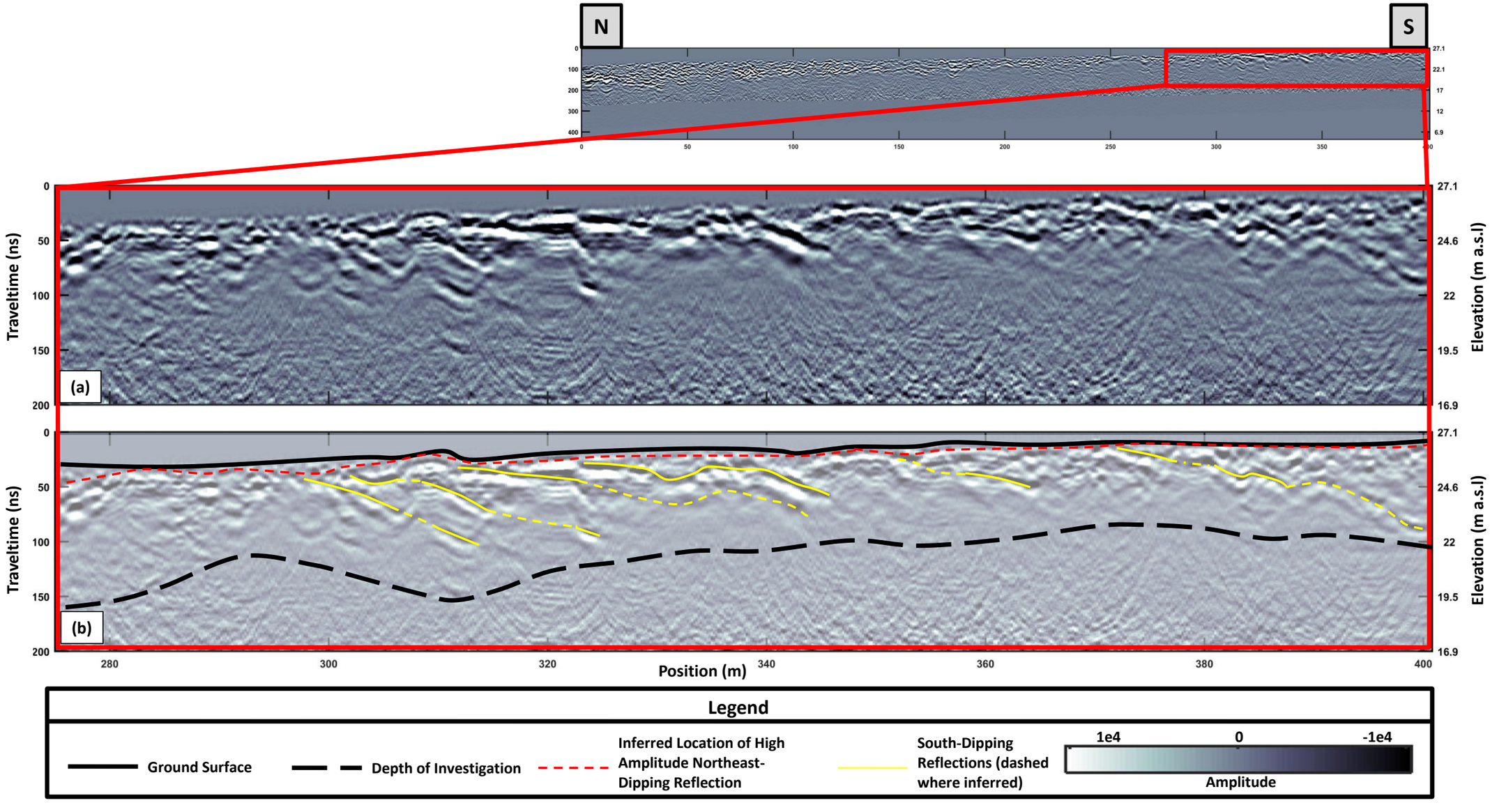

Figure 96: Observations of south-dipping reflections Line 4. Full Line 4 in top left showing location of close-up section. (a) Close-up section of south-end of Line 4. (b) Annotated observations of reflections.

The observed south-dipping reflections in Figure 96 have measured dips of 0-3˚ along their more flat lying portions and up to and 12˚ as they steepen to the south. Their geometry appears to be sigmoidal as they have a more horizontal character near the surface and then become steeper as the reflections extend deeper into the subsurface. Observations of the shape of these reflections at greater depths to determine if dips become more horizontal again, as would be expected for true sigmoidal shapes [*Mitchum Jr. et al.*, 1977; *Vail*, 1987], are limited by the depth of investigation at this location.

6.2.2 Reflection Interpretations

6.2.2.1 High Amplitude Northeast-Dipping Reflection

The distinctive high amplitude reflection that is shown to dip shallowly to the northeast in Lines 1-4 was interpreted to be the unconformable contact between the upper and lower carbonate packages comprising the 2nd terrace strata (Figure 9). In outcrop this contact is clearly evident and has been previously mapped by *Laya et al.* [2015] (Figure 97a). The outcrop observations of the unconformity correlate well with the subsurface mapping of the high-amplitude northeast-dipping reflections, as shown in Figure 97b.

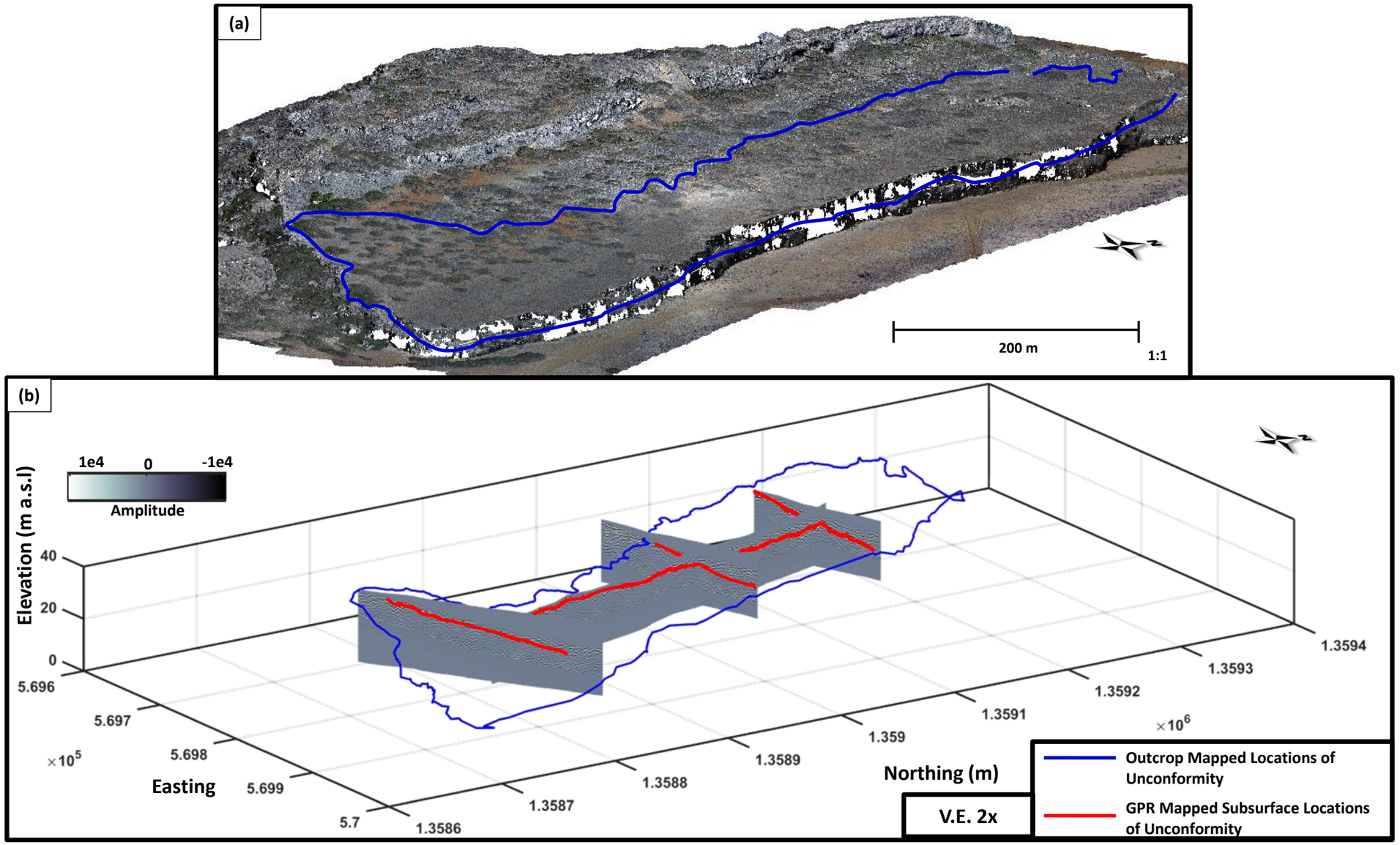

Figure 97: Outcrop versus GPR observations of unconformity. **(a)** Previously mapped unconformity contact overlain on digital outcrop model. **(b)** GPR lines 1-4 showing unconformity mapping in relation to outcrop.

This correlation provides strong evidence for the observed continuous GRP reflection being the signature of the unconformity (Figure 97b). Given this assertion, the high amplitude of the reflection could be due to the unconformity being manifest as an air-filled boundary in the subsurface. *Sulaica* [2015] describes the upper package in the Seru Grandi outcrop as consisting of coral boundstones and grainstones while the lower package consists of dolomitized rocks. This contrast in lithology may serve as a barrier to meteoric water flow, and waters that infiltrate into the upper package are forced to flow laterally along the unconformity once they reach its depth. This preferential pathway would likely cause increased dissolution and karstification along the unconformity. When no water is present, air filling the boundary between the packages would result in a strong reflection due to the contrast in dielectric permittivity between air and limestone (ε_r=1 for air and ε_r=4-8 for limestones [*Davis and Annan*, 1989]).

To better understand the three-dimensional subsurface geometries of the unconformity, a surface was gridded between the GPR interpretations and the outcrop-mapped contact. Figures 98-100 show this surface with elevation, dip, and dip direction respectively rendered by the color of the surface.

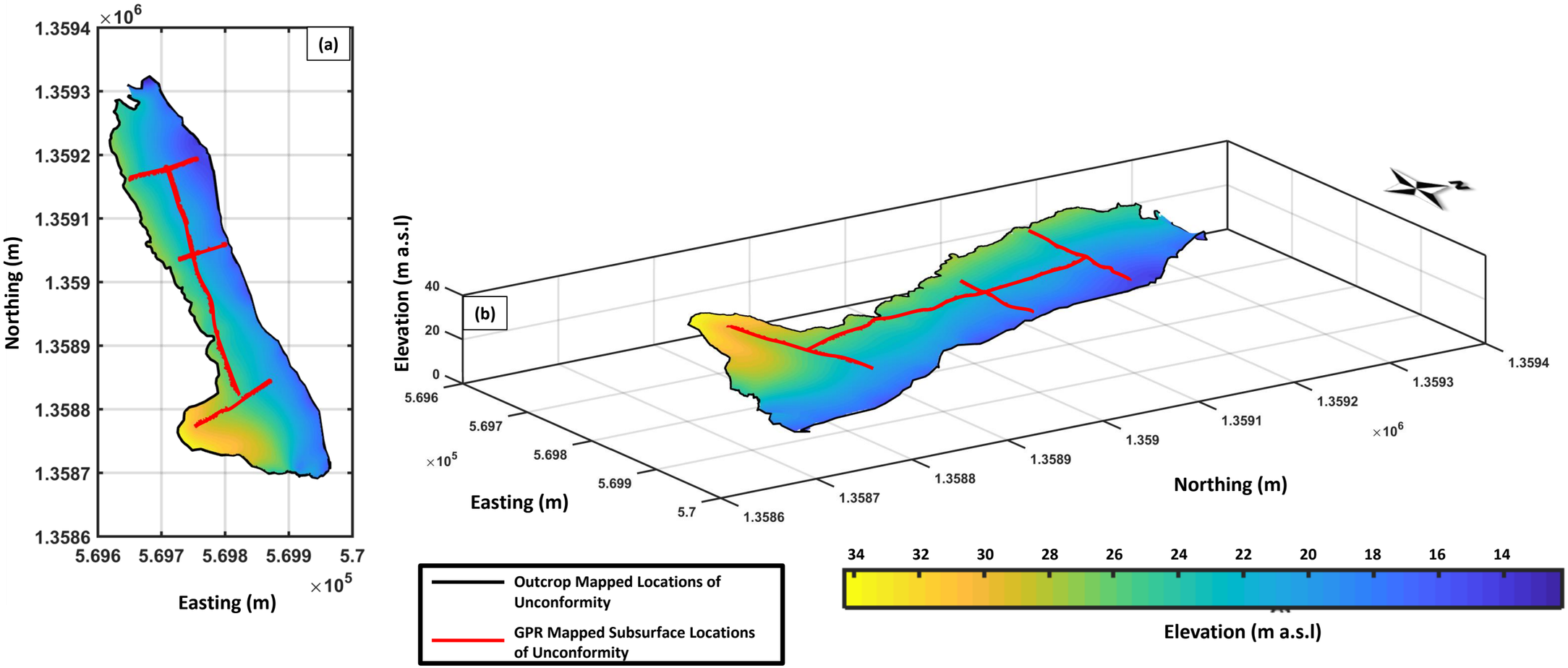

Figure 98: Interpreted surface of unconformity: elevation. Vertical exaggeration 2x. **(a)** Map view of surface. **(b)** Perspective view of surface.

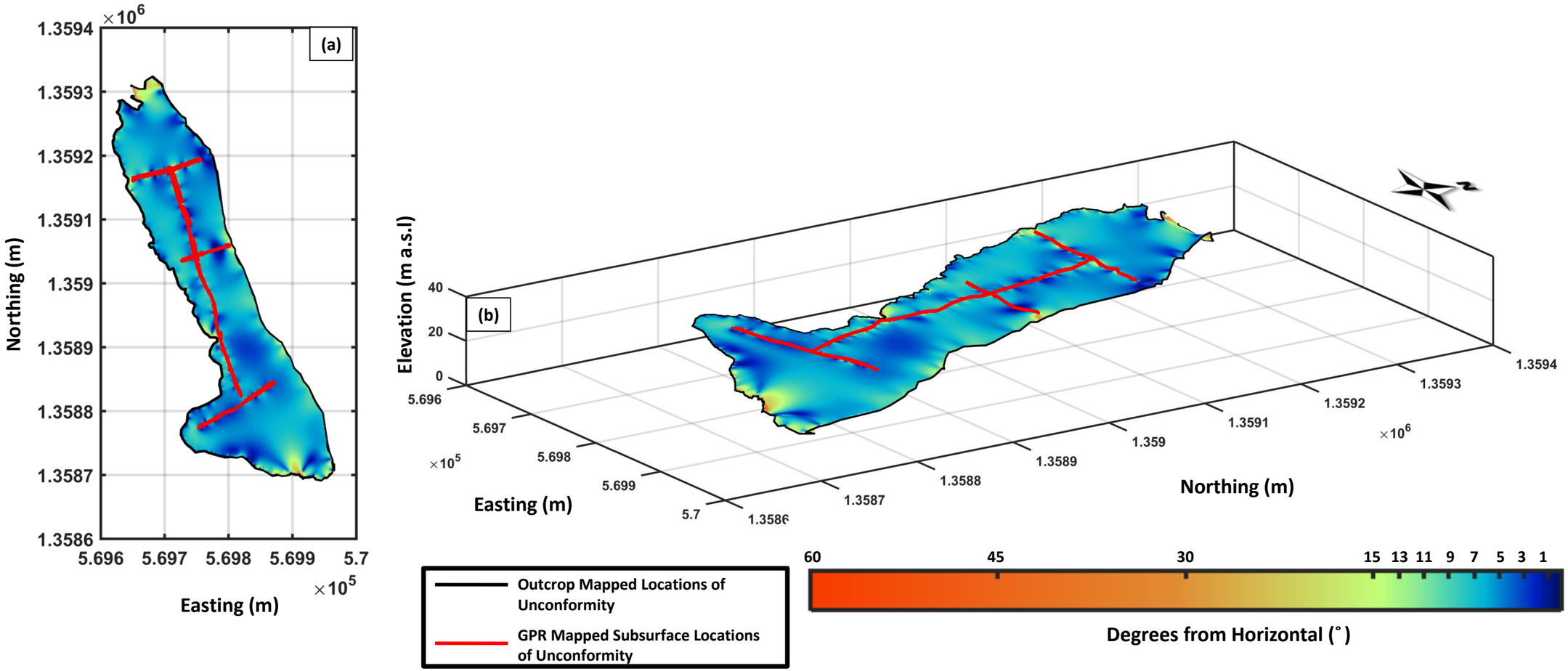

Figure 99: Interpreted surface of unconformity: dip. Vertical exaggeration 2x. **(a)** Map view of surface. **(b)** Perspective view of surface.

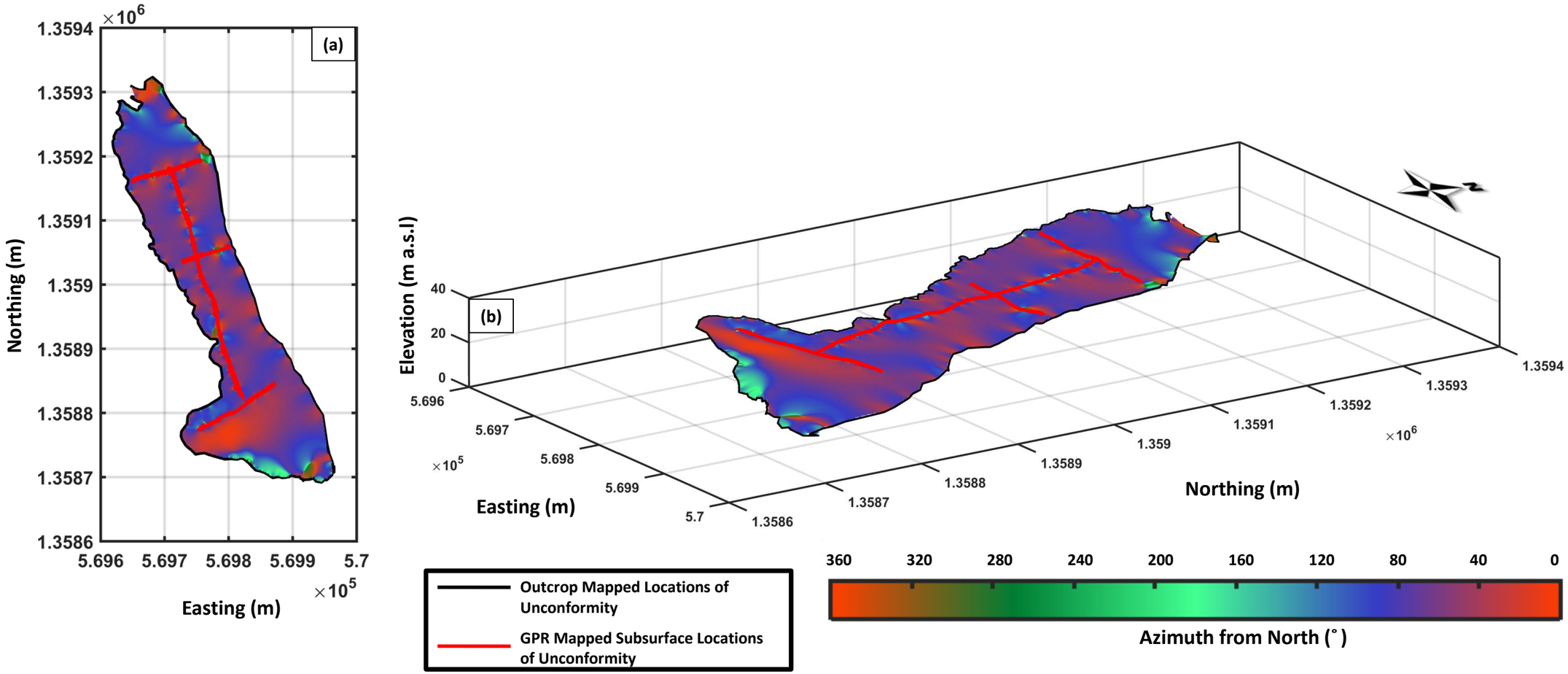

Figure 100: Interpreted surface of unconformity: dip direction. Vertical exaggeration 2x. **(a)** Map view of surface. **(b)** Perspective view of surface.

The maximum elevation of the interpreted unconformity is in the southeast at just over 34 m above sea level, and elevation decreases to the northeast were it is interpreted to be ~14 m a.s.l (Figure 98). In Figure 99, the dip of the contact is shown to be largely between 3-7˚. Local-scale irregularities of the unconformity as mapped in the GPR lines as well as the outcrop mapping can be seen have dips up to 13˚. There are some interpolation effects of the gridding algorithm that is used to connect the surface between the interpretations that produce unrealistic dips in the 30-60˚ range. However, these artifacts mainly occur near the edges of the gridded surface (example: southern end of surface in Figure 99b) and do not affect the general trends observed. The dip direction maps in Figure 100 show that the interpreted unconformity dips to the east-northeast with azimuths between 40-90˚ (strike between 310˚-360˚). Again, local heterogeneities observed in the GPR reflection interpretations and the outcrop mapping of the contact generate a wider range of dip directions. Similarly to the dip maps, artifacts of interpolation mainly occur near the edges of the dip-direction surface.

The geomorphology of the region surrounding Seru Grandi prominently displays wave cut platforms and cliffs. The presence of these features indicates that wave energy is the primary mechanism for erosion in the northern portion of the island [*Bandoian and Murray,* 1974]. In fact, studies have argued that in addition to daily wave bombardment, Bonaire may have been subject to a tsunami impact in the recent geologic past [*Engel and May,* 2012]. The front cliff-face of Seru Grandi itself is a wave-cut cliff with the top of the outcrop (where the GPR survey was performed) being a relict wave-cut platform

(Figure 97a). The approximate strike of this surface is 340˚ with a dip of ~2˚ as measured from the digital outcrop model (Figure 97a). The strike of the unconformity as interpreted from the GPR data nearly parallels the strike of the outcrop surface. Therefore, the unconformable surface may represent a past wave-cut platform that underwent submersion due to sea-level rise. This submersion would have allowed new corals to grow atop the old platform thus creating the observed upper-package sediments

However, as previously mentioned, the dip of the unconformity (3-7˚ on overage) is greater than that of the surface of acquisition (~2˚). If the unconformity in the subsurface represents a past wave-cut platform, this means that it had a gradient sloping towards the sea that was larger than the one that represents the top surface of the modern Seru Grandi outcrop. Work by *Trenhaile* [1987, 2000, 2005] on modeling and mapping wave-cut platforms of rocky coasts in describes many factors that affect the slope of the platforms, several of which are:

Spring tidal range: Larger ranges tend to produce wave-cut platforms with steeper gradients.

Timespan of erosion: The longer a platform is exposed to wave action the steeper the gradient of the platform will be.

Wave energy: Higher incident wave energies tend to produce platforms with less-steep gradients.

With the dip of the interpreted unconformity being larger than that of platform slope atop Seru Grandi, it can be inferred that one or more of the controls on platform gradient were different during the respective timeframes of their evolution. By understanding the differences in these controls, information about relative ocean conditions in the geologic past can be gained. However, GPR data alone does not provide information to further suggest which controls on wave-cut platform gradient can be attributed to the difference in slope. Further study would be required to make such distinctions.

6.2.2.2 Concordant Reflections in Lines 1 and 2

The parallel to sub-parallel east-dipping reflections seen in the higher elevations of Line 1 as well as the more gently west-dipping reflections seen at similar locations in Line 2 stand out in the section due to their relative continuity compared to many other observed reflections. The heavy karstification observed by the GPR survey is likely the cause for the discordant and chaotic nature of many reflections seen in the lines. This is due to high amounts of EM wave scattering. Yet, this level of karstification is observed only in the upper package of the 2nd terrace sediments at Seru Grandi. The concordant reflections seen in Line 1 and 2 exist below the interpreted unconformable contact between the upper and lower packages and therefore are inferred to reveal minimal karstification. Due to the limited extent of these reflectors that were identified in the

GPR data, confidence is low in further geologic interpretations. However, these reflections may be associated with barrier reef or coral buildup deposits within the lower package as they occur up-dip from the clinoform geometries that represent platform slopes [*Lucia*, 2007], which previous workers have observed at the cliff-face of Seru Grandi.

6.2.2.3 South Dipping Reflections at End of Line 4

The south-dipping reflections seen in Line 4 of the Seru Grandi GPR data appear below the high-amplitude reflection that has been interpreted as the unconformity between the upper and lower sediment packages. These south-dipping reflections were observed to have sigmoidal geometries with dips up to 12˚. Similar shapes have been observed at the cliff-face of Seru Grandi. These have been interpreted as clinoforms within the lower package [*Laya et al.*, 2015; *Sulacia et al.*, 2015]. Given that the south-dipping reflections in Line 4 GPR data were interpreted to exist in the lower package, these reflections were interpreted as similar clinoform surfaces. A comparison of outcrop-observed clinoforms with the GPR-interpreted clinoforms in the Line 4 is shown in Figure 101 .

Comparison of GPR Interpreted Clinoforms to Outcrop

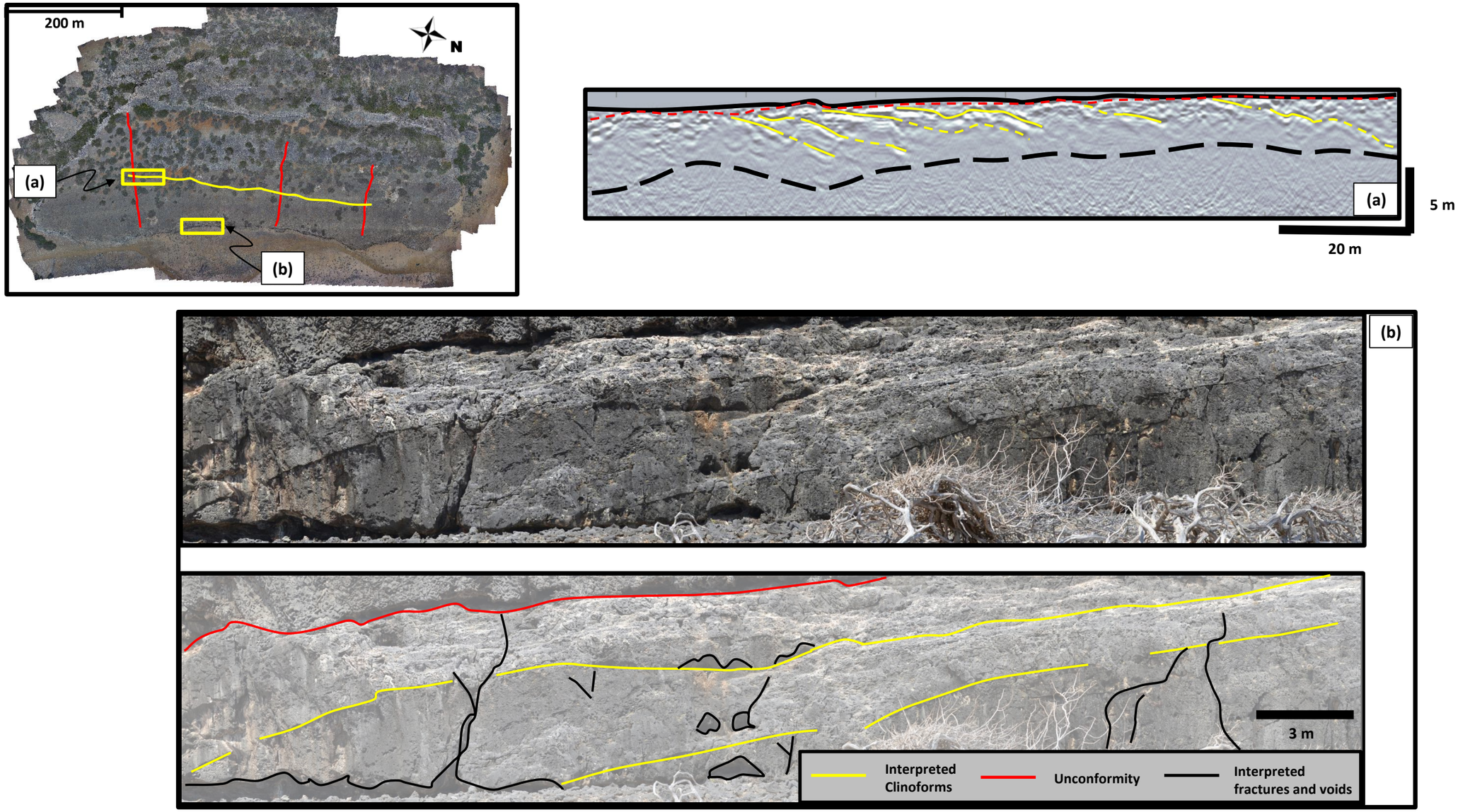

Figure 101: Comparison of GPR interpreted clinoforms to outcrop observations. Inset map in top left showing locations of **(a)-(b)**. **(a)** Interpreted clinoforms (yellow) in Line 4 (from Figure 96). **(b)** Outcrop observations of clinoforms at cliff face of Seru Grandi.

In Figure 101, the same clinoform geometries observed in outcrop can be seen in the southern end of GPR Line 4. The clinoforms observed in outcrop have been described with dips up to 20˚ [*Laya et al.*, 2017] at their steepest portions. As the full extent of the clinoforms interpreted in the Line 4 GPR data were not observed due to lack of signal penetration, steeper dips of these reflectors comparable with the clinoforms in outcrop cannot be confirmed. Significant fractures and voids can also be seen in Figure 101b. Similarly to clinoforms observed within the cross-island transect, EM scattering or reflections due to such karstic features may account for some of the discontinuities observed in the clinoform GPR reflections in Line 4 (Figure 101a). The interpretation of clinoforms in the GPR data implies that these features extend throughout the lower package at least as far landward as the southern end of Line 4. Clinoforms were observed in the GPR data only below the reflection interpreted as the unconformity between the upper and lower packages. This supports the outcrop observations that the clinoforms exist only within the lower package sediments at Seru Grandi.

7. CONCLUSIONS

This thesis describes the use of ground penetrating radar to investigate the subsurface carbonate geologies of the island of Bonaire. A detailed processing workflow was implemented for the two datasets collected on the island which focused on creating GPR images suitable for geologic interpretations.

For the regional scale investigation along the cross-island transect a modified k-means clustering algorithm was developed to aid in interpretation. This algorithm, which uses structure-parallel vectors derived from image structure tensors, classified the long continuous transect into 8 groups based on the orientations of features within the dataset. The results of the clustering were essential in determining the structural aspects of a set of radar facies after *Neal*, [2004]. By mapping these radar facies across the transect, regional-scale information about the structural geometries of the island was revealed. Specifically:

(1) The southwestern portion of the transect was shown to contain features interpreted as transitions between subtidal to foreshore lithofacies. These transitions imply relative sea-level changes during deposition of these units.

(2) The south-central portion so the transect was identified to contain radar facies suggestive of previous high-energy environments bounding a lower-energy lagoon.

These interpretations are supported by the presence of dolomite observed in the area which may have been created by hypersaline infiltration in such a lagoon.

(3) The previously mapped eolianite deposits at the top of the transect were demarked clearly in the GPR data, which provided additional evidence for such interpretations.

(4) The northeastern potion of the transect was shown to contain an abundance of radar facies attributed to clinoform geometries of platform slope deposits. These facies do not show transitional behavior with other radar facies such as the subtidal to foreshore deposits interpreted in the southeast. This implies differing controls on structural evolution of the Bonaire when comparing the modern-day leeward and windward sides of the island.

In the local scale investigation of the Seru Grandi outcrop, three-dimensional subsurface mapping was performed to identify geometries and extents of previously identified outcrop features. The unconformity exiting between the upper and lower packages of the 2nd terrace state was identified in the subsurface. Mapping and interpretation identified that this unconformity represents a wave cut platform that underwent submersion allowing for the deposition of the upper-package sediments. Observed differences in gradient between the unconformity surface and the exposed wave-cut platform defining the surface of Seru Grandi suggests differences in eternal controls during the creation of these surfaces.

In addition, observations of clinoform structures were made in the southern portion of the Seru Grandi survey. These interpreted structures were shown to exist within the lower package of the 2nd terrace strata which correlates well with observations of similar features at the outcrop cliff-face further to the west. This interpretation suggests that the clinoforms are a pervasive structure within the lower package strata.

This project represents the first geophysical investigations of the interior of the island of Bonaire. The carbonate lithology and arid climate allowed for the use of GPR, a non-traditional tool, to be used for geologic investigation. Interpretations of the data presented here suggest new insights into the geologic evolution of the island, yet they require assessment and confirmation than cannot be obtained through the GPR data in this project alone. Although large compared to other GPR surveys in general, the depths of investigation for the GPR surveys performed on Bonaire in thus study do not allow for the interpretation of deeper structures such as the carbonate/volcanic basement contact. Geophysically, potential field methods such as magnetics and gravity may be able to constrain the depth to basement along the transect. In addition, increased lithologic sampling along the bike trail would be able to support the detailed environments of deposition that were here-suggested to occur along the cross-island transect. As previously mentioned for the Seru Grandi outcrop, further work into identification and understanding of remnant features of the wave-cut platforms at the side would provide information relating to past ocean conditions and climate.

REFERENCES

Annan, A. P. (1973), Radio Interferometry Depth Sounding: Part I—Theoretical Discussion, *GEOPHYSICS*, *38*(3), 557–580, doi:10.1190/1.1440360.

Annan, A. P. (1993), Practical Processing of GPR Data, in *Proceedings of the Second Government Workshop on Ground Penetrating Radar*, Columbus, Ohio.

Annan, A. P. (1996), Transmission Dispersion and GPR, *J. Environ. Eng. Geophys.*, *1*(B), 125–136, doi:10.4133/JEEG1.B.125.

Annan, A. P. (2003), *Ground Penetrating Radar Principles, Procedure & Applications*, Sensors and Software, Mississaugua, ON, Canada.

Annan, A. P. (2009), Electromagnetic Principles of Ground Penetrating Radar, in *Ground Penetrating Radar Theory and Applications*, edited by H. M. Jol, pp. 1–40, Elsevier.

Asprion, U., and T. Aigner (2000), An Initial Attempt to Map Carbonate Buildups using Ground-Penetrating Radar: An Example from the Upper Jurassic of SW-Germany, *Facies*, *42*(1), 245–252, doi:10.1007/BF02562575.

Astrahan, M. M. (1970), *Speech Analysis by Clustering, or the Hyperphoneme Method*, Stanford, California, USA.

Bandoian, C. A., and R. C. Murray (1974), Plio-Pleistocene Carbonate Rocks of Bonaire, Netherlands Antilles, *Geol. Soc. Am. Bull.*, *85*(August), 1243–1252.

Bracewell, R. (1986), *The Fourier Transform and Its Applications*, McGraw-Hill, New York.

Bradford, J. H. (2007), Frequency-dependent Attenuation Analysis of Ground-Penetrating Radar Data, *GEOPHYSICS*, *72*(3), J7–J16, doi:10.1190/1.2710183.

Bradford, J. H., and J. C. Deeds (2006), Ground-penetrating Radar Theory and Application of Thin-bed Offset-dependent Reflectivity, *GEOPHYSICS*, *71*(3), K47–K57, doi:10.1190/1.2194524.

Brookfield, M. E. (1977), The Origin of Bounding Surfaces in Ancient Aeolian Sandstones, *Sedimentology*, *24*(3), 303–332, doi:10.1111/j.1365-3091.1977.tb00126.x.

de Buisonjé, P. . (1974), Neogene and Quaternary Geology of Aruba, Curaçao and Bonaire., Universiteit Utrecht, The Netherlands.

Cai, X., F. Nie, and H. Huang (2013), Multi-View K-means Clustering on Big Data, in *Proceedings of the Twenty-Third International Joint Conference on Artificial Intelligence*, pp. 2598–2604.

Cassidy, N. J. (2009a), Electrical and Magnetic Properties of Rocks, Soils and Fluids, in *Ground Penetrating Radar Theory and Applications*, edited by H. M. Jol, pp. 41–72, Elsevier.

Cassidy, N. J. (2009b), Ground Penetrating Radar Data Processing, Modelling and Analysis, in *Ground Penetrating Radar Theory and Applications*, edited by H. M. Jol, pp. 141–176, Elsevier.

Clarbout, J. F. (1985), *Imaging the Earth's Interior*, Blackwell Scientific Publications, Palo Alto, California.

Daniels, D. J. (Ed.) (2007), Properties of Materials, in *Ground Penetrating Radar*,

Radar, Sonar, Navigation and Avionics Series 15, pp. 73–97, The Institution of Engineering and Technology, London, United Kingdom.

Davis, J. L., and A. P. Annan (1989), Ground-Penetrating Radar for High-Resolution Mapping of Soil and Rock Stratigraphy, *Geophys. Prospect.*, *37*(5), 531–551, doi:10.1111/j.1365-2478.1989.tb02221.x.

Deffeyes, K. S., F. J. Lucia, and P. K. Weylt (1964), Dolomitization: Observations on the Island of Bonaire, Netherlands Antilles, *Science (80-.).*, *143*(3607), 678–679, doi:10.1126/science.143.3607.678.

Deffeyes, K. S., J. F. Lucia, and P. K. Weyl (1965), Dolomitization of Recent and Plio-Pleistocene Sediments by Marine Evaporite Waters on Bonaire, Netherlands Antilles, *Soc. Econ. Paleontol. Minerol.*, (SEPM Special Publication 13), 71–88.

Du, L., P. Zhou, L. Shi, H. Wang, M. Fan, W. Wang, and Y. D. Shen (2015), Robust Multiple Kernel K-means Using L2,1-Norm, in *Proceedings of the Twenty-Fourth International Joint Conference on Artificial Intelligence*, pp. 3476–3482.

Dujardin, J.-R., and M. Bano (2013), Topographic Migration of GPR Data: Examples from Chad and Mongolia, *Comptes Rendus Geosci.*, *345*(2), 73–80, doi:10.1016/j.crte.2013.01.003.

Engel, M., and S. M. May (2012), Bonaire's Boulder Fields Revisited: Evidence for Holocene Tsunami Impact on the Leeward Antilles, *Quat. Sci. Rev.*, *54*, 126–141, doi:10.1016/j.quascirev.2011.12.011.

Engheta, N., C. H. Papas, and C. Elachi (1982), Radiation Patterns of Interfacial Dipole Antennas, *Radio Sci.*, *17*(6), 1557–1566, doi:10.1029/RS017i006p01557.

Everett, M. E. (2013), Ground-penetrating Radar, in *Near-Surface Applied Geophysics*, pp. 249–293, Cambridge University Press, Cambridge.

Farr, T. G. et al. (2007), The Shuttle Radar Topography Mission, *Rev. Geophys.*, *45*(2), RG2004, doi:10.1029/2005RG000183.

Fehmers, G. C., and C. F. W. Höcker (2003), Fast structural Interpretation with Structure-oriented Filtering, *GEOPHYSICS*, *68*(4), 1286–1293, doi:10.1190/1.1598121.

Forte, E., M. Pipan, D. Casabianca, R. Di Cuia, and A. Riva (2012), Imaging and Characterization of a Carbonate Hydrocarbon Reservoir Analogue using GPR Attributes, *J. Appl. Geophys.*, *81*, 76–87, doi:10.1016/j.jappgeo.2011.09.009.

Gerlitz, K., M. D. Knoll, G. M. Cross, R. D. Luzitano, and R. Knight (1993), Processing Ground Penetrating Radar Data to Improve Resolution of Near-Surface Targets, in *Symposium on the Application of Geophysics to Engineering and Environmental Problems 1993*, pp. 561–574, Environment and Engineering Geophysical Society.

Golub, G. H., and C. F. Van Loan (1996), Matrix Analysis, in *Matrix Computations*, pp. 48–87, Johns Hopkins University Press, Baltimore, Maryland, USA.

Griffiths, D. J. (1999), *Introduction To Electrodynamics*, 3rd ed., Prentice Hall, Upper Saddle River, New Jersey.

Hale, D. (2006), Recursive Gaussian Filters, *CWP Rep.*, *546*, 269–278.

Hale, D. (2009), Structure-oriented Smoothing and Semblance, *CWP Rep.*, *635*, 261–270.

Van der Hilst, R., and P. Mann (1994), Tectonic Implications of Tomographic Images of

Subducted Lithosphere Beneath Northwestern South America, *Geology*, *22*(5), 451–454, doi:10.1130/0091-7613(1994)022<0451:TIOTIO>2.3.CO;2.

Hippolyte, J.-C., and P. Mann (2011), Neogene–Quaternary Tectonic Evolution of the Leeward Antilles Islands (Aruba, Bonaire, Curaçao) from Fault Kinematic Analysis, *Mar. Pet. Geol.*, *28*(1), 259–277, doi:10.1016/j.marpetgeo.2009.06.010.

Jain, A. K. (2010), Data Clustering: 50 Years Beyond K-means, *Pattern Recognit. Lett.*, *31*(8), 651–666, doi:10.1016/j.patrec.2009.09.011.

Jorry, S. J., and G. Biévre (2011), Integration of Sedimentology and Ground-penetrating Radar for High-resolution Imaging of a Carbonate Platform, *Sedimentology*, *58*(6), 1370–1390, doi:10.1111/j.1365-3091.2010.01213.x.

de Kleine, M. P. E., and M. A. J. Bakker (2009), Subsurface Characterization in a Karstified Limestone Area Using Ground-Penentrating Radar: Bonaire, Netherlands Antilles, in *Symposium on the Application of Geophysics to Engineering and Environmental Problems 2009*, pp. 489–498, Environment and Engineering Geophysical Society.

Laya, J. C., J. Sulaica, and M. E. Tucker (2015), Digital Outcrop Modeling of an Isolated Carbonate Platform. Stratigraphy and Diagenesis. Bonaire Dutch Caribbean Carbonate Reservoir Analogs, in *AAPG Annual Convention and Exhibition*, American Association of Petroleum Geologists, Denver, Colorado.

Laya, J. C., F. F. Whitaker, M. Tucker, and T. Gabellone (2017), Facies Control on Dolomitisation Within the Neogene Succession of Bonaire, Netherlands Antilles, in *AAPG Annual Convention and Exhibition*, Houston, Texas.

Lehmann, F., and A. G. Green (2000), Topographic Migration of Georadar Data: Implications for Acquisition and Processing, *GEOPHYSICS*, *65*(3), 836–848, doi:10.1190/1.1444781.

Lehmann, F., D. V. Mühll, M. van der Veen, P. Wild, and A. G. Green (1998), True Topographic 2-D Migration of Georadar Data, in *Symposium on the Application of Geophysics to Engineering and Environmental Problems 1998*, pp. 107–114, Environmental and Engineering Geophysical Society.

Lucia, F. J. (2007), *Carbonate Reservoir Characterization*, 2nd ed., Springer, Berlin.

MacQueen, J. (1967), Some methods for Classification and Analysis of Multivariate Observations, in *Proceedings of the Fifth Berkeley Symposium on Mathematical Statistics and Probability*, vol. 1, edited by L. M. Lecam and J. Neyman, pp. 281–297, University of California Berkeley Press, Oakland, California, USA.

Menezes, P. T. L., J. M. Travassos, M. A. M. Medeiros, and P. Takayama (2016), High-resolution Facies Modeling of Presalt Lacustrine Carbonates Reservoir Analog: Morro do Chaves Formation Example, Sergipe-Alagoas Basin, Brazil, *Interpretation*, *4*(2), SE63-SE74, doi:10.1190/INT-2014-0213.1.

Milligan, G. W. (1980), An Examination of the Effect of Six Types of Error Perturbation on Fifteen Clustering Algorithms, *Psychometrika*, *45*(3), 325–342, doi:10.1007/BF02293907.

Mitchum Jr., R. M., P. R. Vail, and J. B. Sangree (1977), Seismic Stratigraphy and Global Changes of Sea Level, Part Six: Stratigraphic Interpretation of Seismic Reflection Patterns in Depositional Sequences, in *Seismic Stratigraphy* —

applications to hydrocarbon exploration, pp. 117–134.

Neal, A. (2004), Ground-penetrating Radar and Its Use in Sedimentology: Principles, Problems and Progress, *Earth-Science Rev.*, *66*(3–4), 261–330, doi:10.1016/j.earscirev.2004.01.004.

Nuttall, A. (1981), Some Windows with Very Good Sidelobe Behavior, *IEEE Trans. Acoust.*, *29*(1), 84–91, doi:10.1109/TASSP.1981.1163506.

Olhoeft, G. R. (1998), Electrical, Magnetic, and Geometric Properties that Determine Ground Penetrating Radar Performance, in *Seventh Int'l Conf. on Ground Penetrating Radar*, pp. 177–182, Lawrence, Kansas, USA.

Reams, R. (1999), Hadamard Inverses, Square Roots and Products of Slmost Semidefinite Matrices, *Linear Algebra Appl.*, *288*, 35–43, doi:10.1016/S0024-3795(98)10162-3.

Reynolds, J. M. (1997), *An Introduction to Applied and Environmental Geophysics*, 1st ed., John Wiley & Sons Ltd, Chichester, England.

Schneider, W. A. (1978), Integral Formulation for Migration in Two and Three Dimensions, *GEOPHYSICS*, *43*(1), 49–76, doi:10.1190/1.1440828.

Sensors and Software Inc. (2016), EKKO_Project,

Shannon, C. E. (1948), A Mathematical Theory of Communication, *Bell Syst. Tech. J.*, *27*(3), 379–423, doi:10.1002/j.1538-7305.1948.tb01338.x.

Steinley, D. (2006), K-means Clustering: A Half-Century Synthesis, *Br. J. Math. Stat. Psychol.*, *59*(1), 1–34, doi:10.1348/000711005X48266.

Stoffers, A. L. (1956), The of Vegetation the Netherlands Antilles, Utrecht.

Sulacia, J., J. C. Laya, and M. E. Tucker (2015), Analysis of Carbonate Isolated Platform, Geometries and Facies Distribution of Pleistocene Carbonates in Bonaire, Southern Caribbean, in *AAPG Annual Convention and Exhibition*, Denver, Colorado.

Sulaica, J. (2015), Facies Distribution and Paleogeographic Evolution of Neogene Carbonates in Bonaire, Netherlands Antilles, Texas A&M University, College Station, Texas, USA.

Trenhaile, A. . (2000), Modeling the Development of Wave-cut Shore Platforms, *Mar. Geol.*, *166*(1–4), 163–178, doi:10.1016/S0025-3227(00)00013-X.

Trenhaile, A. S. (1987), *The Geomophology of Rock Coasts*, Oxford University Press, New York City, USA.

Trenhaile, A. S. (2005), Modelling the Effect of Waves, Weathering and Beach Development on Ahore Platform Development, *Earth Surf. Process. Landforms*, *30*(5), 613–634, doi:10.1002/esp.1166.

Vail, P. R. (1987), Seismic Stratigraphy Interpretation Using Sequence Stratigraphy Part I : Seismic Stratigraphy Interpretation Procedure, *AAPG Stud. Geol.*, *1*(27), 1–10, doi:-.

Van Vliet, L., and P. Verbeek (1995), Estimators for Orientation and Anisotropy in Digitized Images, in *Proceedings of the first Conference of the Advanced School for Computing and Imaging*, pp. 442–450, Advanced School for Computing and Imaging, Heijen, The Netherlands.

Weickert, J. (1995), Multiscale Texture Enhancement, in *Proceedings Computer*

Analysis of Images and Patterns, 6th International Conference, CAIP '95 Prague, Czech Republic, September 6–8, 1995, vol. 970, pp. 230–237.

Widess, M. B. (1973), How Thin is a This Bed?, *GEOPHYSICS*, *38*(6), 1176–1180, doi:10.1190/1.1440403.

Wiggins, J. W. (1984), Kirchhoff Integral Extrapolation and Migration of Nonplanar Data, *GEOPHYSICS*, *49*(8), 1239–1248, doi:10.1190/1.1441752.

Yilmaz, Ö. (2001), *Seismic Data Analysis*, Society of Exploration Geophysicists.